

Conceptual Design Report
for
Experimental Search for Lepton Flavor Violating $\mu^- - e^-$
Conversion at Sensitivity of 10^{-16}
with a Slow-Extracted Bunched Proton Beam
(COMET)

J-PARC P21

June 23, 2009

The COMET Collaboration

Y.G. Cui, R. Palmer

Department of Physics, Brookhaven National Laboratory, USA

Y. Arimoto, Y. Igarashi, S. Ishimoto, S. Mihara, T. Nakamoto, H. Nishiguchi, T. Ogitsu,
 C. Omori, N. Saito, M. Tomizawa, A. Yamamoto, K. Yoshimura
High Energy Accelerator Research Organization (KEK), Tsukuba, Japan

P. Dornan, P. Dauncey, U. Egede, A. Kurup, J. Pasternak, Y. Uchida,
Imperial College London, UK

Y. Iwashita

Institute for Chemical Research, Kyoto University, Kyoto, Japan

V. Kalinnikov, A. Moiseenko, D. Mzhavia, J. Pontecorvo, B. Sabirov, Z. Tsamaiadze, and
 P. Evtukhovich
Joint Institute for Nuclear Research (JINR), Dubna, Russia

M. Aoki, Md.I. Hossain, T. Itahashi, Y. Kuno*, E. Matsushita, N. Nakadozono, A. Sato,
 S. Takahashi, T. Tachimoto, M. Yoshida,
Department of Physics, Osaka University, Osaka, Japan

M. Koike, J. Sato, M. Yamanaka

Department of Physics, Saitama University, Japan

Y. Takubo

Department of Physics, Tohoku University, Japan

D. Bryman

*Department of Physics and Astronomy, University of British Columbia, Vancouver,
 Canada*

R. D'Arcy, M. Lancaster, M. Wing

Department of Physics and Astronomy, University College London, UK

E. Hungerford

Department of Physics, University of Houston, USA

T. Numao

TRIUMF, Canada

* Contact Person

Contents

1 Executive Summary	9
1.1 Response on the J-PARC PAC questions on March 6, 2009	10
2 Physics Motivation	13
2.1 Introduction	13
2.1.1 History I — the establishment of the concept of lepton flavor	13
2.1.2 History II — the discovery of lepton flavor violation in neutrinos . .	14
2.2 New physics and μ^-e^- conversion	15
2.3 Supersymmetric models	16
2.3.1 General feature	16
2.3.2 Models with the seesaw mechanism	17
2.4 Little Higgs models	18
2.5 Extra dimensional models	20
2.5.1 Anarchic Randall-Sundrum model	20
2.5.2 UED models	21
2.6 μ^-e^- conversion at LHC era	22
2.7 Phenomenology of μ^-e^- conversion	23
2.7.1 What is a μ^-e^- conversion process ?	23
2.7.2 Signal and background events	23
2.7.3 μ^-e^- conversion vs. $\mu^+ \rightarrow e^+\gamma$	24
2.8 Present experimental status	24
2.8.1 μ^-e^- conversion	24
2.8.1.1 SINDRUM-II	25
2.8.1.2 MECO	26
2.8.1.3 Mu2e	26
2.8.2 $\mu^+ \rightarrow e^+\gamma$ Decay	28
2.8.3 Why is μ^-e^- conversion the next step ?	28
3 Overview of COMET	30
3.1 Introduction to the COMET experiment	30
3.2 Advantages of the COMET experiment	32
3.3 Summary of signal sensitivity and backgrounds	32
4 Proton Beam	34
4.1 Requirements for the proton beam	34
4.1.1 Proton energy	34
4.1.2 Proton beam power	35

4.1.3	Proton time structure	35
4.2	Proton accelerator operation	37
4.2.1	Proton linac operation	37
4.2.2	RCS operation	38
4.2.2.1	Choice of harmonic number	38
4.2.2.2	Emittance control	39
4.2.3	Main ring operation	39
4.2.3.1	Collimator setting	40
4.2.3.2	Beam emittance at 8 GeV	40
4.2.3.3	Bunched slow beam extraction	41
4.3	Proton beam transport	43
4.3.1	Proton beam optics design	43
4.3.1.1	Matching section	44
4.3.1.2	AC dipole section	44
4.3.1.3	Final focusing section	47
4.3.2	G4beamline simulation	48
4.3.3	Proton beam line hardware	61
4.3.4	Magnet system	61
4.3.5	Power supply system	61
4.3.6	Vacuum system	61
5	Muon Beam	63
5.1	Pion production	63
5.1.1	Pion production yields	63
5.1.2	Comparison of different hadron production codes	65
5.1.3	Pion production target	65
5.1.3.1	Target material	65
5.1.3.2	Target length and radius	66
5.1.3.3	Target tilt angle	67
5.1.3.4	Target heating	67
5.2	Pion capture	69
5.2.1	Pion capture in a solenoidal magnetic field	69
5.2.2	Layout of the pion capture system	70
5.2.2.1	Superconducting solenoid design	71
5.2.2.2	Radiation heating and radiation dose	72
5.2.3	Adiabatic transition from high to low magnetic fields	72
5.3	Muon transport	73
5.3.1	Requirements for muon transport	73
5.3.2	Beam optics of curved solenoids	74
5.3.2.1	Dispersive beam shifts in curved solenoids	74
5.3.2.2	Dipole fields for drift compensation	75
5.3.3	Curved solenoid tuning	76
5.3.3.1	G4beamline field distribution	77
5.3.3.2	EM studio field distribution	78
5.3.3.3	Particle tracking	79
5.3.3.4	Curved solenoid tuning conclusions	80
5.3.4	Muon beam collimators	81
5.3.5	Distributions of the muon beam	81

5.3.5.1	Momentum distributions	81
5.3.5.2	Time distributions	82
5.3.5.3	Muon momentum dispersion	82
5.3.5.4	Muon beam transverse profiles	83
5.3.6	Late-arriving particle tagger	83
5.3.7	Specifications of magnets in the muon beam line	85
6	Detector	91
6.1	Muon-stopping target	91
6.1.1	Material for muon-stopping target	92
6.1.2	Geometrical configuration of the muon-stopping target	92
6.1.3	Graded magnetic field at the muon-stopping target	93
6.1.4	Muon stopping efficiency	94
6.1.5	Energy loss of outgoing electrons	94
6.2	Muon beam stop	94
6.3	Electron transport solenoid	95
6.3.1	Requirements for electron transport	95
6.3.2	Curved solenoid in electron transport	97
6.3.2.1	Compensation dipole field	98
6.3.3	Radius of the electron transport solenoid	98
6.3.4	Decay-in-orbit background rate	98
6.3.5	Decay-in-orbit (DIO) blocking slit	99
6.3.6	Electron transport acceptance	99
6.4	Detector solenoid	100
6.5	Electron tracker	101
6.5.1	Overview	101
6.5.2	Design of the electron tracker	103
6.5.3	Expected performance of the electron tracker	104
6.5.4	Response of the straw detector to ionizing events	107
6.5.5	Pulse saturation and pile-up	111
6.5.5.1	Backgrounds induced by pattern recognition errors	111
6.5.6	Mechanical construction and maintenance	111
6.5.6.1	Anode wire and wire supports	115
6.5.6.2	Drift gas	116
6.5.6.3	Deformation of straw tubes	117
6.5.7	Straw operation in vacuum	119
6.5.8	Readout electronics	119
6.5.8.1	DAQ architecture	119
6.5.8.2	Front end ICs	120
6.5.8.3	Digitizer	121
6.5.8.4	Tracker readout	122
6.5.8.5	Data rates	123
6.5.8.6	Signal bus lines	123
6.5.8.7	Cable and connections	123
6.5.8.8	Mounting and servicing	124
6.5.8.9	Transmitted data structure	124
6.5.8.10	Low voltage cower and cooling	125
6.5.8.11	High voltage	125

6.6	Electron calorimeter	126
6.6.1	Overview	126
6.6.2	Crystal selection	126
6.6.3	Photon detector	127
6.6.3.1	Avalanche photodiode	127
6.6.3.2	Multi pixel photon counter	128
6.6.4	Electronics	128
6.6.5	Performance	129
6.7	Detector rates	132
6.7.1	Decay-in-Orbit (DIO) electrons	132
6.7.2	Back scattering electrons	133
6.7.3	Beam flash muons	134
6.7.3.1	Muon decays in the electron calorimeter	134
6.7.4	Particle and photon emission from nuclear muon capture	134
6.7.4.1	Protons from muon nuclear capture	135
6.7.4.2	Neutrons from muon nuclear capture	135
6.7.5	Target bremsstrahlung	135
6.7.6	Cosmic muons	135
6.8	Muon intensity monitor	135
7	Cosmic Ray Shield	137
7.1	Outer shield	137
7.2	Inner shield	138
7.3	Cosmic active veto system	138
8	Data Acquisition System	139
8.1	Basic trigger concept	139
8.2	Data acquisition	140
8.2.1	Data flow rate estimation	140
8.3	Network based DAQ system	141
9	Simulation and Analysis	142
9.1	Software requirements	142
9.1.1	Proton beam and pion production	142
9.1.2	Particle transport	143
9.1.3	Particle interactions	143
9.1.4	Detector simulation	143
9.1.5	Simulation framework	144
9.2	Present status and future plans	144
10	Calibration System	146
11	Sensitivity and Backgrounds	148
11.1	Signal Sensitivity	148
11.1.1	Muon yields	148
11.1.2	Total signal acceptance	148
11.1.3	Geometrical acceptance	149
11.1.3.1	Solid angle with a magnetic mirroring effect	149

11.1.3.2 The muon beam stop	150
11.1.3.3 The electron transport	150
11.1.4 Acceptance in the event selections	151
11.1.4.1 Track reconstruction	151
11.1.4.2 Track quality	151
11.1.4.3 Transverse momentum	151
11.1.4.4 E/p ratio	151
11.1.4.5 Helix pitch	151
11.1.4.6 Electron momentum	151
11.1.4.7 Time window of the measurement	152
11.1.5 Single event sensitivity	153
11.2 Background rejection	157
11.2.1 Intrinsic physics background	158
11.2.1.1 Muon decay in orbit	158
11.2.1.2 Radiative muon capture	160
11.2.1.3 Muon capture with neutron emission	161
11.2.1.4 Muon capture with charged particle emission	162
11.2.2 Beam-related prompt background	164
11.2.2.1 Radiative pion capture	164
11.2.2.2 Beam electrons	166
11.2.2.3 Muon decay in flight	167
11.2.2.4 Pion decay in flight	167
11.2.2.5 Neutron induced background	167
11.2.3 Beam related delayed background	168
11.2.3.1 Radiative capture of delayed pions	168
11.2.4 Cosmic ray background	168
11.2.4.1 Electrons induced by cosmic muons	169
11.2.4.2 Direct hit of cosmic muons	169
11.2.5 Summary	171
12 Superconducting Solenoid	172
12.1 Pion capture solenoids	172
12.1.1 Pion capture solenoid layout	172
12.1.2 Conductor choice and quench protection	172
12.1.3 Influence of radiation	175
12.2 Muon transport solenoids	176
12.2.1 Conductor choice	176
12.2.2 Quench protection	176
12.2.3 Negative field gradient at the muon transport	176
12.3 Muon-stopping target solenoid	177
12.4 Cryogenics system for capture, transport and target solenoids	177
12.5 Electron transport solenoid and detector solenoid	177
12.5.1 Conductor choice	177
12.6 Alternative magnet design	179

13 Experimental Layout	181
13.1 Layout at the NP hall	181
13.2 Proton beam dump	182
13.3 Radiation safety and radiation shielding	183
13.4 Magnetic field safety	184
13.5 Infrastructure	184
13.5.1 Power requirements	184
13.5.2 Cooling water requirement	185
13.5.3 Refrigeration Requirement	186
14 Cost Estimate	188
14.1 Superconducting solenoids	188
14.2 Proton beam line	189
14.3 Civil construction and infrastructure	190
14.4 Detectors	190
14.5 Summary of cost estimate	190
15 Schedule	192
15.1 Technical design report	192
15.2 Main ring	192
15.3 Proton transport line	192
15.4 Magnets and pion production target	193
15.5 Experimental area	193
15.6 Detector	193
15.7 Data acquisition	193
15.8 Simulation	193
15.9 Offline analysis	194
16 R&D Plan	196
16.1 Measurement of intrinsic proton beam extinction	196
16.2 Electron tracker	197
16.3 Electron calorimeter	197
16.4 Cosmic veto system	198
16.5 Superconducting magnet	199
16.6 Pion production target	199
17 Summary	201

Chapter 1

Executive Summary

This report presents the conceptual design of a new experiment, COMET (COherent Muon to Electron Transition), to search for coherent neutrino-less conversion of muons to electrons ($\mu^- - e^-$ conversion), in the presence of a nucleus, $\mu^- + N(A, Z) \rightarrow e^- + N(A, Z)$, with a single event sensitivity $B(\mu^- N \rightarrow e^- N) < 10^{-16}$.

Flavor transitions between the charged leptons (Charged Lepton Flavor Violation, cLFV) have great potential to reveal new physics phenomena beyond the Standard Model. Many models of such physics, such as those based on supersymmetric grand unification (SUSY-GUT), supersymmetric seesaws (SUSY-Seesaw) and extra dimensions, require the existence of cLFV that is accessible to realizable future experiments.

Muons provide the best laboratory to study cLFV as they can be produced in substantial numbers and have a sufficiently long lifetime for precise measurements of their decays. Present accelerators can produce about 10^{15} muons/year, and it is anticipated that it will be possible to produce 10^{18} - 10^{19} muons/year with a new high intensity source that is proposed in conjunction with the main J-PARC proton synchrotron ring (MR).

The main processes which are accessible for cLFV are the decays $\mu \rightarrow e\gamma$, $\mu \rightarrow eee$ and $\mu^- - e^-$ conversion. Of these, $\mu^- - e^-$ conversion has the best sensitivity to new physics, as the potentially measurable branching ratio of about 10^{-16} is significantly better than the limits expected with current technology for the $\mu \rightarrow e\gamma$, $\mu \rightarrow eee$ processes. Within the Standard Model, modified to take account of neutrino oscillation, the expected rate is less than 10^{-50} and so any observation of a $\mu^- - e^-$ conversion would be a clear signal of physics beyond the Standard Model. A measurement $\leq 10^{-16}$ for $\mu^- - e^-$ conversion, which is the COMET goal, is a factor of 10,000 better than that of current experiments.

COMET will use a bunched proton beam, slow-extracted from the J-PARC MR. Beam bunching will be necessary to reject beam-related backgrounds. The experimental setup consists of high magnetic-field solenoids for pion capture, C-shaped curved solenoids with momentum selection, and a C-shaped curved solenoid spectrometer. The experiment will require about 2×10^{18} stopping muons, which, with the expected transmission of muons in our muon beamline, will require about 8.5×10^{20} 8 GeV protons on target.

In the chapters that follow, details of the physics motivation and the conceptual design of the components needed for the COMET experiment are presented, together with a possible layout, a preliminary cost estimation, and a technology-limited schedule.

1.1 Response on the J-PARC PAC questions on March 6, 2009

In the J-PARC PAC report dated as 6th March 2009, the four questions and concerns, which should be addressed in the present CDR, were given. Brief comments to the four questions and concerns are presented in the following.

- 1. The COMET proponents should present the experiment's sensitivity as a function of time with a total exposure of 8×10^{20} protons on target.**

The updated single event sensitivity of 2.6×10^{-17} is estimated for 8.5×10^{20} protons, as shown in Table 11.3. A proton exposure of 8.5×10^{20} corresponds to about 2×10^7 seconds with the average beam current in the proton beam line of $7 \mu\text{A}$. When no signal events nor background events are found, the single event sensitivity should be improved linearly with the amount of proton exposure.

- 2. The CDR should serve as basis for a plausible cost range and operations schedule. The COMET proponents and the MTF should present a breakdown of the elements of the cost range as well as drivers and milestones for a plausible schedule. The cost and schedule estimate should include accelerator modifications, required beamlines, detector elements and civil construction.**

The cost estimate of the COMET experiment is given in Chapter 14. The estimated cost ranges from about 75 Oku Japanese yen to 90 Oku Japanese yen. The breakdown of the cost elements, which includes accelerator modifications, a required proton beam line, a muon beam line, the detector element, and civil construction, is presented in Chapter 14. These costs were made with assistance from the Muon Task Force (MTF) group. In particular, the experiment layout and civil construction, which are summarized in Chapter 13, is based on discussions with the MTF.

A plausible schedule for construction and operation is given in Chapter 15. A preferable construction schedule would start from year 2012 and last 4 years. A modest budget in year 2011 is required. The period of construction of superconducting magnets is expected to be 3 years with one preceding year to manufacture superconductor wire.

A COMET run period from year 2016 to 2018 is considered. In the first year, we plan an engineering run of about 1/10 of the total proton exposure (8×10^{19}), followed by two physics runs, each of which with a proton exposure of about 3.8×10^{20} in the two year period of 2017 and 2018. If the COMET run period is significantly delayed from this schedule, it would be difficult for COMET to be competitive with the Fermilab Mu2e experiment.

- 3. The COMET proponents should present a plausible plan for how collaboration resources, cooperative agreements with the Fermilab Mu2 collaboration, KEK resources, J-PARC resources and industry can provide the resources required to meet the schedule and performance goals of the experiment.**

Regarding the resources in the COMET collaboration, each of the international groups in the COMET collaboration will start to prepare and submit their funding requests. It would be difficult for them to obtain funding without a stage-1 scientific approval of COMET by the J-PARC PAC. Furthermore, it would be easier with a stage-1 scientific approval for COMET to acquire more collaborators. Therefore, the stage-1 scientific approval is considered to be the most important milestone to obtain collaboration resources and to expand the collaboration.

Under the US-Japan cooperative program, COMET and Mu2e are collaborating in two R&D programs. These are the problem of proton beam extinction and the design of superconducting solenoids. The budget size is in the order of 100 k US\$. Recently the agreement “Joint efforts with the Fermilab Mu2e collaboration” was signed, and joint work on selected items, R&D and design, will start soon. The budget size for COMET under the US-Japan cooperative program will be increased before the Tevatron shut down, and we are expecting support from KEK for this work.

The hardware design related to accelerator modification, a proton beam line, and civil construction would be done with KEK experts. As shown in Chapter 15, the basic design of a proton beam line and an extension of the experimental hall should be completed by the end of Japanese fiscal year of 2010, so that a budget request can be made for the Japanese fiscal year of 2012. In terms of tests of proton extinction, engineering support on the design and fabrication of AC dipole magnets should be available in 2011.

With very cooperative support from the KEK cryogenic center, the design of the superconducting solenoid has been developed. Recently a magnet-manufacture company has become involved in the design work. In this field, the COMET collaboration has received tremendous help from KEK. The next stages should be some prototyping which requires significant budgetary support from KEK.

4. What are the relative strengths/weakness of the proposed COMET and Mu2e experiments ? What are the strategic advantages and risks of the both experiments going forward and making measurements ?

The COMET design is more advanced, The advantages of the COMET design are summarized in Chapter 3. In short, the COMET design has the following advantages. They are

- a **C-shape muon transport** in the muon beam line (from the pion production to the muon-stopping target), which would produce a large dispersion of the muon beam. As a result, momentum selection would be better, and
- a **C-shape electron transport** in the COMET spectrometer (from the muon-stopping target to the detector), which would suppress low-energy background events like decay-in-orbit (DIO) electrons and particularly protons from nuclear muon capture. As a result, the detector rate would be reduced significantly and a probability of mis-tracking is highly suppressed. *At the same time, it is not necessary to have a proton absorber.* Mu2e must shield their electron spectrometer from protons produced in nuclear capture of stopping muons so that COMET will yield a better energy resolution for electron detection. Also because of suppression of low-energy particles, the detector geometry can be

made simpler, such as a setup of straw-chamber planes transverse to the field axis and an electron calorimeter whose front face is perpendicular to the field axis.

The COMET design is based and tested on on-going R&D programs of the critical elements for the COMET beam line and detector. For instance, prototyping of superconducting coils for the muon transport by the MUSIC project at Osaka University, proton extinction measurements and others.

Potential strategic advantages of both COMET and Mu2e proceeding parallel is that one can confirm or refute the finding of the other experiment. Particularly if a signal is seen, an additional experiment will be required to confirm such a significant result. In addition, it is possible that one of the experiments, which have significant differences, may not succeed in reaching the proposed level of sensitivity due to technical or experimental limitations of the design. A potential risk is the division of resources such that neither experiment could be successful.

Chapter 2

Physics Motivation

2.1 Introduction

The origin of the flavors of elementary particles is a puzzling enigma. Their properties and structure should reflect the nature of the physics beyond the Standard Model (SM). Flavor physics is thereby believed to provide a path to the new physics. The flavor-changing neutral current (FCNC) processes are of particular interest since they are expected to include the effect of new physics that are observable in high-precision experiments. Among the FCNC processes, the charged lepton flavor violation (LFV) processes has recently attracted much attention from both theoretical and experimental points of views. The search for LFV processes has notable advantages, including the following. (1) LFV can have **sizable contributions from new physics** and thus can manifest themselves in future experiments. (2) LFV gives **no sizable contribution in the Standard Model** unlike the FCNC process of the quarks; such contributions give serious background events and limit the sensitivity to the new physics.

2.1.1 History I — the establishment of the concept of lepton flavor

“Can a muon convert into an electron ?” This has been a big question since 1937, when the muon was first discovered[1]. Its mass was about 200 times heavier than the electron’s, and hence at first it was conjectured to be Yukawa’s meson[2]. Soon afterwards, however, it was found that its lifetime was too long and its interaction cross section too weak for it to be the Yukawa meson[3, 4]. This led to the idea of two mesons, which was the first theoretical notion of the muon[5, 6]. The leptonic nature of the muon was soon confirmed experimentally[7]. Furthermore, masses aside, the nature of the muon and the electron were found to be quite similar[8].

“Who ordered that?”, the famous comment by Rabi, suggests how puzzling the existence of the new lepton was at that time. It was considered that the muon could be an excited state of the electron. If this were correct, a consequence of this would be that the muon should decay into an electron and a photon. In 1947 Hincks and Pontecorvo[9] experimentally searched for the process $\mu^+ \rightarrow e^+ + \gamma$. This was the first search for lepton flavor violation of charged leptons (cLFV). They found a negative result and set an upper bound for the branching ratio of this process of less than 10%. Almost at the same time, it was suggested that the muon could decay into three particles[10]. One of them would be the electron and the others two neutral particles, namely neutrinos. Note that the neutrinos were assumed to be identical — thus far, the concept of lepton flavor had not arisen.

Since then, successive searches for muon LFV have been carried out, for example for the neutrinoless $\mu^- - e^-$ conversion process ($\mu \rightarrow e; N$, with N a nuclei), and $\mu \rightarrow e + \gamma$ [11, 12, 13]. All the results were negative and set strong limits on these branching ratios.

Such a stringent limit on muon decay led to the idea that there are two kinds of neutrino[14, 15]. This was the first notion of lepton flavor — muon flavor (L_μ) and electron flavor (L_e). This was verified experimentally at Brookhaven National Laboratory (BNL) by observing that only muons were produced by neutrinos which come directly from pion decay[16].

Then the concept of generations of particles was developed[17]. It was extended to three generations[18] and hence the concept of lepton flavor was also extended to include a third flavor, the tau L_τ . All ideas are finally integrated into the Standard Model (SM), in which lepton flavor conservation is guaranteed by an exact symmetry, owing to massless neutrinos.

2.1.2 History II — the discovery of lepton flavor violation in neutrinos

Following the initial quest for cLFV, searches with various elementary particles, such as muons, taus, kaons, and others have been carried out. The upper limits have been improved at a rate of two orders of magnitude per decade, as can be seen in Figure 2.1. The present upper limits of various LFV decays are listed in Table 2.1, where it can also be seen how high the sensitivity of the muon system is to LFV. This is mostly because of the large number of muons available for present experimental searches (about $10^{14} - 10^{15}$ muons/year). Moreover, an even greater number of muons (about $10^{19} - 10^{20}$ muons/year) will be available in the future, if new highly intense muon sources are realized.

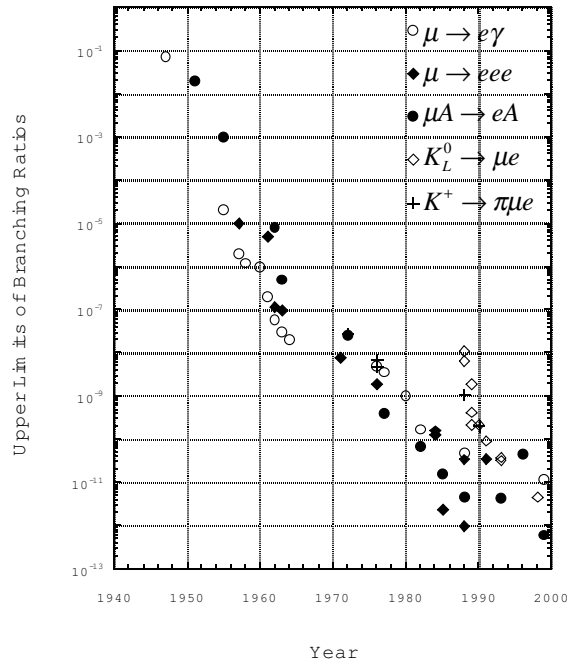


Figure 2.1: History of searches for LFV in muon and kaon decays

While all of these earlier searches gave negative results for LFV, LFV among neutrino species has been experimentally confirmed with the discovery of neutrino oscillations[33, 34],

Table 2.1: Present limits of LFV of the muon, tau, pion, kaon and Z boson.

Reaction	Present limit	Reference
$\mu^+ \rightarrow e^+ \gamma$	$< 1.2 \times 10^{-11}$	[19]
$\mu^+ \rightarrow e^+ e^+ e^-$	$< 1.0 \times 10^{-12}$	[20]
$\mu^- Ti \rightarrow e^- Ti$	$< 6.1 \times 10^{-13}$	[21]
$\mu^- Au \rightarrow e^- Au$	$< 7 \times 10^{-13}$	[22]
$\mu^+ e^- \rightarrow \mu^- e^+$	$< 8.3 \times 10^{-11}$	[23]
$\tau \rightarrow e\gamma$	$< 3.9 \times 10^{-7}$	[24]
$\tau \rightarrow \mu\gamma$	$< 3.1 \times 10^{-7}$	[25]
$\tau \rightarrow \mu\mu\mu$	$< 1.9 \times 10^{-7}$	[26]
$\tau \rightarrow eee$	$< 2.0 \times 10^{-7}$	[26]
$\pi^0 \rightarrow \mu e$	$< 8.6 \times 10^{-9}$	[27]
$K_L^0 \rightarrow \mu e$	$< 4.7 \times 10^{-12}$	[28]
$K^+ \rightarrow \pi^+ \mu^+ e^-$	$< 2.1 \times 10^{-10}$	[29]
$K_L^0 \rightarrow \pi^0 \mu^+ e^-$	$< 3.1 \times 10^{-9}$	[30]
$Z^0 \rightarrow \mu e$	$< 1.7 \times 10^{-6}$	[31]
$Z^0 \rightarrow \tau e$	$< 9.8 \times 10^{-6}$	[31]
$Z^0 \rightarrow \tau\mu$	$< 1.2 \times 10^{-5}$	[32]

and lepton flavor conservation is now known to be violated. The phenomenon of oscillation means that neutrinos are massive and hence the SM must be modified so that neutrinos are massive and LFV can occur. Furthermore, there are other reasons which compel us to modify the SM, including the existence of dark matter, and stability of the weak scale against quantum corrections. These indicate that new physics beyond the SM will reveal itself at TeV scale. This scale is within the scope of the Large Hadron Collider and expected cLFV experiments including COMET.

2.2 New physics and $\mu^- - e^-$ conversion

Charged LFV has not been observed experimentally. Indeed, it is well known that in the minimally extended SM, which includes vanishingly small neutrino masses to account for neutrino oscillation, the predicted rate for cLFV is too small to be observed. For example, the prediction for $\text{Br}(\mu \rightarrow e\gamma)$ is given by the graph in Figure 2.2 [35, 36, 37, 38],

$$\text{Br}(\mu \rightarrow e\gamma) = \frac{\alpha}{2\pi} \left| \sum_k U_{ek} U_{\mu k}^* \frac{m_{\nu_k}^2}{m_W^2} \right|^2 \simeq \frac{\alpha}{2\pi} \left| U_{e3} U_{\mu 3}^* \frac{\delta m_{\text{atm}}^2}{m_W^2} \right|^2 < 10^{-54}. \quad (2.1)$$

Here $U_{\beta i}$ is the Maki-Nakagawa-Sakata Matrix[17] with β denoting a charged lepton flavor eigenstate and i a neutrino mass eigenstate with mass m_i , and m_W is the W boson mass, and α is the fine structure constant. Note that the GIM mechanism[39] leads to a prediction dependent on differences in the masses of the neutrinos. For the $\mu \rightarrow e\gamma$ process, a similar suppression arises due to gauge symmetry.

Therefore, the discovery of LFV would imply new physics beyond not only the SM but also beyond “neutrino oscillations”. In fact, all new physics or interactions beyond the Standard Model would predict LFV at some level. Examples of such new physics models

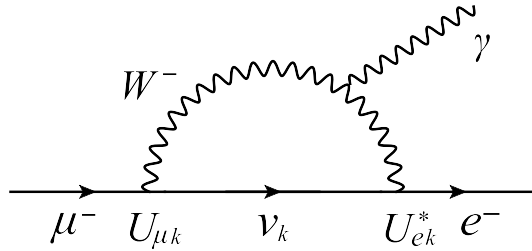


Figure 2.2: One of the diagrams of massive neutrino contributions to a μ to e transition ($\mu \rightarrow e \gamma$).

include supersymmetric (SUSY) models, extra dimension models, little Higgs models, models with new gauge bosons Z' , models with new heavy leptons, lepto-quark models and etc.. Each gives a prediction for flavor changing neutral currents (FCNC), including cLFV. In the following three subsections, we discuss relations between $\text{Br}(\mu \rightarrow e\gamma)$ and $\text{Br}(\mu \rightarrow e; N)$ for several new physics models.

Although expected at the LHC, discrimination of these new physics models will be very difficult[40]. The search for $\mu^- - e^-$ will be crucial in discriminating between these models, and it is especially synergistic with the $\mu \rightarrow e\gamma$ search. Thus the argument for studying the physics of cLFV throughout the next decade is very robust[41].

2.3 Supersymmetric models

2.3.1 General feature

Supersymmetric extensions to the SM are the leading candidates for physics beyond the SM. In this class of model, a form of parity, called R-parity, is often imposed to suppress FCNC, rapid proton decays and other phenomena. In this case the source for cLFV is the soft mass matrix ($m_{\tilde{l}}^2$) for sleptons, the scalar partners of the leptons. In principle, this can be arbitrary and a large FCNC can be introduced. However strong constraints are imposed on these parameters. For example, the branching ratio of $\mu \rightarrow e + \gamma$ is given similarly with Eq. (2.1) by

$$\text{Br}(\mu \rightarrow e\gamma) = \frac{\alpha}{2\pi} \left| \sum_k \tilde{U}_{ek} \tilde{U}_{\mu k}^* \frac{\delta m_k^2}{m_S^2} \right|^2 \left(\frac{m_W}{m_S} \right)^4, \quad (2.2)$$

where m_S is the typical scale of scalar masses, \tilde{U} denotes the mixing matrix between sleptons and leptons, and δm_k^2 is the mass squared difference between the k^{th} and the 1st sleptons. To suppress this, the conditions that, by some mechanism, \tilde{U} is almost diagonal and/or δm_k^2 is small enough compared with m_S^2 have to be assumed. To implement these conditions at the weak scale, it is often assumed that at a certain scale M_G ,

$$\tilde{U} = 1 \text{ and } \delta m_k^2 = 0, \quad (2.3)$$

and an observable effect arises as a radiative correction. As a result, $\tilde{U} \simeq 1$ and $\delta m_k^2 \simeq 0$ are maintained at the weak scale.

Under this condition, the SUSY contribution to a muon-to-electron transition ($\mu \rightarrow e \gamma$) is given by Figure 2.3, where the mixing between a smuon ($\tilde{\mu}$) and a selectron (\tilde{e}) is denoted by $\Delta m_{\tilde{\mu}\tilde{e}}^2$, and plays a key role.

This slepton mixing parameter, $\Delta m_{\tilde{\mu}\tilde{e}}^2$ (or similarly $\Delta m_{\tilde{e}\tilde{\mu}}^2$) is given by the off-diagonal element of the slepton mass matrix ($m_{\tilde{l}}^2$) that is given in Eq. (2.4)¹.

$$m_{\tilde{l}}^2 = \begin{pmatrix} m_{\tilde{e}\tilde{e}}^2, \Delta m_{\tilde{e}\tilde{\mu}}^2, \Delta m_{\tilde{e}\tilde{\tau}}^2 \\ \Delta m_{\tilde{\mu}\tilde{e}}^2, m_{\tilde{\mu}\tilde{\mu}}^2, \Delta m_{\tilde{\mu}\tilde{\tau}}^2 \\ \Delta m_{\tilde{\tau}\tilde{e}}^2, \Delta m_{\tilde{\tau}\tilde{\mu}}^2, m_{\tilde{\tau}\tilde{\tau}}^2 \end{pmatrix} \quad (2.4)$$

Therefore, the determination of these SUSY contributions would enable us to study the structure of the slepton mass matrix, and then more importantly the “SUSY soft breaking” that is the origin of SUSY particle masses. It should be noted that the slepton mixing is difficult to study, as precisely as in cLFV studies, at high energy collider experiments such as the LHC. Hence, studies of cLFV would provide a **unique opportunity to study slepton mixing**. In the following, the SUSY contributions to LFV are presented in more detail.

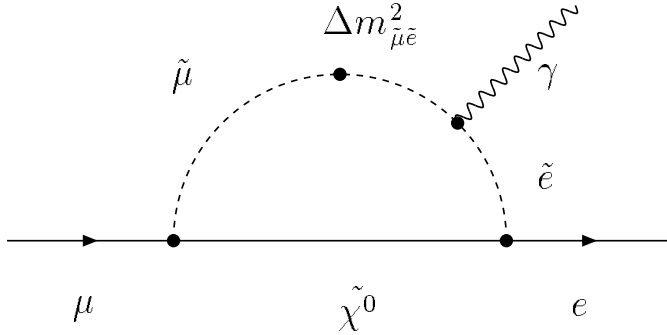


Figure 2.3: One of the diagrams of SUSY contributions to a μ to e transition ($\mu \rightarrow e \gamma$). $\Delta m_{\tilde{\mu}\tilde{e}}^2$ indicates the magnitude of the slepton mixing.

2.3.2 Models with the seesaw mechanism

There are several mechanisms which give the conditions in Eq. (2.3). Among these, gravity-mediated soft breaking is the most often employed. It gives the conditions in Eq. (2.3) at the gravity scale (=Planck, $\sim 10^{19}$ GeV) or grand unified scale ($\sim 10^{16}$ GeV). Non-zero off-diagonal matrix elements can then be induced by radiative corrections from M_G to the weak scale ($\sim 10^2$ GeV).

To reproduce lepton mixing and the neutrino masses, the seesaw mechanism[42] has been studied most extensively. In this mechanism, three right-handed neutrinos N_i are introduced. Mass terms for the neutrinos are given by the Yukawa coupling between the lepton doublets (L_α) and the right-handed neutrinos and the Majorana mass term for the right-handed neutrinos:

$$W = \bar{N}_i f_\nu^{i\alpha} L_\alpha H_u + \frac{1}{2} \bar{N}_i M_{R_i} \bar{N}_j. \quad (2.5)$$

¹It is noteworthy that the SUSY contributions to the muon $g - 2$ and the muon electric dipole moments are the real and an imaginary parts of the diagonal element $m_{\tilde{\mu}\tilde{\mu}}^2$, respectively.

It induces Eq. (2.4)[43]

$$(\Delta m_L^2)_{\alpha\beta} \simeq -\frac{(6+a_0^2)m_0^2}{16\pi^2}(f_\nu^\dagger f_\nu)_{\alpha\beta} \log \frac{M_G}{M_R}. \quad (2.6)$$

Here m_0 denotes the SUSY breaking scale and a_0 , a parameter for A term breaking, is an $O(1)$ parameter.

Thus in a SUSY model with the seesaw mechanism, slepton mixing can be induced from neutrino mixing. LFV processes in muon decays are then also expected to occur[44, 45, 46]. An example of the branching ratio is shown in Figure 2.4.

$\mu \rightarrow e\gamma$ in the MSSMRN with the MSW large angle solution

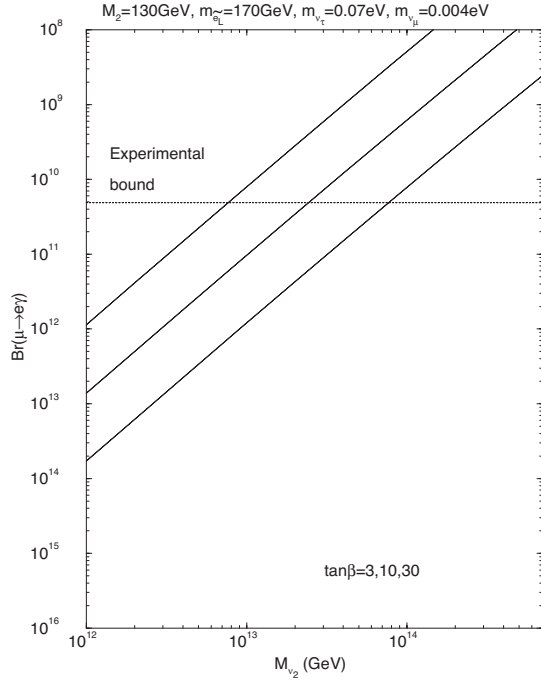


Figure 2.4: Predictions of $\mu^+ \rightarrow e^+\gamma$ branching ratio in SUSY-seesaw models. The three lines correspond to the cases of $\tan\beta = 30, 10, 3$ from top to bottom, respectively. Taken from[45].

The most important result here is the robust relation between the branching ratio of $\mu \rightarrow e + \gamma$ and that of μ to e conversion. In this model, $\mu^- - e^-$ conversion is dominated by a dipole operator similar to Figure 2.3, with a quark line attached at the other end of the photon line. Therefore the important relation[47]

$$\frac{\text{Br}(\mu \rightarrow e; N)}{\text{Br}(\mu \rightarrow e\gamma)} \sim \alpha \quad (2.7)$$

is achieved. The details of this depend on the nucleus, as can be seen in Figure 2.5.

2.4 Little Higgs models

In Little Higgs models[48, 49], Higgs bosons appear as a quasi-Nambu-Goldstone boson to ensure its stability against quantum corrections. There are several implementations of this idea. Among them the model with T-parity[50] is the most extensively studied. In this model, to prevent the little hierarchy problem, mirror fields of the ordinary fields are introduced. These have odd T-parity, while ordinary fields are even under T-parity. This parity works similarly to R-parity in SUSY models.

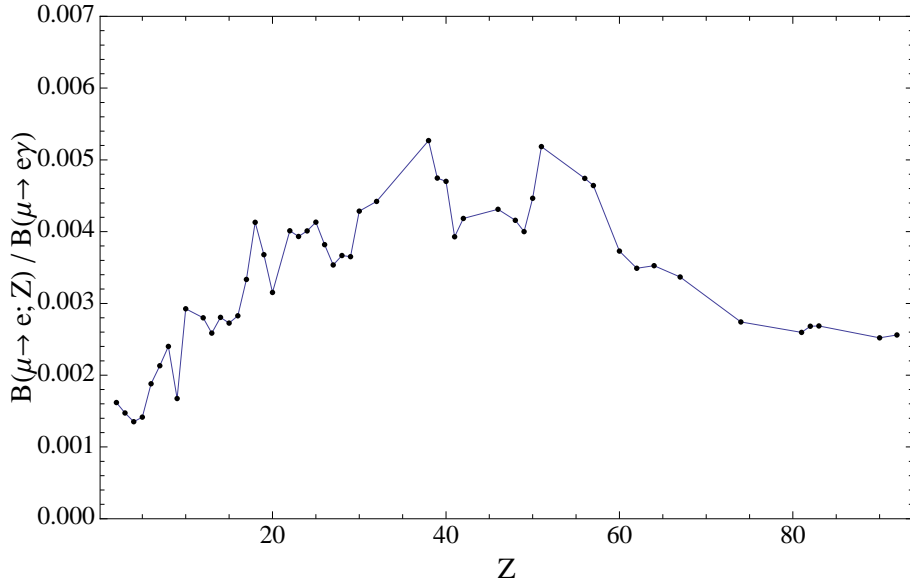


Figure 2.5: Prediction of the branching ratio of $\mu^- -e^-$ conversion in various nuclei in SUSY-seesaw models normalized to the branching ratio of $\mu \rightarrow e\gamma$. Taken from[47].

The source of LFV arises from the misalignment between mirror fields and the ordinary fields[51]. There is no principle to forbid large FCNC and current limits on cLFV strongly constrain models. In Figure 2.6, the predictions for $\mu^- -e^-$ conversion and $\mu \rightarrow e\gamma$ are shown with an appropriate assumption taken for the misalignment.

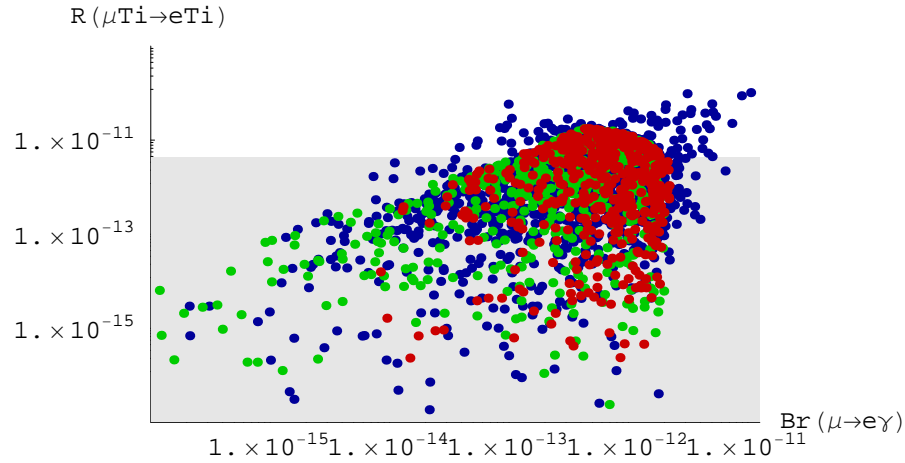


Figure 2.6: Prediction of the branching ratio of $\mu^- -e^-$ conversion and of $\mu \rightarrow e\gamma$ in Little Higgs Models. Taken from[53].

The contribution to $\mu \rightarrow e\gamma$ is depicted in Figure 2.7. In addition to the GIM suppression,

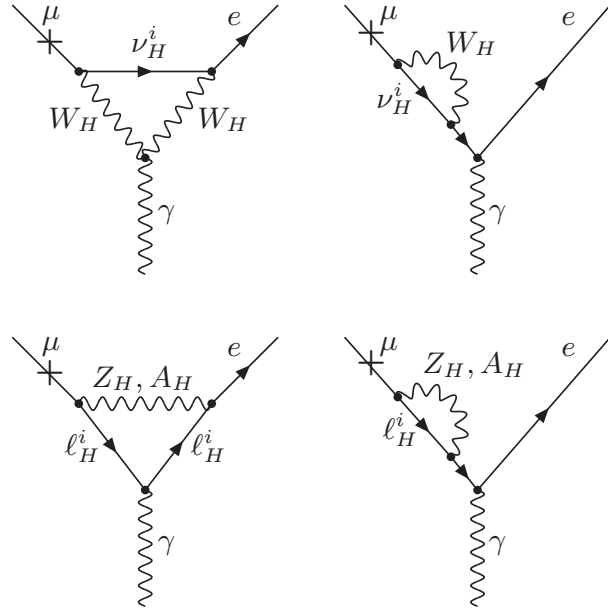


Figure 2.7: Diagrams for $\mu \rightarrow e\gamma$ in Little Higgs Models. Taken from[53].

sion, there is another accidental cancellation among these diagrams. Therefore, unlike the SUSY case these diagrams do not give a leading contribution to $\mu^- - e^-$ conversion, and box and Z penguin diagrams dominate the amplitude for $\mu^- - e^-$ conversion[52, 53, 54]. Incidentally, due to T-parity conservation, there is no tree-level contribution to $\mu^- - e^-$ conversion and hence both branching ratios are loop-suppressed.

Thus the branching ratios in this model are almost equal as shown in Figure 2.6

$$\frac{\text{Br}(\mu \rightarrow e; N)}{\text{Br}(\mu \rightarrow e\gamma)} \sim 1. \quad (2.8)$$

2.5 Extra dimensional models

There are many kinds of models involving extra dimensional space. Here we discuss two models. The first is the Randall-Sundrum model[55] and the second is a universal extra dimensional model (UED)[56]

2.5.1 Anarchic Randall-Sundrum model

To explain the hierarchy among Yukawa couplings, the SM fields are permitted to propagate in the full 5D space [57, 58]. In this scenario, the SM fields are localized at a different point of 5th dimension. Yukawa couplings are quite sensitive to the position and this fact explains the hierarchy among the Yukawa couplings in effective 4D theory with $O(1)$ group 5D couplings. These $O(1)$ couplings indicate a large mixing among generation in a full 5D theory. It manifests itself in the self-couplings of the 1st Kaluza-Klein (KK) gauge bosons and the ordinary fermions as follows.

First we note that in the interaction basis (e_F, μ_F, τ_F) , the gauge coupling ‘‘universality’’

among fermions are modified:

$$g^{SM}(\bar{e}_F, \bar{\mu}_F, \bar{\tau}_F) A^{(n)} \begin{pmatrix} \alpha_e & 0 & 0 \\ 0 & \alpha_\mu & 0 \\ 0 & 0 & \alpha_\tau \end{pmatrix} \begin{pmatrix} e_F \\ \mu_F \\ \tau_F \end{pmatrix}. \quad (2.9)$$

Here g^{SM} stands for the gauge coupling in the SM corresponding to the gauge field A . Since it is the self-coupling of the 1st KK gauge bosons, $\alpha_{e,\mu,\tau}$ are not necessarily equal to 1. In the mass eigenstate, (e, μ, τ) , therefore, there arise LFV couplings

$$g^{SM}(\bar{e}, \bar{\mu}, \bar{\tau}) A^{(n)} U_{L(R)} \begin{pmatrix} \alpha_e & 0 & 0 \\ 0 & \alpha_\mu & 0 \\ 0 & 0 & \alpha_\tau \end{pmatrix} U_{L(R)}^\dagger \begin{pmatrix} e \\ \mu \\ \tau \end{pmatrix} \quad (2.10)$$

Here $U_{L(R)}$ are the mixing matrices to diagonalize the mass matrix given in the basis of the interaction state. Note that since $\alpha_{e,\mu,\tau}$ are not equal, the effect of the mixing matrices remains. In principle, it causes a large LFV effect. With the appropriate assumption, the prediction for cLFV is given in Figure 2.8. There is not a strong correlation between $\mu \rightarrow e\gamma$ and $\mu^- - e^-$. The branching ratios are predicted to be rather large and give a similar magnitude:

$$\frac{\text{Br}(\mu \rightarrow e; N)}{\text{Br}(\mu \rightarrow e\gamma)} \sim 1. \quad (2.11)$$

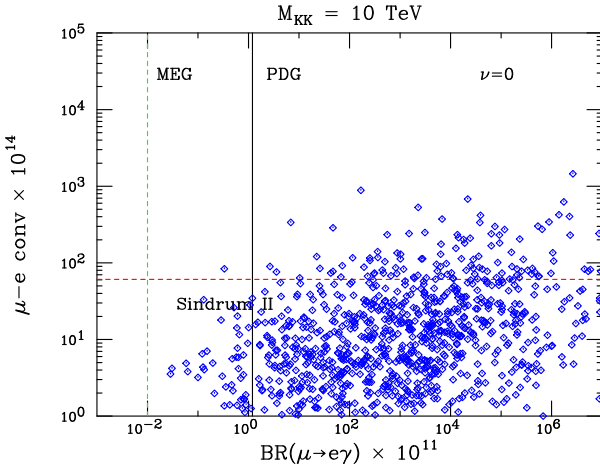


Figure 2.8: Prediction of the branching ratio of $\mu^- - e^-$ conversion and for $\mu \rightarrow e\gamma$ in anarchic Randall-Sundrum models. Taken from[59].

2.5.2 UED models

In this class of model, in general, there is no misalignment between ordinary matter and the KK particles. Therefore even if neutrino masses are introduced[60], no LFV effect beyond the SM and neutrino contribution in Eq. 2.1 arises. Hence

$$\text{Br}(\mu \rightarrow e; N) \sim \text{Br}(\mu \rightarrow e\gamma) < 10^{-54}. \quad (2.12)$$

Note that with information from LHC even if we do not see any cLFV signal, it will serve a very important information, since in many case new physics must predict no cLFV.

2.6 $\mu^- - e^-$ conversion at LHC era

There are many other models to account for neutrino LFV (lepton mixing and neutrino masses), the existence of dark matter, the stability of the electroweak scale and so on. All of them predict a new particle at TeV scale which will be found LHC. Each model has its prediction for $\text{Br}(\mu \rightarrow e\gamma)$ and $\text{Br}(\mu \rightarrow e; N)$. These are parametrised in the effective operator as

$$\mathcal{L} = \frac{a_{\mu e}^2 m_\mu}{\Lambda} \bar{e} \sigma^{\mu\nu} F_{\mu\nu} \mu + \frac{b_{\mu e}^2}{\Lambda} \bar{e} \mu \bar{q} q. \quad (2.13)$$

Here Λ indicates a typical new physics scale and $a_{\mu e}^2$ and $b_{\mu e}^2$ stand for couplings and/or loop factors. The current limits of cLFV[19, 20, 21] give a stringent limit on these effective scales as $\Lambda/a_{\mu e}, \Lambda/b_{\mu e} > 10^3$ TeV. It means, for example, if these operators are loop suppressed, the scale explored by the new generation cLFV experiment is the TeV range. This is shown in Figure 2.9 for the SUSY case.

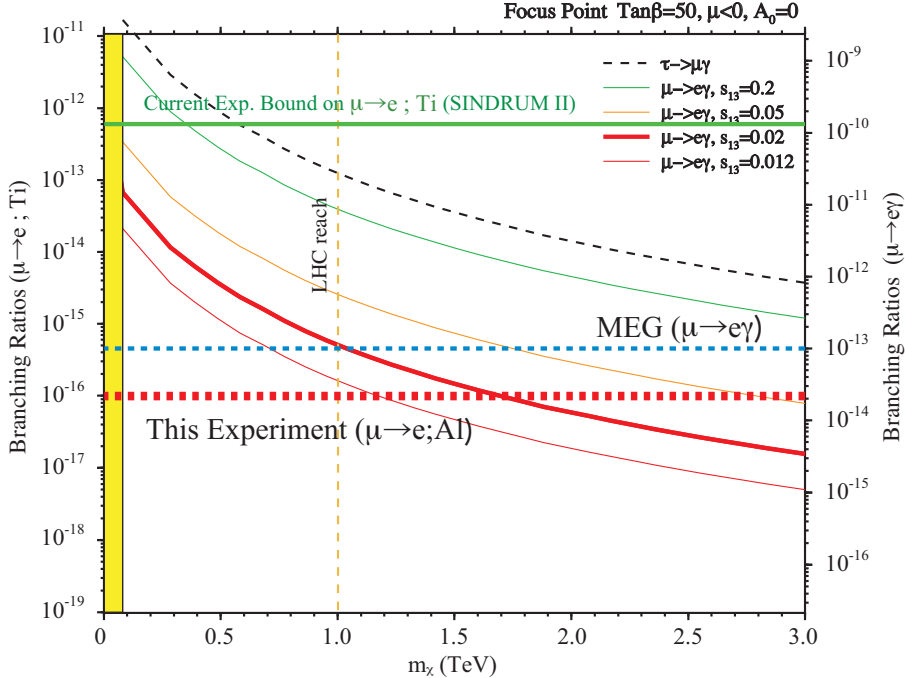


Figure 2.9: Prediction of the branching ratio of $\mu^- - e^-$ conversion in Ti in the SUSY-seesaw models as a function of SUSY mass scale (neutralino). The sensitivity of the proposed experiment is also shown [61].

In general, the relation between $a_{\mu e}$ and $b_{\mu e}$ is model dependent. For example in a SUSY model they are both loop suppressed and are related with each other tightly while in a Little Higgs model, they are both loop suppressed but are not related so much. Therefore the relation between $\mu \rightarrow e\gamma$ and $\mu \rightarrow e; N$ shows a characteristic feature for each model. It is expected that the LHC will find evidence for new physics. It is, however very difficult to discriminate a true model from other candidates. It is, therefore, essential to determine the relation between $a_{\mu e}$ and $b_{\mu e}$.

This demonstrates that the $\mu^- - e^-$ conversion search has outstanding physics motivation, even in the LHC era and after MEG experiment.

2.7 Phenomenology of $\mu^- - e^-$ conversion

2.7.1 What is a $\mu^- - e^-$ conversion process ?

One of the most prominent muon LFV processes is coherent neutrino-less conversion of muons to electrons ($\mu^- - e^-$ conversion), $\mu^- + N(A, Z) \rightarrow e^- + N(A, Z)$. When a negative muon is stopped by some material, it is trapped by an atom, and a muonic atom is formed. After it cascades down energy levels in the muonic atom, the muon is bound in its $1s$ ground state. The fate of the muon is then to either decay in orbit ($\mu^- \rightarrow e^- \nu_\mu \bar{\nu}_e$) or be captured by a nucleus of mass number A and atomic number Z , namely, $\mu^- + (A, Z) \rightarrow \nu_\mu + (A, Z - 1)$. However, in the context of physics beyond the Standard Model, the exotic process of neutrino-less muon capture, such as

$$\mu^- + N(A, Z) \rightarrow e^- + N(A, Z), \quad (2.14)$$

is also expected. This process is called $\mu^- - e^-$ conversion in a muonic atom. This process violates the conservation of lepton flavor numbers, L_e and L_μ , by one unit, but the total lepton number, L , is conserved. The final state of the nucleus (A, Z) could be either the ground state or one of the excited states. In general, the transition to the ground state, which is called coherent capture, is dominant. The rate of the coherent capture over non-coherent capture is enhanced by a factor approximately equal to the number of nucleons in the nucleus, since all of the nucleons participate in the process.

2.7.2 Signal and background events

The event signature of coherent $\mu^- - e^-$ conversion in a muonic atom is a mono-energetic single electron emitted from the conversion with an energy of $E_{\mu e} \sim m_\mu - B_\mu$, where m_μ is the muon mass and B_μ is the binding energy of the $1s$ muonic atom.

From an experimental point of view, $\mu^- - e^-$ conversion is a very attractive process. Firstly, the e^- energy of about 105 MeV is far above the end-point energy of the muon decay spectrum (~ 52.8 MeV). Secondly, since the event signature is a mono-energetic electron, no coincidence measurement is required. The search for this process has the potential to improve sensitivity by using a high muon rate without suffering from accidental background events, which would be serious for other processes, such as $\mu^+ \rightarrow e^+ \gamma$ and $\mu^+ \rightarrow e^+ e^+ e^-$ decays.

The electron is emitted with an energy $E_e \approx m_\mu$, which coincides with the endpoint of muon decay in orbit (DIO), which is the only relevant intrinsic physics background event. Since the energy distribution of DIO falls steeply above $m_\mu/2$, the experimental setup can have a large signal acceptance and the detectors can still be protected against the vast majority of decay and capture background events. Energy distributions for DIO electrons have been calculated for a number of muonic atoms[62, 63] and energy resolutions of the order of 0.1% are sufficient to keep this background below 10^{-18} .

There are several other potential sources of electron background events in the energy region around 100 MeV, involving either beam particles or cosmic rays. Beam-related background events may originate from muons, pions or electrons in the beam. Apart from DIO, muons may produce background events by muon decay in flight or radiative muon

capture (RMC). Pions may produce background events by radiative pion capture (RPC). Gamma rays from RMC and RPC produce electrons mostly through e^+e^- pair production inside the target.

There are three methods to suppress the beam-related background events:

- Beam pulsing

Since muonic atoms have lifetimes of the order of 1 μs , a pulsed beam with buckets that are short compared with this lifetime would allow the removal of prompt background events by performing measurements in a delayed time window. As will be discussed below there are stringent requirements on beam extinction during the measuring interval.

- Beam purity

The lifetime of the pion (26 ns) is much shorter than the lifetime of muon (2200 ns). Thus, if the beam momentum is low enough, most of beam pions will decay away as they transport through a muon beamline. If the beam momentum is less than 70 MeV/c, the level of pion contamination will be decreased by an order of magnitude for each 10 m.

- Beam Momentum

The in-flight decay of beam muons would produce 100 MeV/c electrons if the beam momentum is larger than 70 MeV/c. Beam electrons would be also a source of 100 MeV/c electron background. Thus, if the beam momentum is restricted to be lower than 70 MeV/c, these backgrounds can be suppressed.

2.7.3 μ^-e^- conversion vs. $\mu^+ \rightarrow e^+\gamma$

There are considered to be two possible contributions in the μ^-e^- transition diagrams. One is a photonic contribution, and the other is a non-photonic contribution. For the photonic contribution, there is a definite relation between the μ^-e^- conversion process and the $\mu^+ \rightarrow e^+\gamma$ decay. Suppose the photonic contribution is dominant, the branching ratio of the μ^-e^- conversion process is expected be smaller than that of μ^-e^- decay by a factor of the fine structure constant α (a few hundred). This implies that the search for μ^-e^- conversion at the level of 10^{-16} is comparable to that for $\mu^+ \rightarrow e^+\gamma$ at the level of 10^{-14} .

If the non-photonic contribution dominates, the $\mu^+ \rightarrow e^+\gamma$ decay would be small whereas the μ^-e^- conversion could be sufficiently large to be observed. It is worth noting the following. If a $\mu^+ \rightarrow e^+\gamma$ signal is found, the μ^-e^- conversion signal should also be found. A ratio of the branching ratios between $\mu^+ \rightarrow e^+\gamma$ and μ^-e^- carries vital information on the intrinsic physics process. If no $\mu^+ \rightarrow e^+\gamma$ signal is found, there will still be an opportunity to find a μ^-e^- conversion signal because of the potential existence of non-photonic contributions.

2.8 Present experimental status

2.8.1 μ^-e^- conversion

Table 2.2 summarizes the history of searches for μ^-e^- conversion. From Table 2.2, it is seen that over about 30 years the experimental upper limits has been improved by 5 orders of magnitude. In the following, the past and future experiments of searching for μ^-e^- conversion will be described.

Table 2.2: Past experiments on $\mu^- - e^-$ conversion. (* reported only in conference proceedings.)

Process	upper limit	place	year	reference
$\mu^- + Cu \rightarrow e^- + Cu$	$< 1.6 \times 10^{-8}$	SREL	1972	[64]
$\mu^- + {}^{32}S \rightarrow e^- + {}^{32}S$	$< 7 \times 10^{-11}$	SIN	1982	[65]
$\mu^- + Ti \rightarrow e^- + Ti$	$< 1.6 \times 10^{-11}$	TRIUMF	1985	[66]
$\mu^- + Ti \rightarrow e^- + Ti$	$< 4.6 \times 10^{-12}$	TRIUMF	1988	[67]
$\mu^- + Pb \rightarrow e^- + Pb$	$< 4.9 \times 10^{-10}$	TRIUMF	1988	[67]
$\mu^- + Ti \rightarrow e^- + Ti$	$< 4.3 \times 10^{-12}$	PSI	1993	[68]
$\mu^- + Pb \rightarrow e^- + Pb$	$< 4.6 \times 10^{-11}$	PSI	1996	[69]
$\mu^- + Ti \rightarrow e^- + Ti$	$< 6.1 \times 10^{-13}$	PSI	1998*	[21]
$\mu^- + Au \rightarrow e^- + Au$	$< 7 \times 10^{-13}$	PSI	2006	[22]

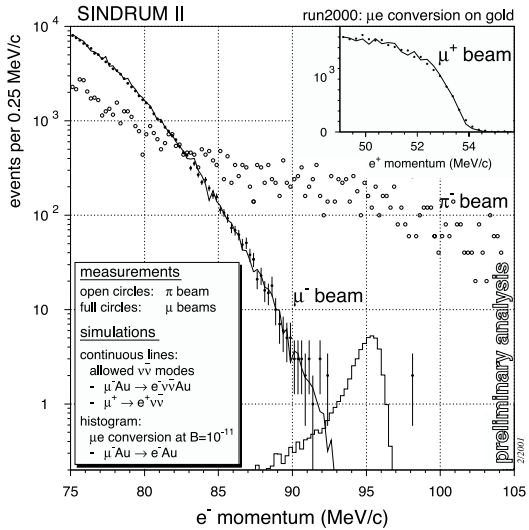


Figure 2.10: Recent results by SINDRUM II. Momentum distributions for three different beam momenta and polarities: (i) 53 MeV/c negative, optimized for μ^- stops, (ii) 63 MeV/c negative, optimized for π^- stops, and (iii) 48 MeV/c positive, optimized for μ^+ stops. The 63 MeV/c data were scaled to the different measuring times. The μ^+ data were taken using a reduced spectrometer field.

2.8.1.1 SINDRUM-II

The latest search for $\mu^- - e^-$ conversion was performed by the SINDRUM II collaboration at PSI. Figure 2.10 shows their results. The main spectrum, taken at 53 MeV/c, shows the steeply falling distribution expected from muon DIO. Two events were found at higher momenta, but just outside the region of interest. The agreement between measured and simulated positron distributions from μ^+ decay means that confidence can be high in the accuracy of the momentum calibration. At present there are no hints concerning the nature of the two high-momentum events: they might have been induced by cosmic rays or RPC, for example. They set the current upper limit on $B(\mu^- + Au \rightarrow e^- + Au) < 7 \times 10^{-13}$ [22].

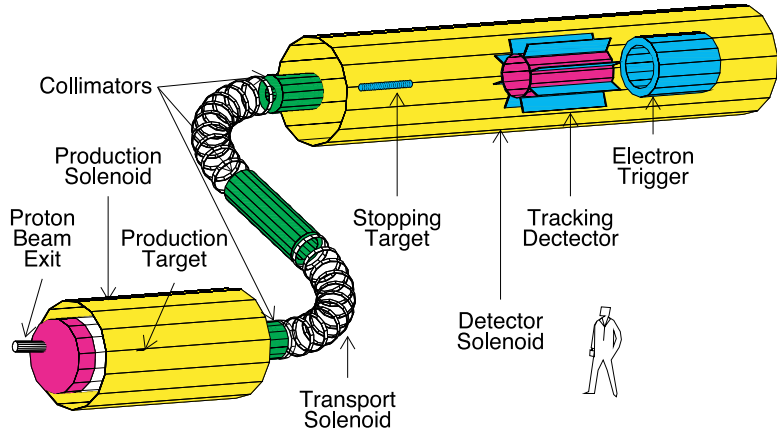


Figure 2.11: Setup of the MECO experiment.

2.8.1.2 MECO

There was an experimental proposal at BNL, which was called the MECO experiment[70], aiming to search with a sensitivity of 10^{-16} . This project was planned to combat beam-related background events with the help of a pulsed 8 GeV/c proton beam. Figure 2.11 shows the proposed layout. Pions are produced by 8 GeV/c protons crossing a 16 cm long tungsten target, and muons from the decays of the pions are collected efficiently with the help of a graded magnetic field. Negatively charged particles with 60–120 MeV/c momenta are transported by a curved solenoid to the experimental target. In the spectrometer magnet, a graded field is also applied. A major challenge is the requirement for proton extinction in between the proton bursts. In order to maintain the pion stop rate in the ‘silent’ interval, a beam extinction factor better than 10^{-8} – 10^{-9} is required. Unfortunately, the MECO experiment was canceled in 2005, owing to the NSF funding problems.

2.8.1.3 Mu2e

However, the revival of the MECO experiment has been actively made at the Fermi National Laboratory (Fermilab). It is called the “Mu2e experiment” (see Fig. 2.12). The muon beam line and detector for the Mu2e experiment are almost the same as those of the MECO experiment. The aimed experimental sensitivity is also the same. The experimental proposal was stage-one approved at Fermilab fall, 2008 [71]. The Mu2e experiment would strongly compete with the COMET experiment.

The Mu2e experiment will use the Fermilab proton source, and the desired proton beam structure from their 8 GeV Booster can be made by reusing the 8 GeV Debuncher and Accumulator storage rings, which are both housed in the anti-proton beam enclosure. At this moment, anti-protons from the production target are transported into the Debuncher ring where they are phase-rotated and stochastically cooled, and then are transferred into the Accumulator ring, where they are momentum stacked. For the Mu2e experiment, proton bunches from the Fermilab Booster are transported through the Recycler ring and injected directly into the Accumulator ring, where they are momentum-stacked. Then, they are

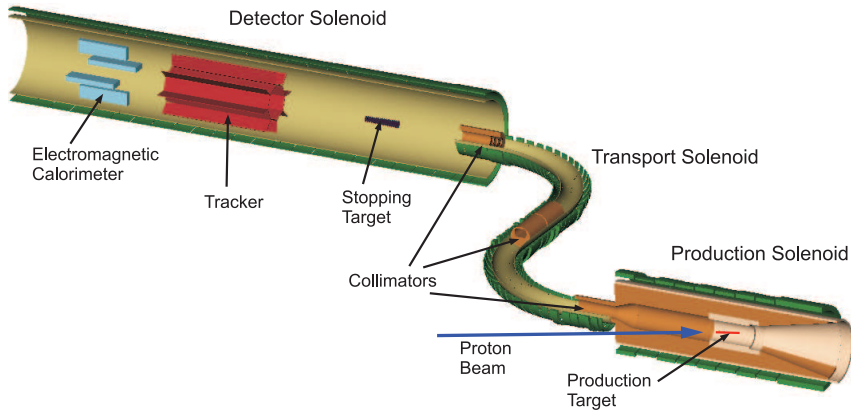


Figure 2.12: A schematic layout of the Mu2e experiment.

transferred into the Debuncher ring and rebunched into a single short bunch. Finally the beam would be resonantly extracted in a such way that the single bunch would cause a bunch train. The proton accelerator complex at Fermilab relevant to the Mu2e experiment is shown in Fig. 2.13.

There are several scenarios on proton delivery for the Mu2e experiment. In the period of the NO ν A program after the Tevatron shutdown, the Mu2e would receive about 4×10^{20} protons for several years, with the upgrades of the Booster repetition and improvement of the beam transmission efficiency of the Booster. In Fermilab, there are proton upgrade plans, such as the “SuperNuMI” (SNuMI) plan, where the beam power to the NuMI beam line would increase to roughly 1.2 MW, and more ambitiously the “Project-X” plan, where a new 8 GeV linac with superconducting RFs would increase to 2 MW (3×10^{21} protons/sec). In both cases, the number of protons delivered from the Fermilab proton source would increase.

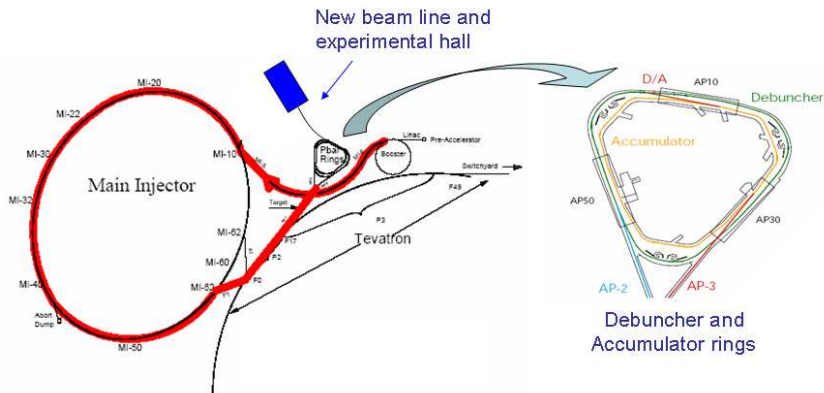


Figure 2.13: Fermilab proton accelerator complex relevant to the Mu2e experiment.

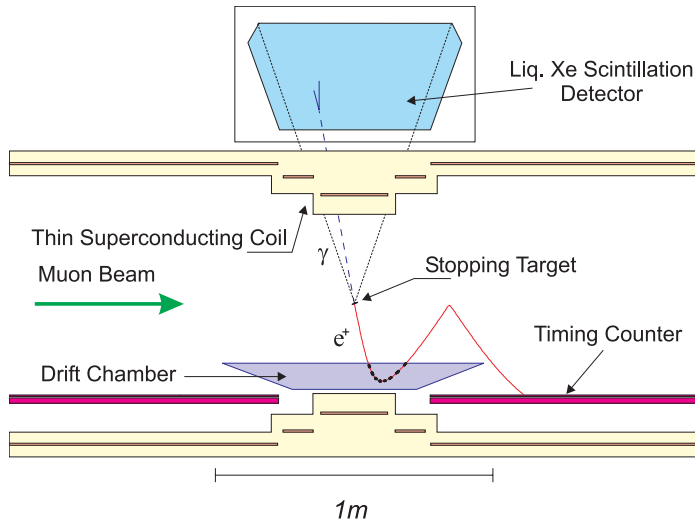


Figure 2.14: Setup of the MEG experiment.

2.8.2 $\mu^+ \rightarrow e^+\gamma$ Decay

The present experimental limit for $\mu^+ \rightarrow e^+\gamma$ is 1.2×10^{-11} , which was obtained by the MEGA experiment at LANL in the US[19].

A new experiment called MEG at PSI[72], which aims to achieve a sensitivity of 10^{-13} in the $\mu^+ \rightarrow e^+\gamma$ branching ratio, is under construction. A schematic view of the detector is shown in Fig. 2.14. The improved experiment will be expected to utilize a continuous muon beam of 100% duty factor at PSI. Utilizing the same instantaneous beam intensity as MEGA, the total number of muons available can be increased by a factor of 16. A further improvement is the use of a novel liquid xenon scintillation detector of the “Mini-Kamiokande” type, which is a 0.8 m^3 volume of liquid xenon observed by an array of 800 photomultipliers from all sides. For e^+ detection, a solenoidal magnetic spectrometer with a graded magnetic field is to be adopted. The engineering run has been started in 2007, and physics data taking is expected to start soon.

2.8.3 Why is $\mu^- - e^-$ conversion the next step ?

Considering its marked importance to physics, it is highly desirable to consider a next-generation experiment to search for LFV. There are three processes to be considered; namely, $\mu^+ \rightarrow e^+\gamma$, $\mu^+ \rightarrow e^+e^+e^-$, and $\mu^- - e^-$ conversion.

The three processes have different experimental issues that need to be solved to realize improved experimental sensitivities. They are summarized in Table 2.3. The processes of $\mu^+ \rightarrow e^+\gamma$ and $\mu^+ \rightarrow e^+e^+e^-$ are detector-limited. To consider and go beyond the present sensitivities, the resolutions of detection have to be improved, which is, in general, very hard. In particular, improving the photon energy resolution is difficult. On the other hand, for $\mu^- - e^-$ conversion, there are no accidental background events, and an experiment with higher rates can be performed. If a new muon source with a higher beam intensity and better beam quality for suppressing beam-associated background events can be constructed, measurements of higher sensitivity can be performed.

Furthermore, it is known that in comparison with $\mu^+ \rightarrow e^+\gamma$, there are more physical

Table 2.3: LFV processes and issues

Process	Major backgrounds	Beam	Sensitivity Issues
$\mu^+ \rightarrow e^+ \gamma$	accidental	DC beam	detector resolution
$\mu^+ \rightarrow e^+ e^+ e^-$	accidental	DC beam	detector resolution
$\mu^- - e^-$ conversion	beam-associated	pulsed beam	beam qualities

processes that $\mu^- - e^-$ conversion and $\mu^+ \rightarrow e^+ e^+ e^-$ could contribute to. Namely, in SUSY models, photon-mediated diagrams can contribute to all the three processes, but the Higgs-mediated diagrams can contribute to only $\mu^- - e^-$ conversion and $\mu^+ \rightarrow e^+ e^+ e^-$. In summary, with all of the above considerations, a $\mu^- - e^-$ conversion experiment would be the natural next step in the search for lepton flavour violation.

Chapter 3

Overview of COMET

3.1 Introduction to the COMET experiment

The aim of the COMET experiment is to search for coherent neutrino-less conversion of muons to electrons in a muonic atom ($\mu^- - e^-$ conversion),

$$\mu^- + N(A, Z) \rightarrow e^- + N(A, Z), \quad (3.1)$$

at a signal sensitivity of less than 10^{-16} , at the Japanese Proton Accelerator Research Complex (J-PARC). Here COMET stands for COherent Muon to Electron Transition. This sensitivity goal is **a factor of 10,000 better** than that of the current experimental limit¹.

COMET is designed to be carried out in the Nuclear and Particle Experimental Hall (NP Hall) using a bunched proton beam slow-extracted from the J-PARC main ring (MR). The experimental setup consists of the muon beam line and the detector section. The muon beam line is composed of the pion capture solenoids with high magnetic field, and the muon transport with curved and straight solenoids. The detector section is composed of the muon stopping target, the electron transport for $\mu^- - e^-$ conversion signals, and the detector. A schematic drawing of the experimental setup is shown in Fig. 3.1.

In order to improve the sensitivity by a factor of 10,000 over the current limit, several important features have been considered, as highlighted below.

- **Highly intense muon source:** The total number of muons needed is of the order of 10^{18} to achieve an experimental sensitivity of 10^{-16} . Therefore, a highly intense muon beam line has to be constructed. Two methods are adopted in this experiment to increase the muon beam intensity. One is to use a proton beam of high beam power. The other is to use a system of collecting pions, which are the parents of muons, with high efficiency. In the muon collider and neutrino factory R&D, superconducting solenoid magnets ,producing a high magnetic field surrounding the proton target, have been proposed and studied for pion capture over a large solid angle. With the pion capture solenoid system, about 8.5×10^{20} protons of 8 GeV are necessary to achieve the number of muons of the order of 10^{18} .
- **Pulsed proton beam:** There are several potential sources of electron background events in the energy region around 100 MeV, where the $\mu^- - e^-$ conversion signal is expected. One of them is beam-related background events. In order to suppress

¹The present published limit is $B(\mu^- + \text{Au} \rightarrow e^- + \text{Au}) = 7 \times 10^{-13}$ from SINDRUM-II at PSI [22].

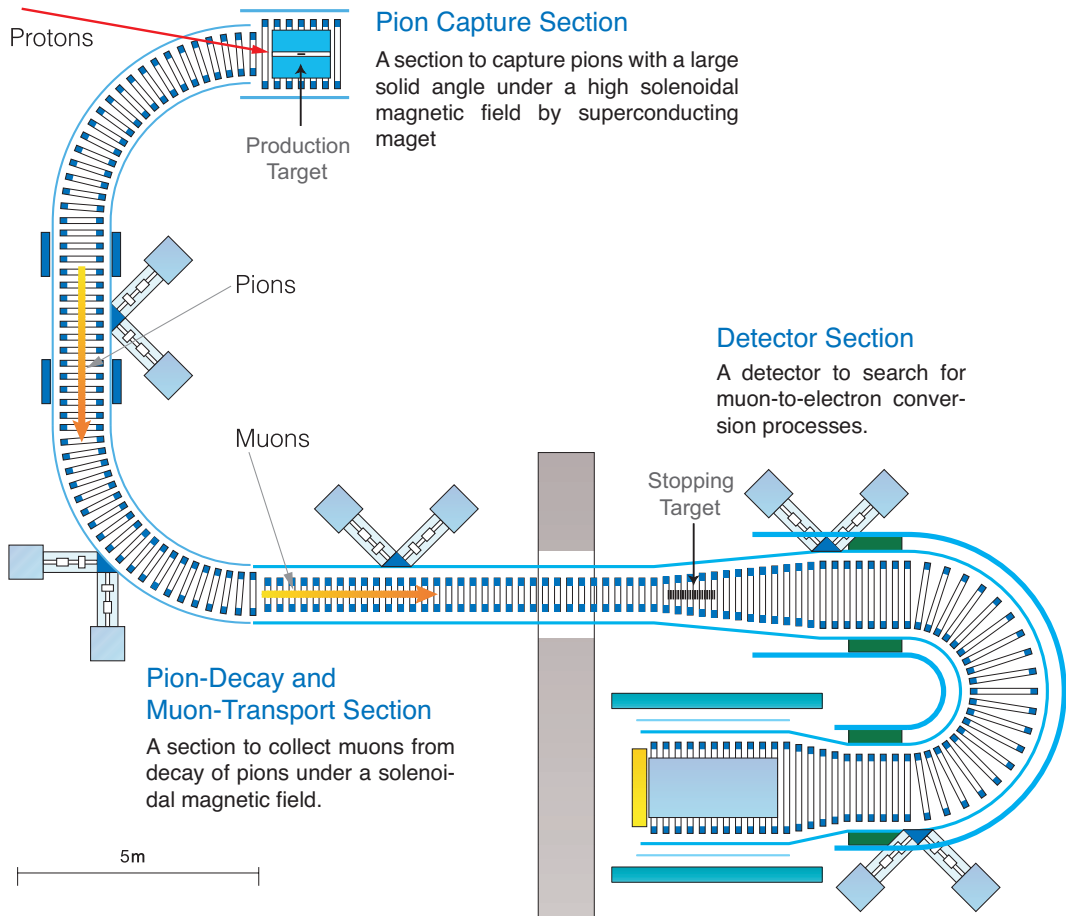


Figure 3.1: Schematic layout of the muon beamline and detector for the proposed search for $\mu^- - e^-$ conversion, the COMET experiment.

the occurrence of beam-related background events, a pulsed proton beam utilizing a beam extinction system is proposed. Since muons in muonic atoms have lifetimes of the order of 1 μ sec, a pulsed beam with beam buckets that are short compared with these lifetimes would allow removal of prompt beam background events by allowing measurements to be performed in a delayed time window. As will be discussed below, there are stringent requirements on the beam extinction during the measuring interval. Tuning of the proton beam in the accelerator ring as well as extra extinction devices need to be installed to achieve the required level of beam extinction.

- **Curved solenoids for charge and momentum selection:** The captured pions decay to muons, which are transported with high efficiency through a superconducting solenoid magnet system. Beam particles with high momenta would produce electron background events in the energy region of 100 MeV, and therefore must be eliminated with the use of curved solenoids. The curved solenoid causes the centers of the helical motion of the electrons to drift perpendicular to the plane in which their paths are curved, and the magnitude of the drift is proportional to their momentum. By using this effect and by placing suitable collimators at appropriate locations, beam particles of high momenta can be eliminated.

These features were originally developed at the MELC experiment at the Moscow Meson Factory, but the experiment was not carried out. They have been adopted by the MECO experiment, which was cancelled in the US.

3.2 Advantages of the COMET experiment

The design of COMET has several advantages. These are mainly due to the C-shape design of the muon transport and the electron transport:

- **C-shape muon transport in the muon beam**

Instead of the S-shape that was adopted by MECO, the C-shape muon transport in the muon beam line (from the pion production to the muon-stopping target) is adopted in COMET. This requires an additional compensating dipole field, which can be produced using separate dipole coils or by tilting the solenoid coils. Since the muon momentum dispersion is proportional to a total bending angle, the C-shape beamline will produce a larger separation of the muon tracks as a function of momentum. As a result, the momentum selection will be better.

- **C-shape electron transport in the detector**

Instead of a straight solenoid, the C-shape electron transport (from the muon-stopping target to the detector) is adopted in the COMET spectrometer. The principle of momentum selection is the same as that used in the muon transport system, but, in the spectrometer, electrons of low momenta which mostly come from muon decay in orbit (DIO) are removed. As a result, the detector rate will be reduced significantly and the probability of false-tracking is highly suppressed. The tracking detector rate, including the direct hit of DIO electrons and secondary electrons from scattering and photon conversion, is expected to be less than 1 MHz. This is almost two orders of magnitudes less than the expected detector rate for the MECO experiment. Another advantage of using a curved solenoid for the electron transport is that it will eliminate the need for a proton absorber. Mu2e must shield their electron spectrometer from protons produced by the nuclear capture of stopping muons, therefore, COMET will have a better energy resolution. Also because of the suppression of low-energy particles, the detector geometry can be made simpler, such as a setup of straw-chamber planes transverse to the field axis and an electron calorimeter whose front face is perpendicular to the field axis.

3.3 Summary of signal sensitivity and backgrounds

The expected signal sensitivity for $\mu^- - e^-$ conversion signals and background events for the COMET experiment are summarized here. Detailed descriptions can be found in Chapter 11. With 2×10^7 sec running, the number of muons stopped in the muon-stopping target is estimated for the present design of the muon beam. A net signal acceptance, which is composed of the detector geometry and the event selection, is also evaluated for the present design of the detector. Based on these, a single event sensitivity of 2.6×10^{-17} for $\mu^- + \text{Al} \rightarrow e^- + \text{Al}$ can be achieved for 2×10^7 sec.

Background events are estimated from four categories intrinsic physics backgrounds; beam-related prompt backgrounds; beam-related delayed backgrounds; and cosmic-ray and

other backgrounds. The total expected number of background events for the above sensitivity is expected to be less than 0.4 events.

Chapter 4

Proton Beam

This chapter describes the proton beam used to produce a high-intensity muon beam. The J-PARC main ring (MR) is used to supply a pulsed 8 GeV proton beam, which is slow extracted, maintaining its bunch structure, into the J-PARC Nuclear and Particle Experimental Hall (NP Hall). The pulsed proton beam then hits the pion production target located inside the pion capture solenoid magnet. The produced pions decay to muons as they are transported from the pion production target to the muon stopping target. These muons are momentum selected by the curved solenoid transport channel as described in Section 5.3.

4.1 Requirements for the proton beam

The J-PARC MR will deliver a proton beam with an intensity of 3.3×10^{14} protons per cycle and a cycle time of about 0.3 Hz. Protons from the J-PARC MR are extracted either to the NP Hall by slow extraction, or to the neutrino experimental hall (T2K) by fast extraction. When operated in the slow extraction mode, the average beam current and duty factor are 15 μA and 0.2 respectively.

Since COMET requires the highest possible intensity of muons on the stopping target, the intensity of the proton beam needs to be as high as possible in order to maximise the production of pions which will decay to muons.

4.1.1 Proton energy

The number of pions (and therefore their daughter muons) produced by a proton beam is proportional to proton beam power, which is given by the product of the beam energy and beam current. This is due to the fact that the pion cross-section increases linearly with proton beam energy. The required beam power is approximately the same as that for the MECO experiment at BNL-AGS and the Mu2e experiment at Fermilab. The reason for the relatively low proton beam energy, i.e. 8 GeV, is twofold. One is to suppress production of anti-protons, and the other is to ease the requirements of the beam extinction system, where a lower beam energy is easier to deflect, as described in Section 4.3.1.2. Increasing the beam power can be realized in two ways: increasing the beam energy or increasing the beam current. The cross section of anti-proton production, $p + p \rightarrow p + p + p + \bar{p}$, whose threshold is at 5.6 GeV, rapidly increases above a proton beam energy of 10 GeV as shown in Figure 4.1. Thus a proton beam energy of 8 GeV is used in the current design. At this

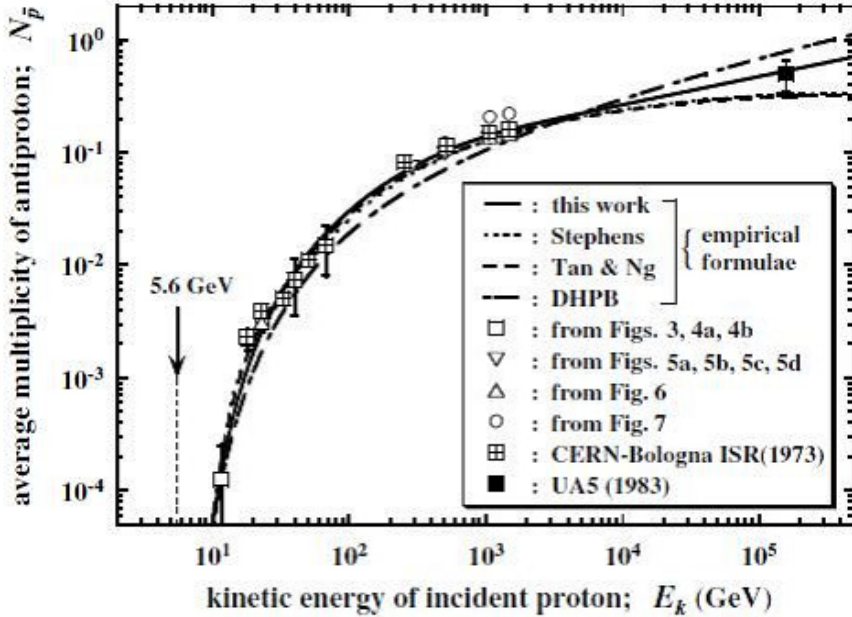


Figure 4.1: Average multiplicity of anti-proton production as a function of the incident proton energy [73].

energy, even if anti-protons are produced, most of them can be eliminated by inserting a stopping foil in the muon transport line.

4.1.2 Proton beam power

The proton beam power of the current design is $8 \text{ GeV} \times 7 \mu\text{A}$ (4.4×10^{13} protons/second), which will provide enough muons for COMET to achieve its physics goal within a few years of running. A reduced beam power would affect the running time of the experiment and thus the achievable sensitivity. However, even with a reduced sensitivity of say 10^{-15} , the physics impact would still be significant. Therefore, if the required beam power could not be delivered from the beginning of the experiment, it would be acceptable to start with a lower intensity and then increase it without having a catastrophic effect on the physics goal. In this case the beam power could be upgraded by increasing the repetition cycle of the accelerator. For example, reducing the acceleration and extraction cycle time by a factor of two will provide twice the beam power without modifying the proton time structure.

4.1.3 Proton time structure

The proton beam needs to be pulsed with a time separation of the order of $1 \mu\text{s}$, which corresponds to the lifetime of a muon in a muonic atom. The signal electrons will be emitted from the stopping target and enter the detector during the interval between proton pulses. On the other hand, the beam related background will come within a few 100 ns after the proton pulse since these are mostly prompt processes. This timing information is very important for distinguishing signal events from background events. It is also very important to reduce the number of residual protons between pulses as these will produce beam related

background in the signal timing window. For COMET to achieve its expected sensitivity the residual protons between pulses needs to be 10^9 times smaller than the number of protons in the main pulse. In order to achieve this stringent goal a dedicated “beam extinction” system is used and is described in Section 4.3.1.2.

The number of protons in a pulse is mainly determined by the performance of the detector. In the COMET design, the detector has an excellent ability to eliminate low energy charged particles as well as neutral particles. From Monte Carlo simulations, the fraction of charged particle tracks entering the sensitive part of the detector is 10^{-8} – 10^{-7} of those emerging from the muon stopping target. Thus, if we want to limit the number of tracks hitting the detector in a micro second to less than 10 tracks, the number of protons in a pulse should be 10^{11} or less. This means the number of pulses per cycle should be an order of 100 or more. On the other hand, it is quite helpful to reduce the total live time of the detector for suppressing cosmic-ray backgrounds. From that point of view, the number of pulses per cycle should be as small as possible. Table 4.1 summarizes the required parameters of the pulsed proton beam. Figure 4.2 shows a typical time structure for the pulsed proton beam suitable for the COMET experiment.

Table 4.1: Pulsed proton beam for the COMET experiment.

Beam Power	56 kW
Energy	8 GeV
Average Current	7 μ A
Beam Emittance	$10 \pi \text{mm}\cdot\text{mrad}$
Protons per Bunch	$< 10^{11}$
Extinction	10^{-9}
Bunch Separation	$1\sim2 \mu\text{s}$
Bunch Length	100 ns

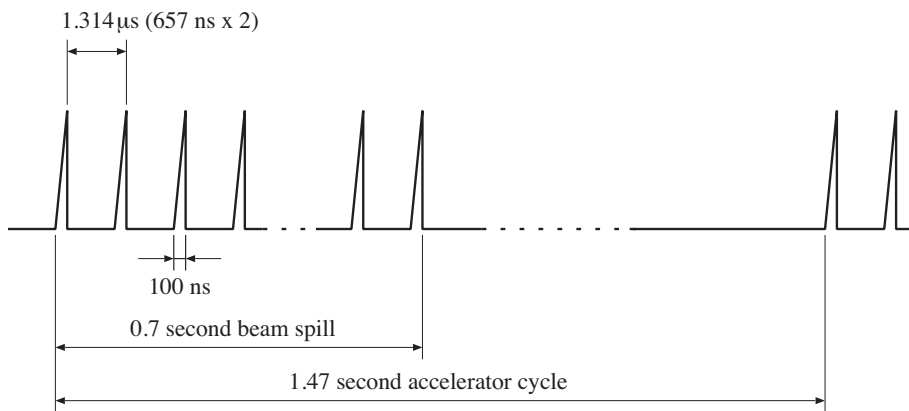


Figure 4.2: Bunched proton beam in a slow extraction mode.

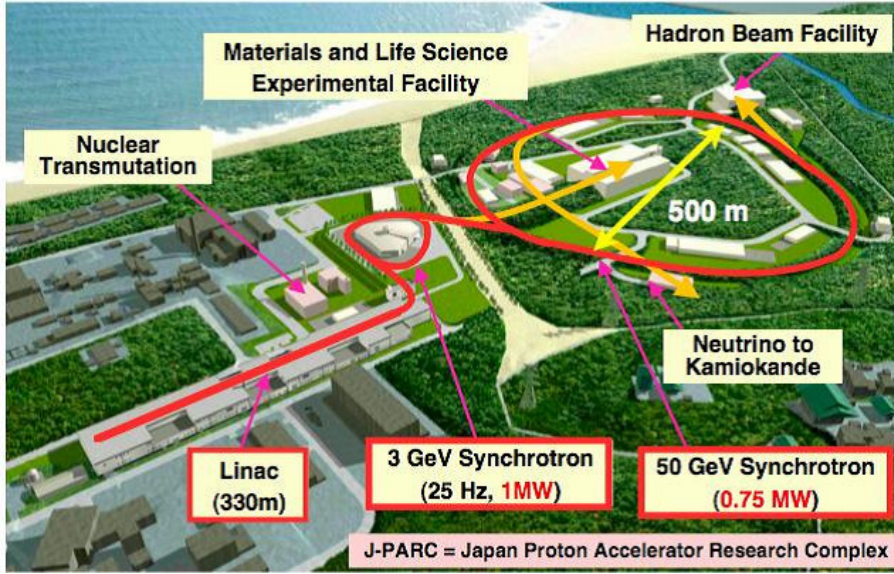


Figure 4.3: J-PARC accelerator layout.

4.2 Proton accelerator operation

In this section the proton accelerator operation scheme for the COMET experiment is described. As already mentioned above and also in the COMET proposal, COMET requires a special operation mode of the J-PARC main ring in order to obtain the required beam structure. The time between two consecutive bunches should be as long as the muon life time when bound by a nucleus, i.e. $\sim 1 \mu\text{s}$, and the bunch width should be small ($\sim 100 \text{ ns}$) compared to this. In addition to this the proton beam has to be transported to the pion production target whilst keeping its pulse structure. This can be realized using the bunched slow extraction technique. The requirements on the time structure is satisfied by operating the main ring by filling only four out of eight buckets in the case when the ring is operated at a harmonic number of eight. The four filled buckets are distributed along the ring in such a way that one empty bucket exists between two filled buckets. Since the time difference between two consecutive bucket is 657 ns, which is determined by the acceleration RF frequency, the bunch-bunch width will be $1.341 \mu\text{s}$. This satisfies the COMET proton pulse separation requirement.

The J-PARC accelerator chain, shown in Figure 4.3, consists of a linac, a Rapid-Cycling Synchrotron (RCS) and the Main Ring (MR). The operation scheme of each component to realize the beam required by the COMET experiment will be explained in the following sections.

4.2.1 Proton linac operation

The proton linac operation will be almost same as that in the normal operation mode [74]. The proton beam bunch structure needed to fill the RCS is formed by a high-frequency chopper cavity and scraper (Figure 4.4) installed in the linac system. The chopper has a very fast rise time of 10 ns in order to form a gap in the bunch structure to allow the RCS to be filled without producing huge losses. Figure 4.5 shows the linac bunch time structure,

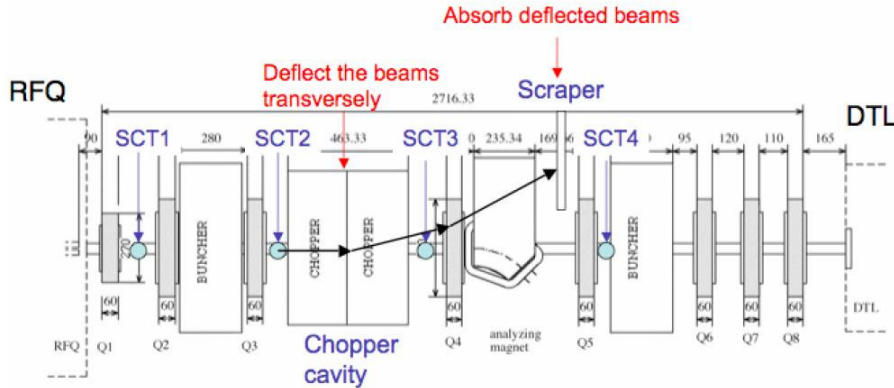


Figure 4.4: Overview of the chopper system.

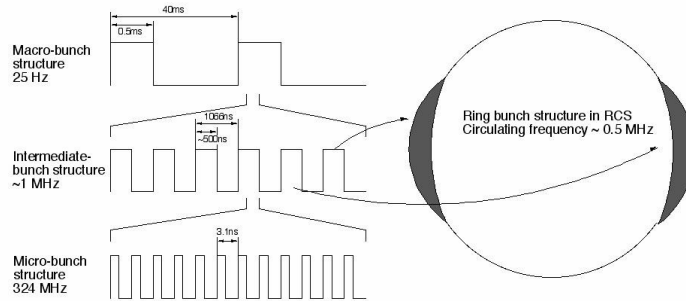


Figure 4.5: Linac bunch structure (left) and RCS bunch structure (right).

which has a micro-bunch structure at 324 MHz, the intermediate bunch structure used to fill the RCS and the merged bunch structure in the RCS, which has a rate of 25 Hz. Protons in the intermediate bunch are used to repeatedly fill the RCS to form the macro-bunch structure in the RCS. In order to create the intermediate bunch structure, 48% of the micro bunches are removed by the chopper system. This may cause a heat load problem if the repetition cycle is increased to obtain higher beam powers.

4.2.2 RCS operation

The RCS accepts the beam from the linac, accelerates it to 3 GeV, and then passes it to the MR for further acceleration. The injection energy of the RCS is currently set to be 181 MeV and will be upgraded to 400 MeV in the future. 600 MeV injection is also planned in the second phase of construction by installing super-conducting acceleration cavities.

4.2.2.1 Choice of harmonic number

The harmonic number, h , of the RCS is 2 in the normal operation scheme. This is determined by the acceleration RF frequency. The accelerator design is done based on this number and thus hardware components are optimized for this configuration. In order to

realize the required proton pulse separation of $\sim 1 \mu\text{s}$ in the MR, it is necessary to fill only one out of the two buckets in the RCS and keep another bucket empty. The two buckets (one filled and one empty) are passed to the MR four times successively. This RCS bunch configuration is possible by changing the chopping time structure in the linac. This has been done during accelerator studies performed in 2009. A drawback of this scheme is the possible leakage of particles from the filled bucket to the empty bucket in an RCS acceleration cycle, which is caused by the different intermediate-bunch structure produced by the linac chopper. A systematic study of this leakage effect on the proton beam extinction is required.

Another possible scheme of the RCS acceleration is to use a harmonic number of 1. This scheme is actually considered for a future upgrade of the MR power since the number of protons in one bucket in the RCS can probably be increased more in an $h=1$ operation mode compared to an $h=2$ operation mode. Thus the $h=1$ operation mode is preferred for increasing the number of protons in the MR. For the COMET beam acceleration, the $h=1$ operation mode is preferred since there is only one bucket that contains all the protons, therefore leakage of protons outside the bucket in the RCS will be strongly suppressed. It is necessary to modify the hardware for changing the RCS harmonic number since the acceleration RF frequency needs to be modified. Modification of RF frequency may require an increase in acceleration voltage. If this is the case, the RF cavities will need to be rebuilt to avoid the possible increase in heat load. In addition this modification may cause a change in the bunch length in the RCS and so will affect the bunch length in the MR. A careful study of whether this effect would have a significant impact on the experiment needs to be done before adopting this solution.

4.2.2.2 Emittance control

The acceptance of the MR slow extraction line and hadron transport line is limited to $25\pi\text{mm}\cdot\text{mrad}$. The beam emittance is smaller than this in normal operating conditions due to adiabatic damping. However, in the accelerator operation for COMET, the proton beam is accelerated only up to 8 GeV and therefore the damping effect is smaller than for a 30 GeV beam. This results in the 8 GeV beam having an emittance larger than the acceptance of the slow extraction and hadron transport lines. The emittance in the nominal scenario is $54 \pi\text{mm}\cdot\text{mrad}$ at 3 GeV and shrinks during further acceleration in the MR but only down to $38 \pi\text{mm}\cdot\text{mrad}$ at 8 GeV. The strategy for improving the emittance is twofold. First, the number of protons per bunch is reduced to minimize the space charge effect while at the same time the MR repetition rate is increased to as high as possible. For the current design operation cycle of 1.47 s, as illustrated in Figure 4.6, this will probably be possible.

Second, the acceleration of the proton beam in the MR could be done with an emittance smaller than nominal. This can be achieved by reducing the painting area in the RCS and narrowing the collimator apertures in the transport line and MR. A simple estimate indicates that the beam emittance at 8 GeV will be $10\text{--}15 \pi\text{mm}\cdot\text{mrad}$, which is below the acceptance limit of the extraction line.

4.2.3 Main ring operation

The operation scheme of the MR for COMET is different from the normal scheme, especially the pulse structure. As already mentioned above, the COMET beam needs to be pulsed with pulse separation of $\sim 1 \mu\text{s}$ and the pulse width $\sim 100 \text{ ns}$. This will be realized by filling

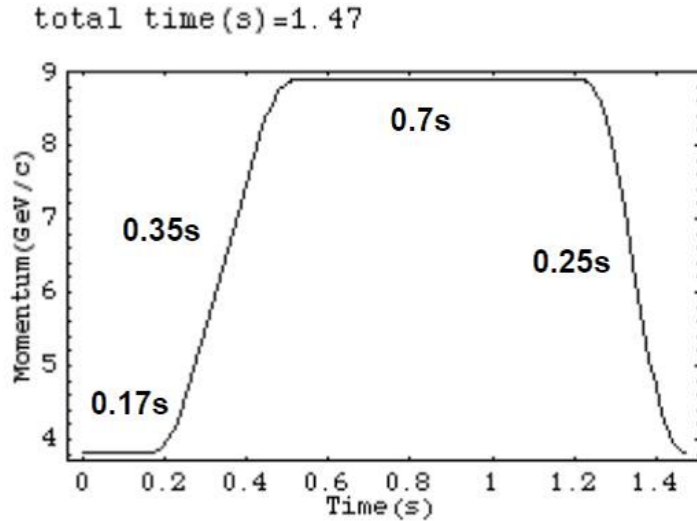


Figure 4.6: Main ring acceleration pattern.

every other bucket, which gives a total of four out of eight buckets filled in the MR. The scheme is illustrated in Figure 4.7 for the case of the RCS operating with one filled bucket at $h=2$. The other possibility is to operate the RCS with $h=1$, which requires modification of the RF frequency in the RCS. Furthermore the MR operated with $h=4$, as illustrated in Figure 4.8, will be best for COMET from the point of view of the beam extinction since there are no empty buckets in either the RCS or the MR.

4.2.3.1 Collimator setting

The collimator in the injection line from the RCS to the MR will be optimized to limit the initial emittance of the proton beam before injection. The collimator consists of a series of slits and capture jaw to prevent the scraped beam from being transferred into the MR. In the normal operation mode the collimator is set to limit the beam emittance to be less than $54 \pi\text{mm}\cdot\text{mrad}$.

4.2.3.2 Beam emittance at 8 GeV

There may be emittance growth during acceleration in spite of adiabatic damping. This is expected to be small in the COMET beam acceleration but a detailed study is desired while establishing stable operation of J-PARC.

As already described, the beam emittance needs to be reduced to less than $25 \pi\text{mm}\cdot\text{mrad}$ in order to extract the beam to the NP hall. It is believed that this can be achieved by reducing the number of protons per bunch, to limit the painting area at injection from the linac to the RCS and reducing the collimator gap at injection from the RCS to the MR. Current estimates show that a beam emittance of $<15 \pi\text{mm}\cdot\text{mrad}$ can be achieved in the MR.

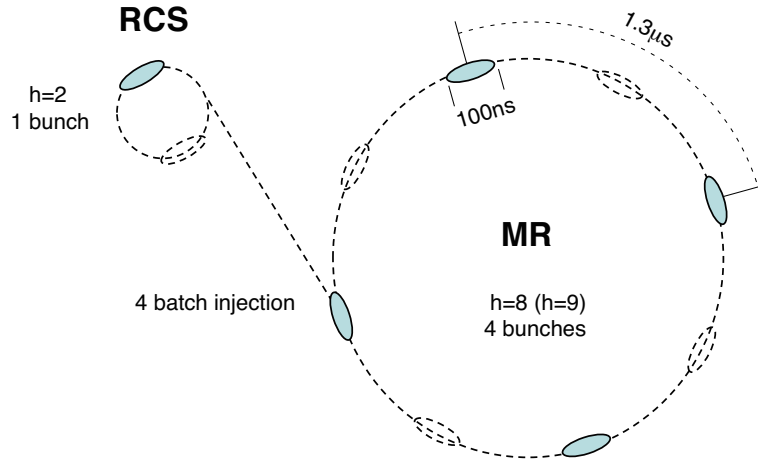


Figure 4.7: COMET beam acceleration bunch configuration with $h=8$.

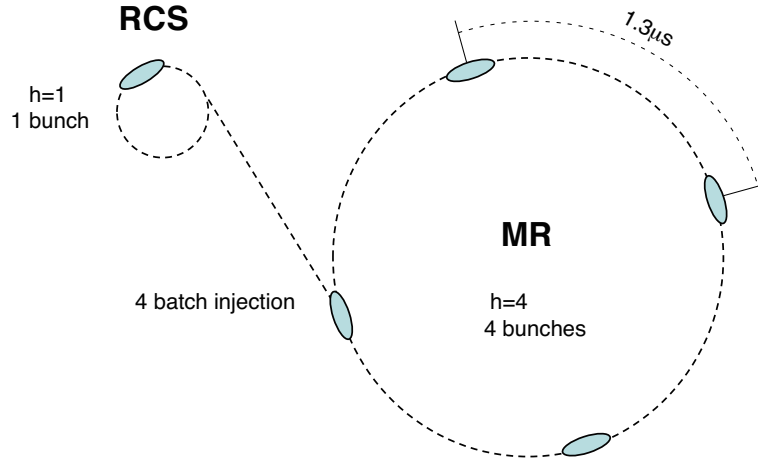


Figure 4.8: COMET beam acceleration bunch configuration with $h=4$.

4.2.3.3 Bunched slow beam extraction

The beam in the MR needs to be extracted and delivered to the pion production target whilst maintaining the pulse structure of the beam. Hardware components used in the COMET beam extraction system are the same as those used in the normal extraction of the 30 GeV beam from the MR. Bump magnets change the beam orbit in the MR, two Electro-Static Septa (ESS) separate part of the beam from the core and transfer it to the following extraction line. These and a series of septum magnets are located around the extraction point in the MR as shown in Figure 4.9.

The procedure of normal slow extraction at 30 GeV is described elsewhere [75]. Protons stored in the MR oscillate (betatron oscillation) in the horizontal plane. The frequency of oscillation, i.e. the tune ν , is usually an integer to avoid beam divergence during acceleration. After beam acceleration is completed, sextupole magnets are excited for extraction and then a 3rd order resonance ($Q_x=22.3333$) is produced. Afterwards, a set of quadrupole magnets are slowly adjusted to shift ν to the resonance at 22.3333 so that the beam edge

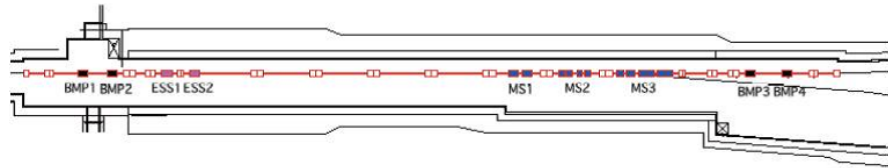


Figure 4.9: Layout of the slow extraction equipment in the MR. BMP1-4 show the bump magnets, ESS1 and ESS2 are the electro-static septa and MS1-3 are the septum magnets.

can be expanded to be scraped by the ESS.

It is important to keep the beam intensity flat during extraction. This is realized by spill control using dedicated quadrupole magnets installed in the MR and feedback signals from beam monitors both in the MR and the extraction line [76]. Two kinds of quadrupole magnets are employed for this purpose. The macroscopic beam structure is controlled by Extraction Quadrupole (EQ) magnets located at the 1st arc in the MR. The EQ magnets have a magnetic field gradient of 2 T/m (less than 1/10 of the field gradient of the normal quadrupole magnets in the MR) and have a laminated core structure made of 0.1 mm thick steel to achieve quick response. Two EQs are used in series to cancel out the effect of beta modulation. These are mainly used to keep the spill shape flat. The other kind of quadrupole magnets, called Ripple Quadrupole (RQ) magnets, are located near the EQs in the MR and are used to remove the ripple noise (a few kHz – 100 kHz) caused by the power supply. The RQ has a similar structure to that of the EQ but its magnetic field gradient is only 0.2 T/m, which allows it to respond faster than the EQ.

The COMET beam extraction is executed in principle in the same manner. What is different in the COMET case is that all extraction parameters have to be adjusted and optimized for 8 GeV operation. In addition to this, the RF voltage needs to be kept at a certain value in order to maintain the pulse structure during extraction. In normal slow extraction of the protons from the MR, the RF cavity voltage is usually switched off in order to yield a flat time structure of the proton beam. However, for the COMET experiment, the RF cavity voltage is not switched off so that the proton pulse structure is maintained when pions are produced at the target. This is referred to as the bunched slow extraction method. It will probably be necessary to reduce the voltage in order to minimize the heat load in the cavities. This needs to be optimized. It is also necessary to modify the feedback time constant for slow extraction. The COMET beam has a time structure of \sim 1 MHz and this needs to be taken into account in spill control. Extraction of the COMET beam is simulated by using a simple particle tracking method. In Figure 4.10, particle phase space distributions are shown after extraction at the ESS. Sharp edges in $x - x'$ and $x - y$ distributions are due to separation at the ESS. It can be seen that in the right-bottom figure that the longitudinal distribution of the particles is less than 20 m. This corresponds to a bunch width of less than 70 ns, which satisfies the COMET beam requirement.

J-PARC is a high-intensity machine and thus the loss during acceleration must be minimised. This is a big challenge for the accelerator group and is being achieved step by step whilst increasing the beam power. It is believed that the COMET requirement for an extremely “pure” beam, i.e. a very small amount of residual protons outside the pulse, should be achievable and there is large room for collaboration on this.

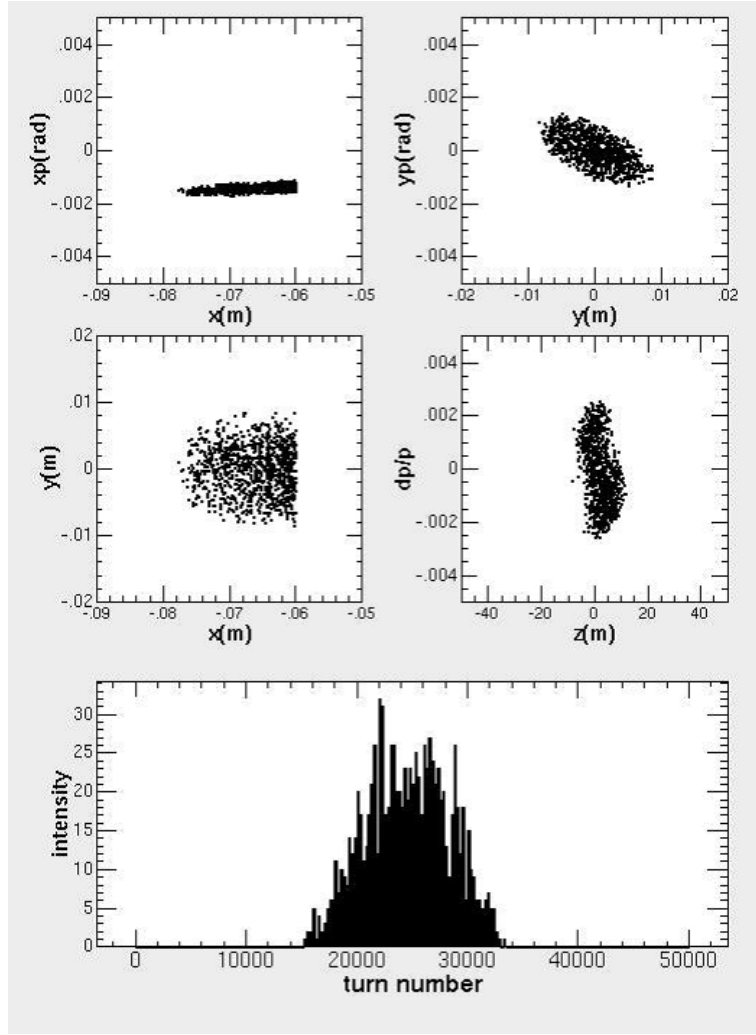


Figure 4.10: Simulations of the phase space distributions of the beam extracted from the MR.

4.3 Proton beam transport

The proton beam transport line is used to take the 8 GeV beam extracted from the MR and deliver it to the pion production target. In spite of the different extraction method to be employed in COMET, the beam transport scheme is the same for COMET and the other experiments at the NP Hall which use the normal slow extracted beam.

4.3.1 Proton beam optics design

The entire layout of the proton beam line is shown in Figure 4.11. The beam line consists of a matching section, an AC dipole section and a final focus section. The matching section is necessary to shape the beam envelope to fit the acceptance of the following section. The next section, the AC dipole section, is as long as 30 m where protons in empty buckets are swept out by AC dipoles driven by sinusoidal currents to improve the beam extinction. The

final section transfers the proton beam to the pion production target and focuses the beam to a 4 mm radius.

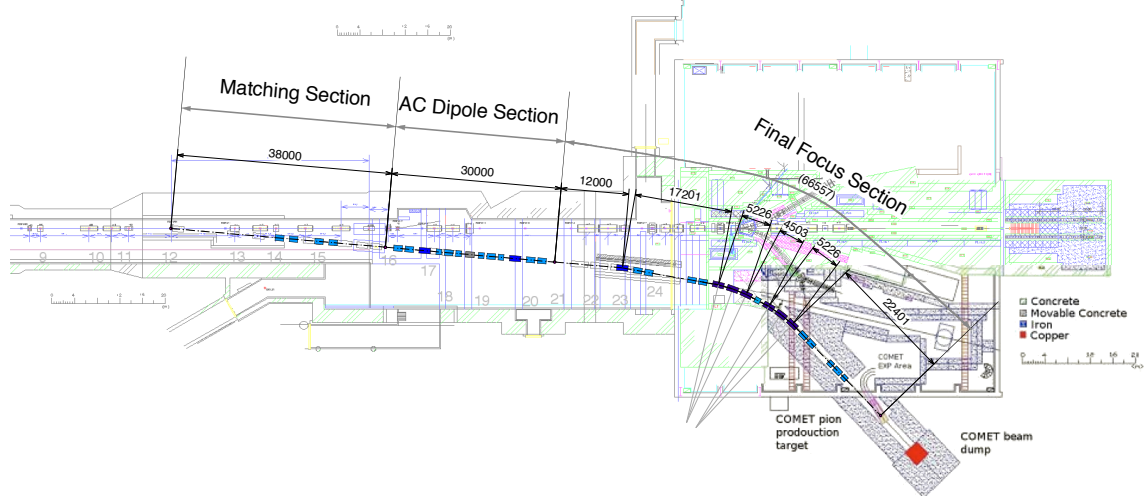


Figure 4.11: Entire layout of proton beamline.

4.3.1.1 Matching section

The matching section consists of two Quadrupole doublets and one vertical bending magnet. This section starts at a switching magnet located on the A line to switch (or separate) the primary beam to the B line. The proton beam is transported along this B line to the COMET pion production target. The proton beam is transported in this matching section point-to-parallel in the x direction and parallel-to-point in the y direction. The design of the optics was done with TRANSPORT [77]. The designed layout of the matching section is shown in Figure 4.12. The quadrupole magnet parameters are summarized in Table 4.2.

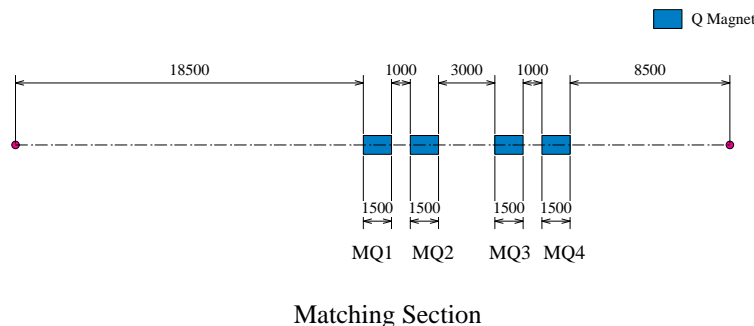


Figure 4.12: Layout of matching section.

4.3.1.2 AC dipole section

The AC dipole section is a key section in the proton beam transport line. The section consists of two AC dipoles and a collimator between them. Focusing elements are placed in

Table 4.2: Quadrupole magnet parameters in the matching section.

Q magnets	Gradient [T/m]
MQ1	-5.927
MQ2	4.929
MQ3	3.079
MQ4	-7.143

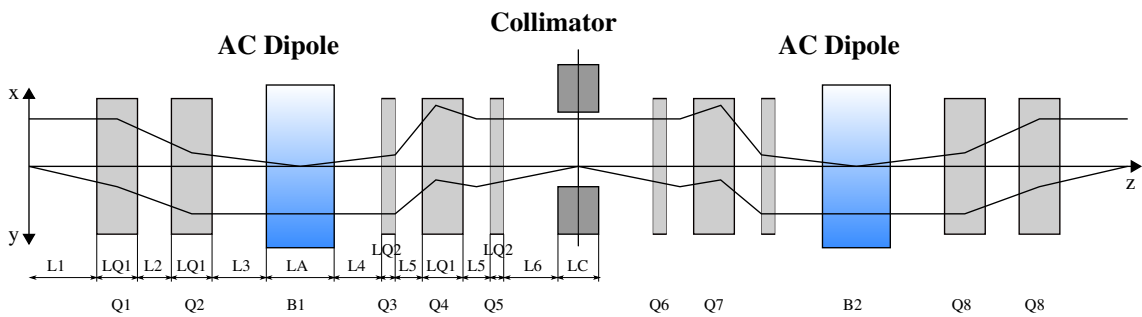


Figure 4.13: Schematic view of AC dipole section.

front of and behind each AC dipole. The AC dipole field is set in the horizontal direction thus protons are kicked in the vertical (y) direction. A schematic layout of the optical components is shown in Figure 4.13, where Q_n and B_n indicate quadrupole magnets and dipole magnets (AC dipoles), respectively.

Protons are delivered to the AC dipole section when the first AC dipole field is zero. These will go through undeflected to the final focusing section while protons that arrive at different times will be swept out by the non-zero field of the AC dipoles. The sweeping angle depends on the phase of the B field when protons arrive in this section. Those protons deflected through a large angle by the first AC dipole are stopped by the collimator, while protons deflected through a small angle will be transmitted through it. The second AC dipole is necessary to eliminate out-of-time protons from being delivered to the final focusing section. The field direction of the second AC dipole is set opposite to that of the first AC dipole so that it will compensate the deflection of the first AC dipole and the proton beam will be moved back to the original beam axis. Figure 4.14 illustrates how the beam profile is moved in the vertical direction in the AC dipole section.

The B field of the first AC dipole is varied as $B(t) = B_0 \sin(2\pi ft)$, where the frequency f is set to fit the bunch-bunch period ($T = 1.3 \mu\text{s}$) of the proton beam, i.e. $f = 1/2T = 0.385 \text{ MHz}$. The amplitude of the B field is currently set to be 600 Gauss. In this case, protons at the edge of the bunch (the width, τ , is assumed to be 100 ns) see a magnetic field of $B(\tau/2) = 72.3$ Gauss. Figure 4.15 shows the change of the AC dipole field coincident with the passage of the proton beam through the section.

Larger apertures for the AC dipole are preferred to ease the requirements on the optics of the beam transport section. However larger apertures requires a larger driving power and thus they are currently restricted to $\pm 5 \text{ mm}$ in x direction and $\pm 25 \text{ mm}$ in y direction. The length of the AC dipoles is designed to be 2 m. To transmit the proton beam, the beam should form a waist within the AC dipoles in the x direction and a parallel shape in

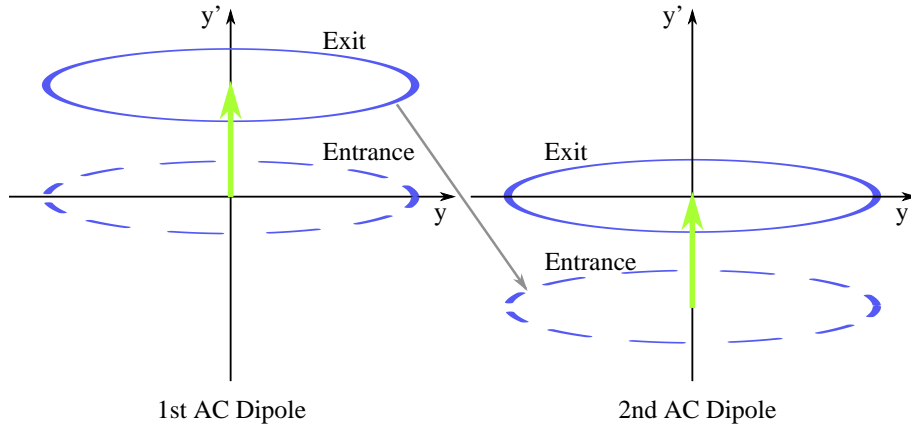


Figure 4.14: Behavior of 2-D phase beam ellipse at the AC dipoles.

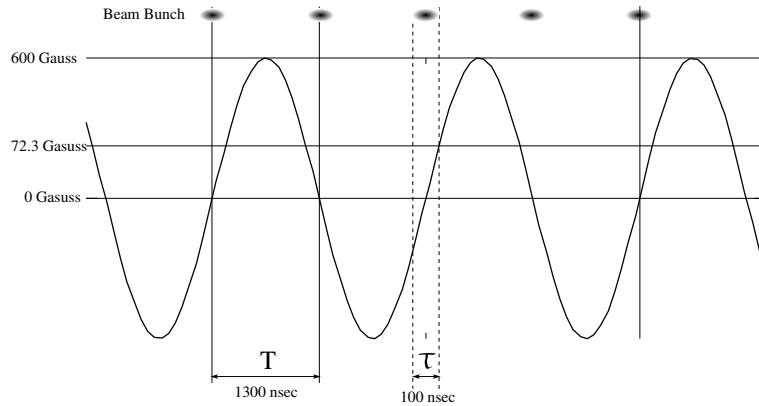


Figure 4.15: Relative timing between proton beam bunch and AC field. It is assumed that bunch width $\tau = 100$ ns and space between beam pulses $T = 1.3 \mu\text{s}$.

the y direction. In addition, the beam should be focused in the y direction (Figure 4.13) at the collimator. The two dimensional beam phase ellipse at the second AC dipole should be the same as that at the first AC dipole so that the beam can be returned to the central axis.

The optics design to satisfy these requirements has been optimized by using the TRANSPORT program for a proton beam momentum of $8.889 \text{ GeV}/c$. In this design the section is separated into four sub-sections as follows.

- ADS1: from the end of the matching section to the center of the 1st AC dipole.
- ADS2: from the end of ADS1 to the center of the collimator.
- ADS3: from the end of ADS2 to the center of the 2nd AC dipole.
- ADS4: from the end of ADS3 to the end of the AC dipole section.

Constraints on the transfer matrices for each sub-section are summarized in Table 4.3. The optics elements are aligned symmetrically with respect to the central plane of the collimator

Table 4.3: Constraints applied to the AC dipole section in the TRANSPORT calculation.

	<i>x</i> direction	<i>y</i> direction
ADS1	parallel-to-point	point-to-parallel
ADS2	point-to-parallel	parallel-to-point and waist-to-waist
ADS3	parallel-to-point	point-to-parallel and waist-to-waist
ADS4	point-to-parallel	parallel-to-point

as shown in Figure 4.13. The length of the drift space and optics elements are manually adjusted, and those values are summarized in Table 4.4. The geometric configuration of components is shown in Figure 4.16.

Table 4.4: Length of drift spaces and optics elements.

Position	Length
L_1	1.5 m
L_2	0.5 m
L_3	1.0 m
L_4	1.0 m
L_5	0.5 m
L_6	0.75 m
L_{Q1}	1.5 m
L_{Q2}	1.0 m
L_A	2.0 m
L_C	1.5 m

Field gradients of quadrupole magnets, Q_1 , Q_2 , Q_3 , Q_4 , and Q_5 are calculated so that the optics can satisfy constraints summarized in Table 4.3. The obtained field gradients for each Q magnet are summarized in Table 4.5.

4.3.1.3 Final focusing section

The layout of the final focusing section is shown in Figure 4.17. The section consists of dipole magnets to bend the beam to the COMET pion production target and focusing

Table 4.5: Field gradients for quadrupole magnets in the AC dipole section.

Q magnet	Field gradient [T/m]
Q_1	6.365
Q_2	-6.609
Q_3	-11.173
Q_4	-10.716
Q_5	13.001

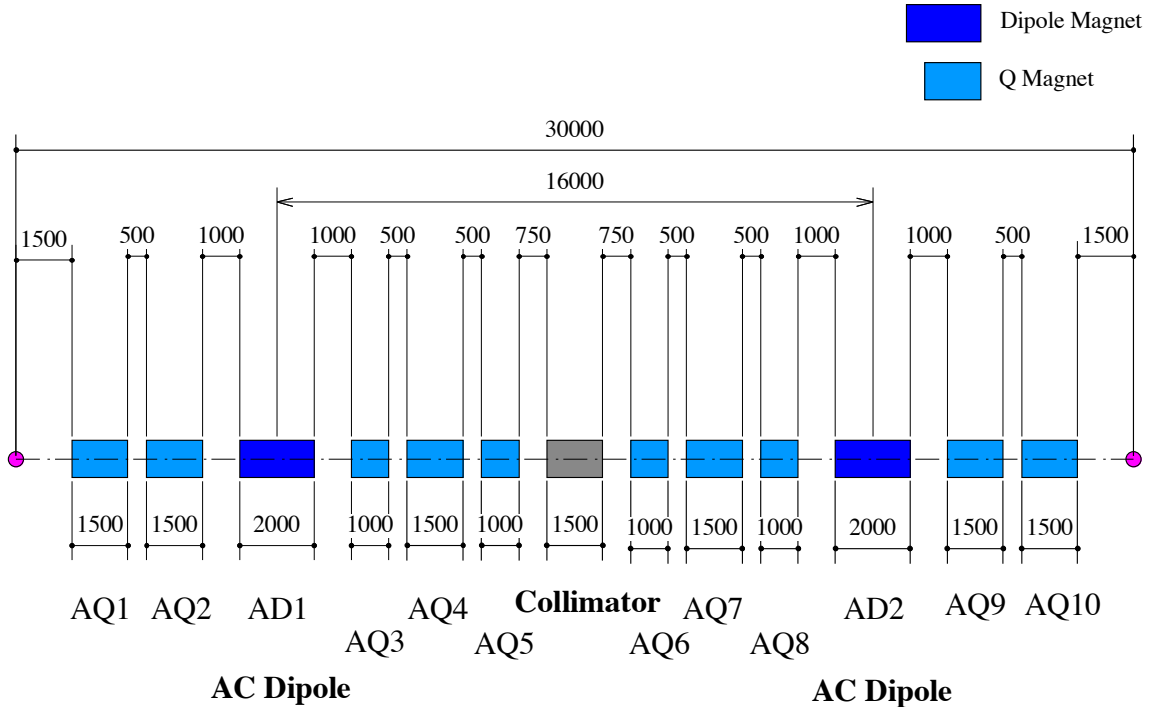


Figure 4.16: Geometric configuration of the AC dipole section.

quadrupole magnets located in front and behind them.

Calculated beam envelope profiles and divergences are shown in Figures 4.18 and 4.19 as a function of the proton beamline. The start point is the switching magnet. This shows that it is possible to provide a sufficiently small profile (<4 mm) at the target. Figure 4.20 shows the η functions in the transport line. It can be seen that the η functions successfully vanish at the target.

4.3.2 G4beamline simulation

Beam tracking simulations were done using G4beamline. Figure 4.21 shows the layout of the transport line used in the simulations.

The initial beam profiles at the switching magnet need to be optimized so that the beam can be transmitted through the AC dipole apertures under the beam emittance condition of $\epsilon_x = 5\pi\text{mm}\cdot\text{mrad}$ and $\epsilon_y = 10\pi\text{mm}\cdot\text{mrad}$. Initial beam profile parameters of $\delta x = 0.02\text{ m}$, $x' = 0.00025\text{ rad}$, $\delta y = 0.003\text{ m}$ and $y' = 0.00333\text{ rad}$ were used in the simulations. The behavior of the 2-dimensional phase-space ellipses at the AC dipoles are shown in Figure 4.22. It is assumed that there is a constant B field of 0.073 T at both AC dipoles, which is the case when the edge of the beam bunch arrives at the AC dipole section. It can be seen that at the exit of the 2nd AC dipole the ellipse is pulled back to the original position at the entrance of 1st AC dipole.

Particle tracking simulations were also done with applying an AC field to the AC dipoles. In this simulation protons are distributed on an ellipse in 2-dimensional phase space ($dt-dP$) where $dt = \pm 50\text{ ns}$ and $dP = \pm 0.3\%$ at the location of the switching magnet (i.e. the initial tracking position). Tracking results are presented in Figure 4.23. The left (right) figures show result of proton beam tracking in the main (empty) bucket. The upper (lower) figures

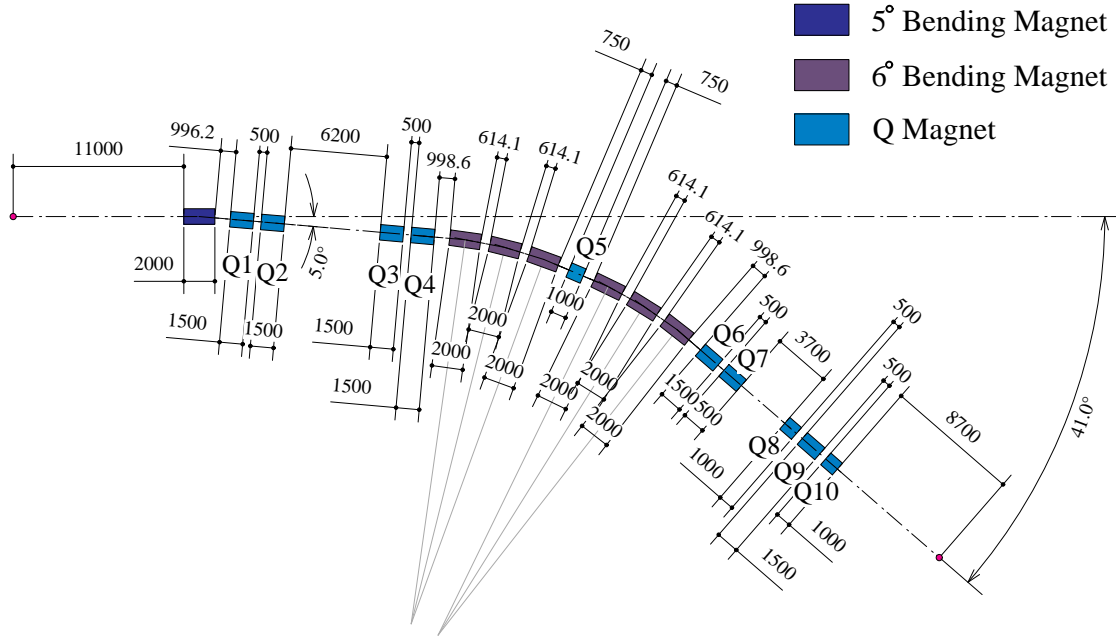


Figure 4.17: A layout of the final focusing section.

are the beam envelopes in the x (y) direction as a function of the length from the entrance of the AC dipole section. Collimators are placed at the center of the AC dipole section. The aperture limit of the collimator is assumed to be ± 15 mm in x and ± 9 mm in y , respectively. The collimator length is assumed to be 1500 mm. It can be seen that protons in the main bucket are transmitted to the exit of the section while protons in the empty bucket are stopped by the collimator and do not reach the exit of the section.

Momentum distributions at the entrance and exit of the collimator are shown in Figure 4.24 for the proton beam arriving out of time (in an empty bucket) at the AC dipole section. It can be seen that the main part of the beam is stopped or degraded in the AC dipole section. Figures 4.25–4.28 show simulated time distributions, momentum spectra, and profiles of the proton beam at various locations on the beam line. As seen in Figure 4.29, out-of-time protons are displaced by the 1st AC dipole and scraped by the collimator although particles with a large displacement in the y direction still remain in the time window. Figure 4.28 shows distributions of the beam on the pion production target. As can be seen, out-of-time protons in the beam are clearly suppressed at the target due to the AC dipole section and the final bend in the final focusing section. The reason for a peak around 5500 MeV/c is not completely understood. Some protons in this peak are above the anti-proton production threshold which could cause unwanted backgrounds, however, these protons arrive at the target promptly and should easily be identified. Figure 4.30 shows the relation of the arrival time with proton momentum at particular locations along the beam line. The current simulation is limited by statistics but it is safe to conclude that this design for the transport line has the capability to reduce off-timing protons by a factor of more than 1000.

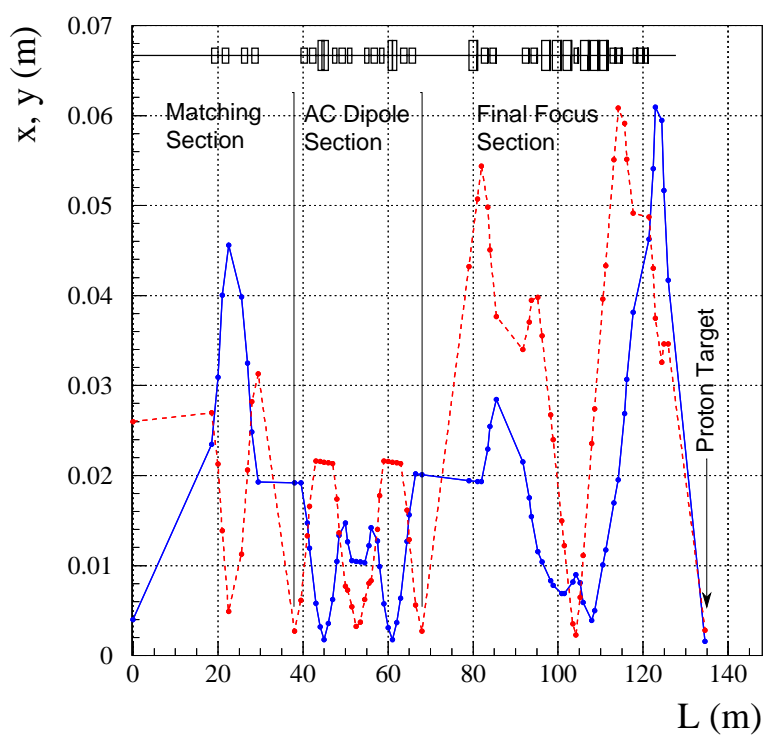


Figure 4.18: Proton beam envelope as a function of the beamline length, x in blue and y in red.

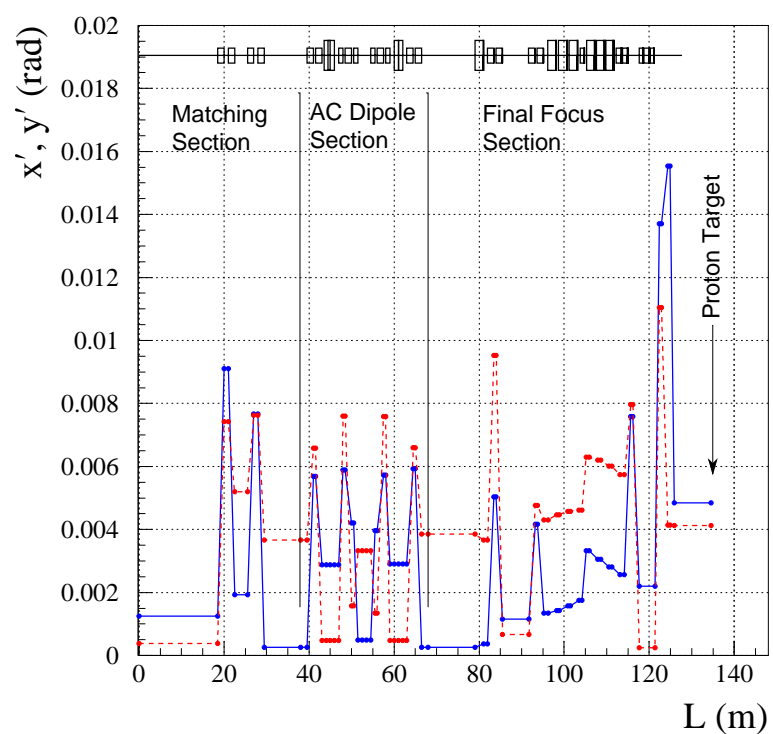


Figure 4.19: Proton beam divergence as a function of the beamline length, x' in blue and y' in red.

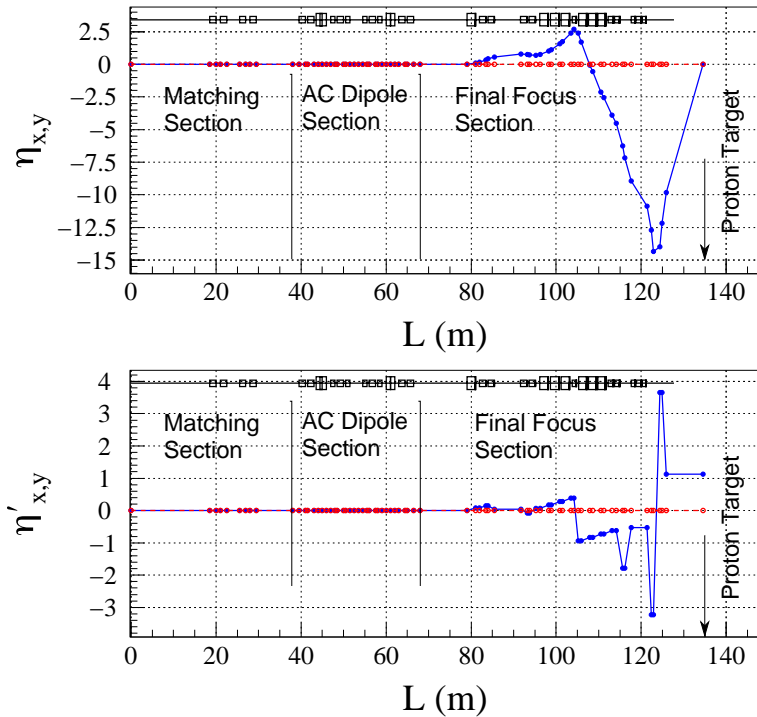


Figure 4.20: Accelerator η functions. Upper: η_x (blue) and η_y (red). Lower: η'_x (blue) and η'_y (red).

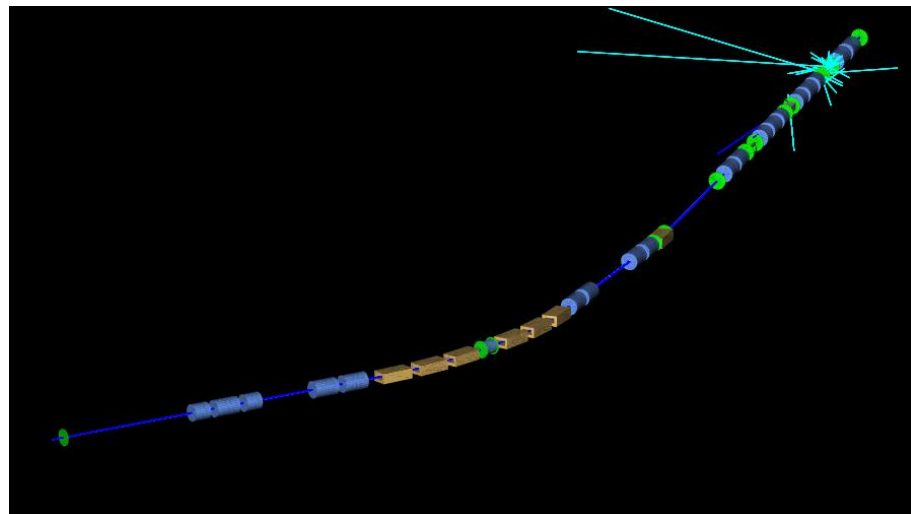


Figure 4.21: Layout of the proton beam transport line employed in the G4beamline simulations.

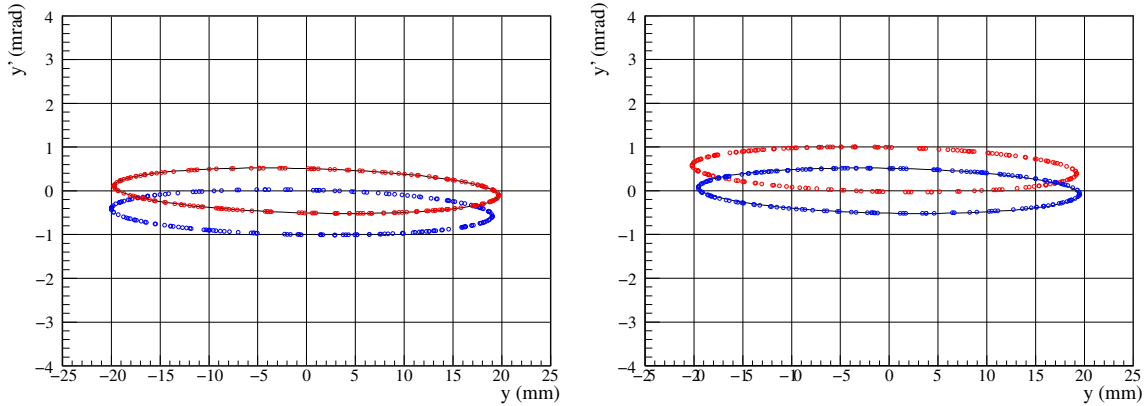


Figure 4.22: 2-dimensional phase-space ellipse at both AC dipoles when the B field of the AC dipoles is set to be 0.073 T. Left: at the 1st AC dipole. Right: at the 2nd AC dipole. Red and blue points indicate ellipses at entrance and exit, respectively.

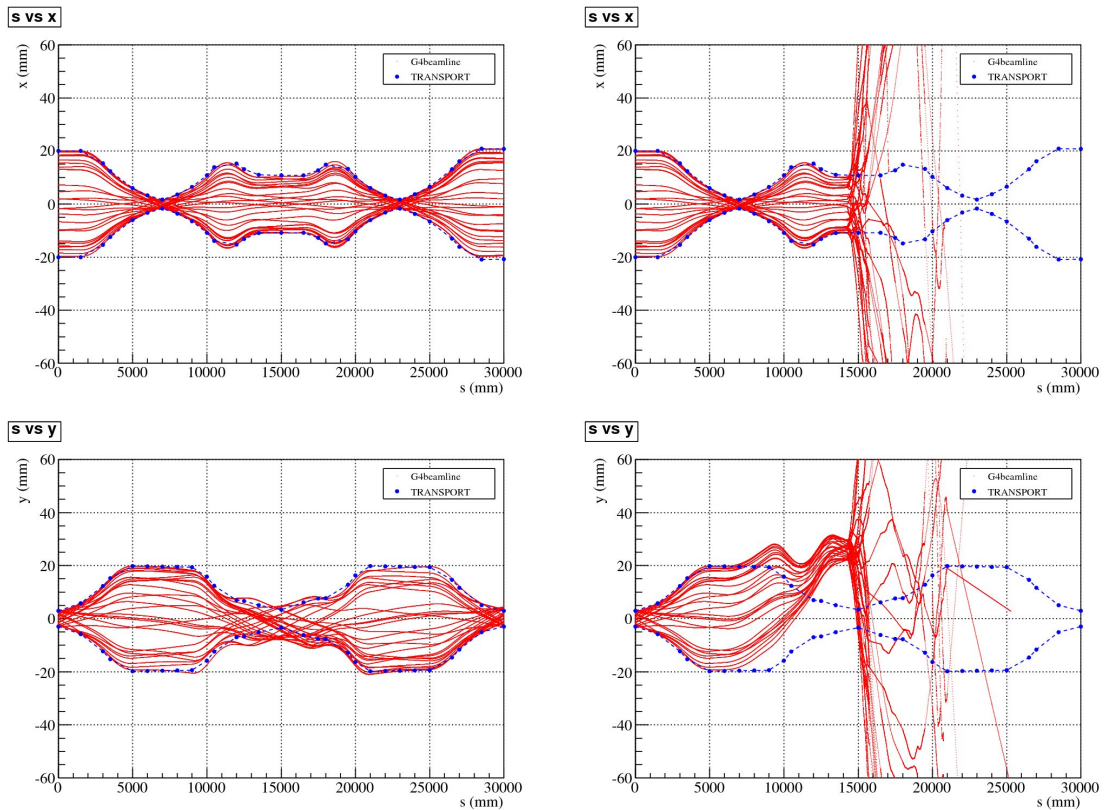


Figure 4.23: Upper (Lower): $x(y)$ vs length from the AC dipole entrance. Left: Proton beam in a main bucket. Right: Proton beam in an empty bucket.

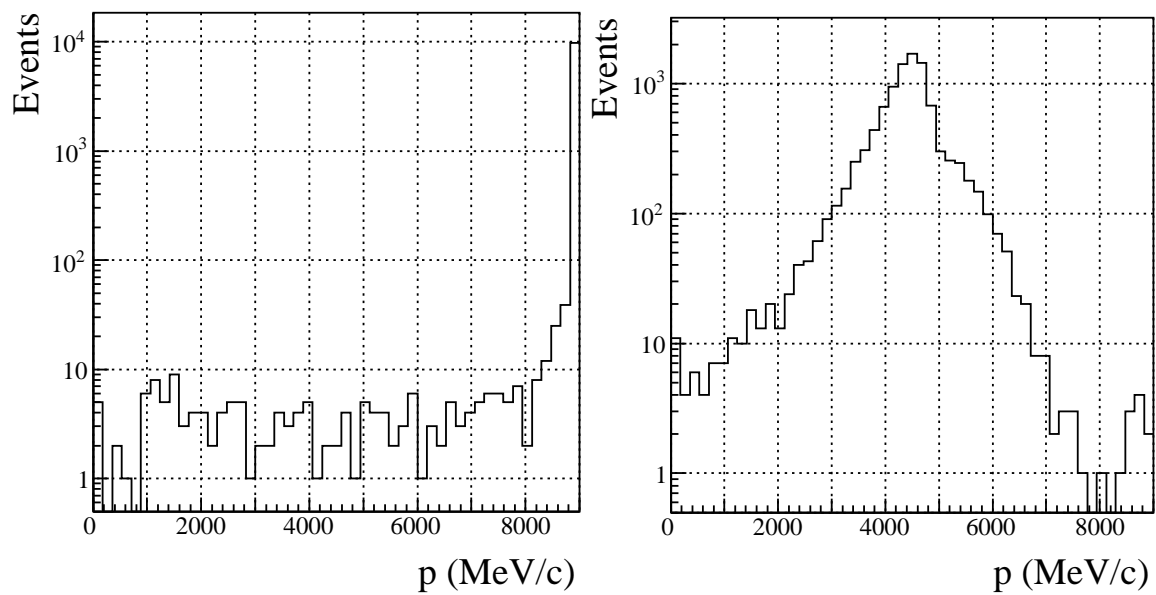


Figure 4.24: Left (Right): Momentum distributions of the proton beam in an empty bucket phase at the entrance (exit) of the collimator, where the AC dipole is operated in AC mode.

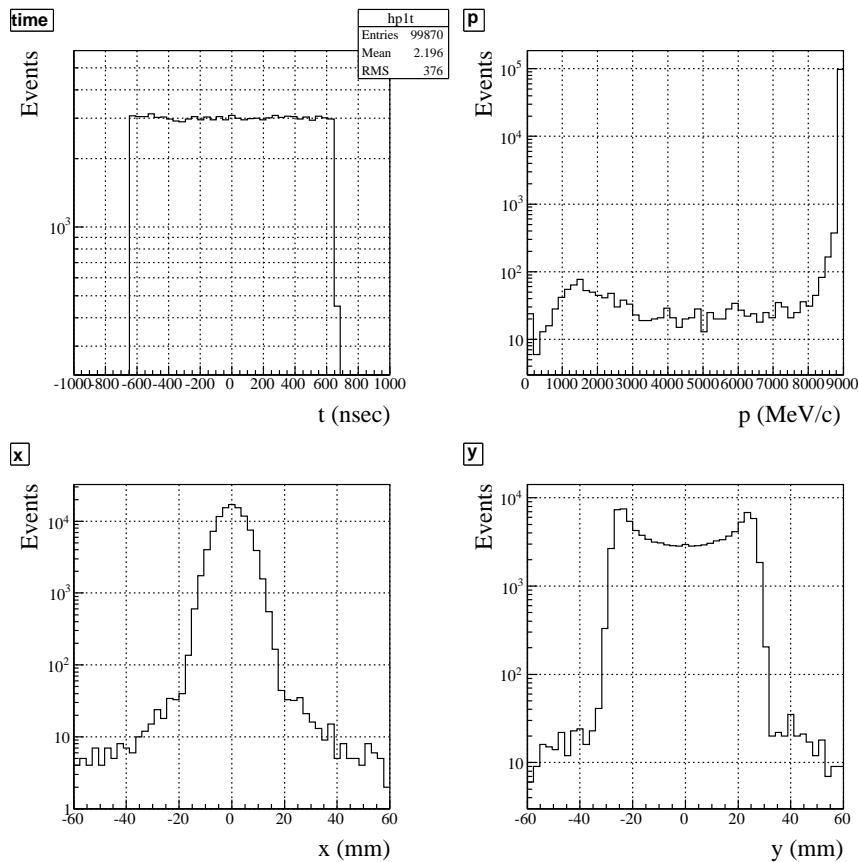


Figure 4.25: Time distribution, momentum spectrum, and profiles of the beam at the entrance of the collimator. Upper left: Supposed time spectrum of the proton beam as an input. Upper right: Momentum spectrum of the proton beam. Lower left: Beam profile in the x direction. Lower right: Beam profile in the y direction.

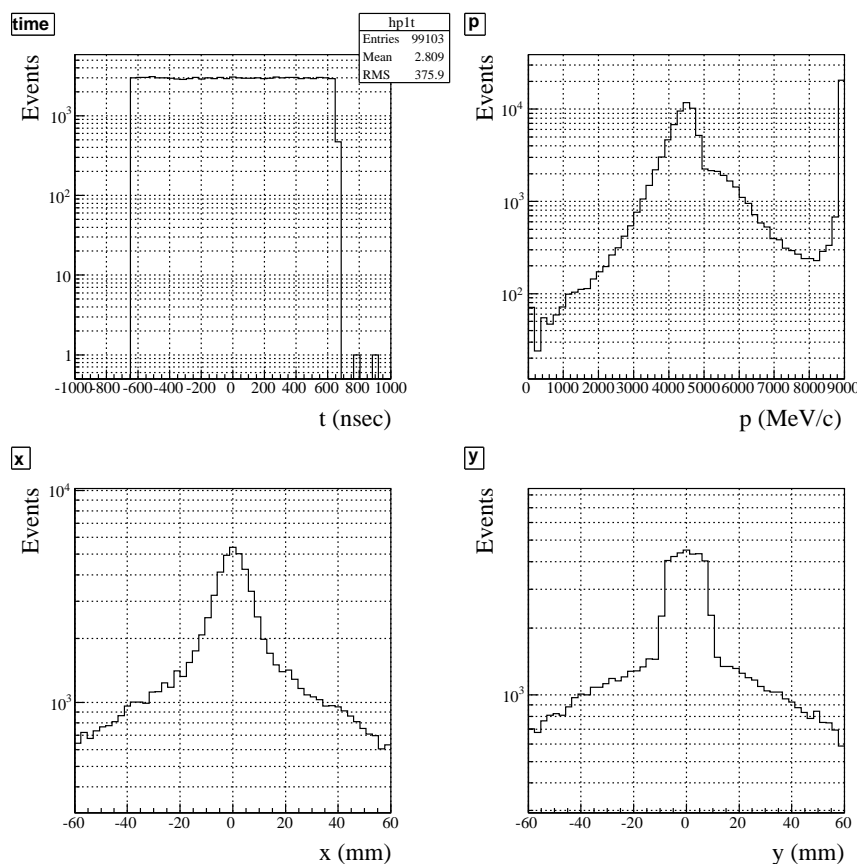


Figure 4.26: Time distribution, momentum spectrum, and profiles of the beam at exit of the collimator. Upper left: Time spectrum of the proton beam. Upper right: Momentum spectrum of the proton beam. Lower left: Beam profile in the x direction. Lower right: Beam profile in the y direction.

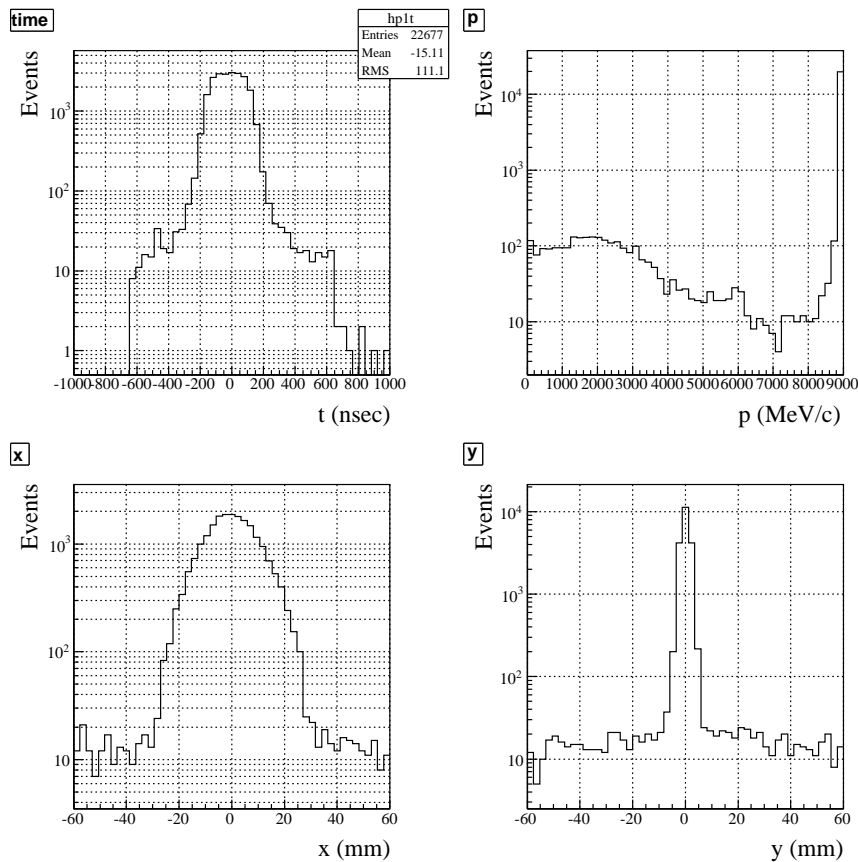


Figure 4.27: Time distribution, momentum spectrum, and profiles of the beam at the entrance of the final focus section. Upper left: Time spectrum of the proton beam. Upper right: Momentum spectrum of the proton beam. Lower left: Beam profile in the x direction. Lower right: Beam profile in the y direction.

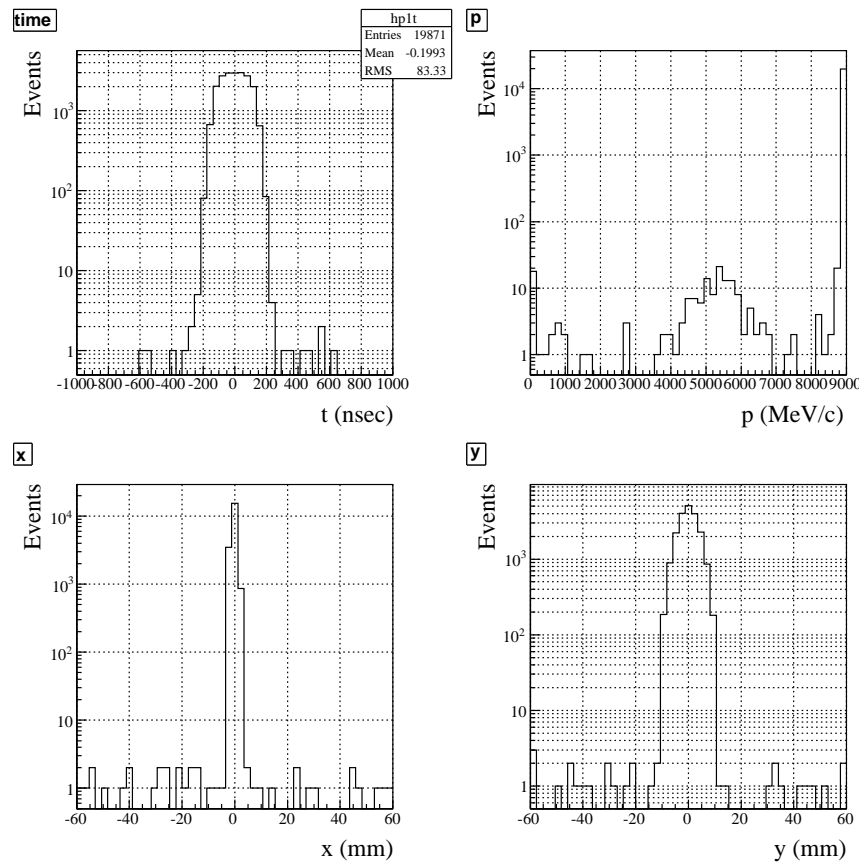


Figure 4.28: Time distribution, momentum spectrum, and profiles of the beam on the pion production target. Upper left: Time spectrum of the proton beam. Upper right: Momentum spectrum of the proton beam. Lower left: Beam profile in the x direction. Lower right: Beam profile in the y direction.

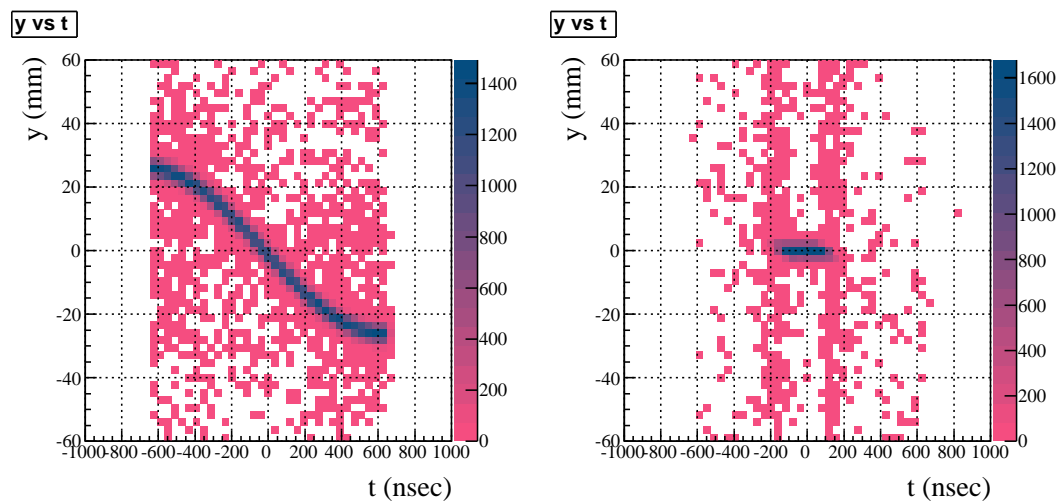


Figure 4.29: Time vs y profile at the entrance of the collimator (left) and at an exit of the AC dipole section (right).

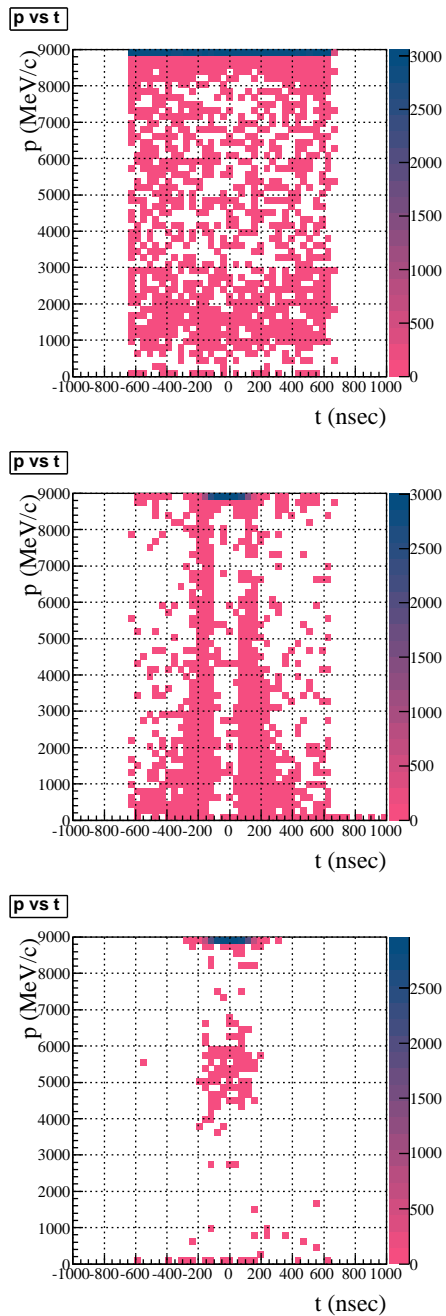


Figure 4.30: Time vs p at the entrance of the collimator (top), at the entrance of the final focus section (middle), and at the exit of the final focus section (bottom).

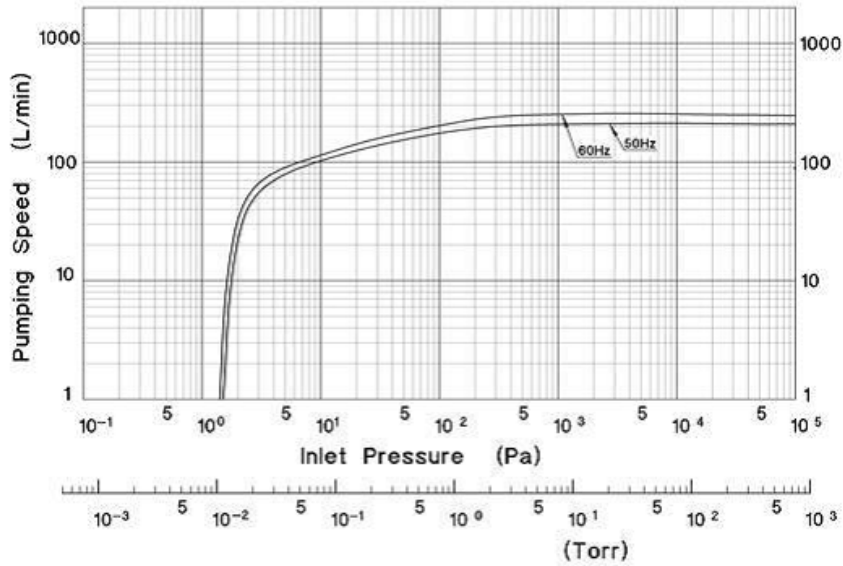


Figure 4.31: Pumping speed of ISP-250B oil-free pump.

4.3.3 Proton beam line hardware

In this section, the proton beam line hardware is described. Most of the hardware elements introduced in the proton beam transport line are conventional, thus we do not need any special development except for the AC dipole magnet. Auxiliary components such as power supply and vacuum systems are also standard.

4.3.4 Magnet system

Most of the beam transport line magnets will be shared with the 30 GeV line and they are therefore required to be able to transport a proton beam of 30 GeV. The beam is bent in the NP hall for the COMET experiment to transport the beam onto the target. For this bending we need a series of bending magnets probably with a C-shape for beam branching. An interlock system is necessary for radiation safety and needs to be designed to allow for different magnet excitation configurations such that the experimental area can be accessed both in the high momentum proton beam line and COMET beam line without shutting down the accelerator.

4.3.5 Power supply system

The power supply system can be the same as those used in the A-line beam transport line. The necessary electricity and cooling water is listed in Section 13.5 and is based on the estimates for the A-line magnets.

4.3.6 Vacuum system

Since we need to reduce beam loss and unexpected radiation doses, it is necessary to evacuate the transport line beampipe. The required level of 0.1–1 Pa can be realized without any

difficulty by installing scroll vacuum pumps at about every 20 m of the beam line. Oil-free scroll will be used to prevent radiation contaminated oil mist from being distributed in the environment. Figure 4.31 show a typical performance of such pump¹. This type of pump has been introduced in the A-line and its actual performance has been already proved in the operation of the A-line.

¹ISP-250B Oil-free scroll vacuum pump, ANEST IWATA

Chapter 5

Muon Beam

This chapter describes the muon beam proposed for the COMET experiment. An 8 GeV proton beam from the J-PARC Main Ring (MR) is collided with a target to produce pions. The pions thus produced are captured with high efficiency using a 5 T superconducting solenoid magnet surrounding the pion-production target. The muons, which are produced by pion decays, are captured and transported through subsequent solenoids and are brought to a muon-stopping target in the detector solenoid. The muon beam line is composed of a combination of straight and curved superconducting solenoids. The curved solenoids are used to select the charge and momentum of muons in the beam line and have a compensating dipole magnetic field overlaid. The expected muon beam intensity is enormous, about $10^{11} \mu^-/\text{sec}$, which would be the highest in the world. In the following sections describe the pion production, pion capture and muon transport in detail.

5.1 Pion production

5.1.1 Pion production yields

The COMET experiment uses negatively-charged low-energy muons, which can be easily stopped in a muon-stopping target. The low-energy muons are mostly produced by in-flight decay of pions of low energy. Therefore, the production of low energy pions is of major interest. At the same time, high-energy pions, which could potentially cause background events, should be eliminated as much as possible.

The π^- production yields by protons incident on gold are presented in Figs. 5.1 for different momentum regions. They were produced by a hadron production code, MARS15 (2004)[78]. It can be seen that there is a maximum at a transverse momentum (p_T) around 100 MeV/c for a longitudinal momentum (p_L) of $0 < p_L < 200$ MeV/c for both the forward and backward scattered pions. The maximum total momentum for backward scattered pions is about 120 MeV/c, whereas that for forward scattered pions is about 200-400 MeV/c. It can also be seen that high-energy pions are suppressed in the backward direction. The yields of low energy pions are not so different, lying within a factor of two between the forward and backward directions. Thus backward pions are less contaminated by high energy pions while retaining those having low energy. For these reasons, it has been decided to collect pions emitted backward with respect to the proton beam direction.

Figure 5.2 shows yields of pions and muons as a function of proton energy. As seen in Figure 5.2, the pion yield increases almost linearly with proton energy, therefore with

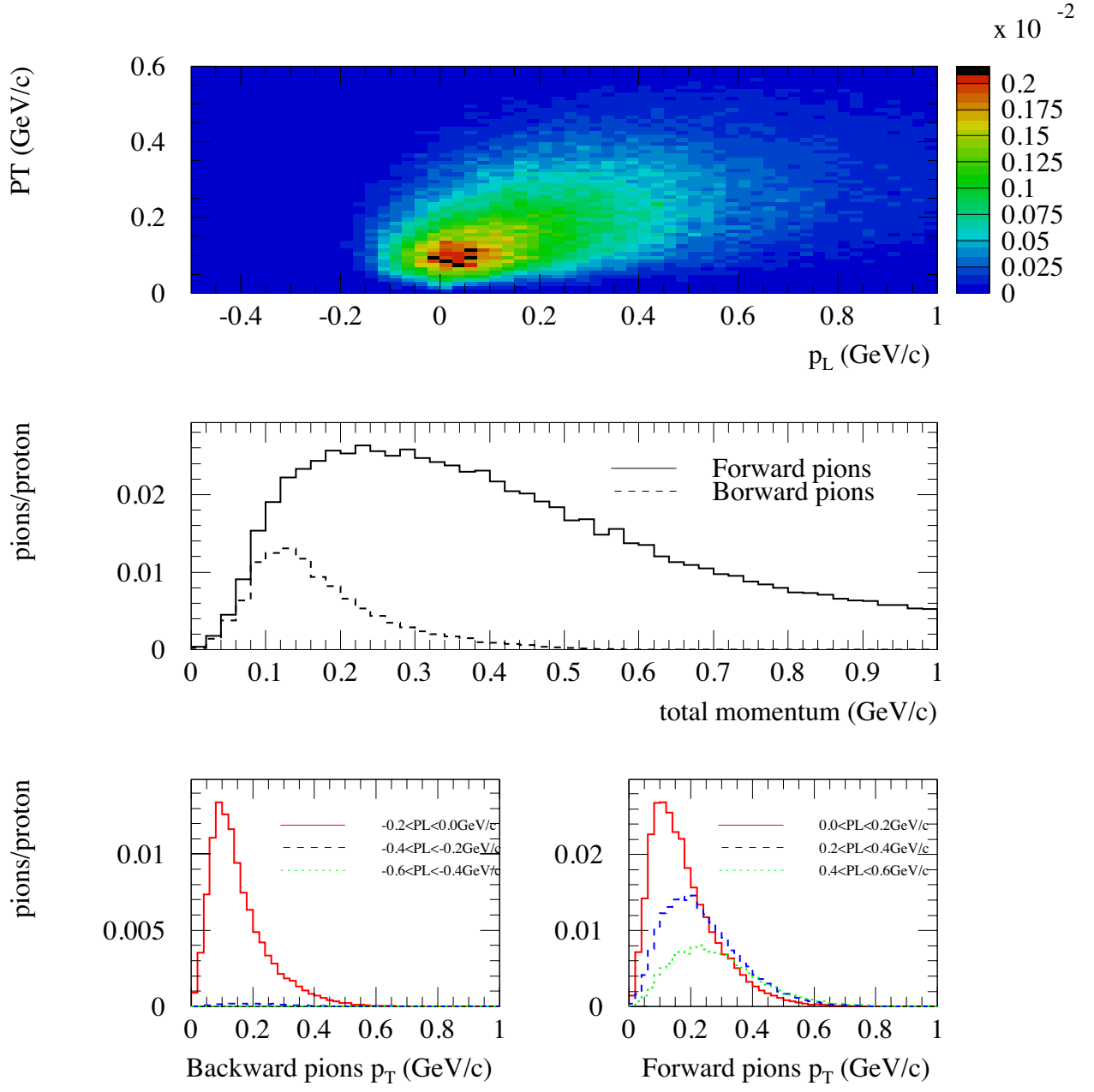


Figure 5.1: Pion production in a gold target. (top) Correlation between p_L and p_T . (middle) Total momentum distributions for forward and backward π^- s. (bottom-left) p_T distributions for $-0.2 < p_L < 0$ GeV/c, $-0.4 < p_L < -0.2$ GeV/c, and $-0.6 < p_L < -0.4$ GeV/c. (bottom-right) p_T distributions for $0 < p_L < 0.2$ GeV/c, $0.2 < p_L < 0.4$ GeV/c, and $0.4 < p_L < 0.6$ GeV/c.

proton beam power. Also it is seen that at a very high proton energy (> 30 GeV), pion production yield starts to be saturated.

The choice of proton energy can be determined from consideration of the pion production yield and backgrounds. In particular backgrounds from proton beam between beam pulses

(extinction) and antiproton production. At this moment, our choice of proton energy is 8 GeV, as described in Section 4.

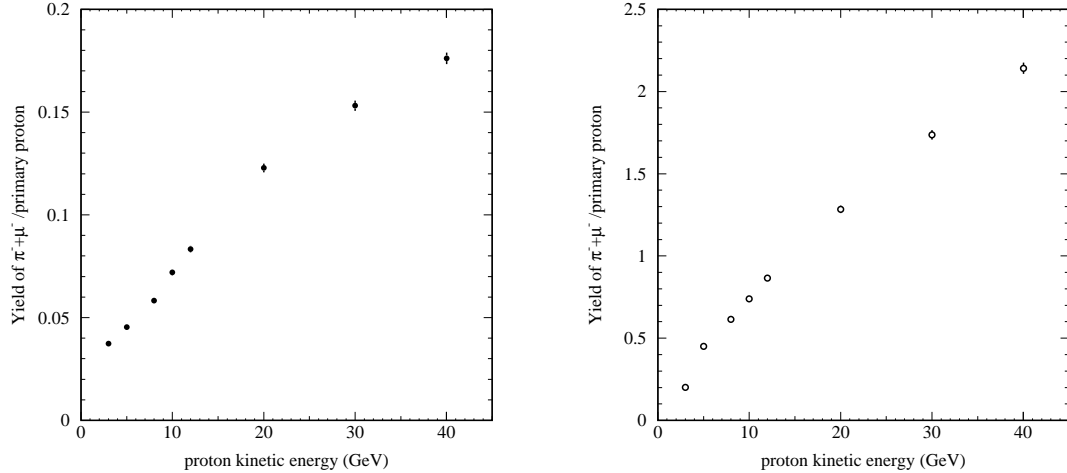


Figure 5.2: Yields per proton of backward pions and muons (in left) and forward pions and muons (in right) from a graphite target in a magnetic field of 5 Tesla as a function of proton energy.

5.1.2 Comparison of different hadron production codes

In order to study the pion production yields, Monte Carlo simulations have been performed using three different types of hadron codes, namely QGSP, QGSP_BIC in the Geant4 [79] physics lists and MARS [78]. It is noted that the MARS code is a hadron production code developed at Fermilab. Figure 5.3 shows momentum spectra of π^- forward and backward production from a tungsten target for different hadron codes. As seen in Figs. 5.3, a difference of a factor of about two exists. The π^- yields at low-energy are summarized in Table 5.1.

Table 5.1: Ratios of π^-/p for different hadron codes.

Hadron codes	π^-/p backward ($p < 500$ MeV/c)	π^-/p forward ($p < 500$ MeV/c)
MARS	0.11	0.15
QGSP	0.10	0.75
QGSP_BIC	0.22	0.41

5.1.3 Pion production target

5.1.3.1 Target material

Pion production cross section is higher for heavier materials, as shown in Figure 5.4. The production cross section is almost 2 times larger for tungsten than graphite. Although our

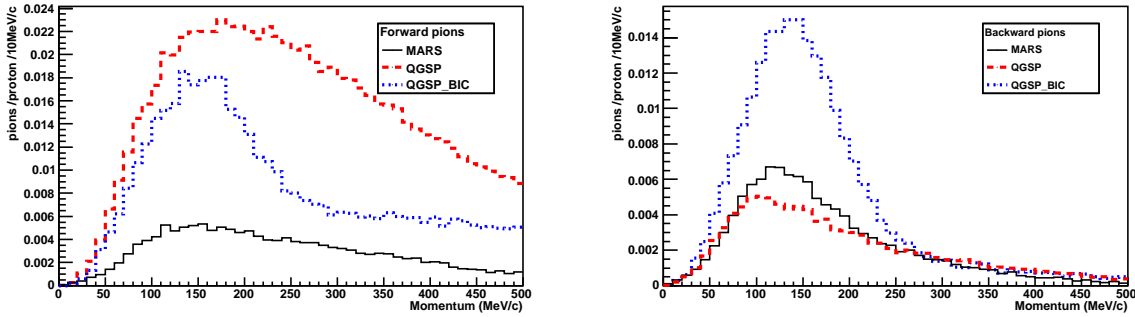


Figure 5.3: Negative pion production of forward (left) and backward (right) directions from a tungsten target as a function of their momenta for different hadron production codes. QGSP_BIC gives twice higher pion yields than MARS.

original target material was graphite, the present candidate for the target material is either platinum, gold or tungsten. However, if it is a metal target, it would melt when exposed to an incident high power proton beam. Therefore target cooling is necessary. The current target design for this experiment is based on a water-cooled rod of heavy material.

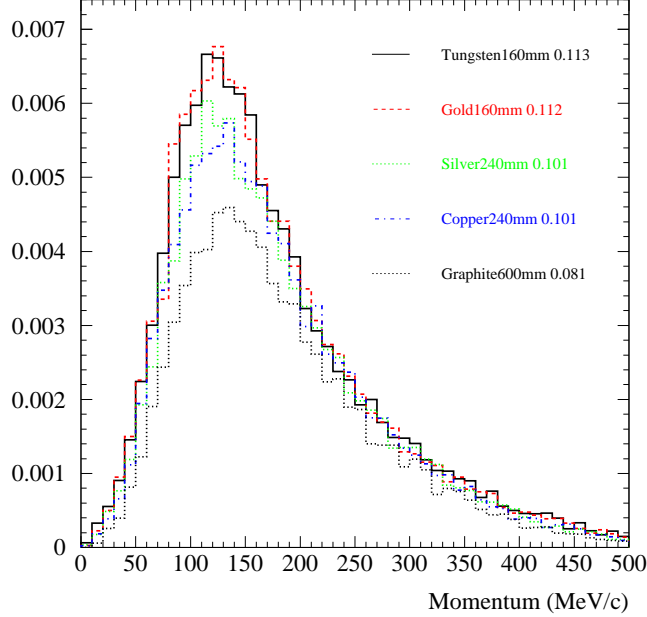


Figure 5.4: Pion yields for various target materials.

5.1.3.2 Target length and radius

Figure 5.5 shows pion yields as a function of a graphite target length. The pion yield at low energy is almost proportional to the target length up to about 1.5 interaction lengths

(60 cm). Although the longer target provides more pion yields, it must be optimized considering radiation heat loads to the pion capture solenoid in which the target is embedded. In the current design with a tungsten target, the length (which corresponds to 1.5 interaction lengths) is about 16 cm.

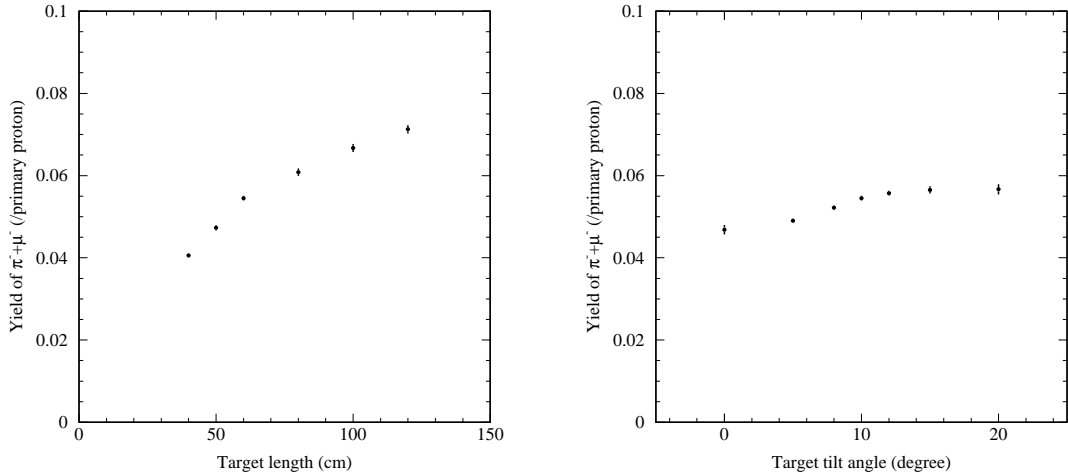


Figure 5.5: Yields of backward pions from a graphite target in 5 Tesla magnetic field as a function of target length (left figure) and target tilt angle (right figure).

Figure 5.6 shows muon yields for various cases of target radius and proton beam size. Low-momentum muons ($p_\mu < 80$ MeV/c) are counted after transfer in a 15 m straight solenoid. The yield of pions at low energy decreases as the radius of the target increases. This result can be explained by absorption of pions at low energy. It has been found that the optimum radius is about 0.6 cm for a gold target.

5.1.3.3 Target tilt angle

The pion production target is embedded in a solenoid magnet to capture and transport the generated pions. Since the proton beam is injected into the solenoid magnet through a gap in the coils, the proton beam axis and the target should be tilted with respect to the solenoid axis. Figure 5.5 shows the pion yields as a function of tilt angle of a graphite target. As seen in Fig. 5.5, the pion yield is almost saturated around a tilt angle of 10 degree.

5.1.3.4 Target heating

Target heating by proton bombardment was simulated by MARS15(2004). Densities of energy deposition in a tungsten target are shown in Figure 5.7. Here, the length and diameter of the tungsten target are 16 cm and 0.8 cm, respectively. From the simulation, a total heat of 3.4 kW for a proton beam of 8 GeV and 7 μ A was obtained. And the maximum heat density is found to be about 170 joule/g/ 10^{14} protons.

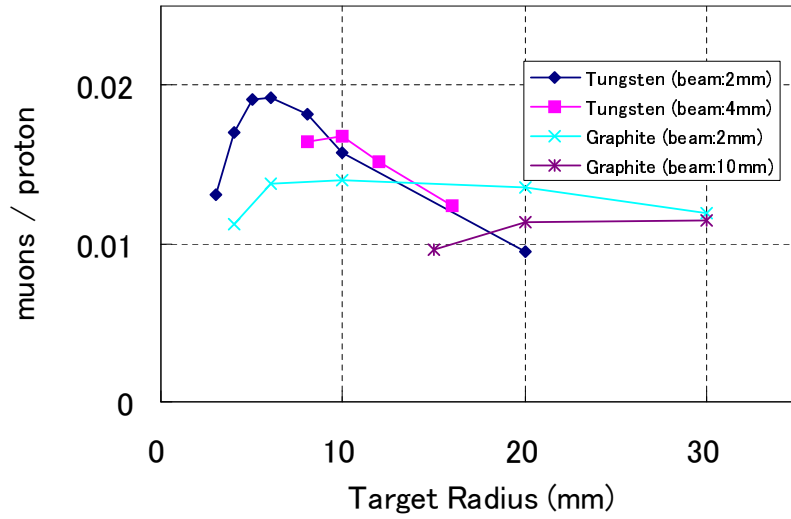


Figure 5.6: Muon yields for various cases of target size and proton beam size. Low-momentum muons ($p_\mu < 80$ MeV/c) are counted after transfer in a 15 m straight solenoid.

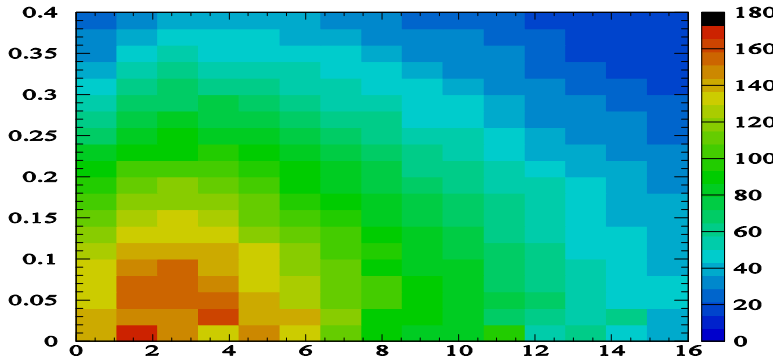


Figure 5.7: Energy deposit density in a tungsten target for a proton beam of 8 GeV and 7 μA .

Cooling of a tungsten target by water has been considered. The estimation by the ANSYS CFD analysis was made with the assumption of steady state conditions. The result is shown in Figure 5.8, where the size of the tungsten target is 0.8 cm in diameter and 16 cm in length. The inlet temperature of the cooling water is about 300 K.

Table 5.2 summarizes the ANSYS analysis results, where pressure drops and target temperature are shown for different thickness of the coolant layer surrounding the target, and the flow rate of water. From these, it can be concluded that target cooling by water can be made.

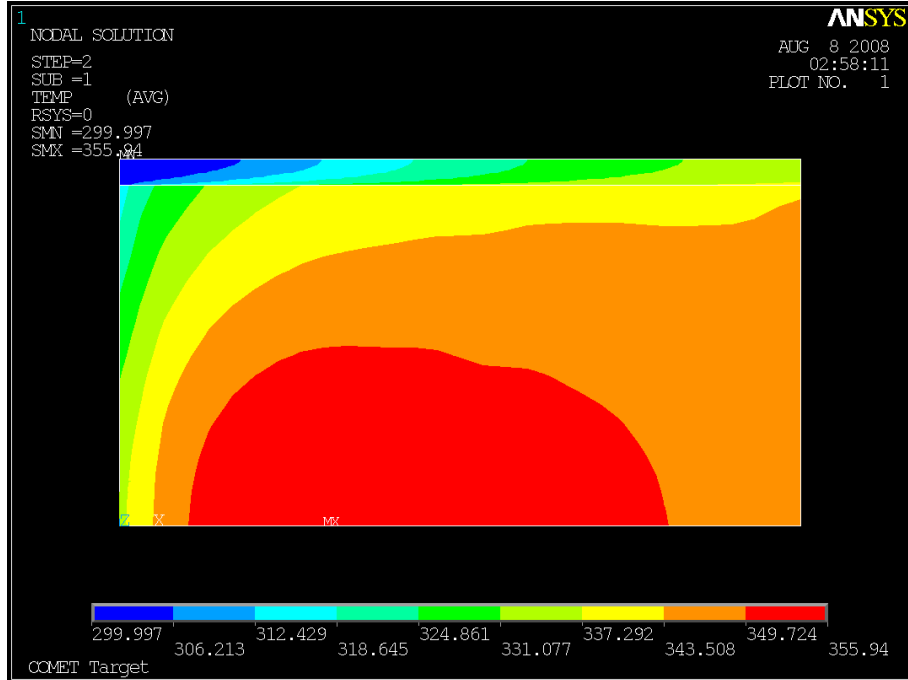


Figure 5.8: Tungsten target cooling by water. Color indicates temperature from 300 K (Blue) to 356 K (Red). Water with initial temperature of 300 K flows in a thin layer surrounding the target rod from the left to the right.

Table 5.2: Parameters in cooling of tungsten target by water obtained by ANSYS analysis. The length and diameter of the target is 16 cm and 0.8 cm, respectively. Inlet water temperature is fixed to be 300 K. Proton beam power is assumed to be $8 \text{ GeV} \times 7 \mu\text{A}$.

Thickness of coolant layer (mm)	0.3	0.3	1.0
Flow rate (ℓ/min)	2	5	17
Speed (m/s)	3	10	10
Pressure drop (MPa)	0.099	0.476	0.080
Maximum fluid temperature (K)	343	322	322
Target temperature (K)	356	343	343

5.2 Pion capture

5.2.1 Pion capture in a solenoidal magnetic field

To collect as many pions (and cloud muons) of low energy as possible, the pions are captured using a high solenoidal magnetic field with a large solid angle. Figure 5.9 shows a layout of the pion capture system, which consists of the pion production target, high-field solenoid magnets for pion capture, and a radiation shield. In this case, pions emitted into a half hemisphere can be captured within the transverse momentum threshold (p_T^{\max}). This p_T^{\max} is given by the magnetic field strength (B) and the radius of the inner bore of solenoid

magnet (R) as

$$p_T^{\max}(\text{GeV}/c) = 0.3 \times B(\text{T}) \times \frac{R(\text{m})}{2}. \quad (5.1)$$

The optimization of the magnetic field of the capture solenoid was performed by looking at the muon yields 10 m downstream from the target; the exit of the transport solenoid located downstream of the capture solenoid magnet. Note that most pions decay into muons in the transport solenoid magnet. As shown in Fig. 5.10, it was observed that the higher the pion capture magnetic field, the better the muon yield at the exit of the pion decay system. Therefore, a higher magnetic field is preferable. According to Section 5.1, placing p_T^{\max} at around 100 MeV/c would be sufficient. Furthermore, since we are interested in the muon momentum being less than 75 MeV/c, a solenoid magnet with the bore radius of 15 cm can accept most of the parent pions of such low-energy muons. Detailed optimization of the bore radius strongly depends on the available technology of the superconducting solenoid magnet. In the current design, we employ conservative design values, namely of $B = 5 \text{ T}$, $R = 15 \text{ cm}$ and a length of 1.4 m.

5.2.2 Layout of the pion capture system

Figure 5.11 shows a schematic view of the system of pion production and capture. It consists of a proton target, a surrounding radiation shield, a superconducting solenoid magnet for pion-capture with a 5 Tesla magnetic field, There is a matching section needed to connect to the transport solenoid system with a 2 Tesla field. The radiation shield is inserted between the pion production target and the coil which generates 5-Tesla magnetic field.

Backward-scattered pions are captured in the 5-Tesla magnetic field and focused forward in the degrading magnetic field. The matching section has a large bore due to the increasing diameter of the pion orbits in the tapered magnetic field, and to contain both the coils of the matching and capture sections in the large cryostat.

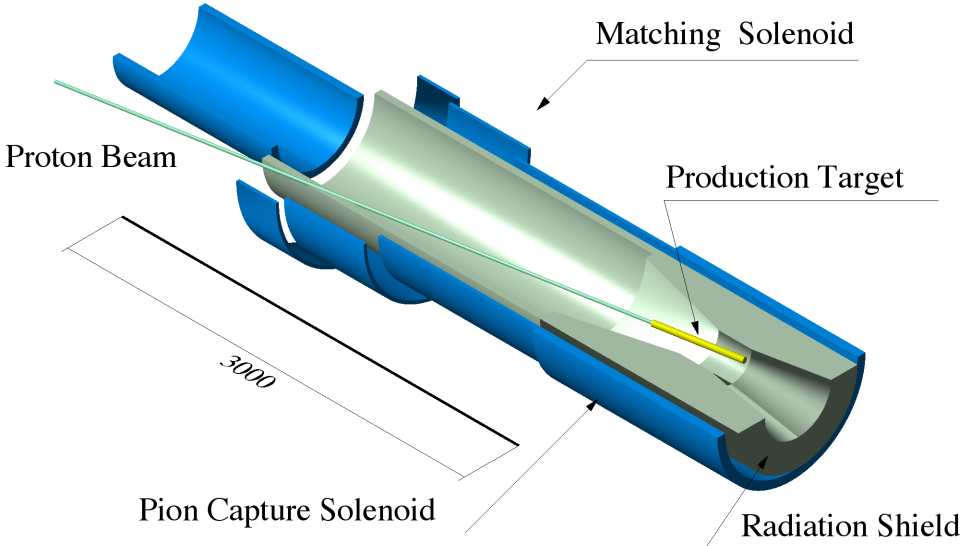


Figure 5.9: Layout of the pion capture system, which consists of the pion production target (proton target), the pion capture solenoid magnets, and its radiation shield.

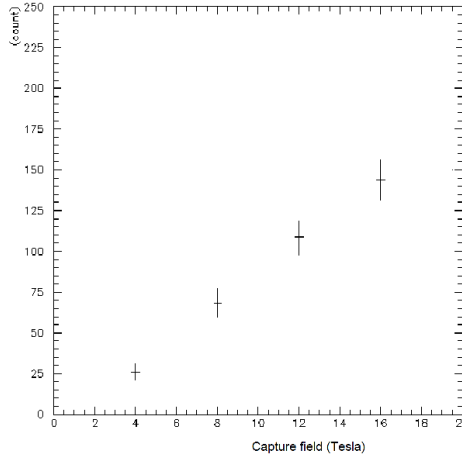


Figure 5.10: Muon yields at 10 m from the entrance of the pion decay system as a function of magnitudes of a pion capture field.

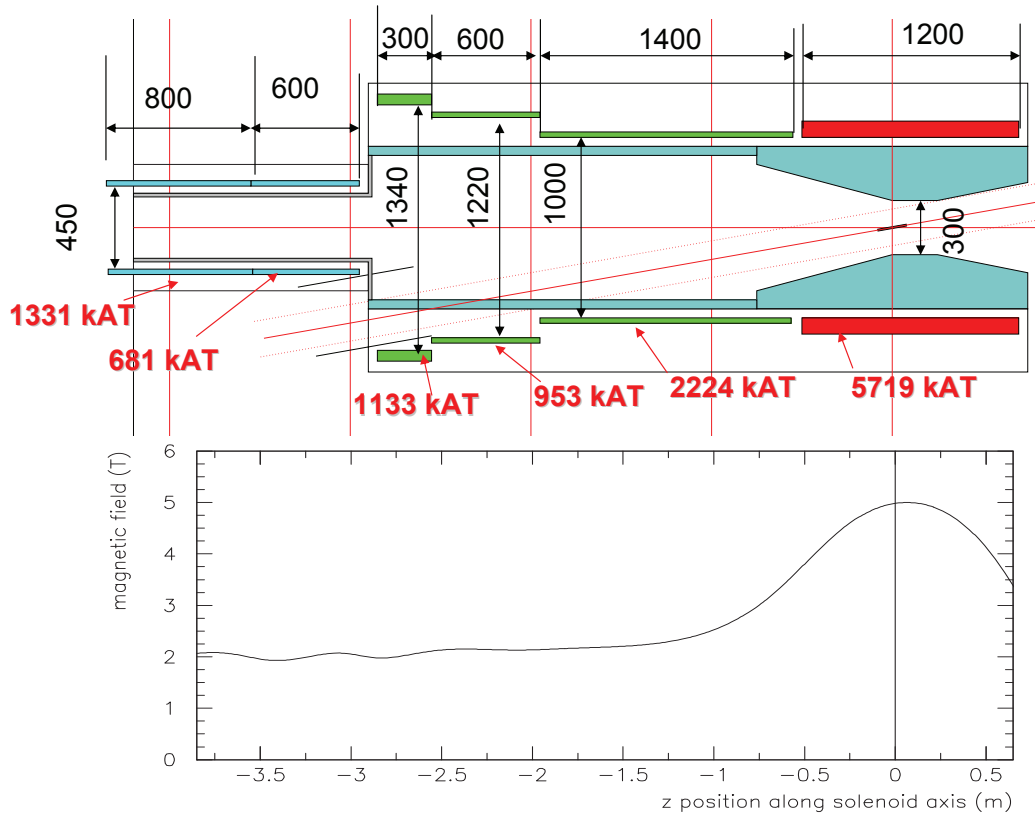


Figure 5.11: A layout of the pion capture solenoid system.

5.2.2.1 Superconducting solenoid design

The details of the design of the pion capture solenoids can be found in Chapter 12. If copper is used as the stabilizer of the superconducting coils, a total thickness of the coil might be

about 20 cm or more, and a total impact on the 4.5 K refrigeration load is over 1 kW. In order to overcome this difficulty, we have started a design using an aluminum-stabilized superconducting coil.

To achieve a low heat load enough below 100 W, a 30 cm-thick tungsten shield is necessary. An inner radius of the 5-Tesla coil is 50 cm. The inner bore of the shield is tapered to keep it away from beam protons and high-energy pions, which are scattered forward. To collect backward-scattered pions, the proton beam should be injected through the barrel of the solenoid, and should be tilted with respect to the solenoid axis by 10 degrees. The solenoid coils near the proton beam duct should have a larger radius to escape the beam halo. In the current design, the coil edge is designed to be placed greater than 10-cm from the beam axis.

5.2.2.2 Radiation heating and radiation dose

Radiation dose from proton bombardment on the pion production target was estimated by MARS15 (2004). The radiation heat comes mostly from neutrons. One of the purpose of this study is to estimate heat loads by radiation in the pion capture solenoid that surrounds the pion production target, as well as a total radiation dose in it. To reduce radiation at the pion capture solenoid, radiation shielding made of tungsten is inserted between the pion production target and the pion capture solenoid magnet. The maximum thickness of the radiation shielding is about 30 cm.

In this MARS simulation, the density of superconducting coils of about 4 g/cm³ and the thickness of the coils is 9 cm with 1cm-thick aluminum support structure (being located at from 50 cm to 60 cm radially from the solenoid axis). The energy deposited for each component is presented in Fig.5.12. It was found that an average energy deposited at the pion capture solenoid coils including matching section to the transport solenoid is about 39 W for a proton beam of 8 GeV and 7 μ A. A total radiation dose for 8×10^{20} protons is about 0.6 MGy.

5.2.3 Adiabatic transition from high to low magnetic fields

Since the pions captured at the pion capture system have a broad directional distribution, it is intended to make them more parallel to the beam axis by changing a magnetic field adiabatically. From the Liouville theorem, a volume in the phase space occupied by the beam particles does not change. Under a solenoidal magnetic field, the relation between the radius of curvature (R) and the transverse momentum (p_T) leads to the relation given by

$$p_T \times R \propto \frac{p_T^2}{B} = \text{constant}, \quad (5.2)$$

where B is a magnitude of the magnetic field. Suppose the magnetic field decreases gradually, p_T also decrease, yielding a more parallel beam. This is the principle of the adiabatic transition. Namely, when a magnetic field is reduced by a factor of two, p_T decreases by $1/\sqrt{2}$. On the other hand, since

$$p_T \times R \propto B \times R^2 = \text{constant}', \quad (5.3)$$

the radius of curvature increase by a factor of $\sqrt{2}$. Therefore, the inner radius of a magnet in the pion decay section has to be $\sqrt{2}$ times that of the pion capture solenoid. With the cost of a beam blow up, a pion beam becomes more parallel. Furthermore, it is not effective

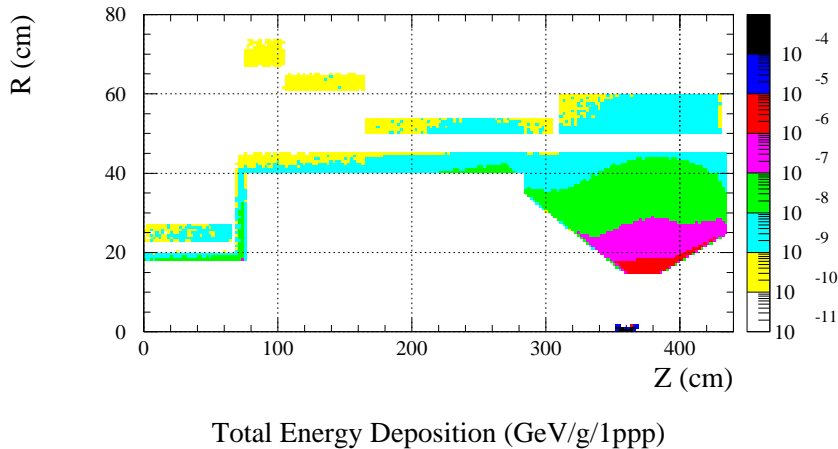


Figure 5.12: Energy deposit at the pion capture solenoid and radiation shielding.

in reality to have a long magnet with a high magnetic field, connected to a magnetic field that has to be lowered at some point. Figure 5.13 illustrates the principle of adiabatic transition.

5.3 Muon transport

5.3.1 Requirements for muon transport

Muons and pions are transported to the muon-stopping target through the muon beamline, which consists of curved and straight superconducting solenoid magnets. A schematic layout of the muon beamline, including the capture and detector sections, is shown in Fig. 5.14. It is composed of two 90° curved solenoid magnets and a straight solenoid magnet between the two.

The requirements for the muon transport section are

- the muon transport should be long enough for pions to decay to muons. For instance, for about 20 meters, the pion survival rate for pions with the reference momentum is about 2×10^{-3} ,
- the muon transport should have a high transport efficiency for muons with a momentum of 40 MeV/ c , and
- the muon transport should select muons with low momentum and eliminate muons of high momenta ($p_\mu > 75$ MeV/ c) to avoid backgrounds from muon decays in flight.

The last item above is one of the important requirements for the muon beamline; an ability to select electric charge and momenta. That is, negatively-charged muons with momenta

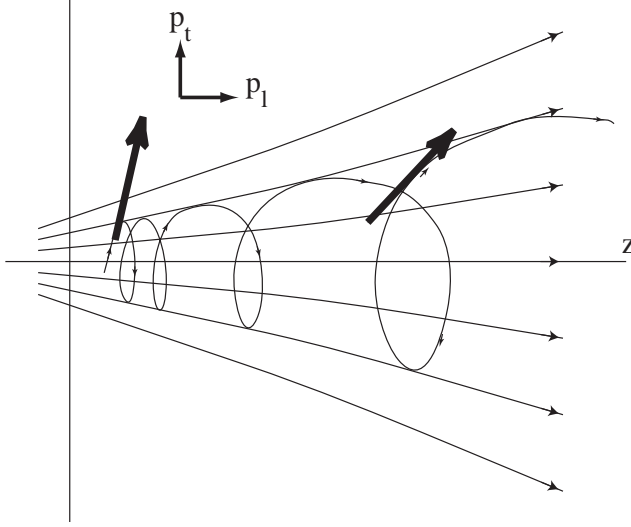


Figure 5.13: Adiabatic transition from a high magnetic field to a low magnetic field. This adiabatic transition reduces the magnitude of transverse magnetic field.

around 40 MeV/c should be selected. At the same time, it is necessary to eliminate energetic muons having a momentum larger than 75 MeV/c, since their decays in flight would produce spurious signals of ~ 105 MeV electrons. Therefore, such energetic muons and other unwanted particles need to be strongly suppressed before the stopping target using the curved solenoid with a late-arrival particle tagger and a beam collimator.

5.3.2 Beam optics of curved solenoids

5.3.2.1 Dispersive beam shifts in curved solenoids

The selection of electric charge and momentum of beam particles can be performed by using curved (toroidal) solenoids, which makes the beam dispersive. It is known that, in a curved solenoid, the center of the helical trajectory of a charged particle drifts towards the perpendicular direction to the curved solenoid plane. The magnitude of drift (D [m]) is given by

$$D = \frac{1}{qB} \left(\frac{s}{R} \right) \frac{p_L^2 + \frac{1}{2}p_T^2}{p_L}, \quad (5.4)$$

$$= \frac{1}{qB} \left(\frac{s}{R} \right) \frac{p}{2} \left(\cos \theta + \frac{1}{\cos \theta} \right), \quad (5.5)$$

where q is the electric charge of the particle (with its sign), B [T] is the magnetic field at the axis, and s [m] and R [m] are the path length and the radius of curvature of the curved solenoid, respectively. Here, $s/R (= \theta_{bend})$ is a bending angle θ_{bend} and D is proportional to θ_{bend} . p_L and p_T [GeV/c] are longitudinal and transverse momenta, respectively. θ is a pitch angle of the helical trajectory. Charged particles with opposite signs move in opposite directions. This can be used for charge and momentum selection if a suitable collimator is placed after the curved solenoid.

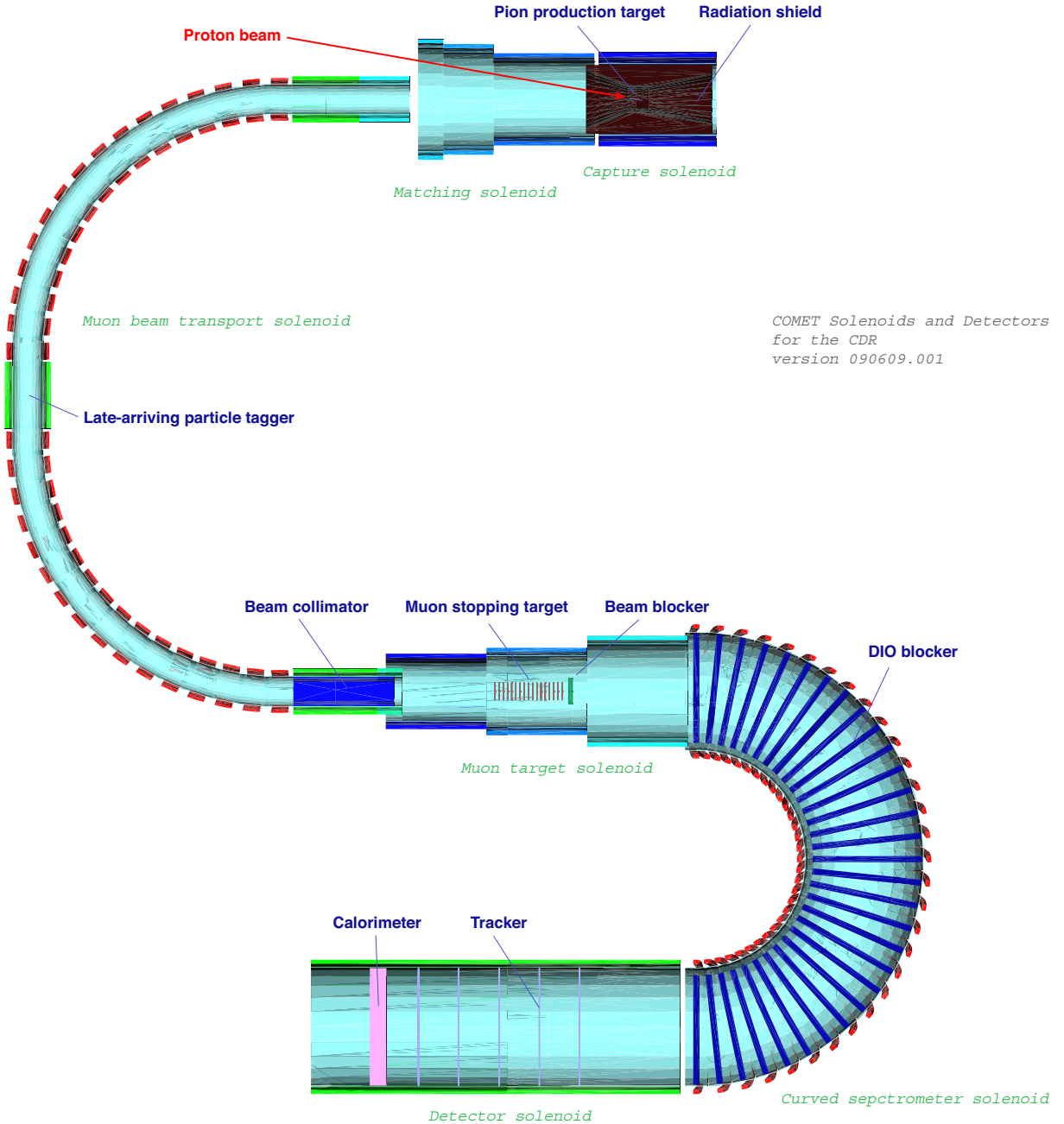


Figure 5.14: Present design of the solenoid channel used in the tracking studies.

5.3.2.2 Dipole fields for drift compensation

To keep the center of the helical trajectories of the muons with reference momentum p_0 in the bending plane, a compensating vertical dipole field should be applied. The magnitude of the compensating dipole field is given by

$$B_{\text{comp}} = \frac{1}{qR} \frac{p_0}{2} \left(\cos \theta_0 + \frac{1}{\cos \theta_0} \right), \quad (5.6)$$

where the trajectories of negatively charged particles with momentum p_0 and pitch angle θ_0 are corrected to be on-axis.

The present design of the COMET beamline utilizes two curved solenoids with a bending angle of 90° in the same bending direction. Each of them has a magnetic field of 2 T and a radius of curvature of 3 m. Adjusting the inner radius of the solenoid to act as the collimator would bring down cost of this design.

To keep the center of trajectory of the low energy muons, a compensating field of 0.030 T for the first 90° and 0.050 T for the second 90° were applied. We propose two options to realize this dipole field: tilting coils and additional dipole coils. In the tracking simulation these compensating fields are calculated by tilting the solenoid coils.

Figure 5.15 shows a result from finite element method (FEM) calculations of the dipole coils with superconducting wire that is wound on each element of the transport solenoid coils. The average field strength is about 0.03 T in the calculation, and the field integral along the solenoid axis is controlled within $\pm 5\%$ of the midplane.

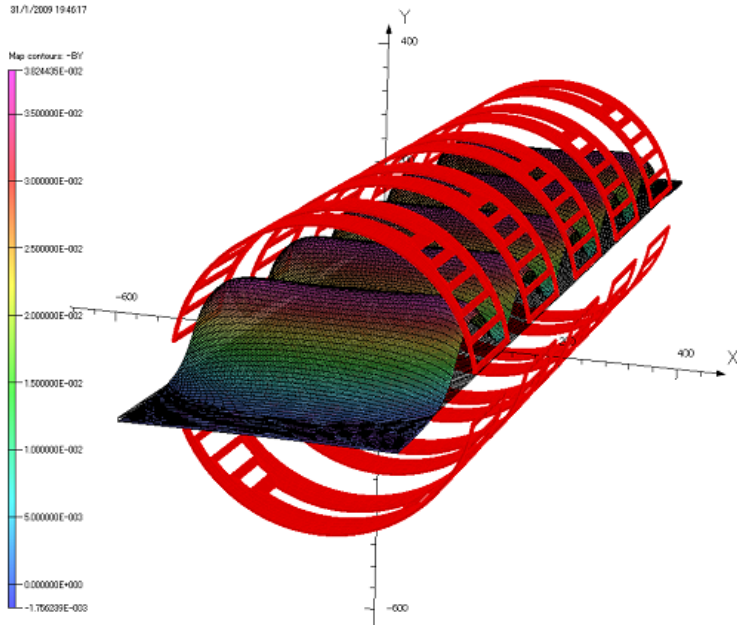


Figure 5.15: Dipole field for drift compensation in the transport solenoid calculated by FEM analysis. The average field strength is about 0.03 T.

5.3.3 Curved solenoid tuning

In order to compensate for the vertical drift of particles in the curved transport channels, a vertical dipole field is produced by tilting the sections of the curved transport channel. This is a cost effective way of producing the dipole field, however, using this method means that the relative magnitude of the vertical dipole field component is fixed by the geometry and thus is fixed once the solenoid has been manufactured. It may be necessary to tune the magnitude of the vertical dipole component after manufacture to correct for manufacturing tolerances and thermal contraction due to cooling the magnets to superconducting operating temperatures.

It may be possible to have some control over the vertical dipole component by powering alternate solenoids with a different current. Simulations were done to demonstrate whether this method could provide the ability to control the momentum distribution, vertical dispersion and composition of the beam at the stopping target. For these simulations, only the muon transport has been considered and only the simple scenario where all solenoids in the bent transport channel have identical geometries and only two different power supplies are used.

5.3.3.1 G4beamline field distribution

Initial simulations were done using G4beamline [80] by taking the existing baseline design of the COMET beamline. The geometry was altered to include the tilt of the solenoids but all other parameters were kept the same. Figure 5.16 shows the model that was simulated and Figure 5.17 shows the tilt of the solenoids, which is 1.43° . All the solenoids in the

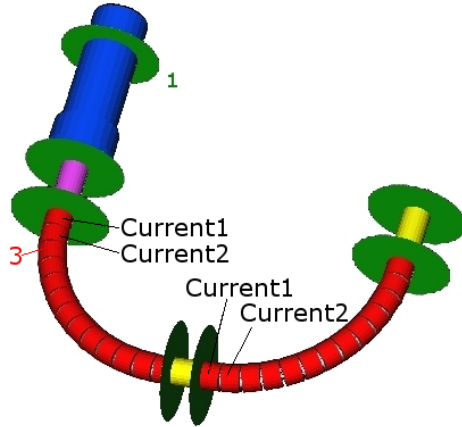


Figure 5.16: G4beamline model of the muon transport channel. The blue solenoids are the pion capture channel, the red solenoids are the curved, tilted solenoids for pion decay and muon transport and the final yellow solenoids end just before the stopping target. The virtual detector (green circle) labeled 1 shows the position of the pion production target. Alternate solenoids in the transport channel (in red) were powered with a different current. Field measurements were made at the center of the solenoid labeled 3.

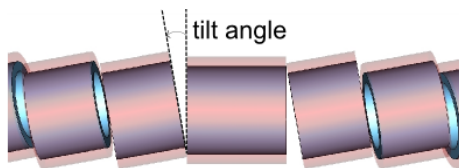


Figure 5.17: Drawing of the curved, tilted muon transport channel of the COMET beamline showing the tilt used to produce the vertical dipole field. The tilt angle shown here is exaggerated as the angle used in the simulations is 1.43° .

G4beamline simulations are ideal solenoids composed of infinitely-thin current sheets. Four different scenarios for powering the curved, tilted solenoids were investigated, see Table 5.3.

Table 5.3: Values for Current1 and Current2 used in the simulations. Current1 was applied to every other solenoid starting with the first one and Current2 was applied to the other solenoids, see Figure 5.16.

	Current1 (A)	Current2 (A)
1	631890	631890
2	758268	758268
3	631890	1263780
4	631890	315945

Figure 5.18 shows the B_x , B_y and B_z field components at the centre of the third solenoid (labelled 3 in Figure 5.16) for the different powering schemes. The z direction is parallel to the axis of each solenoid and the x axis is in the plane of the bend. As can be seen, by supplying alternate solenoids with a different current it is possible to adjust, to some extent, the vertical dipole component (i.e. B_y) independently.

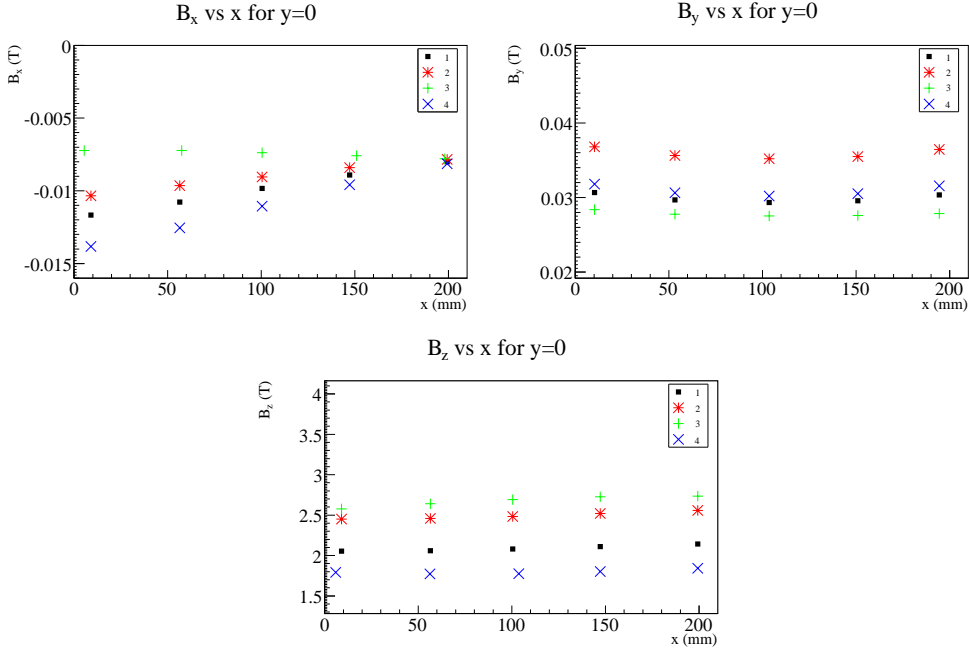


Figure 5.18: Results of the G4beamline simulation. The plots show the B_x , B_y and B_z components as a function of x for the different powering schemes described in Table 5.3.

5.3.3.2 EM studio field distribution

To obtain a more accurate field distribution of the beamline, a 3-D magnetostatic simulation using EM Studio [81] was done. The geometry was kept the same as in the G4beamline simulations. Preliminary designs of the superconducting solenoids have a non-magnetic steel wall inside the coils and an iron yoke outside. To obtain a comparison with the G4beamline model the iron yoke was not considered and the permeability of the steel was set to 1.

Figure 5.19 shows the B_x , B_y and B_z field distributions, for the same location as in the G4beamline simulation, for the same four current scenarios listed in Table 5.3. The

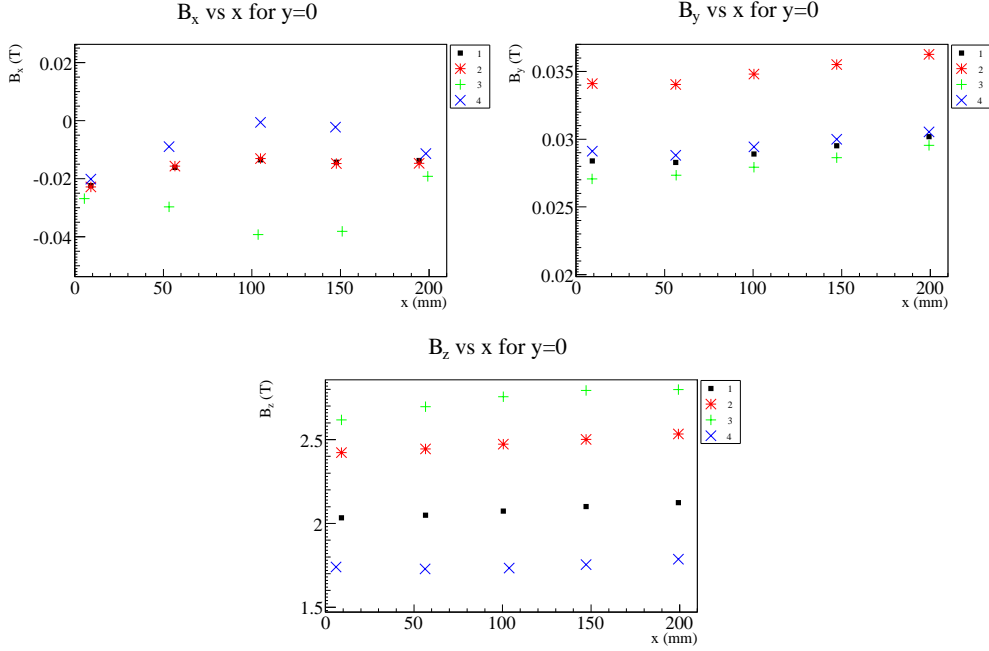


Figure 5.19: Results of the EM Studio simulation. The plots show the B_x , B_y and B_z components as a function of x for the different powering schemes described in Table 5.3.

B_y and B_z components show good agreement with the G4beamline simulation but the B_x component shows significant differences, though the absolute magnitude of the differences are small. This is likely due to the way in which fringe fields are considered in G4beamline. However, the fact that the B_x component in the EM Studio simulations does not follow the same trend as in the G4beamline simulations will complicate tuning the beam transported by the channel.

5.3.3.3 Particle tracking

To understand the effect of altering the field in the solenoids, some preliminary tracking studies have been done using the G4beamline model of the muon transport channel. Initially, a simple muon beam was tracked through 90° of the curved solenoid. The input beam contained on-axis, parallel muons with a momentum range of $10\text{--}150$ MeV/ c . Figure 5.20 shows the momentum distribution as a function of the vertical position after the muons were tracked through half of the curved solenoid. This figure shows that it is possible to affect the vertical dispersion produced by the transport channel by powering alternate solenoids with a different current.

Since the COMET experiment requires a very low background rate it is important to track particles using a realistic beam to determine the composition of the beam at the stopping target. An input beam produced by a MARS [78] simulation of 8 GeV protons on a graphite target was tracked through the whole G4beamline model. Figure 5.21 shows the momentum distribution of muons and Table 5.4 shows the composition of the beam at the stopping target for the different current scenarios.

Although it is possible to affect the momentum distribution of muons at the stopping target by powering alternate solenoids with a different current, the change in the muon

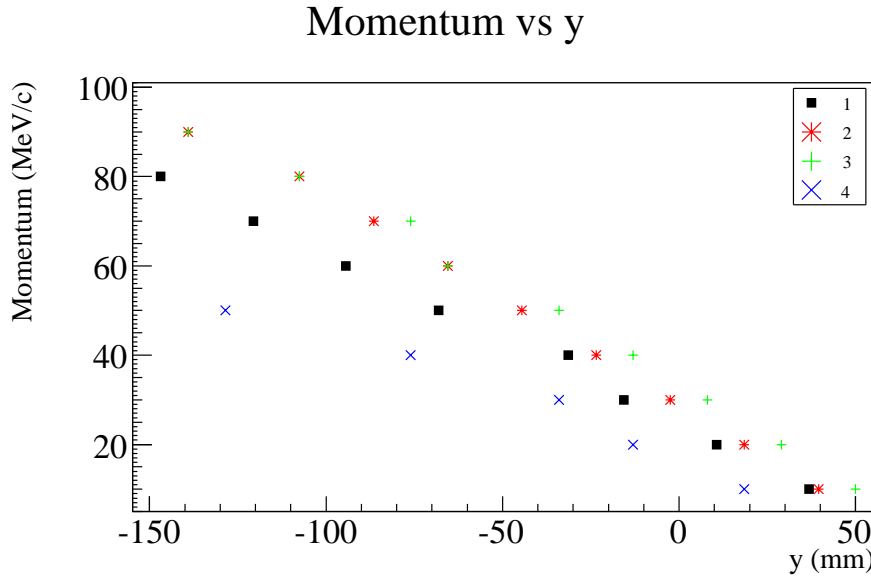


Figure 5.20: Momentum as a function of vertical position for an on-axis, parallel muon beam with a momentum range of 10–150 MeV/ c .

Table 5.4: Fractional beam composition at the stopping target for the four different scenarios.

	μ^-	μ^+	e^-	e^+	π^-	π^+	p^+
1	0.89	0.02	0.055	0.030	0	0	0.0024
2	0.89	0.011	0.072	0.029	0	0	0.001
3	0.91	0.014	0.063	0.009	0	0	0.0006
4	0.96	0.027	0	0	0.018	0	0

yield is quite significant. This may be detrimental if tuning the solenoid requires reducing the current.

5.3.3.4 Curved solenoid tuning conclusions

By powering alternate solenoids with a different power supply it is possible to independently control the vertical dipole component of the curved, tilted solenoids. The simulations using EM Studio show deviations of the B_x component compared to the G4beamline solenoid model. To make the model more accurate it will be necessary to include the iron yoke. The effect of this on the transport of particles will need to be investigated. Thus, tracking with a field map from the EM Studio simulations is essential.

It is also important to study the mechanical forces applied to the support structure of the solenoid as having significantly different currents in adjacent solenoids may put significant additional stress on the support structure. It will also be useful to study the effect of thermal contraction on an optimised version of the muon transport channel, tuning of the momentum spectrum to obtain the best yield and apply this method to the electron spectrometer to allow tuning of the momentum selection.

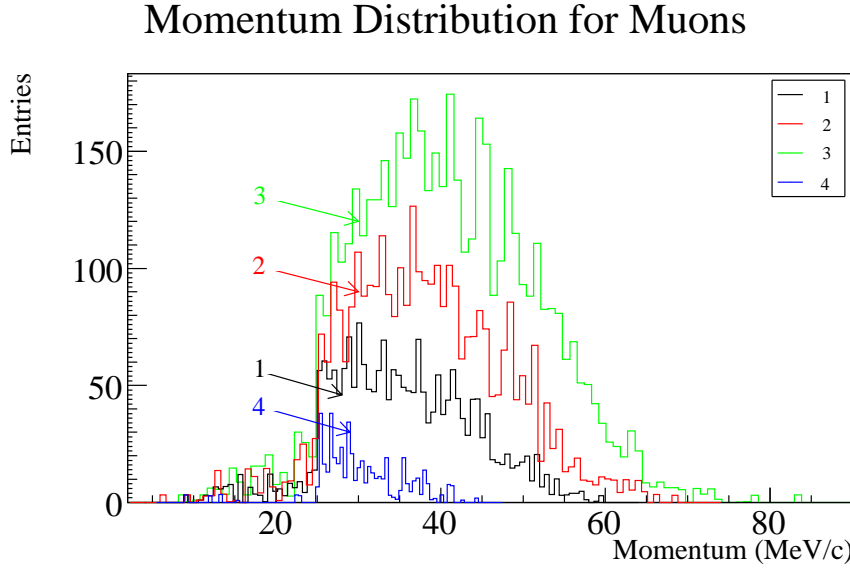


Figure 5.21: Momentum distribution of muons at the end of the muon transport channel for the different scenarios.

5.3.4 Muon beam collimators

The muon beam collimators are placed in front of the muon-stopping target to eliminate muons that would not be stopped in the muon-stopping target and other charged particles that would become backgrounds. The function of the beam collimator and the beam blocker is to block the beam particles so that they do not enter the torus section. Table 5.5 shows geometrical dimension of the beam collimator, the beam blocker and the muon-stopping target. The loss in the muon stopping rate due to the beam collimator is only 11%.

5.3.5 Distributions of the muon beam

Tracking simulation studies were performed using G4beamline, which is a single-particle tracking code based on GEANT4. The magnetic field of the solenoids can be computed by G4beamline using a realistic configuration of coils and their current settings. A magnetic field configuration used in the studies is shown in Figure 5.27. MARS was used to generate secondary particles from the production target. The particles were recorded on the surface of the production target. Then particle tracking was performed using G4beamline using QGSP_BIC as the physics model.

5.3.5.1 Momentum distributions

Figure 5.22 shows the momentum distributions of different charged particles in the muon beam, such as μ^- s, π^- s, and e^- s at the first 90° bend, just before the beam collimator, and after the beam collimator. It can be seen that the momentum selection around 40 MeV/c is properly done by the curved solenoids and the beam collimator. The averaged beam rates are summarized in Table 5.6.

Table 5.5: Geometrical dimensions of the muon beam collimator, beam blocker and muon stopping target.

Beam Collimator	
Inner Radius	150 mm
Lower Jaw	-100 mm from the beam center
Length	1.2 m
Material	Tungsten
Muon Stopping Target	
Shape	Layers of flat disks
Disk Radius	100 mm
Disk Thickness	200 μm
Number of disks	17
Disk spacing	50 mm
Material	Aluminum
Beam Blocker	
Radius	150 mm
Length	40 mm
Material	Tungsten
Position	100 mm downstream of the last target disk

Table 5.6: Average beam rates (Hz) of μ^- s, π^- s, and e^- s at different positions in the muon beam line.

Particle type	at the first 90° bend	before the collimator	after the collimator
μ^-	9×10^{11}	6×10^{11}	3×10^{11}
π^-	5×10^{10}	2×10^9	6×10^8
e^-	3×10^{12}	5×10^{12}	3×10^{12}

5.3.5.2 Time distributions

Figure 5.23 shows the time distributions of different charged particles in the muon beam, such as μ^- s, π^- s, and e^- s at the first 90° bend, just before the beam collimator, and after the beam collimator. It can be seen that the full time width of the muon beam is about less than 200 nsec. The width is determined by different helical pitches of the muon trajectories. The time distribution of electrons is very sharp earlier in the pulse though with a small tail throughout the rest of the time.

5.3.5.3 Muon momentum dispersion

After the 180° bending of the COMET muon beamline, the muon beam becomes very dispersive. Momentum dispersion of the muons at the end of the muon beamline (just before the beam collimator located at the end of the muon beamline) is presented in Fig. 5.24 as a function of vertical position. This momentum dispersion is very important and useful for eliminating high energy muons above 75 MeV/c, which would otherwise contribute to

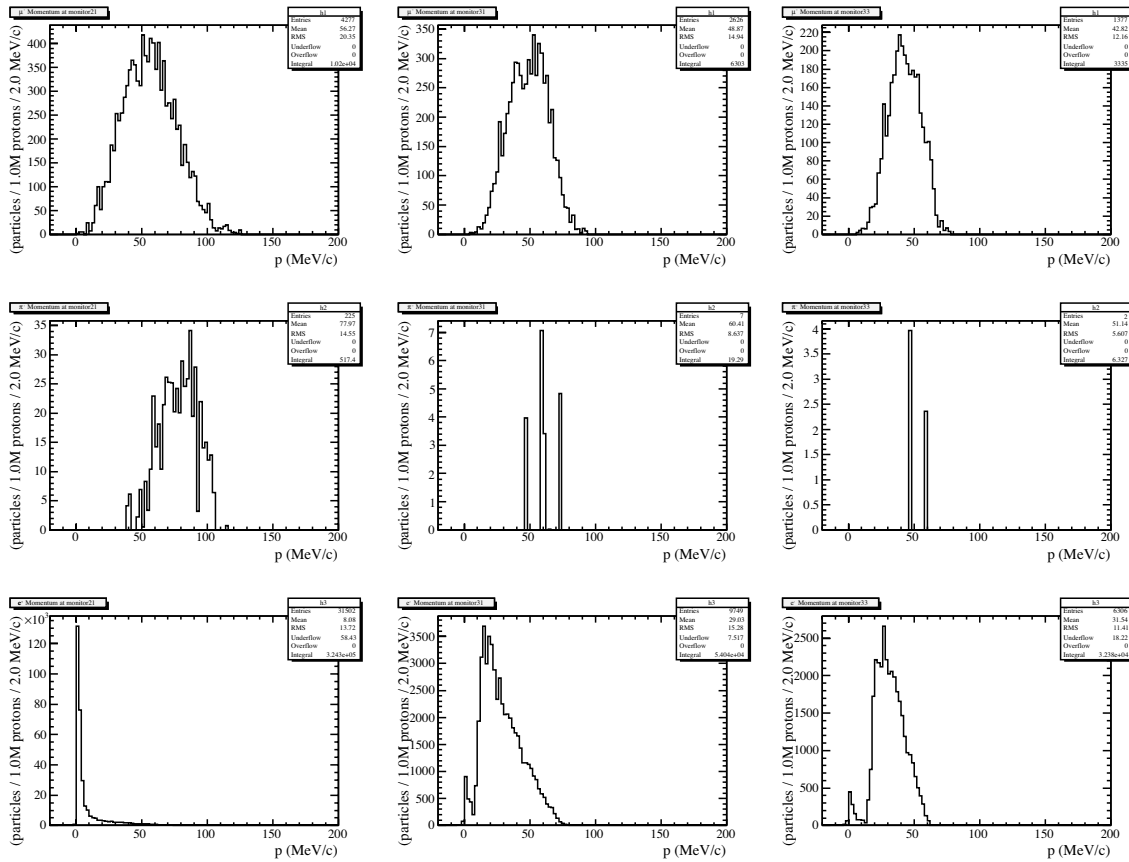


Figure 5.22: Momentum distributions of μ^- (top), π^- (middle) and e^- (bottom). Left figures : after the first 90° bend of the transport solenoid. Center figures : just before the beam collimator. Right figures : after the beam collimator.

background events by their decay in flight. The COMET muon beamline has a bending angle of 180° , which is twice larger than that in Mu2E, and therefore the momentum dispersion is twice better.

5.3.5.4 Muon beam transverse profiles

The muon beam profiles at the end of the muon beamline¹ are presented in Fig. 5.25, where the total momentum distribution, correlation of transverse versus longitudinal momenta, the arrival time distribution and the transverse beam profiles are shown.

5.3.6 Late-arriving particle tagger

As shown in Section 11.2, any beam particles arriving at the detector at a late time between the beam pulses could become potentially a critical background source. They could be produced by prompt protons (beam-related prompt background events) or protons leaking between the proton pulses (beam-related prompt background events) or by cosmic muons or

¹The end of the muon beamline is defined here as the front of the muon beam collimators that will be described later.

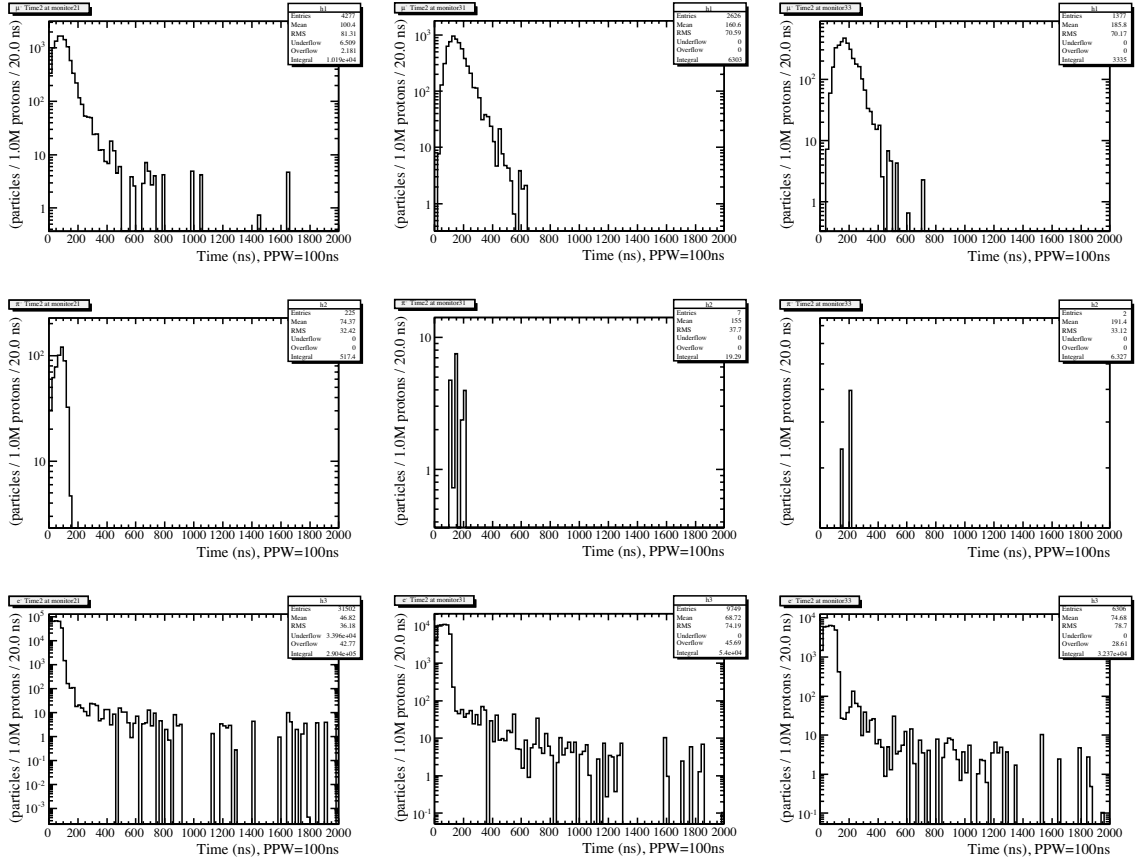


Figure 5.23: Arrival time distributions of μ^- (top), π^- (middle) and e^- (bottom). Left figures : after the first 90 bend of the transport solenoid. Center figures : just before the beam collimator. Right figures : after the beam collimator. Proton pulse width of 100 ns is assumed.

other, unknown sources. Just for additional insurance to suppress such background events, it would be wise to consider a detector, which can be placed in the muon beam line and be used to tag late-arriving particles in a muon beam. The detector might be only turned on when the detection of $\mu^- - e^-$ conversion is active, and otherwise be off at a beam prompt time. This tagging system can be used to examine any beam particle (in particular pion) coming at the same time as $\mu^- - e^-$ conversion signal events.

In the consideration of such a detector, two critical issues to be considered exist. They are

- capability to handle high counting rates, and
- radiation hardness due to energy deposit by charged particles passing through.

For the latter, a number of beam particles (including electrons) are about $10^{12}/\text{sec}$. With 2×10^7 second running, a total number of beam particles is 2×10^{19} . Assuming that beam particles spread over an area of the beam solenoid bore ($\sim 20 \text{ cm}$), the beam size is about $1.2 \times 10^3 \text{ cm}^2$. Therefore about $O(10^{16})/\text{cm}^2$.

Candidates of the detector are either radiation-hard silicon detector or gas chambers with GEM or micromegas. The location of the late-arriving particle tagger is between the two

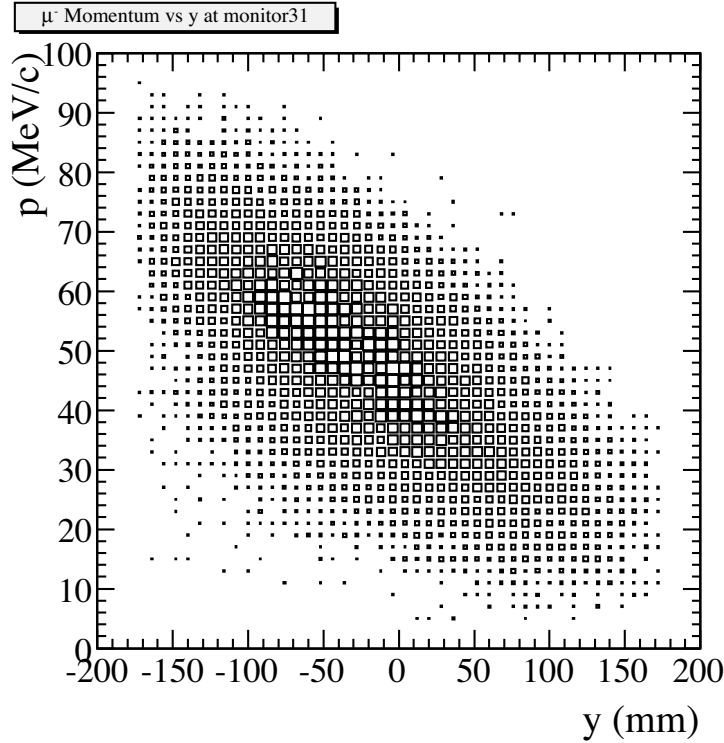


Figure 5.24: Dispersion of the muon beam at the end of the muon beamline (just before the beam collimator).

90° bending solenoids. Details are under study.

5.3.7 Specifications of magnets in the muon beam line

Table 5.7 summarizes specifications of the solenoids and Fig. 5.28 defines the solenoid names. A C-shaped curved solenoid channel is adopted for the muon transport solenoid. At 90° of the muon transport solenoid, a late-arriving particle tagger is installed. This is used to eliminate backgrounds originating from the late-arriving particles by measuring arriving time of the particles. At the same time, the tagger can work as an absorber for protons, neutrons and antiprotons. At the end of the muon transport solenoid, a collimator is located to suppress the unwanted particles. In this section, we discuss the muon transport solenoid and its components.

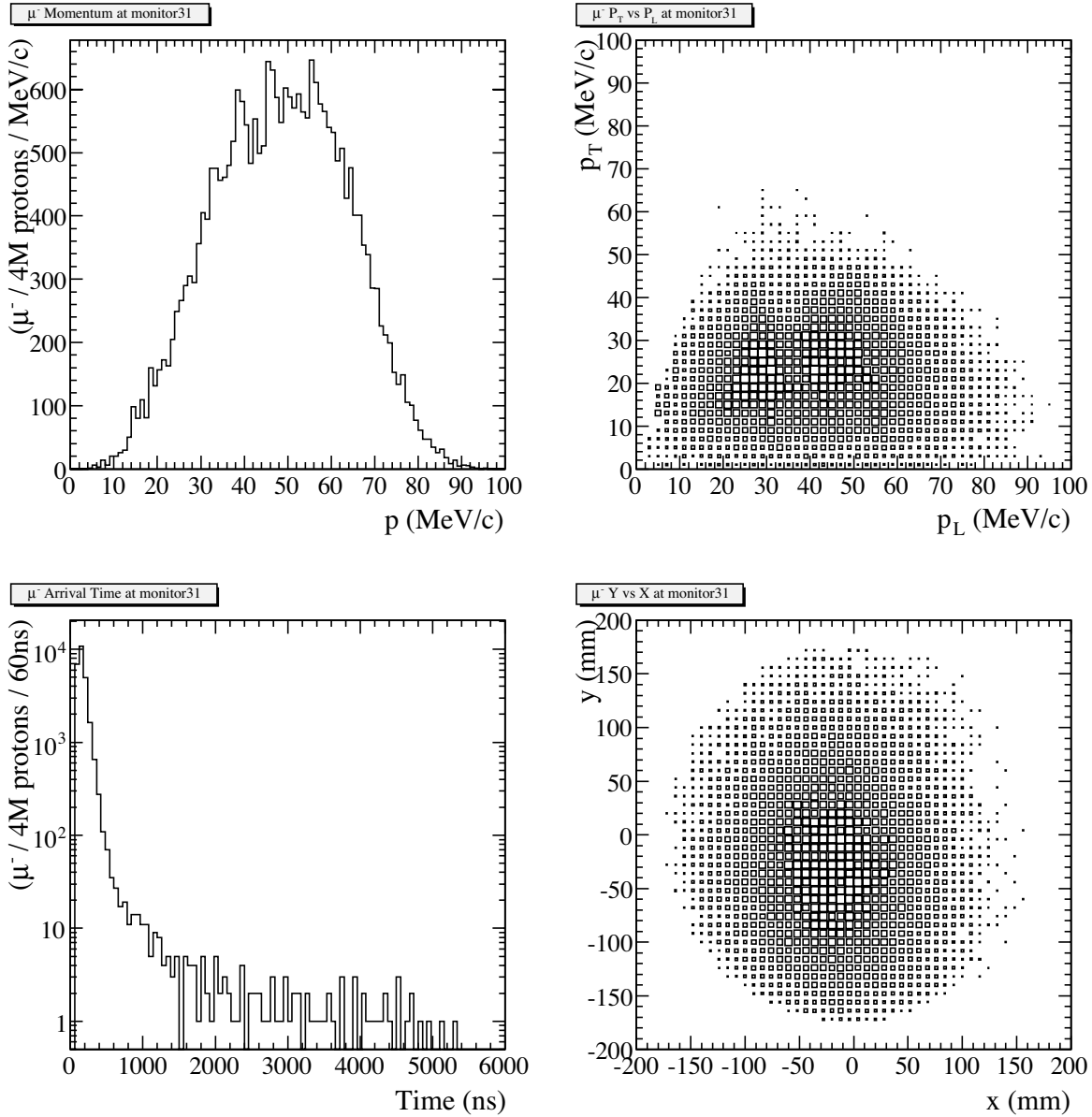


Figure 5.25: Plots for muons just before the beam collimator. Total momentum (top-left), correlation between transverse and longitudinal momentum (top-right), time of flight relative to the time when the proton beam hit the production target (bottom-left), and beam profile (bottom-right) are shown.

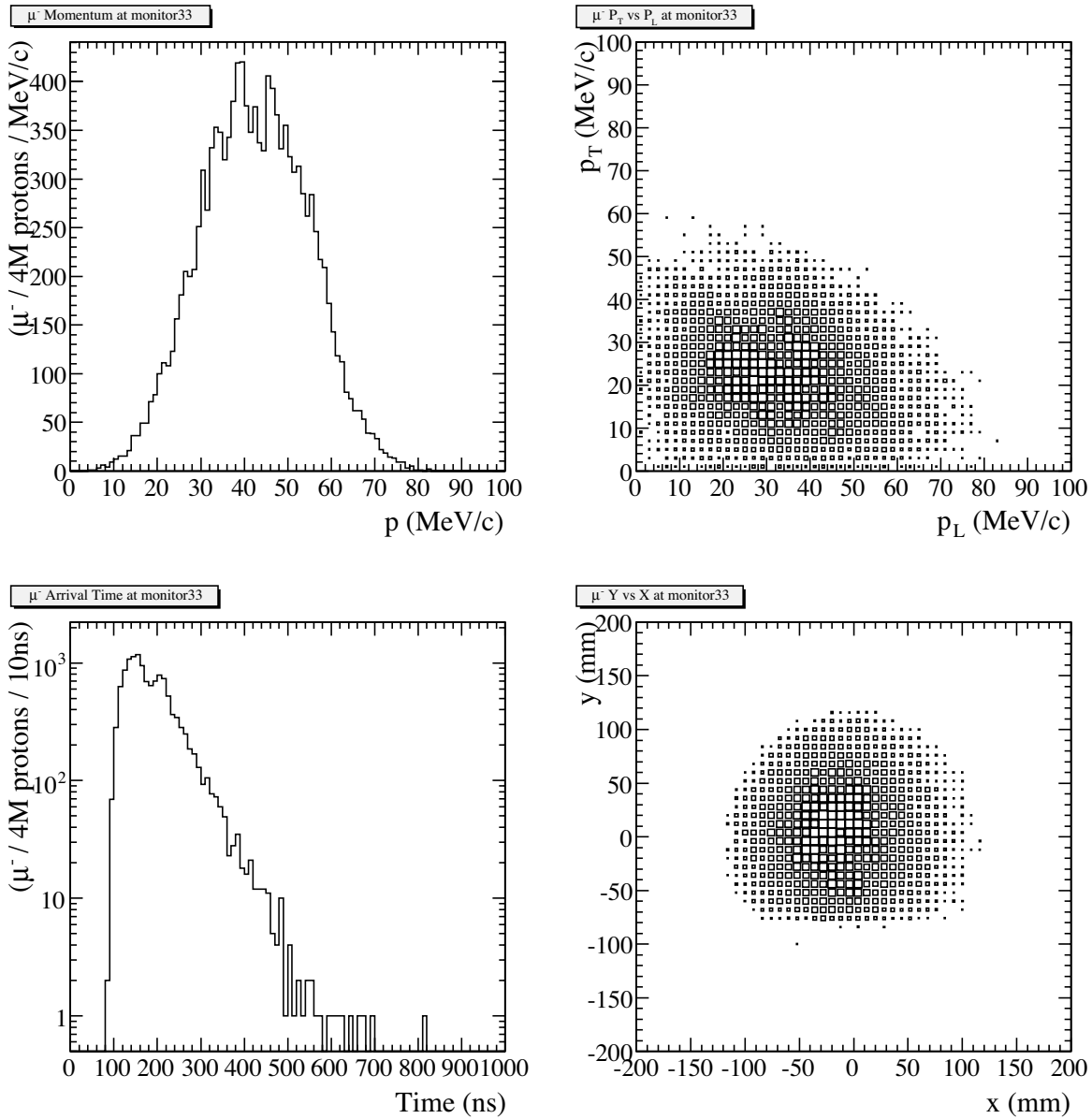


Figure 5.26: Plots for muons just after the beam collimator. Total momentum (top-left), correlation between transverse and longitudinal momentum (top-right), time of flight relative to the time when the proton beam hit the production target (bottom-left), and beam profile (bottom-right) are shown.

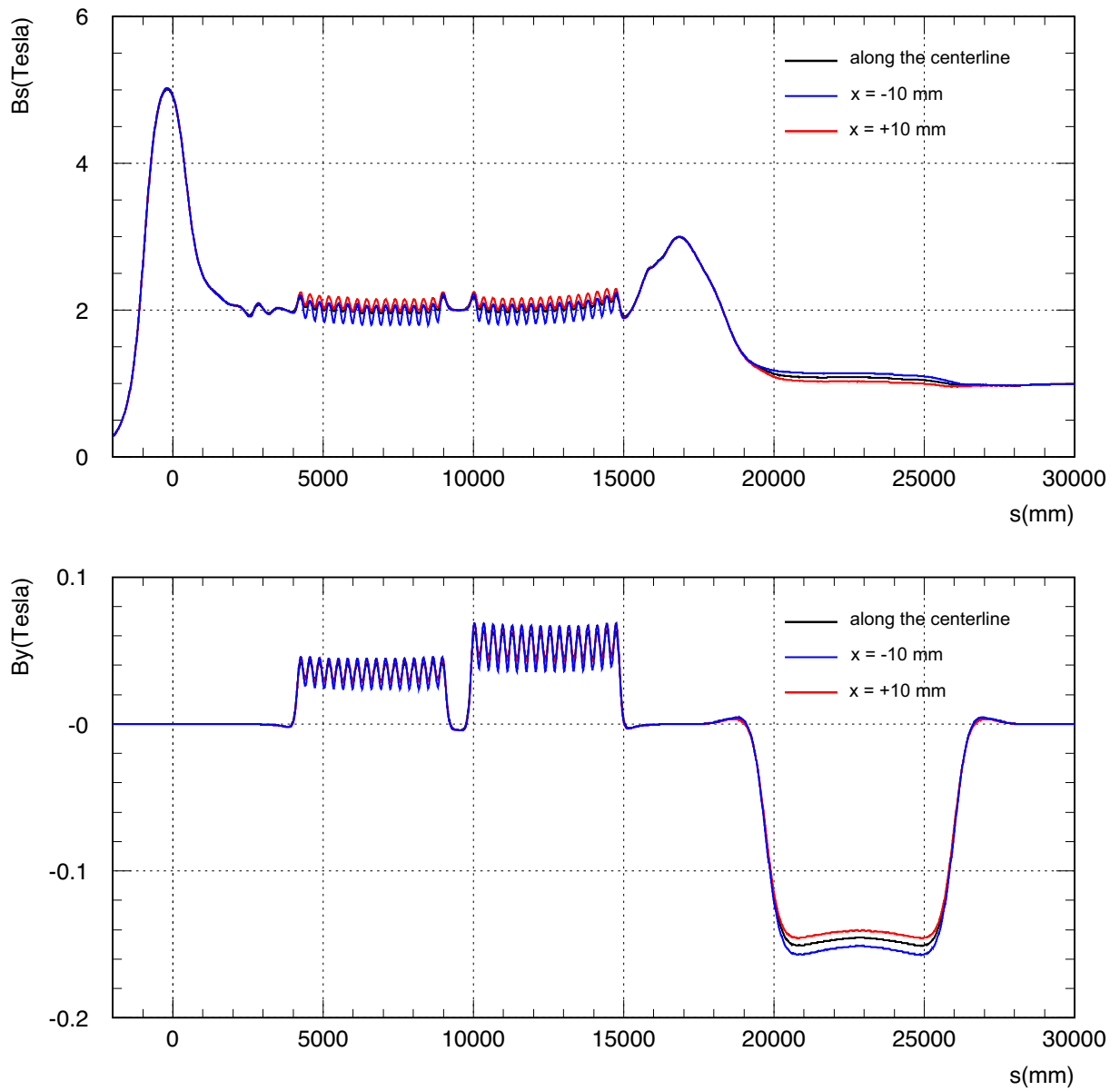


Figure 5.27: The magnetic field configuration of the solenoid channel from the capture section to the detector section of the present experiment. B_s is a central magnetic field of the solenoid magnets. B_y is a correction magnetic field.

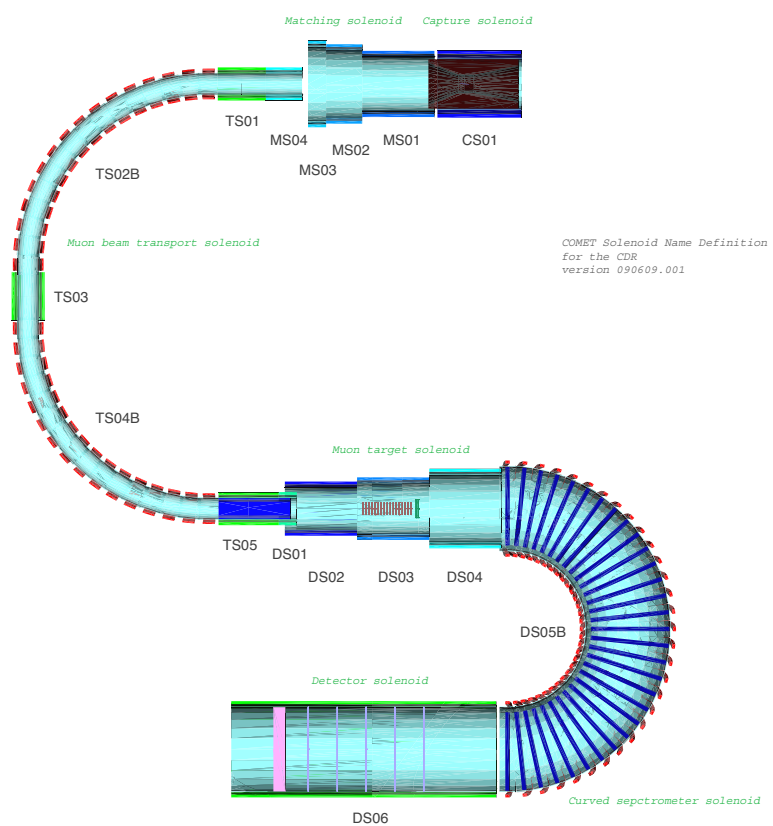


Figure 5.28: Definition of the solenoid name in Table 5.7.

Table 5.7: Specifications of the COMET solenoids.

Name	L_{total} (mm)	B_z (T)	B_y (T)	$L_{segment}$ (mm)	IR_{coil} (mm)	t_{coil} (mm)	J (A/mm ²)	IR_{duct} (mm)	$N_{segment}$	θ_{bend} (deg.)	R_{bend} (mm)
CS01	1200	5-4	0	1200	500	90.0	53.0	420	1	-	-
MS01	1400	4-2	0	1400	500	30.0	53.0	450	1	-	-
MS02	600	2	0	600	610	30.0	53.0	560	1	-	-
MS03	300	2	0	300	670	60.0	62.9	620	1	-	-
MS04	600	2	0	600	225	30.0	37.8	175	1	-	-
TS01	800	2	0	800	225	30.0	55.5	175	1	-	-
TS02B	4912	2	0.030	200	225	30.0	84.0	175	16	90	3000
TS03	800	2	0	800	225	50.0	32.0	175	1	-	-
TS04B	4912	2	0.050	200	225	30.0	84.0	175	16	90	3000
TS05	1200	2	0	1000	225	50.0	24	175	1	-	-
DS01	300	2.5	0	300	225	50.0	8.5	175	1	-	-
DS02	1200	3	0	1200	400	50.0	52.2	350	1	-	-
DS03	1200	2	0	1200	470	50.0	34.3	420	1	-	-
DS04	1200	1	0	1200	610	50.0	16.9	560	1	-	-
DS05B	6356	1	0.145	73	750	50.0	49.4	700	31	180	2000
DS06	4400	1	0	4400	750	50.0	16.1	700	1	-	-

Chapter 6

Detector

Figure 6.1 shows a cutaway view of the COMET detector, overlaid with a typical $\mu^- - e^-$ conversion signal track. The COMET detector consists of the following three components:

- a muon target section, where a muon-stopping target is placed under a graded magnetic field,
- a $\mu^- - e^-$ conversion electron transport section which is composed of a curved solenoid forming a 180° arc, and
- a detector section, where an electron tracker and an electron calorimeter are placed.

In the following, all the three sections are described in detail.

6.1 Muon-stopping target

The muon-stopping target is placed in its own solenoid and connected to the pion-capture solenoid by a curved muon-transport solenoid. The muon-stopping target is designed to

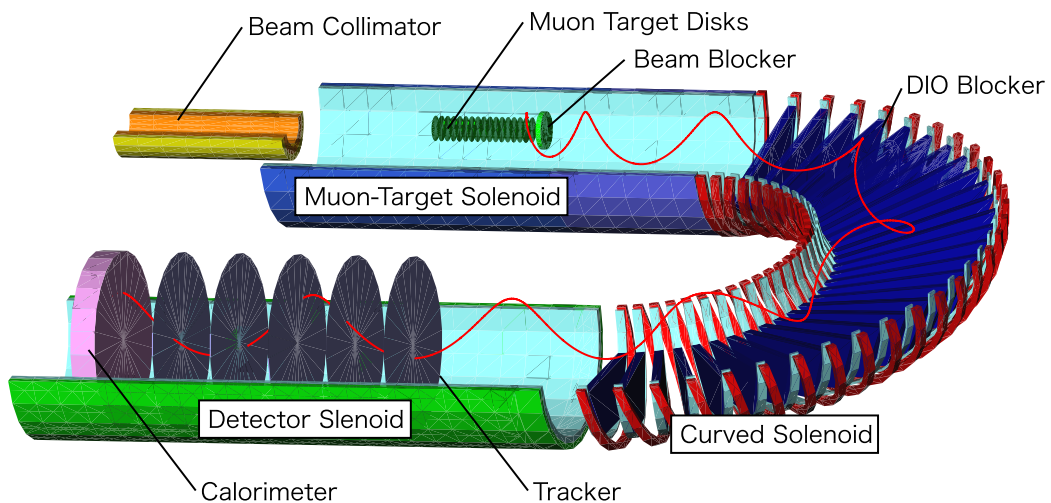


Figure 6.1: A cutaway view of the COMET detector. It consists of the muon-target section, the electron-transport section and the detector section. A typical $\mu^- - e^-$ conversion signal track is shown in red.

maximize the muon-stopping efficiency and the acceptance for the $\mu^- - e^-$ conversion electrons to arrive at the spectrometer. Also, it has to be designed to minimize the energy loss of the $\mu^- - e^-$ conversion electrons as they exit the target in order to minimise the momentum spread of the electrons. It is also important to make the target as small as possible to reduce possible backgrounds.

6.1.1 Material for muon-stopping target

To eliminate beam-related background events arising from both prompt and delayed particles, it is planned that the measurement time window will be opened about 700 nsec after the primary proton pulse, as shown in Section ???. Therefore, it is not suitable to use heavy materials, for which the lifetime of muonic atoms is short. Table 6.1 shows a comparison between several materials. From all these, aluminum is our first choice for a muon-stopping target, and a heavier material will be tried later.

It should be noted that the branching ratio of $\mu^- - e^-$ conversion processes, $B(\mu^- + N \rightarrow e^- + N)$, increases with atomic number Z for small values of Z , and then plateaus above $Z \simeq 30$, and decreases again for $Z > 60$. The branching ratio for aluminum ($Z=13$) is smaller than titanium ($Z = 22$), but by a factor of only 1.7.

Table 6.1: Lifetimes and relative strengths of $\mu^- - e^-$ process for different muon-stopping materials.

	aluminum	titanium	lead
Atomic number	13	22	82
Lifetime of muonic atoms (μ sec)	0.88	0.33	0.082
Relative $\mu^- - e^-$ conversion branching ratio	1	1.7	1.15

6.1.2 Geometrical configuration of the muon-stopping target

The configuration and dimensions of the muon-stopping target have been studied in order to maximize the muon-stopping efficiency and the suppression of backgrounds. The main parameters to be considered are the disk thicknesses and diameters, the number of disks and their spacing, and the magnetic field strength and magnetic field gradient. Monte Carlo simulations have been performed for various target configurations. The target configuration we have chosen is shown in Table 6.2.

Table 6.2: Configuration of the muon-stopping target.

Item	specification
Material	aluminum
Shape	flat disk
Disk radius	100 mm
Disk thickness	200 μ m
Number of disks	17
Disk spacing	50 mm

6.1.3 Graded magnetic field at the muon-stopping target

To maximize the geometrical acceptance, a graded magnetic field at the location of the muon-stopping target is considered. A graded field would be useful in two ways. These are:

- to maximize the acceptance for $\mu^- - e^-$ conversion signals, because it would reflect some electrons emitted in the backward direction, due to magnetic mirroring, and
- to maximize the transmission efficiency of $\mu^- - e^-$ conversion signals at the subsequent electron-transport solenoid and the suppression factor for backgrounds, by making the electrons move in paths more parallel to the axis.

The acceptance of the signal electrons ε_{acc} can be modelled as

$$\varepsilon_{acc} = \frac{1 - \cos \theta^{\text{crit}}}{2}, \quad (6.1)$$

where

$$\theta^{\text{crit}} = \pi - \sin^{-1} \left(\sqrt{\frac{B_{\text{target}}}{B_{\text{in}}}} \right). \quad (6.2)$$

Here, B_{target} and B_{in} are the magnetic fields at and before the muon-stopping target respectively. It can be seen that the higher B_{in} is, the larger the acceptance will be. On the other hand, the maximum polar angle at the detector section $\theta_{\text{detector}}^{\text{max}}$ is given by

$$\theta_{\text{detector}}^{\text{max}} = \sin^{-1} \left(\sqrt{\frac{B_{\text{detector}}}{B_{\text{target}}}} \right), \quad (6.3)$$

where B_{detector} is the magnetic field at the detector solenoid. A larger value of the ratio $B_{\text{detector}}/B_{\text{target}}$ is preferred for improving the background rejection power of the spectrometer solenoid.

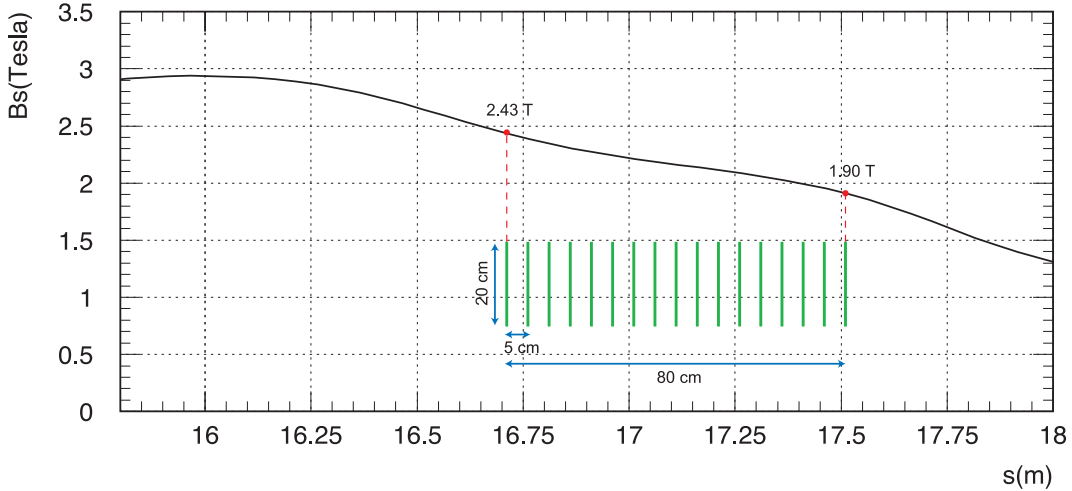


Figure 6.2: Distribution of a magnetic field at the beam axis and the target location.

Figure 6.2 shows the baseline configuration for the graded magnetic field at the stopping target region. Here, B_{in} and B_{detector} are set to 3 T and 1 T, respectively. The aluminum disks of 17 layers are placed where the magnetic field varies between 2.43 T to 1.90 T with a target radius of 100 mm.

6.1.4 Muon stopping efficiency

Monte Carlo simulations were performed to evaluate the muon-stopping efficiency of the target, as described above. These Monte Carlo simulations include the pion production, pion capture, muon transport processes with the momentum selection at the curved solenoids, as well as the potential mirroring-back of muons at the entrance to the muon-stopping target section, where the field strength increases from 2 T to 3 T. The momentum distribution of muons as they enter the stopping target solenoid is shown in Figure 6.3, where the muons which stopped in the target disk are shaded. The net stopping efficiency is 0.29 with this configuration. The relative number of muons stopped in each of the 17 aluminum disks is shown in Figure 6.4.

The time distribution of muons stopped in the muon-stopping target is shown in Figure 6.5.

6.1.5 Energy loss of outgoing electrons

Figure 6.6 shows the momentum distribution for outgoing electrons, having been generated with momentum 105 MeV/c in the muon-stopping target. Their passage through the aluminium is simulated using GEANT3. It is found that the average energy loss without the Landau tail is about 0.4 MeV.

6.2 Muon beam stop

A beam collimator is placed upstream of the stopping target, and a muon beam stop is placed downstream of the last target disk. The beam collimator together with the beam stop prevent beam particles from entering the curved, transport solenoid connecting the stopping target and detector solenoids.

The beam stop is a thick disk with diameter 30 cm, while that of the target disk is 20 cm. The expected rate of particles in the detector would be more than 1 GHz if a beam stop were not used. Figure 6.7 shows the radial position distribution of conversion electrons at the beam stop, where those with $p_T > 50$ MeV/c are indicated separately. From the figure, a beam stop 30 cm in diameter preferentially blocks electrons with transverse momenta smaller than 40 MeV/c. As a result, the number of $\mu^- - e^-$ electrons transported to the detector is decreased by 43%. However, it is known that in order to suppress background from electron scattering, it is necessary to apply a cut $p_T > 50$ MeV/c. This cut is correlated to the acceptance loss due to the beam stop. Therefore, the cumulative net loss of the conversion electrons is increased by an additional 4%.

The beam collimator decreases the number of stopping muons by 11%, and the beam stop reduces the number of conversion electrons entering the detector solenoid by a factor of 2. However, the transverse momentum of the electrons blocked by the beam stop tends to be small, indicating that these electrons would be cut in the data analysis to suppress various backgrounds. The detector rate due to beam particles is anticipated to be less than 300 kHz with the beam collimator and beam stop, as opposed to more than 1 GHz if these are not installed.

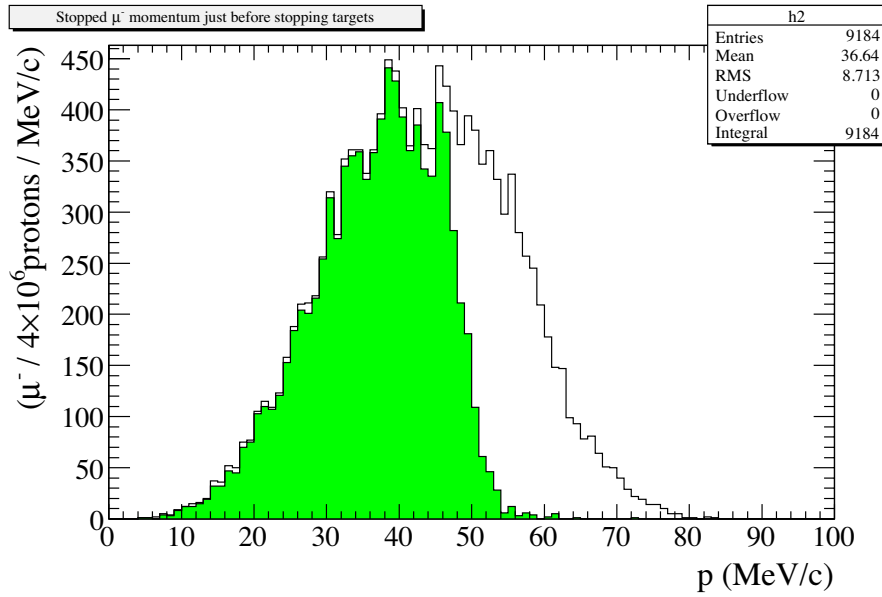


Figure 6.3: Momentum distribution of the muons as they arrive at the muon-stopping target. Of these muons, those that are stopped in the muon-stopping target are given in the shaded histogram.

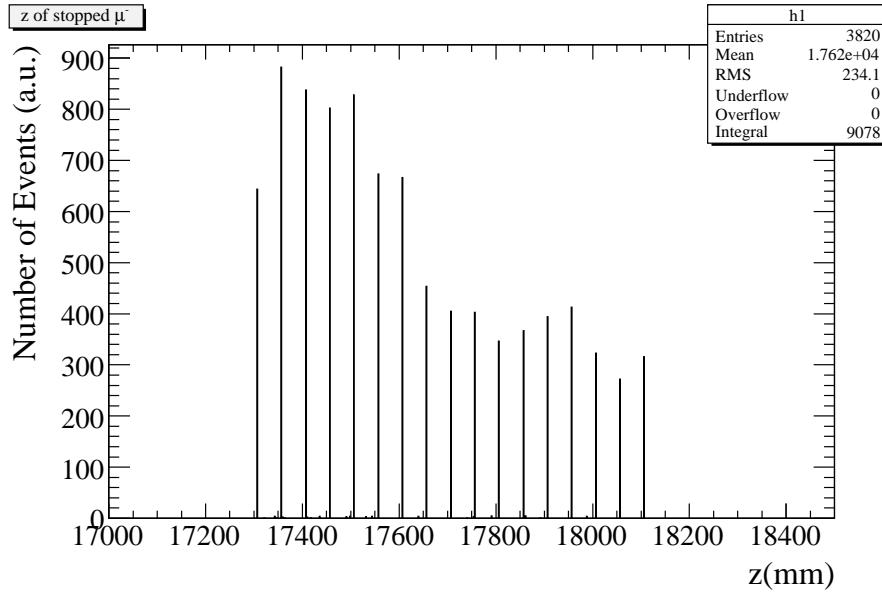


Figure 6.4: The longitudinal distribution of muons stopped in the aluminum foils.

6.3 Electron transport solenoid

6.3.1 Requirements for electron transport

The requirements of the electron transport in the COMET electron spectrometer are:

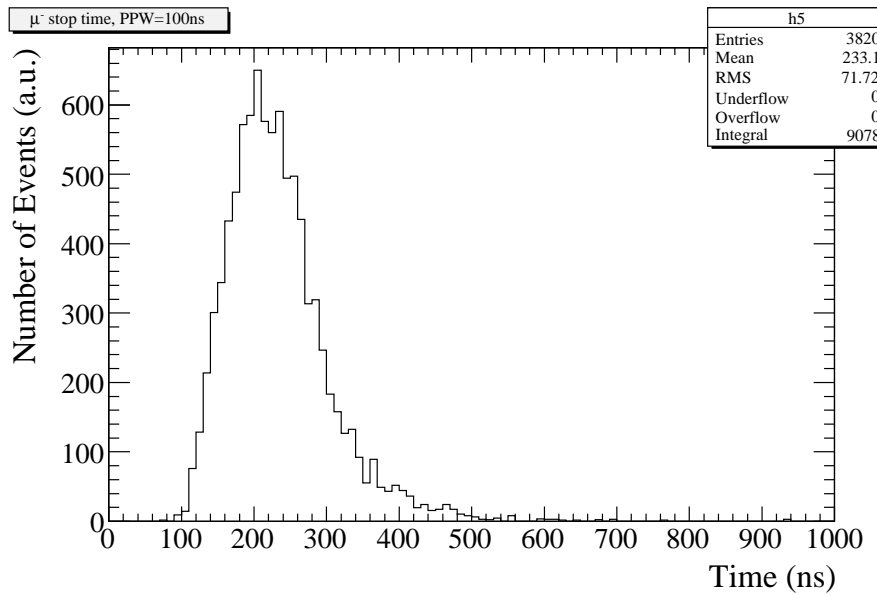


Figure 6.5: The time distribution of the muon stopped time for the aluminum targets. Proton pulses of 100 ns width are assumed.

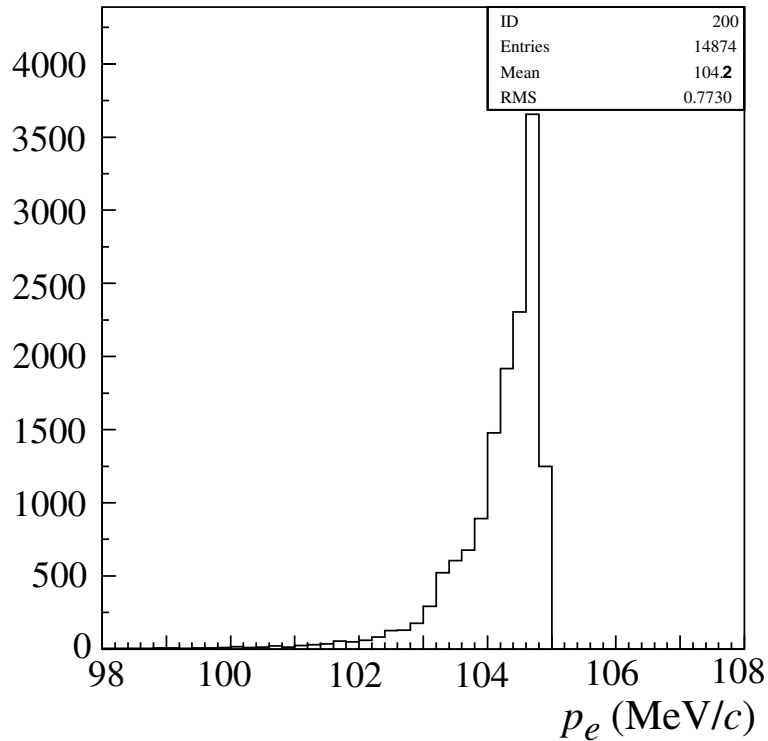


Figure 6.6: Momentum distribution of $\mu^- - e^-$ conversion signal electrons, including the effect of energy loss in the muon-stopping target.

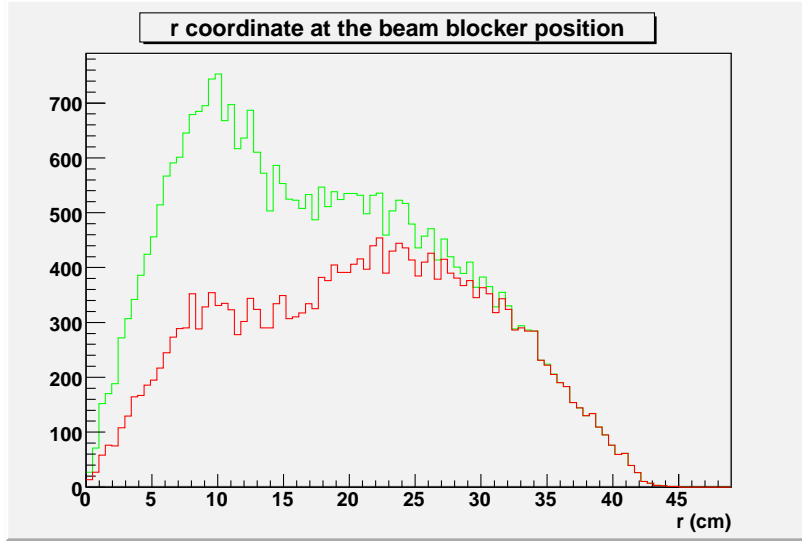


Figure 6.7: Radial coordinate of the $\mu^- - e^-$ electrons at the beam stop position for all electrons (green) and those with $p_T > 50$ MeV/c at the detector (red).

- to remove charged-particle backgrounds of low momenta so as to reduce single counting rates of the detectors, and
- to maximize the transmission of $\mu^- - e^-$ conversion signals.

To meet these requirements, a curved solenoid at the electron transport is adopted in the COMET electron spectrometer. The electron transport consists of curved superconducting solenoids with collimators inside the solenoid.

6.3.2 Curved solenoid in electron transport

The toroidal magnetic field of the curved electron transport solenoid momentum selects charged particles. A charged particle in a uniform toroidal field moves along a helical trajectory, and if the solenoid is slightly curved, the center of the helix drifts perpendicular to the plane of curvature. The amount of the drift, D , is given by;

$$D = \frac{1}{qB_0} \left(\frac{s}{R} \right) \left(\frac{p_L^2 + \frac{1}{2}p_T^2}{p_L} \right). \quad (6.4)$$

In the above q is the charge, B_0 is the magnetic field strength at the center of the helix, R is the radius of the toroid, s is the path length along the center of the helix, and p_L (p_T) is the momentum component parallel (perpendicular) to the magnetic field direction. The above equation may be rewritten as

$$D = \frac{1}{qB_0} \left(\frac{s}{R} \right) \frac{p}{2} \left(\cos \theta + \frac{1}{\cos \theta} \right). \quad (6.5)$$

Here p is the total momentum and θ is the angle between the momentum of the particle and the magnetic field. For the same value of θ , the amount of drift scales with the

total momentum, but the drift is different for different θ when the momentum is constant. However, as $\cos \theta \rightarrow 1$ the angular term approaches 2. Therefore, the magnetic field in the muon-target solenoid is graded to reduce the angle of the momentum vector. The width of the $\cos \theta + 1 / \cos \theta$ distribution at the entrance of the transport solenoid is about 2% (r.m.s). Thus, the difference of drift due to θ is 2 cm and the momentum dispersion is 1 cm/MeV/c at the exit of the transport solenoid.

6.3.2.1 Compensation dipole field

In order transport the 105 MeV/c electrons through the curved solenoid section, a compensation field of 0.17 T along the vertical direction will be applied. The accuracy of the compensation field is defined by the decay-in-orbit (DIO) rejection power rather than the transmission efficiency. The DIO rate changes one order of magnitude if the average compensation field changes only by 6%. This means that the mechanism to fine tune the vertical drift power is necessary.

One method is to use an independent coil for producing the compensation field. The tune of the compensation field becomes very easy. On the other hand, the magnet structure will become complicated since torus coils and compensation coils should be wound in layers.

6.3.3 Radius of the electron transport solenoid

Figure 6.8 shows correlation between the initial $\cos \theta$ and the $\cos \theta$ at the torus entry, where θ is the angle of $\mu^- - e^-$ conversion electron with respect to the solenoid axis. It can be clearly seen that electrons initially emitted to backward direction ($-0.5 < \cos \theta < 0$) were mirror-backed to the torus entry, increasing the geometrical acceptance by a factor of 50%. In addition, the distribution of $\cos \theta$ at the torus entry becomes very narrow by the graded field as shown in Fig. 6.9. Since the power of the vertical drift scales by the factor $\cos \theta + 1 / \cos \theta$ for the same momentum, this narrowness is beneficial to maximize the transmission efficiency of the $\mu^- - e^-$ conversion electrons through the torus section.

According to Fig. 6.9, the maximum p_T of the $\mu^- - e^-$ conversion electron is 75 MeV/c, thus the maximum radius of the helix for $\mu^- - e^-$ conversion electron is about 25 cm. Therefore, the inner radius of the curved solenoid section should be larger than $25 \times 2 + 5 = 55$ cm, where 5 cm comes from the radius of the muon-stopping target disk. The inner radius of the current design is 70 cm.

6.3.4 Decay-in-orbit background rate

Many background particles are generated from the muon-stopping target. They come from muons in the muon-stopping target, contamination in the muon beam and others. Since the background rate is so high, they need to be suppressed so that the electron detectors can work efficiently.

The background rate is mostly dominated by muon decay-in-orbit (DIO) electrons. Its energy spectrum has a distribution to the high energy region near to that of the $\mu^- - e^-$ signal (of about 105 MeV). Figure 6.10 shows a number of DIO electrons normalized to one muon decay as a function of different energy threshold. The DIO event rate in the detector region will be reduced significantly by an energy threshold. For example, an expected number of DIO events for one muon decay is about 10^{-8} for an energy threshold of 80 MeV as shown in Fig. 6.10. In that case, a detection rate is estimated to be of the order of 1 kHz for 10^{11} muons per second in the muon-stopping target.

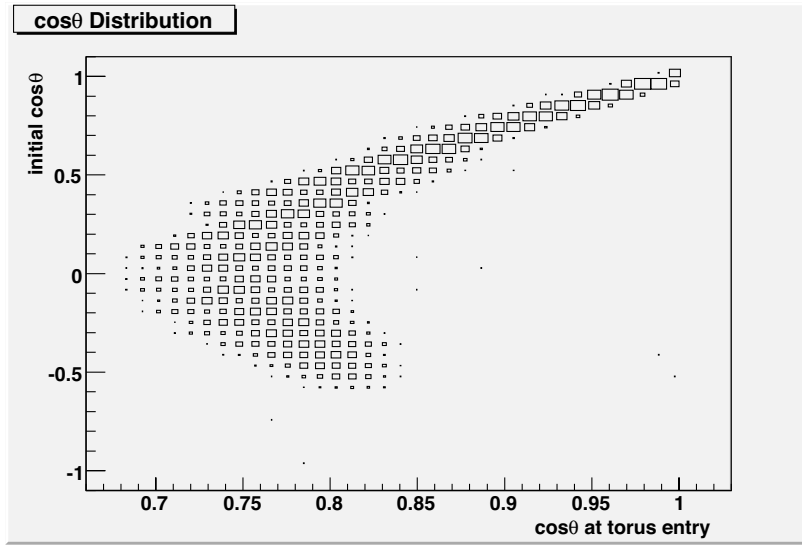


Figure 6.8: Correlation between $\cos \theta$ of the initial state (before the incline by the graded field) and $\cos \theta$ of the torus entry (after the mirror and incline by the graded field).

6.3.5 Decay-in-orbit (DIO) blocking slit

Electrons with $p < 60$ MeV/c are blocked at the exit of the transport solenoid, in order to suppress the detector rate due to DIO electrons. Figure 6.11 shows the difference in the vertical position at the exit of the transport solenoid between $\mu^- - e^-$ conversion electrons and DIO electrons. A half-slit which extends ~ 20 cm below the median plane of the transport solenoid removes most of the DIO electrons. Figure 6.12 shows the DIO electron rate and $\mu^- - e^-$ conversion electron acceptance as a function of the slit position. The DIO electron rate is very sensitive to the slit position while the change in the $\mu^- - e^-$ acceptance is modest.

The DIO stop is composed of Aluminium in order to reduce the number of back scattered electrons. The rate of electrons that hit the detector after backscattering is reduced by almost one half compared to the number if a heavier metallic stop were used.

6.3.6 Electron transport acceptance

The curved solenoid rejects most of the DIO electrons at a cost of acceptance loss to $\mu^- - e^-$ conversion electrons. In order to suppress the detector rate due to the DIO electrons, the height of the DIO blocking slit should be 20 cm below the median plane of the curved solenoid. At this value the acceptance is 47%. In addition to DIO, the background also includes nucleons and photons from nuclear de-excitation following muon capture, electrons from various sources traversing the detector, and bremsstrahlung photons that pair produce or Compton scatter in the tracking detector (often after first scattering somewhere else in the detector solenoid).

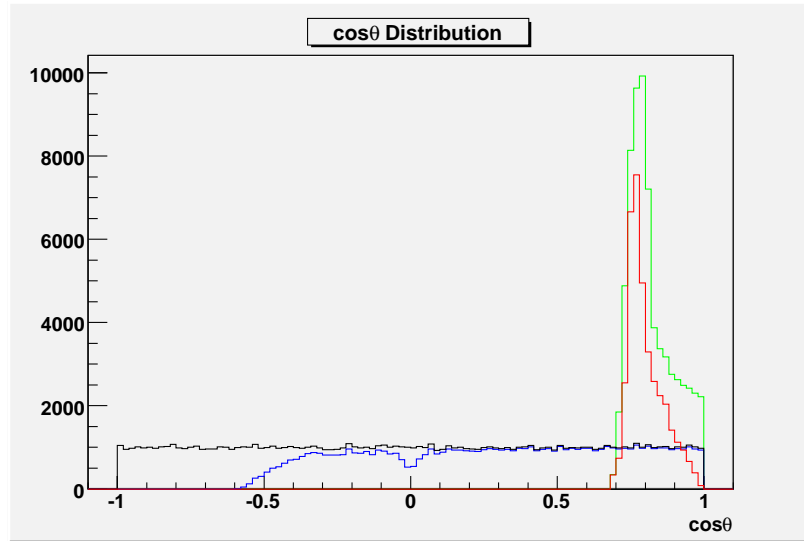


Figure 6.9: Black line indicates $\cos \theta$ of initial electrons. Blue line indicates $\cos \theta$ of electrons entering the torus section. Green line is $\cos \theta$ of electrons at the torus entry without the muon beam stop. Red line is $\cos \theta$ of electrons at the torus entry with the muon beam stop.

6.4 Detector solenoid

A straw tube tracking detector and a calorimeter trigger are mounted within the constant magnetic field of the detector solenoid. The total length of this solenoid is not yet fully

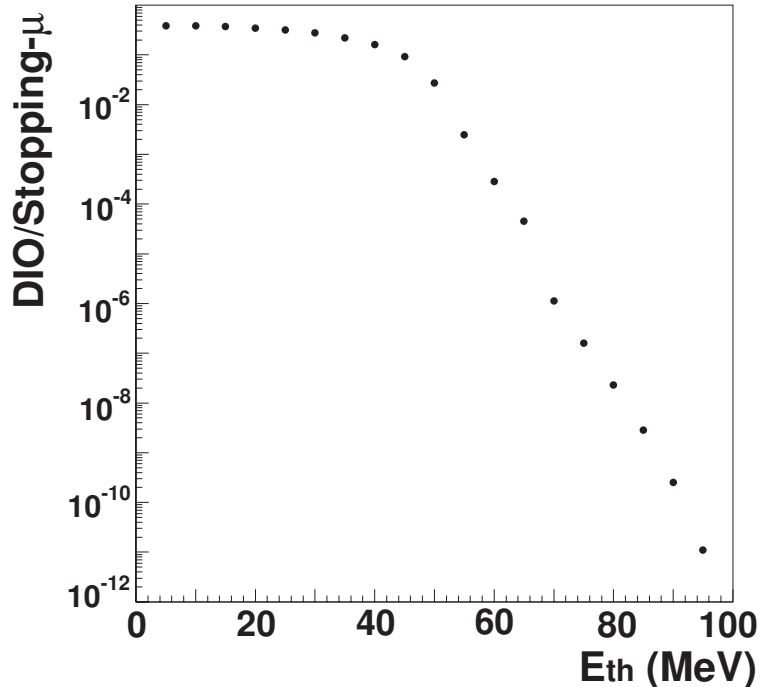


Figure 6.10: A number of DIO events per one muon in the muon-stopping target as a function of energy threshold.

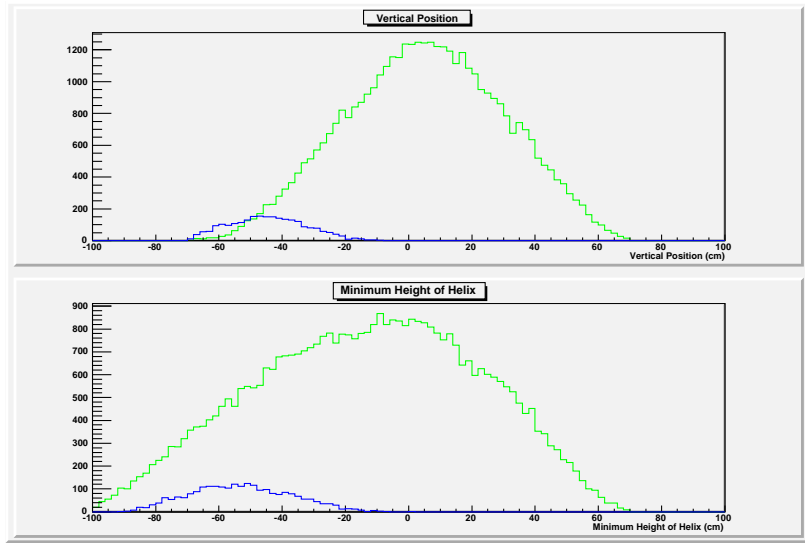


Figure 6.11: Upper plot shows vertical position of electrons from $\mu^- - e^-$ conversion conversion (green) and DIO (blue). Lower plot shows lower height of the helix for $\mu^- - e^-$ conversion signals (green) and DIO (blue).

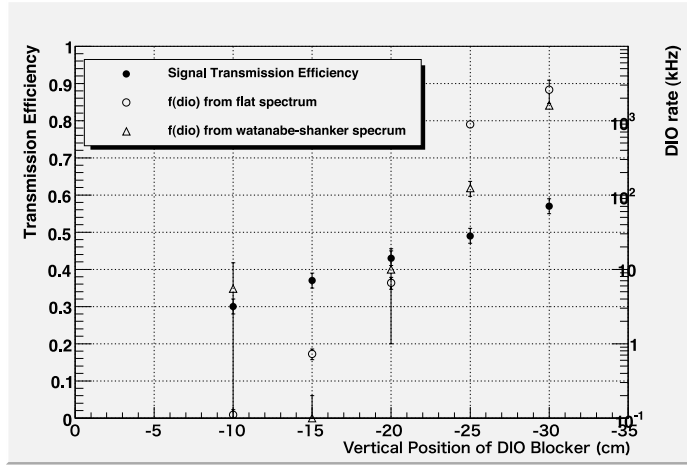


Figure 6.12: Signal electron (105 MeV) transmission efficiency and detector rate from DIO for several different settings of the Ymax cut.

optimized, since it depends on tracker design, but presently, the tracker is at least 3 m in length and has readout electronics enclosed within the vacuum of the detector solenoid.

6.5 Electron tracker

6.5.1 Overview

The tracking detector design is driven by the need to be insensitive to the majority of an approximately 1 kHz of muon decays per second, and the associated backgrounds inherent

to a high flux beam of charged particles. High detector rates can limit the experimental sensitivity in several ways. First, detector occupancy could be so high that the efficiency of obtaining valid position information in the tracker is reduced. This problem may be mitigated by increasing detector granularity and time resolution. Second, noise (accidental) hits may be combined with the trajectory of a lower energy decay-in-orbit (DIO) electron to create an event consistent with the energy of a conversion electron (105 MeV). This is a problem common to many high rate experiments that look for rare events, and it may be suppressed by increasing the time resolution, increasing the redundancy in position measurements, and by analyzing only hits from particles of interest (particle ID). Third, there may be contributions to the trigger rate due to pile-up of lower energy signals in the trigger detector. This possibility may be addressed by increased segmentation, optimizing the geometric design, and by appropriate pulse shaping and timing.

For $\mu^- - e^-$ conversion in particular, a high flux of charged particles passes from a proton production target through a muon beam channel and impacts a stopping target. Beam components that are not stopped at this point are transported to a down-stream beam stop. The beam must be pulsed, so one looks for muon conversions between beam spills taking advantage of the fact that the muon mean lifetime is $2.2\ \mu\text{s}$. Thus muons continue to interact or decay between pulses of the primary beam. Therefore the detector is active (read out) for $\mu^- - e^-$ conversion data only during the last 700ns between each proton beam spill.

In contrast to an earlier design (MECO [82]), COMET places the production target, stopping target, and detector in different solenoids, all connected by curved transport solenoids. Appropriate blocking shields are placed to limit rates and unwanted particles from entering the target and detector solenoids. Also magnetic field lines, which traverse all the solenoids, are carefully designed to avoid traps which could result in the late arrival of particles at the detector.

The tracking detector is located in a uniform magnetic field (1T) region of the detector solenoid. It is designed to measure with good efficiency, the parameters of the helical trajectory of electrons that are emitted from the muon stopping target. These electrons must lie within the angular acceptance of the detector and have momenta near 105 MeV/c. As an electron moves through the detector components, it loses energy and is deflected by scattering. Thus, knowledge of the amount and type of material through which the electron passes, and a careful measurement of the changing helical trajectory are necessary to obtain the best estimate of the initial electron momentum.

Energy loss of the electron has two effects; 1) it broadens the central peak in the resolution function, as well as introducing a small mean energy loss, and 2) it produces a low energy tail. This latter effect decreases the detector acceptance. However, if a sufficient number of position measurements are made, an error measurement in the crossings of an electron trajectory with the detector planes does not significantly contribute to the energy resolution.

The measured helical parameters, when fit in analysis to a helical trajectory, determine the momentum of the electrons. A minimum of 3 position measurements can determine a helix, but many more points are needed to over constrain a fit as uncertainty in the helical parameters is not the only contribution to uncertainty in the momentum measurement. There are also errors in pattern recognition, which does not significantly reduce the detector acceptance, but can generate high energy tails in the resolution distribution. This can overlap the signal region of the spectrum. Thus, accidental events, noise, and detector inefficiencies can conspire to yield a pattern recognition error, and these need to be carefully

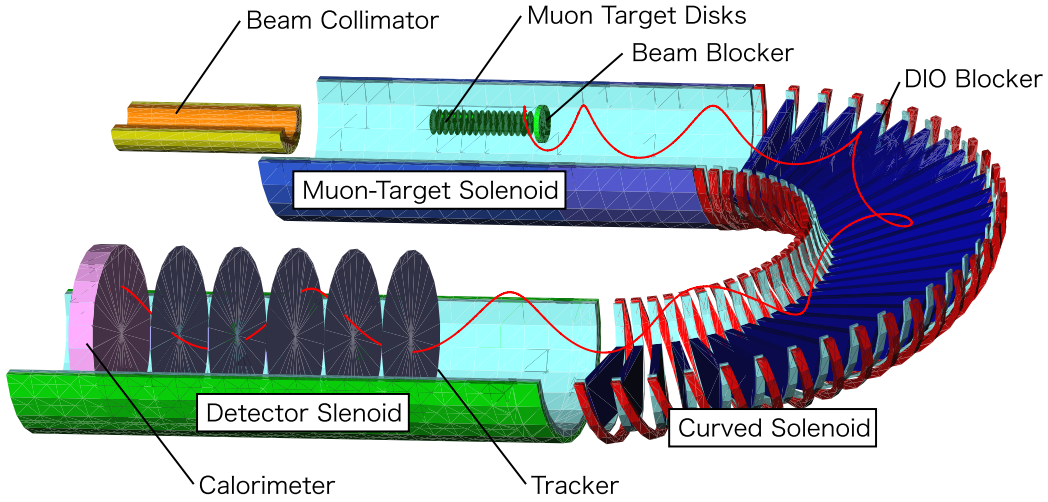


Figure 6.13: Cut view of COMET detector. Red rings around the curved solenoid section are magnet coils, and tilted to produce the compensation field (A field that cancels the drift for a 105 MeV electron)

understood and controlled.

A schematic of the stopping target and detector solenoids is shown in Figure 6.13. The tracking detector is located downstream of a curved transport solenoid and the muon stopping target. The detector consists of a set of 5 straw planes, 48 cm apart, and placed so that the axial direction of the straws is transverse to the axis of the solenoid. Each of the 5 planes contains a set of 4 straw tube arrays. One array measures position in x, and one measures position in y (coordinates rotated by $\pi/2$). An identical (x,y) pair is attached to the first array, but rotated by 45 deg., in order to break hit ambiguities and add redundancy. A hit location is determined by the plane position, the straw position within a plane, and the drift time. There is presently no second coordinate readout, although charge division on a straw anode wire is under consideration. The azimuthal position is obtained from hits in the rotated coordinate measurements. Both timing and pulse height information are recorded from one end of each hit wire. Pulse height is used to discriminate between electron and low-energy, heavily ionizing tracks (*e.g.* protons) which can occur through atomic muon absorption on nuclei. There are 208 straws in each array for a total of 832 straws per plane and 4160 straws in the full 5 planes of the detector. Therefore there are 4160 readout channels.

The calorimeter is positioned behind the tracker. Electrons which pass through the tracker are absorbed in the calorimeter and if the deposited energy lies within a small window around 105 MeV, a trigger signal is generated. Appropriate signals that were previously inserted into a latency pipeline in the readout electronics of the tracking detector are then processed by a second level trigger, and the resulting information, including data from the calorimeter and cosmic ray shield, are stored as an event for further data analysis. In this section, the construction and readout of the tracking detector is mainly addressed.

6.5.2 Design of the electron tracker

The requirement to the tracker system is as follows:

1. should withstand for the total rate of charged particle up to 800 kHz,
2. should withstand for the total flux of gamma up to 8 MHz.

Please note that the signal rate coming from the gamma rays will be much less than 8 MHz as long as the tracker is thin enough to be transparent to the gamma rays. The average energy of gamma is about 0.2 MeV, and the mean free path of these gammas is about 5.5 g/cm^2 . If the thickness of the tracker is thinner than, 0.1 g/cm^2 for examples, the rate from gamma will be only less than 200 kHz. The average number of hits per 100 nsec is only 0.1. Therefore, the track reconstruction error should be negligibly small.

In the current design, the tracker consists of 5 superlayers of a simple strawtube chamber. Each strawtube chamber consists of X, X', Y and Y' planes to provide X and Y information without left-right uncertainty. The total thickness of the tracker is less than 0.1 g/cm^2 since the straw-wall thickness is less than $20 \mu\text{m}$. Therefore, the total rate coming from both electrons and gamma conversions is less than 1 MHz.

The tracker resolution is limited by the following three factors:

1. spatial resolution of the tracker,
2. multiple scattering by the tracker plane,
3. miss of the track reconfiguration.

A transverse momentum of the track should be larger than $50 \text{ MeV}/c$ in order to suppress the beam electron scattering background. The minimum radius of the helix in 1 T magnetic field is 16.7 cm. On the other hand, the momentum resolution is required to be less than $1 \text{ MeV}/c\text{-FWHM}$ to maintain signal acceptance, this corresponds to 0.4%(RMS) of the momentum resolution, and $700 \mu\text{m}$ of the spatial resolution. This spatial resolution can be easily achieved by standard technology of gas tracker.

The multiple scattering will change the momentum direction of the track. The track displacement by the multiple scattering becomes maximum after $\pi/2$ turns of helix, and minimum (zero at the 1st order) after π turns. Therefore, the 2nd superlayer should be placed at the position where the phase of helix turns π from the 1st superlayer. However, if it is exactly at π , the information of the charge of helix is lost. Taking into account of those point of views, the phase advance of the helix between the superlayers should be maximized but not exceed π . In the current design, the distance between the superlayers are chosen to be 480 mm, which corresponds to $2\pi/3$ turns in average. The minimum phase advance of the track is about 1.3 rad, thus 5 superlayers will cover 1 turns of helix for all tracks.

As for the track reconstruction error coming from the accidental background hits, it can be minimized by requiring the number of hits per a superlayer being only one. The reduction of the analysis efficiency by doing this is only 15% since the tracker rate is only less than 1 MHz. This is one of advantages due to the curved solenoid configuration.

6.5.3 Expected performance of the electron tracker

In order to estimate the tracker performance, a Monte Carlo calculation was carried out with a slightly simplified tracker geometry. Each superlayer was approximated by a single film of Polyimide with $160 \mu\text{m}$ thickness. This thickness corresponds to $20 \mu\text{m}$ of the strawtube thickness, while $15 \mu\text{m}$ of the thickness is possible.

figure 6.14 shows the number of total hits on the whole superlayers. Even if we strictly select the events with the number of hits being equal to 5, the loss of the efficiency is only

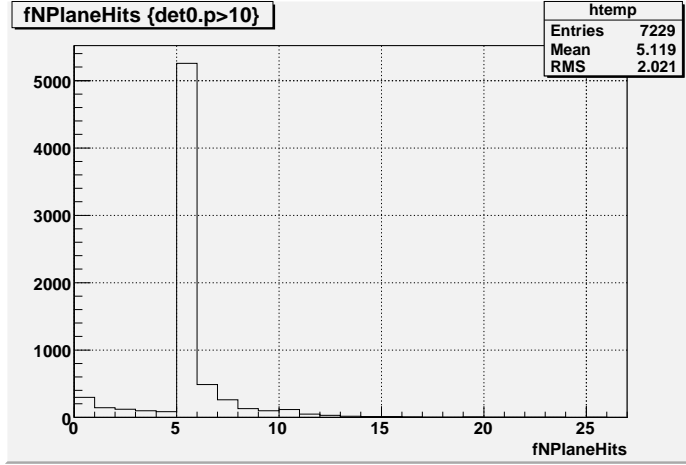


Figure 6.14: Total number of hits in the tracking detector.

12%. In this study, we accept the events with $5 \leq N_{\text{hits}} \leq 8$, and the acceptance loss is only 5%.

The track fitting algorithm we employed takes care of the multiple scattering effect. The track helix was a chain of 4 partial helices. The adjacent helices were connected at the superlayer position with angles, where the angle imitate the deflection by the multiple scattering. In the track fitting procedure, the χ^2 function was formulated by using not only the hit positions but also the deflection angles as follows:

$$\begin{aligned}
 & \chi^2(p, \theta_x, \theta_y, x, y, \theta_{x,1}^{\text{scat}}, \theta_{x,2}^{\text{scat}}, \dots, \theta_{x,n_{\text{scat}}}^{\text{scat}}, \theta_{y,1}^{\text{scat}}, \theta_{y,2}^{\text{scat}}, \dots, \theta_{y,n_{\text{scat}}}^{\text{scat}}) \\
 &= \sum_{i=1}^{n_{\text{det}}} \left(\frac{x_i - X(z_i; p, \theta_x, \theta_y, x, y, \theta_{x,1}^{\text{scat}}, \theta_{x,2}^{\text{scat}}, \dots, \theta_{x,n_{\text{scat}}}^{\text{scat}}, \theta_{y,1}^{\text{scat}}, \theta_{y,2}^{\text{scat}}, \dots, \theta_{y,n_{\text{scat}}}^{\text{scat}})}{\sigma_x} \right)^2 \\
 &= \sum_{i=1}^{n_{\text{det}}} \left(\frac{y_i - Y(z_i; p, \theta_x, \theta_y, x, y, \theta_{x,1}^{\text{scat}}, \theta_{x,2}^{\text{scat}}, \dots, \theta_{x,n_{\text{scat}}}^{\text{scat}}, \theta_{y,1}^{\text{scat}}, \theta_{y,2}^{\text{scat}}, \dots, \theta_{y,n_{\text{scat}}}^{\text{scat}})}{\sigma_y} \right)^2 \\
 &+ \sum_{j=1}^{n_{\text{scat}}} \left(\frac{\theta_{x,j}^{\text{scat}}}{\sigma_{\theta}^{\text{scat}}} \right)^2 + \sum_{j=1}^{n_{\text{scat}}} \left(\frac{\theta_{y,j}^{\text{scat}}}{\sigma_{\theta}^{\text{scat}}} \right)^2
 \end{aligned}$$

where X and Y are the expected x- and y-position of hit, σ_x and σ_y are the spatial resolution of detector, σ_x^{scat} and σ_y^{scat} are the root mean square of the multiple scattering angle distribution. X and Y are the function of parameters defining the chain of partial helix: momentum (p), angles (θ_x, θ_y), position (x, y) of the 1st helix and deflection angles $\theta_x^{\text{scat}}, \theta_y^{\text{scat}}$ on successive superlayers. The number of parameters to be fitted is $n_{\text{param}} = 5 + 2n_{\text{scat}}$, and the degrees of freedom (d.o.f) is $n_d = 5$.

The function minimization for the above χ^2 was performed by using non-linear function minimization package, MINUIT. The detector resolution was conservatively assumed to be $250 \mu\text{m}$. The RMS of the multiple scattering was found to be $\sigma^{\text{scat}\theta} = 0.0025 \text{ rad}$ so that the obtained χ^2 distribution becomes consistent with the one for 5 d.o.f. It was consistent with the expected value of $\sigma^{\text{scat}\theta}$ from the superlayer thickness. Figure 6.15 shows a probability distribution of the track fitting. Peak at $P < 0.05$ may be caused by large angle tail of the multiple scattering, which is not considered in the current fitting function. The fitting

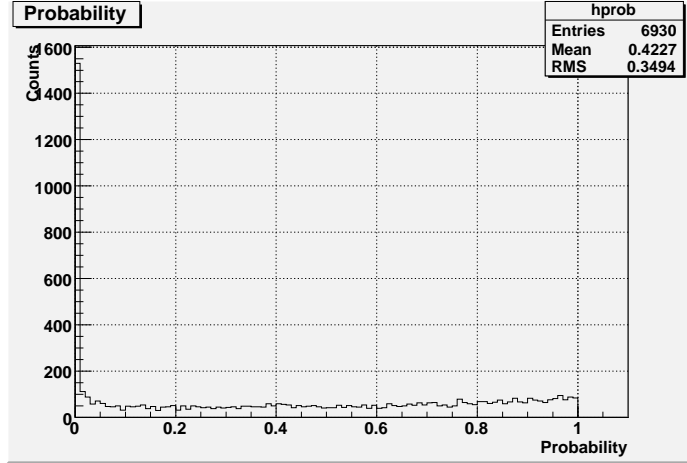


Figure 6.15: Probability distribution of the track fitting with the detector resolution $\sigma_x = \sigma_y = 0.250$ mm, and the uncertainty of the multiple scattering angle $\sigma_\theta^{\text{scat}} = 0.0030$ radian.

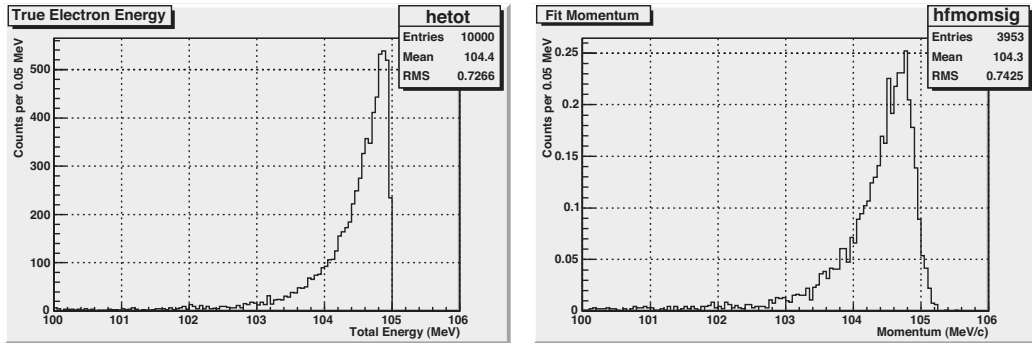


Figure 6.16: Left plot shows true total energy, E^{true} , at the tracker entrance. Right plot shows fit momentum. The detector resolution is $\sigma_x = \sigma_y = 0.250$ mm, and the uncertainty of the multiple scattering angle is $\sigma_\theta^{\text{scat}} = 0.0030$ radian.

algorithm could be improved to save those events, but for the moment, the track with $P < 0.05$ is selected for the good track.

Figure 6.16 shows true momentum spectrum and analyzed momentum spectrum at the tracker entrance.

Figure 6.17 shows the momentum resolution obtained by the track fitting after applying the further event selection ($p_T > 52$ MeV/c). The net momentum resolution from the track fitting is 110 keV/c, and the root-mean-square (rms) of the gross momentum distribution (including the effect of energy loss in the target) is 740 keV/c. The low momentum tail may come from energy loss of the electron by Moller scattering. The high momentum tail extends only up to 1 MeV/c above.

Figure 6.18 shows net momentum resolutions as a function of spatial resolution of detector. There is no significant difference in the momentum resolution even if the detector resolution is as worse as 100 μm . This is because of the current momentum resolution is limited by the multiple scattering. It is also note worth that the gross momentum resolu-

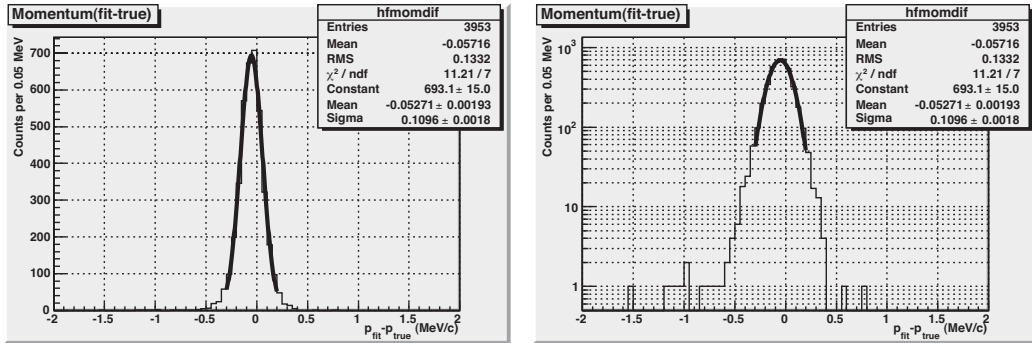


Figure 6.17: A difference between fit momentum and true momentum. Left plot is in linear scale and the right plot is in log scale. The detector resolution is $\sigma_x = \sigma_y = 0.250$ mm, and the uncertainty of the multiple scattering angle is $\sigma_\theta^{\text{scat}} = 0.0030$ radian.

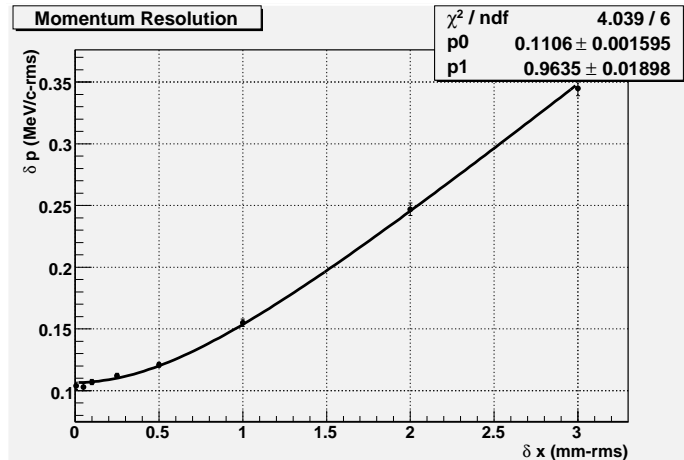


Figure 6.18: Track-fit momentum resolution as a function of spatial resolution of detector plane.

tion is a convolution of the net momentum resolution by the tracker and the energy loss uncertainty in the muon-stopping target. The contribution from the later factor is almost 200 keV/c-RMS. In order to balance the tracker performance with this natural width, The detector resolution could be even 1 mm(RMS), and the detector thickness could be as thick as twice¹.

6.5.4 Response of the straw detector to ionizing events

The simulation of drifting ionization deposited by the movement of a charged projectile through various media has been the subject of many previous studies [83]. For example, the code, GARFIELD, is available from the CERN library [84]. We have adapted a code, previously used to determine the drift time contours in a wire chamber embedded in a magnetic field. In general, this simulation calculates, for the proposed detector geometry,

¹Please note, in that case, the gamma induced tracker rate will be also twice, about 400 kHz

Table 6.3: The Ionization Energies and Ionization Potentials of Various Gases

Gas	W(eV)	I(ev)	Ion Clusters	Total Pairs
H ₂	36.3	15.4	5.2	9.2
He	42.3	24.6	5.9	7.8
Ne	36.4	21.6	12.	39.
Ar	26.3	15.7	29.4	94.
Kr	24.1	14.0	22.	192.
Xe	21.9	12.1	44.	307.
CO ₂	32.8	13.8	34.	91.
C ₂ H ₆	24.4	11.4	21.	103.
CH ₄	28.	13.0	12.	53.
C ₄ H ₁₀	23.	10.8	46.	195.

the charge collected on the anode wire as a function of drift time. The code simulates the ionization by a Vavilov distribution [85], and both the projectile and the drifting ionization move under the influence of the local E and B fields. Recombination of the drifting charge is ignored but diffusion is included. The drift time vs position for each track is determined by recording the time of arrival of the first drifting cluster for the closest distance of approach between the incident track and the anode wire. The first electron arrival cannot be directly measured, as the charge arrives in clusters and the discrimination threshold must be set above a cluster size of one electron. In any event, the readout electronics integrates the signal over ≈ 15 ns. However, it is possible to use pulse shape to extrapolate the time from a threshold measurement backwards to obtain a better estimate of the first arrival time.

A charged particle ionizes the medium through which it travels, depositing on average, an energy loss given by the Bethe-Bloch equation [86]. The number of atomic collisions along any given path is approximated by a Poisson distribution [83], and the energy loss of the traversing particle is obtained from the energy expended in the ionization, and the kinetic energy imparted to the ionized electrons. All of this energy is deposited in the medium if photons from the de-excitation of the ionized atoms are absorbed and the ionized electrons are stopped in the medium. The average energy loss depends on the medium, the projectile velocity, and the charge, having a minimum value [87] (minimum ionizing particle or MIP) when the relativistic γ factor of the projectile is $\approx 3.5\text{-}4.0$. The number of clusters and the primary electrons per cm-atmosphere for a MIP, produced in various gases are listed in Table 6.3.

As an example of an energy loss calculation, Figure 6.19, shows the simulated energy loss for electrons and protons with momenta of 100 MeV/c in 5mm of a chamber gas consisting of 60% Ar and 40% C₂H₆. Note that the energy scale is logarithmic.

To study the drift equations in the presence of a magnetic field, we assume that the direction and velocities of the drifting electrons can be obtained from the application of the Lorentz force with the addition of a dissipative term ($\sigma \vec{V}$, representing resistive flow (collisions)).

$$\frac{d\vec{P}}{dt} = q(\vec{E} + \vec{V} \times \vec{B}) - \sigma \vec{V} \quad (6.6)$$

Note that for equilibrium drift ($\vec{V} = \text{constant}$). Then the drift velocity from the above equation is;

$$V = \left(\frac{qE}{\sigma} \right) \cos(\theta) \quad (6.7)$$

Here θ is the Lorentz drift angle which depends on σ , B , and q . The detector geometry has \vec{B} in the z direction, with the E field in the (x,z) plane. In this case, the Lorentz drift angle is a complicated expression as it no longer lies in the plane containing E. A typical drift trajectory is shown in Figure 6.20. Here we provide views in the (x,z) and (x,y) planes as the drift is 3-dimensional. One can see the spread of the drift trajectories in the y direction from the original positions of ionization due to the $\vec{v} \times \vec{B}$ term of the Lorentz force. The first arrival time as a function of closest approach is linear.

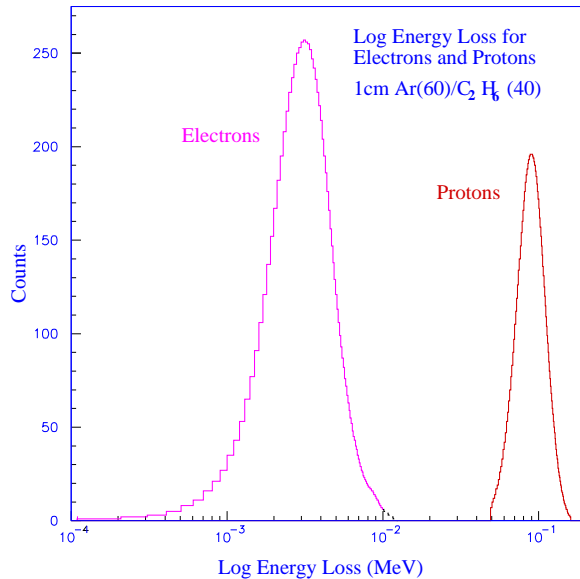


Figure 6.19: A simulation of the energy loss for 100 MeV/c protons and electrons in 5mm of drift gas consisting of 60% Ar and 40% C_2H_6

Drift Velocities have been measured for a number of gases and gas mixtures [88]. In some cases these have been obtained as a function of an applied magnetic field. Appropriate parameters are not readily available for the gases and fields proposed for COMET, although one can use measured drift parameters as a function of the electric field strength in the absence of a magnetic field to extract the mean time between collisions, as a function of the field. Then one use the above equations to obtain the velocities in the various coordinate directions as a function of both the electric and magnetic fields. Generally this seems to produce a somewhat smaller Lorentz angle than measured, in some cases by as much as 10-20% at higher fields. The drift velocity can be corrected for pressure differences by scaling the velocity by the square root of the pressure.

The charge collected on the anode (electrons) as a function of time can be obtained from the simulation. If it is assumed that there is a linear relationship between the number of electrons collected in each time increment, then this number is proportional to the number of positive ions produced by avalanche at the anode wire. These ions are then drifted away from the anode with ionic drift velocity creating the signal on the anode.

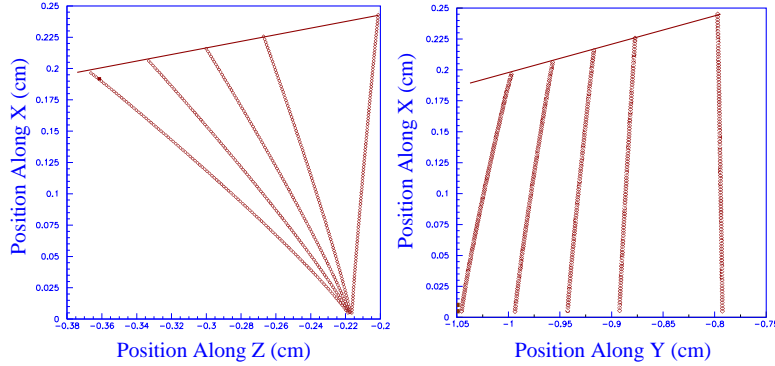


Figure 6.20: The figure shows the calculated drift trajectories for a track through a straw in the tracker in both the (x,z) and (x,y) planes. The gas mixture is 60% Ar and 40% C_2H_6 and the \vec{E} and \vec{B} fields are 1500 V and 1.2 T respectively. The \vec{B} field is in the z direction. The line represents the track trajectory. The point of confluence of the drifting electrons in the left figure is the wire. In the right figure the wire is the y axis

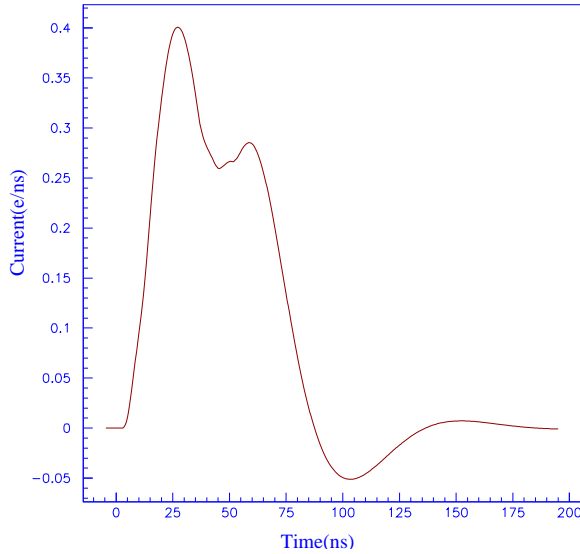


Figure 6.21: The figure shows a simulated current output due to a signal on a straw anode. The pulse shape is a function of the circuit filter, time constant, and time of arrival of the ionization clusters

The resulting electron current is passed through a simple electronic filter simulating a preamplifier circuit, which imposes a bandwidth of ≈ 75 Mhz and an RC time constant of ≈ 15 ns. With appropriate selection of the circuit components, the resulting anode current is shown in Figure 6.21. While the pulse shape varies with the statistical collection of the drifting electrons, it is reasonably consistent with experimentally observed anode signals in an oscilloscope. The bipolar nature of the current is a consequence of the filter circuit and can be adjusted by selection of the various constants.

6.5.5 Pulse saturation and pile-up

Studies of saturation due to heavily ionizing events involved the use of a pulser and an alpha particle source as well as beam tests using an intense, low-energy proton beam. It was found that saturation in the preamplifier can be significantly reduced by a feedback loop to drain charge from the front end when the pulse amplitude exceeds a set threshold. The curved solenoid removes a substantial number of beam flash components reducing the problem of pile-up and saturation.

Pile-up due to dead-time in the calorimeter is a more significant problem. If the maximum calorimeter rates given in Table 6.10 are correct and the summed energy is obtained in 100 ns, then the dead-time due to calorimeter pileup is 6%.

6.5.5.1 Backgrounds induced by pattern recognition errors

We next turn to a discussion of backgrounds due to high energy tails in the resolution function of the spectrometer. In previous studies for MECO, these were shown to be primarily due to an analysis combining hits from a low energy electron and random accidentals (noise clusters). We refer to this as pattern recognition errors.

Background can, in principle, arise from a variety of sources: multiple scattering, large tails in position resolution, etc. MECO found that DIO electrons in this energy range primarily produce background pattern recognition errors [89], but at a level well below the sensitivity of the experiment. These studies were done to determine the number of mis-reconstructed trajectories. They employed GEANT simulations, and used different pattern recognition and background rejection strategies. The calculations proceeded by determining the cluster positions of the DIO electrons and superimposing, on average, an additional 24 noise clusters. This is larger than was expected and allowed an efficient determination of the most probable topology of background events. The studies were statistics limited, but indicated that this type of pattern recognition error for MECO was could be resolved. With the caveat that the MECO and COMET trackers are slightly different and that DIO backgrounds in COMET are substantially lower than for MECO, we anticipate that this type of background will not present a problem for COMET as well. However, any rare decay experiment always finds that a confluence of unforeseen issues produce the background limits to the experiment. Redundancy, shielding, resolution, and timing can mitigate this type of background.

6.5.6 Mechanical construction and maintenance

The tracking detector and its mounting frame fit inside the detector solenoid. The distance between the inner wall of the solenoid and the mounting frame of the detector requires at least 3cm of radius to provide space for mounts and cables.

Figure 6.22 shows a layout view of one plane of the tracking detector. The design assumes 5mm diameter conducting straws, composed of a double layer of over-woven straws composed of metalized Kapton with $\sim 12 \mu\text{m}$ thickness per layer. The glue thickness between the wound Kapton layers is approximately $3 \mu\text{m}$. The construction of the straw is illustrated in figure 6.23. Thinner walled straws are possible, however gas leakage may become significant. Gas leakage for Cu and Al coated Kapton, and Al coated Mylar straws with walls $25 \mu\text{m}$ thick has been measured, and is approximately the same. However, outgas rates from, and radiation damage on, Al coated Mylar straws are significantly larger. For this reason we propose to use $25 \mu\text{m}$ thick Kapton straws metalized by 5000 \AA Cu.

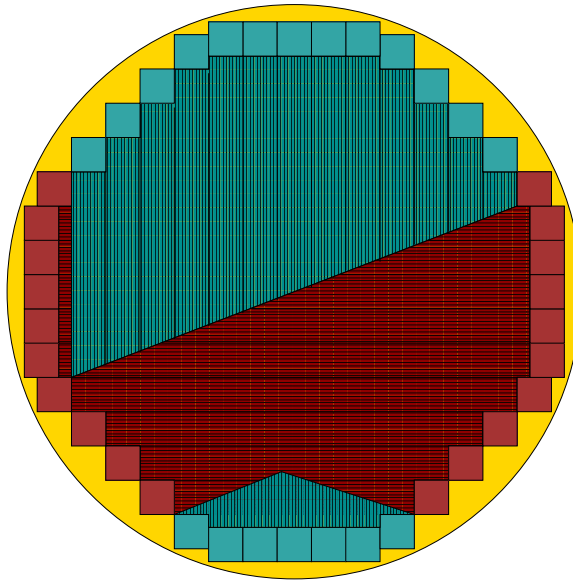


Figure 6.22: A layout of a tracking detector plane. The figure shows straw units of 16 mounted on the front and back of a mounting ring. The manifolds that holds, tensions, and allows the insertion and extraction of gas, HV and signal cables are also shown

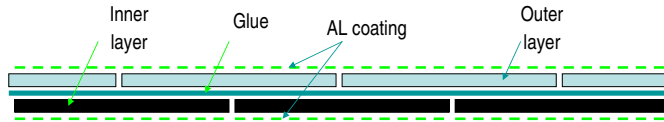


Figure 6.23: A schematic showing the cross section of the wall of a straw. It is constructed by over winding and glueing together two $12\mu\text{m}$ layers of metalized kapton

The straws range in length from 68 to 112 cm. They are mounted on aluminum supports in the shape of rings, with inner and outer radii of 55 and 67cm respectively. There is 3cm between the outer radius of the ring and the radius of the inner wall of the spectrometer cryostat. One x and one y array are mounted on either side of the ring, forming an (x,y) double-array. Another ring with a double-array of straws is then attached, but with the measurement coordinates rotated by 45 degrees; x to x' and y to y' . Gas manifolds, electrical connections, and local readout electronics are also attached to the ring. The gap between the rings is approximately 6cm, providing space to mount the readout electronics. Thus total thickness of a detector plane is ~ 9 cm. Finally, each of the 5 planes and the trigger detector are properly spaced, and rigidly attached to a frame which is designed to slide on linear bearings into the detector solenoid. This allows access to the detector, albeit with the detector vacuum enclosure opened and the detector package extracted from the solenoid.

The support ring of a straw plane is constructed of two layers of $\frac{1}{4}$ inch Al tooling plate, cut in the shape of a ring. The rings, in overlapping arcs, are bonded together by bolts and pins, or are welded together. The ring has an outer diameter of 134cm. The inner diameter is notched so that the active area of the straw does not extend over the Al ring in order to reduce the number of Compton scattered electrons entering the active region of the straws,

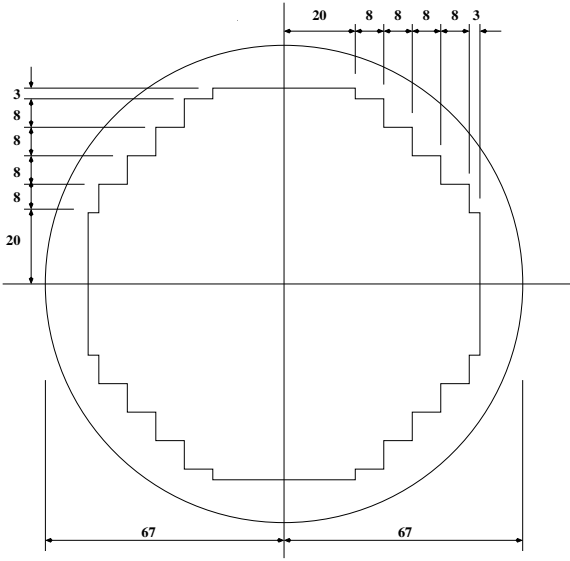


Figure 6.24: The mounting frame for 2 straw arrays, one in front and one behind the ring. The inner diameter of the ring is notched so that the number Compton scattered electrons entering the active area of the straws is reduced.

Figure 6.24. The two rings contain the straw arrays are spaced 6cm apart.

Individual straws are bonded together in units of 16 on an alignment fixture, using a thin layer of casting epoxy [90]. This epoxy easily wicks between the straws, and undergoes minimal shrinkage when set. Feedthroughs are inserted into the ends of straw and the feedthrough is then inserted into a tensioning/gas-manifold. The diameter of the feedthrough end that is inserted into the manifold is less than the straw diameter so that straw units when mounted together form a gap-less array of straws. Gas flows into and out of the manifold through the feedthroughs. The manifold, Figure 6.25 is gas sealed with casting and conducting epoxy, and electrically grounds the straw surface. The straws in each manifold unit are tensioned at approximately 80 g/straw to reduce expansion and sag under gravity. Each tensioned unit is then transferred from a holding fixture to the detector frame ring, and the procedure repeated. Each manifold may be attached to the ring with a spring system in order to keep constant tension on the straws and wires as the straws expand in vacuum. A finished straw array is composed of 13 hexadecimal straw units, on both sides of a ring. Once mounted on the ring, anode wires are strung inside each straw, tensioned, and clamped inside a feedthrough.

Wires are held at high voltage and the conducting straw wall is grounded. One high voltage channel is distributed to the 416 (2×208) wires of each array. The high voltage for each unit of 16 straws in a manifold has a filter capacitor, 8200 pf, to ground and passes through a bias resistor of $100 \text{ k}\Omega$ to each wire. The signal is extracted through a blocking capacitor of 180 pf. Each wire is fused with a 65ma slow-blow fuse to remove broken wires which short to ground. In the event that a short to ground occurs on a wire, the polarity of the HV is reversed and the normally back-biased diode across the bias resistor allows sufficient current to flow around the resistor and through the fuse to open the HV connection. The HV input and signal output from a manifold is constructed on a flex, flat cable on which the components are surface mounted, Figure 6.26. This cable extends from

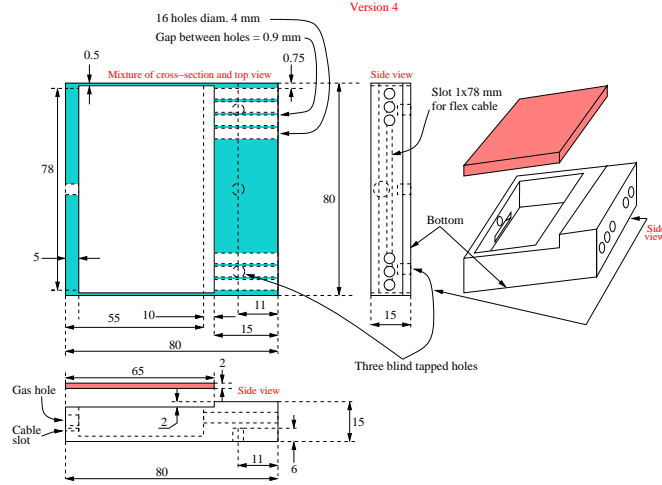


Figure 6.25: A manifold design that feeds and extracts drift gas, provides high voltage, extracts signals, and tensions a unit of 16 straws

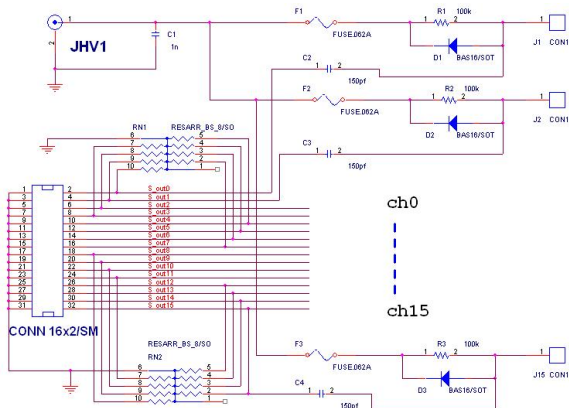


Figure 6.26: The circuit design for the flex cable that connects the electronic readout to the straw anodes through the manifold. The cable provides the HV as well as fusing each channel to remove shorted wires

the preamplifiers outside the gas volume, through a gas seal into the manifold where the HV distribution occurs. There is one HV input line per flex cable, and this line, encapsulated within the Kapton of the flex cable, is insulated against HV discharge/breakdown.

Each plane consisting of the two double-arrays is constructed as a stand-alone unit. These units are then mounted on the detector frame which positions and aligns the planes with respect to each other and the trigger counter. The frame is inserted and removed from the detector solenoid on rails and linear bearings for access and maintenance. A spare plane will be constructed so that it can be swapped, when needed, with a malfunctioning one, decreasing downtime for detector repairs.

The description and placement of the readout electronics are discussed below.

6.5.6.1 Anode wire and wire supports

The sense wire is chosen to be Au coated W containing 3% Re. This wire has excellent properties with respect to creep. The measured creep in a 180 cm, standard W wire is shown as a function of time in Figure 6.27. The problem of creep can be lessened by using good quality wire, smaller tensions, and pre-stressing the wires.

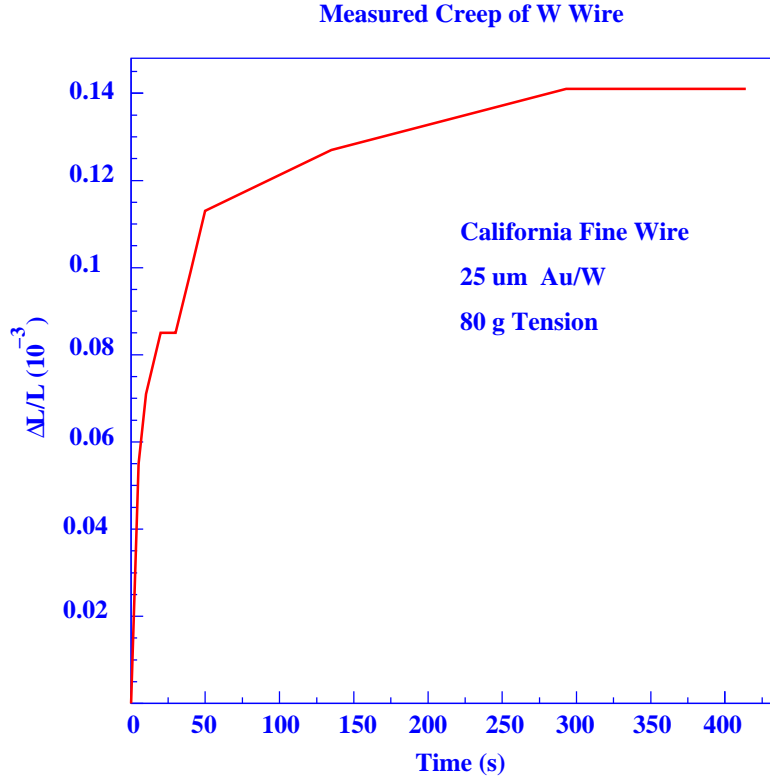


Figure 6.27: The figure shows creep of a standard 25 μm W wire as a function of time

The capacitance per unit length of the anode wires is obtained from the equation.

$$C_l = \frac{2\pi\epsilon_0}{\ln(s/a)} \quad (6.8)$$

Here s is the radius of the straw (2.5mm) and a is the radius of the wire. Table 6.4 gives some parameters of relevance to anode wires of various diameter. In this Table, the equation used to calculate the maximum tension for stable operation does not exactly apply to the case of a straw chamber [see however [91]].

The sense wires are held at high voltage and although this requires a blocking capacitor on each readout channel, maintaining the wires at voltage prevents large current discharge through a wire if a spark occurs since the entire charge stored in the cathode capacitance would then flow through the spark. Note that all the straws are electrically connected to provide cathode ground.

So long as the straws remain stable, we do not expect to require support for the anode wires. Wire stability can be estimated using the following equation derived from the electrostatic force on a non-central anode wire [91].

$$L_c = \pi R(CV)[2\pi\epsilon_0 T]^{1/2} \quad (6.9)$$

Table 6.4: Some Parameters of Relevance for Straws Detectors having Different Anode Wire Diameters

Parameter	Wire Diameter		
	20 μm	25 μm	32.5 μm
Capacitance/length (pf)	10.07	10.49	11.06
Voltage Scaling for Same Charge Gain	0.96	1	1.05
Max Operating Voltage (kV)	1.9	2.0	2.1
Elastic Limit (g)	51	80	135
Max Length for Elastic Limit Tension (m)	0.97	1.1	1.3

Table 6.5: Anode length limits for the tracker

Parameter	Value
Straw radius	$2.5 \times 10^{-3} \text{ m}$
Anode wire radius	$12.5 \times 10^{-6} \text{ m}$
Capacitance/length	$10.5 \times 10^{-12} \text{ f/m}$
Tension	380 0.79 (80 g)
Voltage (Max)	2200 V
Critical Length	1.98 m

with T the tension of the wire, V the voltage, C the capacitance per unit length, L_c the critical wire length for a given tension, and R the straw radius. The wires should be tensioned at about 80 g. Appropriate parameters for straw operation are given in table 6.5. The operational voltage is nominally 1.8 kVA. The straws themselves will be tensioned with approximately 80g.

6.5.6.2 Drift gas

Gas gain as a function of wire diameter and applied voltage is shown in figure 6.28, and the number of ion pairs for various gases is given in Table 6.3. Gas gains are for a gas mixture of 57 % Ar and 43 % C_2H_6 with a planar drift cell geometry of 0.5cm sense wire to field wire. Other gases have different gains.

The drift velocity of various gas mixtures is given in Table 6.6. The radial drift will decrease due to the magnetic field, but in the case of the Ar/ C_2H_6 mixture only about 15%. We intend to use a fast drift gas such as 80% CF4 with 20% isobutane [92]. In addition, we plan to limit the gas gain to approximately 5×10^4 . Although this will also limit the spatial resolution of hits, the requirements of $\Delta x = 200 \mu\text{m}$ are easily obtained. Magnetic fields up to 2 T in CF4/isobutane have been studied [88] in the laboratory. At 1 T, the Lorenz angle is ≈ 45 deg at 1 keV/cm and ≈ 20 deg at 4 keV/cm. The drift velocity in the drift direction varies from $70 \mu\text{m/ns}$ at 1 keV/cm to $120 \mu\text{m/ns}$ at 4 keV/cm. The magnetic field in the detector region is constant (1T) along the axis of the solenoid but

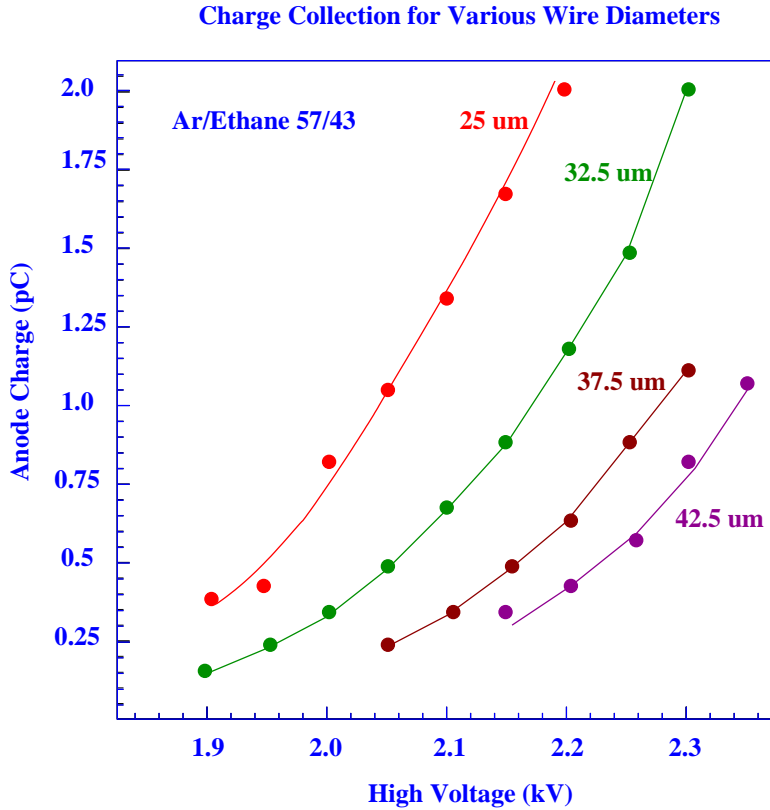


Figure 6.28: The figure shows the gas gain as a function of the sense wire diameter and the applied voltage. The gas used for this measurement is a mixture of 57 % Ar and 43 % C_2H_6 . The measurement used a 5mm radius drift cell.

the E field varies as a function of radial distance r . We expect the drift velocity along the radial direction to be $50 \mu\text{m}/\text{ns}$ at $1 \text{ keV}/\text{cm}$ and $110 \mu\text{m}/\text{ns}$ at $4 \text{ keV}/\text{cm}$.

6.5.6.3 Deformation of straw tubes

Deformation of the straws when loaded by gas pressure and wire tension has been investigated. If treated as a cylinder, the internal gas pressure results in an outward force of 1.9 N per straw, and this exceeds the expected wire tension of 0.78 N (80g). At issue is the extent to which the straw deforms due to this loading. It is noted that long straws are generally placed under an outward tension of about 0.78 N in order to align them before wiring [93]. We tested the fractional stretch of a mylar straw by increasing the pressure in a sealed straw with one end fixed and the other free. The typical fractional change in length is 0.04% (for one atmosphere overpressure). In addition a straw changes dimensions as a function of humidity. The CKM collaboration found that straws of approximately 5mm diameter experienced dimensional changes [94] as given in Table 6.7. is the relative humidity. One notes that the expansion due to atmospheric pressure is only about 40% of the expansion that occurs for an externally applied force of the same magnitude. We observe similar expansions in our measurements. In addition we have observed creep on the order of $\Delta L/L \approx 1.6 \times 10^{-4}$ over the period of 7 days for various tensions, and as a wound straw expands in length it also tends to exert a twisting torque on the end clamp.

Table 6.6: Drift times of various gas mixtures at a nominal operational voltage. The drift distance is calculated for a 0.5 cm diameter straw in the absence of a magnetic field

Gas	Velocity (cm/ μ s)	Drift Time(ns)
Ar/C_2H_6	4.8	52
Ar/CO_2	4.8	52
Ar/CH_4	3.4	74
$Ar/CO_2/CH_4$	4.9	51
Ar/C_4H_{10}	6.1	41
Ar/CF_4	9.5	26
CF_4	8.5	30
CF_4/CH_4	12.	21
$Ar/CH_4/C_4H_{10}$	7.1	35

Table 6.7: Linear expansion data measured for a Kapton straw of 1m length and 5.1 mm in diameter

Parameter	Value
Linear Expansion Coefficient	5.1 μ m/g
Linear Thermal Expansion	9.9 μ m/F°
Linear Humidity Expansion	12.0 μ m/%RH
Linear Pressure Expansion (15 Psi)	380 μ m
Radial Expansion (15 Psi)	6.7 μ m

In order to stabilize the mechanical properties of the straws, we may attach thin carbon wires, lengthwise along the straw surface.

6.5.7 Straw operation in vacuum

The leak rate of various straws which could be used have been tested in vacuum [95]. Tests used straws of two layers of Kapton having several thicknesses, and spiral wound with a half strip overlap. The layers have 5000 Angstroms of copper deposited on the outer walls. Leak rates of both the bulk straw material and the end fittings were tested by measuring the rate of rise of the pressure in an evacuated tube containing sample straws with one atmosphere pressure. The rise of the chamber pressure was measured as a function of time after pumping ceased on the tube. The rise decreased with the prior pumping time, indicating a residual background due to outgassing. The residual rise for a nominal straw after 5 days of pumping corresponded to a leak rate of $\approx 2 \times 10^{-8}$ l/min/m for the bulk straw, and a leak rate of $\approx 3 \times 10^{-9}$ l/min per end. These leak rates, when scaled to the full spectrometer, are well within modest pumping rates. Furthermore, straw tubes have been operated in vacuum in a previous experiments [96].

6.5.8 Readout electronics

6.5.8.1 DAQ architecture

In order to develop a readout architecture, one must make a fundamental choice about the position of the front-end electronics. Obviously placing the electronics in an accessible region outside the detector vacuum chamber provides the most flexibility as it allows manual adjustments, replacements, etc., without breaking the detector vacuum and removing the detector from the solenoid. Additionally, placing the electronics within the detector volume exposes these components to radiation damage and enhances the problem of heat dissipation.

On the other hand, placing most of the electronics some distance away from the detector comes with significant disadvantages, as for example, the substantial cable volume, expense, and sending approximately 4000 signals over 10 m of cable through a vacuum wall with its inherent increased noise and signal degradation. For example with respect to cable volume, if signals are transmitted from preamps through the vacuum wall, then a set of ribbon coaxial cables about 5 cm thick surrounding the entire circumference of the detector would be required. Of course, all electronics must be positioned, in-so-far as possible beyond the turning radius of electrons of interest, but mounting them on the detector supports may require active cooling and somewhat complicates the mechanical structure.

We choose here to discuss a tracker readout system designed to take advantage of modern electronic design using distributed signal processing [97]. All signals are digitized at the front end, and stored in digital pipelines for trigger latency. Once a trigger is presented, only those channels having signals above a set threshold are read, stored in buffers, and then serially transferred to a data acquisition system outside the vacuum wall. At this point the events are rebuilt, analyzed, filtered, and finally committed to permanent storage.

Suppose an electron track generates 60 electron-ion pairs. We propose to use a gas gain of 5×10^4 so the analog signal presented to the anode preamplifier will be 480 fC. We can assume that 10% of this charge is collected within the 6 ns which will be required for the signal to reach its peak. We should then set the discriminator threshold at approximately 16 fC or 2 primary electrons expecting a noise level of 1-2 fC. The total capacitance of the

straw is 30 pF and the characteristic impedance is $317\ \Omega$. Thus, we use a 200 series resistor coupled to a 100 transimpedance preamplifier. We expect the discriminator to have 2-3 ns timing resolution.

The electronics read the anode wires of the detector. In general, the number of readout channels is large (> 4000), power consumption must be severely restricted, and cabling and the electronic footprint are constrained by space limitations. Therefore the readout architecture will take advantage of modern integrated circuit technology, placing a multi-channel IC at the front end of the detector to read, digitize, and buffer the signal. The advantages of a fully digitized, pipelined, dead-timeless front-end, have been implemented in several modern data acquisition, DAQ, systems. From particle flux calculations, including neutron fluence, we expect that “rad-hard” production processes will not be necessary. Thus COMET can use standard CMOS technology.

Because of space limitations we assume a preamplifier placed on the detector plane near the anode wires and cathode strips. These preamplifiers then feed an amplifier/discriminator placed on a digitizing board controlled through a local bus by a readout controller.

6.5.8.2 Front end ICs

Prototypes previously studied for the MECO experiment used an amplifier-shaper-discriminator (ASD) chip, which was designed for the Atlas thin gap chamber [98]. The threshold could be set remotely by computer and it had both timing and analog outputs, and it has 4 independent channels. However, this ASD must be replaced because it is too old to be reproduced in modern foundries, but more modern, lower power consuming preamps are available. Thus we intend to investigate newer amplifier ASICs that have the performance features which meet our needs. For example the ASICs described in [99, 100] have at least some features that we require. If a suitable ASD is not available we propose to develop an Amplifier Shaper Discriminator (ASD) that will meet the requirements of the tracker and perhaps the calorimeter (APD readout) as well. The ASD should have analog (linear) outputs as well as digital (discriminated) outputs. A calibration feature is needed to inject signals of a known size to individual channels. Finally, the power dissipation should be less than about 50mW per channel, and preferably ≤ 35 mW per channel, as these ICs will be used in vacuum. The ASD should have 4-8 channels per package.

The preamp must be able to handle bipolar input signals since the anode wires provide negative pulses and the APDs will provide positive pulses. To some extent any amplifier will amplify signals of either polarity, however usually one polarity is favored as it will have a larger linear dynamic range. We expect a front end capacitance of some 20 pf, which includes the anode wire and readout cable, and a signal amplitude of 2-60 fC.

Furthermore, to optimize noise vs speed trade-off and perhaps the APD readout of the electron calorimeter, it may be desirable to adjust the bias of the input transistor. Therefore it is desirable for the preamplifier to incorporate a means of adjusting the input impedance or the biasing of the input transistor. This technique has been used in the amplifier ASIC of the BaBar drift chamber [101].

The equivalent noise charge should be less than 0.5fC (3000e) in both the tracker applications as well as its potential application in the APD calorimeter readout. Achieving this will depend somewhat on the shaping or filtering employed in the entire processing chain. To maintain maximal flexibility only bandwidth-limiting filtering will be required, e.g. 10ns peaking time for a delta-fn input, in the ASD. Other shaping can occur in subsequent circuitry. For example the ion-tail-cancellation for tracker signals can be performed

on the digitized waveform data. This digitally filtered waveform could then be used off-line to correct the timing of the digital output if necessary. Similarly the rise-time of the amplified APD signals can be stretched by a linear circuit preceding its digitizer.

Each channel of the ASD should have a linear output to drive subsequent circuitry. The tracker electronics will have the ASD and waveform digitizer either on the same PC board or separated by a short flex cable. The linear output should be a differential "current-steering" type (LVDS) to avoid ground bounce and other common-mode noise/instabilities. Each channel should also have a discriminated (digital-LVDS) output with duration corresponding to time-over-threshold, perhaps modified by hysteresis. The threshold should be applicable either chip-wide or on a channel-by-channel basis. In the former case AC coupling with a baseline restorer to reduce threshold dispersion might be needed. However the response of a baseline restorer to over-range signals (i.e. possible overshoot) must be thoroughly investigated before we adopt that approach.

All components would be mounted directly on the support structure of the tracker and perhaps actively cooled by chilled coolant owing through pipes attached to this structure. The 4 preamplifier ICs in units of 8 channels each are mounted onto a daughter board that connects with 4 digitizing ICs (8 channels each) channels to compose a building block. This board covers 16 cm of readout (32 channels of either straws or strips). The 4 building blocks are mounted on a mother board which contains the local buffers and local readout control.

6.5.8.3 Digitizer

Most of the power in any readout system is expended on bus interfaces and impedance matching connections. These factors can be deleted or reduced in a front-end application specific, ASICs. For example, an analysis of power consumption indicates that to drive an AT signal out of the detector vacuum enclosure requires at least 150mW/channel, and in addition, has the difficulty of making tens of thousands of vacuum feed-through connections. An A/D ASIC consumes ~ 30 mW /channel, and can have only ten or twenty readout cables. An example of an older design is the Electronic Front-end Amplitude aNd Timing, ASIC, (Elefant) used in the BABAR experiment at the Stanford Linear Accelerator [102]. It has 8, parallel channels of flash ADC and 8 channels of delay lock loop (DLL) TDC, and a latency buffer to temporarily store the digitized data and send selected events to an event buffer at the presentation of the first level trigger, L1. The L1 trigger is the external physics trigger that initiates the readout sequence, and occurs at some time latency after the detector signals are stored. The chip can handle high single rates, and has low power (250mW/ 8-channel). However, Elefant was designed 7 years ago [9], and although successfully used for drift chamber readout, was fabricated in a $0.8\mu\text{m}$, 3-metal, 2-poly, CMOS process that is obsolete. In addition its 5V I/O is difficult to interface to modern FPGA designs, and its clock speed is insufficient. An upgrade of Elefant was completed for MECO before this experiment was terminated, and while it offers an example of what could be done we propose to now review the suitability of several newer designs with the possibility of making modifications to them as needed.

To illustrate a possible design architecture the block diagram of for the upgraded Elefant prototype architecture is shown in Figure 6.29. All function blocks are built around the latency buffer, which temporarily stores the signal information before the trigger decision is made. The latency time is equal to the depth of the buffer times the clock cycle. This must be more than the time delay to make the trigger decision.

The A to D block processes 8 data channels in parallel, and the ADC and TDC encodes

with 10 bit accuracy. Since the latency buffer alternatively stores the ADC and TDC data, two characteristic bits are used. The prototype design has a 64 bit bus-width. Two dual port SRAMs, (SRAM1 for data storage as an event buffer and SRAM2 for time stamp and hit map storage) are fed by the latency buffer. Upon an L1 trigger, a pre-defined record length (8, 16, or 32 of data words each containing 64-88 bits) are moved from the latency buffer into SRAM1, and a corresponding time stamp is stored into SRAM2. When the data are moved, an 8 bit hit-map is formed, in which a bit is set when at least one TDC hit is recorded in the corresponding channel. The data in these SRAMs are then sequentially moved to the next buffer level under control of a FPGA, which uses the hit-map for zero suppression. A unique component is the hit map, which provides hit occupancy for use in the generation of the event trigger. An external trigger logic circuit could then select appropriate data to be read from the latency buffer. In the low occupancy situation, the system can be self-triggered where all hits can be read into the local bus. In high occupancy situations an external trigger can be constructed by coincidence with additional information so that only a filtered set of events are recorded, thus increasing the bandwidth for this subclass of events.

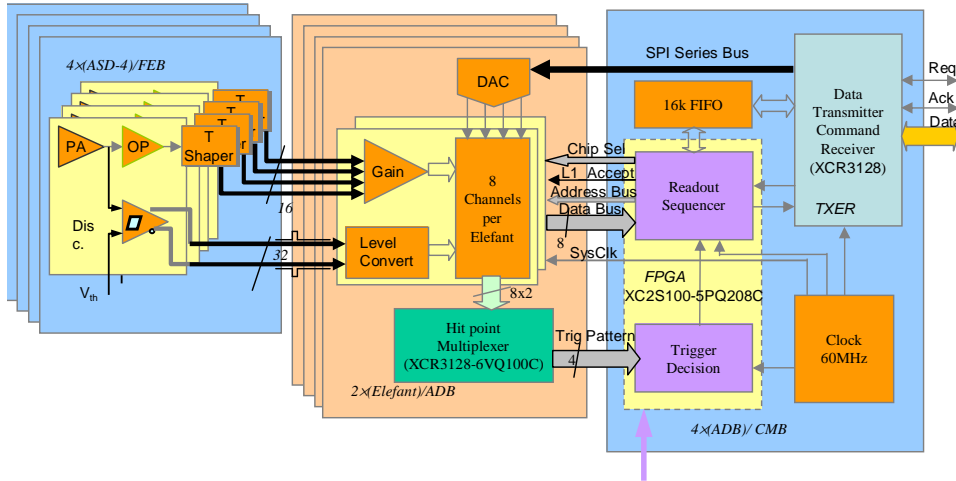


Figure 6.29: A block diagram of the front end architecture for the readout electronics. The figure shows the preamplifier board (ASD), the Elefant digitizer board, and the readout controller.

6.5.8.4 Tracker readout

The COMET electronic system consists of four major components: 1) the tracking detector, 2) the calorimeter front-end, 3) the trigger, and 4) the data acquisition processors. We discuss only the tracking detector in this section. However, note that the calorimeter generates an analog signal proportional to the energy deposited by the energy of an electron after it penetrates the tracker. If this energy lies within a window about 105 MeV a readout of the tracker and cosmic veto is triggered.

As an example of a proposed architecture, signals from the tracker anodes wires are cabled through a preamplifier to shaping amplifiers on the front-end/digitizing, FEB, boards. The FEB process 32 channels/board and contains a four 8 channel digitizing ASICs which

provides a digitized timing output (16 bits) and a digitized waveform containing 15 time slices each containing 16 bits (total of 16 x 16 bits) for each channel. This information is pipelined for latency, gated, readout is zero suppressed, buffered, labeled with a trigger stamp, and transmitted on command to a higher processing level. Each FEB is connected via a backplane to a readout controller, ROC, whose FPGA memory and commands can be programmed interactively. A ROC controls approximately 6.5 FEB and there are 33 ROC in the detector. Each ROC is connected through a local bus (16 bits) to a readout sequencer. Each sequencer controls 4 ROC and uploads data and downloads communication via a serial bus link. There are 18 sequencers which then transmit data and information serially on parallel lines via an optical link through the vacuum wall to a memory in an external memory/processor. All modules are in a shielded enclosure. Data transfer rates of a few hundred Mb/s are possible.

6.5.8.5 Data rates

Data rates are based on the expected single hit structure and background rates in the tracker. If the background rate is 0.6×10^6 per plane as per Table 6.10 and the trigger gate is 167 ns (for an assumed ASIC clock of 60 MHz and readout of 10 clock ticks of the pipeline), then the probability of a plane hit is ~ 0.1 on average. However, most of these are due to DIO or backscattered electrons which penetrate the detector and calorimeter so they should not be included as accidentals as they penetrate the detector entering the calorimeter, unless of course they are incorporated into a triggered event. Photons create local ionization and thus accidentals and we assume from the table ~ 200 kHz of accidental events. This would produce on average about 340 wire hits to be combined with a hit in all 4 arrays of 5 planes of 20 hits that causes a trigger. Assuming a hit multiplicity average of 1.5 this gives $(1.5 \times (20 + 340))$ 540 wires to read per trigger. There are 20 words/trigger and 2 bytes bits/word which results in 173 kbytes/trigger. For 1000 triggers/s the data to be transferred is 173 Mb/s to be transferred over transferred serially over 16 optical lines. A schematic representation of the placement of the readout electronics is shown in Figure 6.30

6.5.8.6 Signal bus lines

The total number of optical serial transfer lines would be (16 data + 6 control) 24. Although the data transfer is designed to be serial, it could be parallel transfer, 16 bits wide. There are additional signals which must be sent to the tracker from the DAQ. These include;

1. a system clock which will be regenerated by the local bus sequencer,
2. a trigger input which could be associated with a readout quadrant of wires,
3. a sync (trigger reset) counter that determines the time stamp placed on the data,
4. a system reset to return the readout to a standard operating condition,
5. a slow control bus that sends control signals and environmental monitor information, and
6. low voltage power of +3.3V (300A) and -3.3V (100A).

6.5.8.7 Cable and connections

Designs for vacuum feedthrough for multi-cable connections can be copied from other detector designs. If we choose to use fiber optic links for data transfer, standard systems are

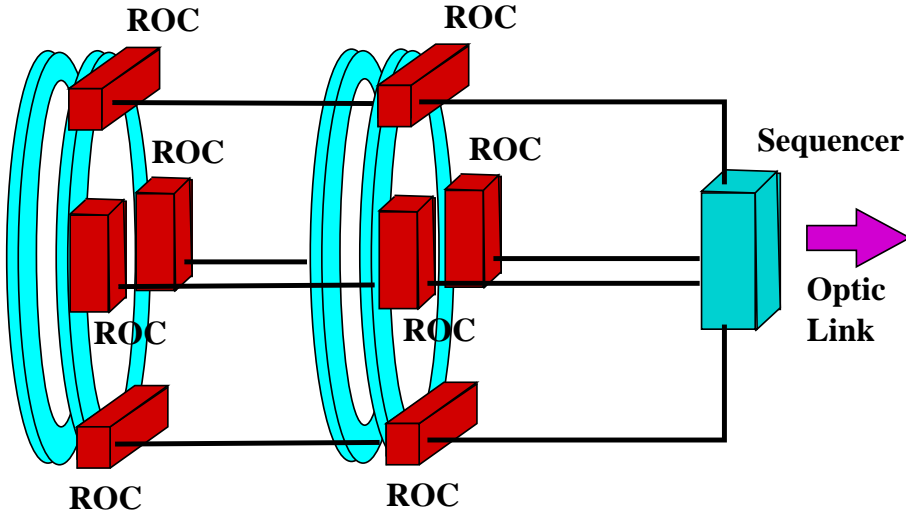


Figure 6.30: The figure shows a schematic view of the placement of the readout electronics for the T-Tracker. The ROC are connected by a local bus to a sequencer at the downstream of the detector vacuum enclosure, which sends data serially out of the vacuum to the data acquisition system and communicates with the DAC by fast and slow controls. Only two of the five tracker planes are shown in the figure. The calorimeter has a similar readout architecture.

installed at ATLAS, CMS, BABAR, and ALICE. We choose to use an optic link to reduce system noise, but copper is also possible. Internal cables must be shielded and treated as transmission lines, and the design keeps all cables, including PCB lands as short as possible.

6.5.8.8 Mounting and servicing

Maintenance of the electronics must be reduced to minimum, as once installed in the vacuum it will not be easy to access the system. Therefore the design must be:

- robust and have adequate operational margins for thresholds, noise limits, and power;
- remotely controlled and have adequate diagnostic information supplied to an operator;
- redundant and sufficiently flexible that channels can be remotely removed without significantly impairing operations.

6.5.8.9 Transmitted data structure

The data structure is to be transmitted to the DAQ processor in the following sequence.

1. Begin Transfer header 1 16bit word
2. Buss number, Status
 - (a) Header 2 16bit words
 - (b) Trigger/time, ROC number, and status

- (c) Data 17 16bit words/channel
 - (d) Channel number, length 1 16bit word
 - (e) TDC - 1 16bit word
 - (f) Wave form - 15 16bit word
 - (g) Repeat Above for All ROC Controlled by a ROC
3. ROC number buss number 1 16bit word
 4. Sequence through all ROCs
 5. EOF

The local memory buffers are flushed into remote memory buffers placed in VME crates outside the detector solenoid. Each event is then reconstructed by assigning one processor in a farm to a particular trigger ID. This event is filtered by this processor for reconstructability and probability that it could be an event of interest. The filtered data set is then committed to permanent storage for off-line analysis. Sufficient data is stored, however, to allow a proper background analysis.

6.5.8.10 Low voltage cower and cooling

In a similar readout system (BaBar), the front end electronics expended 5-6 kW of low voltage power. It is possible that if the ICs are redesigned using more modern technology the power could be reduced. However 5-6 kw is not large and can be easily removed. If required, we proposed to use chilled coolant to maintain a reasonable and static temperature for the readout electronics.

Low voltage power will be separated into units supplying digital and front end analog ICs. Each board will use its own low-ripple regulator to provide its DC voltage. This arrangement reduces ground loop currents and isolates digital noise. Switching power supplies can be used for the digital ICs. The preamplifiers will use linear regulators to further reduce the power noise level down to less than 1 mVPP. We will evaluate the use of ferrite-core inductances in any power supplies in the cryostat.

6.5.8.11 High voltage

Separate High voltage will be individually supplied to each array of each plane (5 planes x 4 arrays). The HV lines enter the downstream gas manifold and are split to supply the 208 channels of straw anodes. Each channel must be fused in order to allow that channel to be removed in case of a malfunction. We envision this process occurring by passing a high current through the fused panel disabling a selected channel. Readout of a channel must occur through a HV blocking capacitor. All these components are within the gas volume contained within the manifold. The gas is held at atmospheric pressure so HV discharge should not present a problem.

We anticipate operational HV of the anode wires at about 2000 V to obtain a gas gain of 5×10^4 . HV will be supplied by commercial units which are computer controlled and monitored.

6.6 Electron calorimeter

6.6.1 Overview

The electron calorimeter is positioned downstream of the tracking detector and serves three purposes:

1. to measure the energy of electrons, where good energy resolution is necessary to produce an efficient trigger and add redundancy to the energy measurement.
2. to provide a timing signal, i.e. a trigger, with respect to which the electron events are referenced.
3. to provide additional position information on the electron track trajectory correlating the measured energy with the track.

Independent and redundant measurements of the energy and momentum of electrons are of critical importance to separate true muon-to-electron conversion from reconstructed tracks that conspire to mimic a signal. Although the likelihood of a combination of lower energy electrons being mistaken for a 105 MeV electron track is small, it must be remembered that the number of low energy electrons between 85 to 95 MeV is a factor of more than a thousand larger than for electrons above 95 MeV. A calorimeter constructed of segmented scintillating crystals can have an energy resolution of better than 5% and an energy-correlated position coordinate accuracy of about 1 cm (rms). Finally, the event topology, given good crystal granularity, helps discriminates between electrons, neutrons and low energy gammas. The crystals need good light yields, fast time response, and fast decay time to reduce pile-up.

6.6.2 Crystal selection

Table 6.8 compares various scintillating crystals, which have a large light yield and a small decay constant. GSO(Ce) and LYSO are attractive crystals in view of their performance. Newly developed inorganic crystals, such as LaBr(Ce) and LGSO, would also result in good performance. We need further studies on their fundamental characteristics which would affect the performance of the calorimeter. The choice of crystal type depends on not only its performance, but also cost of the crystal. Here, we describe one of the plans to construct the electron calorimeter with cerium doped Gd_2SiO_5 (GSO) crystals with dimensions of $3 \times 3 \times 15 \text{ cm}^3$.

Table 6.8: The characteristics of inorganic scintillator crystals.

	GSO(Ce)	LYSO	PWO	CsI(pure)
Density (g/cm ³)	6.71	7.40	8.3	4.51
Radiation length (cm)	1.38	1.14	0.89	1.86
Moliere radius (cm)	2.23	2.07	2.00	3.57
Decay constant (ns)	$600^s, 56^f$	40	$30^s, 10^f$	$35^s, 6^f$
Wave length (nm)	430	420	$425^s, 420^f$	$420^s, 310^f$
Refraction index	1.85	1.82	2.20	1.95
Light yield (NaI(Tl)=100)	$3^s, 30^f$	83	$0.083^s, 0.29^f$	$3.6^s, 1.1^f$

Segmentation is necessary to reduce pile-up and provide position information. The calorimeter will consist of GSO cells which have a $3 \times 3 \text{ cm}^2$ cross-section and are 11 radiation lengths long (about 15 cm for GSO). If the calorimeter covers the full cross-section of the detector region ($55^2\pi = 9053 \text{ cm}^2$), then we will use 1056 crystals which is also a hexadecimal unit compatible with the readout architecture (16×66). From Table 6.10, the total rate in the calorimeter is 9670 kHz which is 92 kHz per crystal if the shower hit multiplicity is 10.

6.6.3 Photon detector

Operation of the calorimeter readout in a 1 T field essentially precludes the use of high-gain, low-noise phototubes. In order to circumvent this problem, we have two candidates of the photon detector for the readout: Avalanche photodiodes (APD) and Multi Pixel Photon Counters (MPPC).

6.6.3.1 Avalanche photodiode

High quantum efficiency photodiodes can be used for the crystal readout, although these have the disadvantage of greater electronic noise due to the thermal noise of the input field-effect transistor. This noise is not easily integrated out of the signal, due to the short shaping times that are required. However the development of large area photodiodes, with large depletion depths which reduce the parallel capacitance, has improved the signal-to-noise ratio. Avalanche photodiodes (APD), with typical gains of 500-1000, are now generally available [103]. MECO was able to achieve an energy spectrum with a full width at half maximum of 4 MeV with a low energy tail from energy leakage. Generally, resolution can be represented by the following form.

$$\sigma_E(E) = A + B\sqrt{E} + CE \quad (6.10)$$

The first term is the contribution from electronic noise. The second is due to photon statistics, and the third term which is proportional to the energy, includes errors in calibration, non-uniform light collection, energy leakage, and temperature and gain drifts. Additional terms, dependent on other powers of E are sometimes included as well. The equivalent noise energy is the ratio of the equivalent charge noise (expressed in units of e) to the collected light (in photoelectrons per MeV).

R&D for the MECO calorimeter found that the series noise contribution can be reduced using two APDs. In the MECO CDR it was found that using 2 PIN diodes, the resolution for a BGO crystal and an RC time constant of 300 nsec was 1.3 MeV/crystal, 0.42 MeV, and 1.7 MeV for electronic noise, photostatistics, and shower fluctuations, respectively. Combining these in the above equation and summing in quadrature over the noise from nine crystals (expected shower size) the expected resolution, exclusive of pileup, would be 4.3 MeV. The signal reaches its maximum at 900 nsec. It is anticipated that both the resolution and shaping time can be significantly reduced when using APD's.

Light collection is also an important parameter and must be carefully studied. A smaller area diode has less capacitance and thus less noise, and if the crystal-diode configuration is carefully constructed (*e.g. wrapped or coated crystal*) light that misses the diode can be reflected and collected later. Thus the selection of an optimum diode(s) and crystal preparation requires R&D. The use of a wave shifter is another approach to light collection. The wave shifter re-emits the light from the crystal at a longer wavelength which is in a

more sensitive region of the diode, and concentrates the light into a smaller area, potentially reducing noise through the use of a smaller APD.

6.6.3.2 Multi pixel photon counter

MPPCs are novel photosensors which take the form of multi-pixel devices with each pixel being an APD, biased to be in Geiger mode and with all pixels connected together in parallel. They are able to provide photon-counting with gains on the order of 10^6 as with PMTs, similar or better photodetection efficiencies and response times, and excellent linearity. They are practically immune to adverse effects from magnetic fields, and require bias voltages of less than 100 V. Typical devices have dimensions of one to a few millimetres squared, and pixel counts ranging from a hundred to the tens of thousands.

For photon-counting applications which require good spatial granularity, or which do not need to cover very large areas, MPPCs can often be the perfect detector. The main drawback of MPPCs is their relatively high noise rates which can be in the hundreds of MHz for signals at the level of a few photoelectron equivalents, but if signals can be measured in coincidence across multiple MPPCs, or thresholds can be set above a few PE, this problem can be overcome.

The T2K near detector (ND280) at J-PARC is the first high-energy physics experiment to opt for the large-scale deployment of MPPCs[106]. The experience from the extensive testing that was carried out as the ND280 collaboration studied the properties of MPPCs and their suitability for their experiment will be directly applicable to the needs of COMET.

Unlike MPPCs at ND280, which read out photons on the order of dozens to a few hundred from 1.2 mm diameter light fibres, for the task of reading out the COMET calorimeter crystals, MPPCs with larger sensitive areas and pixel counts will be better suited. Initial studies on the performance of $3 \times 3 \text{ mm}^2$ MPPCs with 14,400 pixels are shown below.

6.6.4 Electronics

Because of APD noise, the signal from the crystals must be integrated over 100-300 ns. The front-end preamp takes the output current, shaping the signal and sends it to a waveform digitizer. An example of a modern waveform ASIC is the DRS3 used to readout the MEG photon calorimeter [104]. Analysis of the waveform permits the removal of pile-up, improving the energy resolution and trigger efficiency.

Full analysis of the waveform is expected to be undertaken offline. To develop a trigger, calorimeter signals will be processed locally by an FPGA that will cut on energy deposited in shower clusters within the calorimeter. At trigger decision must be made within 500 ns in order to extract valid information from the tracker.

In the case of MPPCs, the front end boards for ND280, designed at Imperial College and based around the Trip-t chip, provide a good example of the type of electronics which are appropriate[108]. These are designed to read out the charge and timing signals from each MPPC, in cycles that are synchronised with the J-PARC MR beam bunches. The individual MPPC bias voltages are supplied by the front end electronics boards, and their signals are digitised by FPGAs through two gain channels to cover the full dynamic range of the photosensors. The electronics are designed to allow self-triggering, although in ND280 they will be triggered by the beam signal and the signals from all the MPPCs recorded.

These electronics are already being used in testing for the ND280 detectors, and should be recording real data from the J-PARC beam by the end of 2009. This will allow us to

accumulate a good body of experience on the operation of MPPCs in real-world conditions at J-PARC, which will no doubt be very useful if MPPCs are chosen for the COMET calorimeter.

6.6.5 Performance

Energy resolutions of the calorimeter was studied using Geant4 with Optical Photon Processes. The resolution depends on crystal, light guide, photon detector, and their geometrical configuration. In this section, we discuss dependence of the resolution on the crystals under a possible configuration of the calorimeter. This selection would be a cost effective case for the photon detector, since the ratio of active area of the photon detector to the cross section of the crystal is set to 0.09.

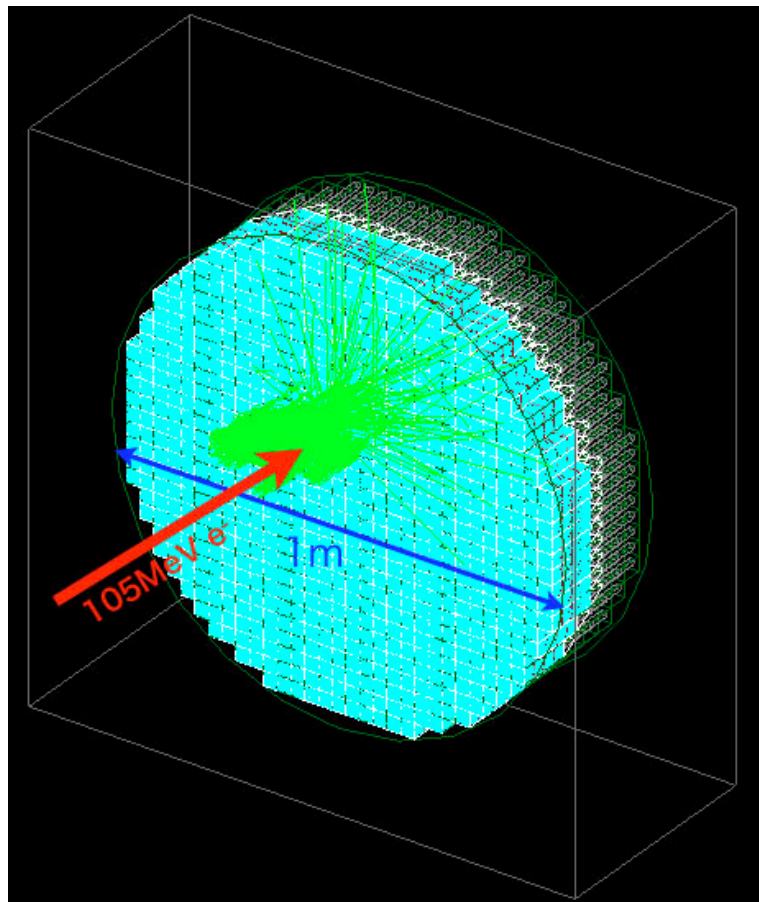


Figure 6.31: A typical event display of the simulation study of the calorimeter. An electron injected to the calorimeter, then optical photons from scintillation processes are ray-traced to the photon detectors.

Figure 6.31 shows a typical event display of this simulation. The calorimeter is a cylinder 1 m in diameter, and consists of 7850 rectangular segments. Figure 6.32 illustrates a segment of the calorimeter. It consists of a crystal, a light guide, and a photon detector. GSO(Ce), LYSO, PWO were studied in this simulation. The crystal has size of $10 \times 10 \times L$ mm, here L is the length of the crystal, 120 mm for GSO(Ce) and LYSO, and 100 mm for PWO. The material of the light guide is set to acrylic resin with a refractive index of 1.49. The

size of the photon detector is $3 \times 3 \text{ mm}^2$, which corresponds the maximum size of MPPC, S10362-33 series of Hamamatsu Co., commercially available at the present moment. The light guide is connected using optical cement with a reflective index of 1.46. The crystal and light guide is wrapped by a Teflon sheet to collect photons effectively.

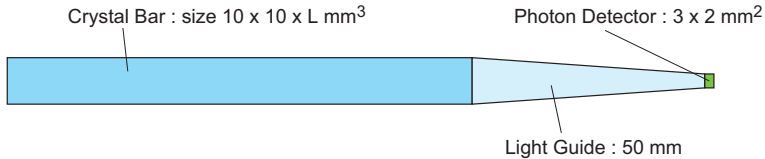


Figure 6.32: A schematic view of a segment of the calorimeter used in the simulation study.

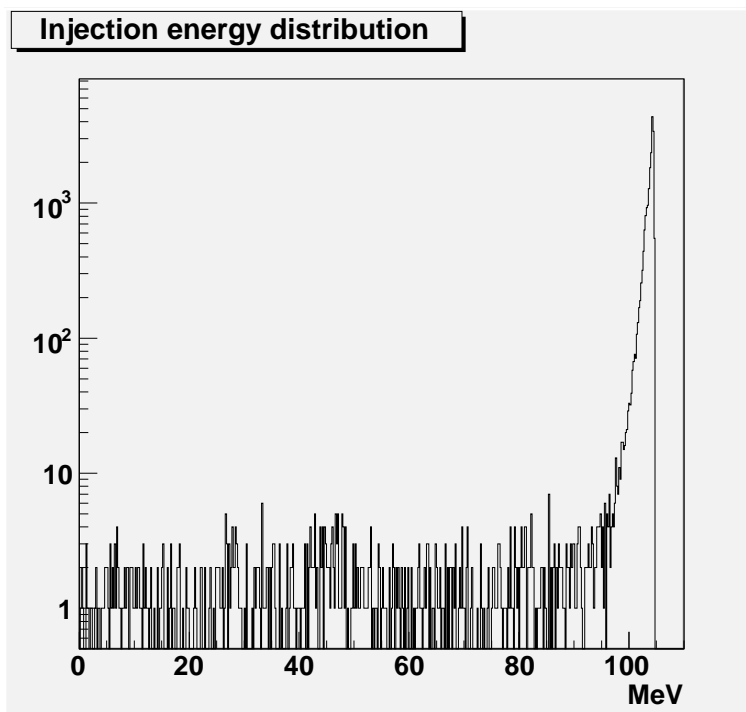


Figure 6.33: The energy distribution of electrons, which are injected to the calorimeter.

Electrons of 105 MeV emitted from the stopping target disks, then transported to the calorimeter. The energy distribution of electron just before the calorimeter is shown in Fig. 6.33. In the calorimeter, electrons interact with the material and scintillation photons are emitted. The photons are ray-traced to the surface of the photon detectors. In order to get simulation result in a reasonable computing time, the photon yield of the scintillation process was reduced by factor of 10 for GSO(Ce) and a factor of 36 for LYSO. Figure 6.34 shows distributions of the number of photons arrived at the photon detectors. We applied a light yield correction considering the light yield factor and a photon detection efficiency (PDE) to estimate the energy resolution.

The energy resolution obtained from this study are summarized in Table 6.9 for PDE=0.25 and 0.75. The PDE of the MPPC depends on its pixel size. The typical PDE of MPPCs at 420 nm are 0.73, 0.45, and 0.25 at room temperature for the pixel size of 100 μm , 50 μm , and 25 μm , respectively [105]. The ADPs have a high PDE in general, for example

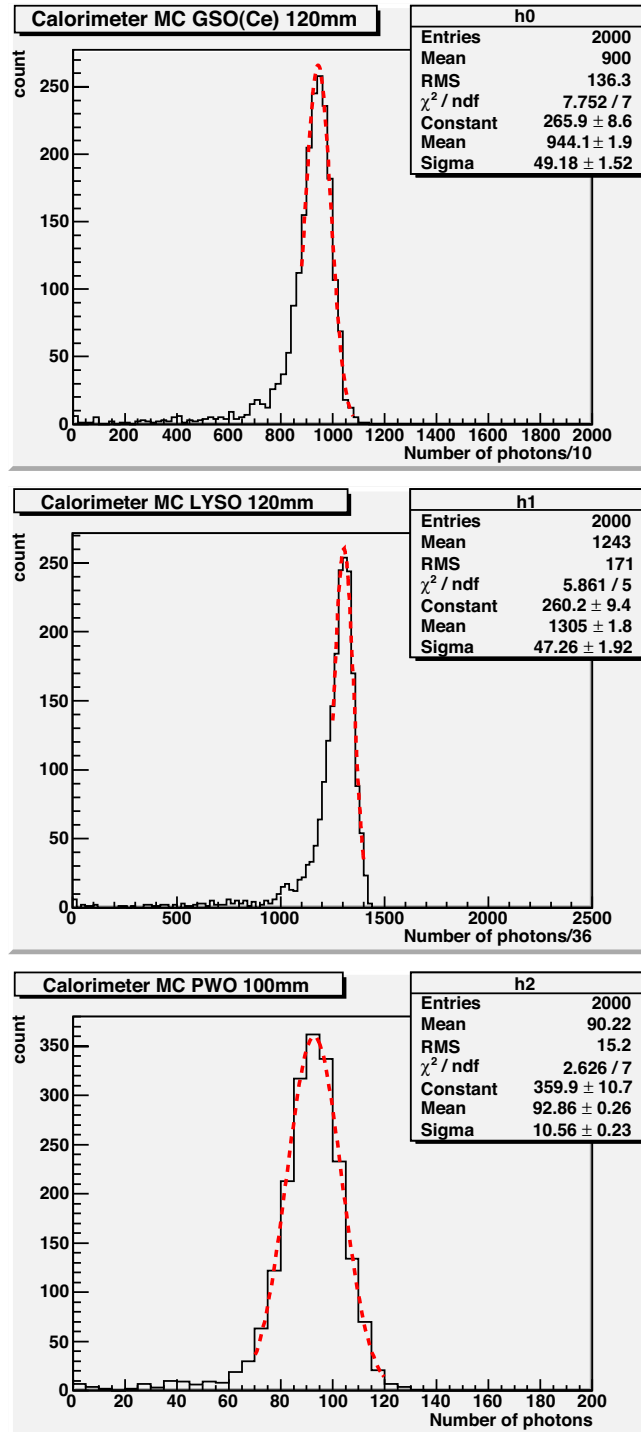


Figure 6.34: Distributions of the number of photons arrived at the photon detectors for GSO(Ce) (top), LYSO (middle), and PWO (bottom). Number of photons emitted by the scintillation process is reduced by some factors.

S8148 of Hamamatsu Co., of which active area is $5 \times 5 \text{ mm}^2$, has PDE of 0.75 at 420 nm for room temperature [107]. The real energy resolution would be worse, since the resolutions

in the table don't include the contributions from electronic noise, non-uniformity of the crystals and light collection, and temperature and gain drifts. GSO(Ce) and LYSO can fulfil the requirement of the energy resolution with this configuration. On the other hand, PWO needs larger ratio of the photon detector area.

Table 6.9: Energy resolutions obtained from this study for PDE=0.25 and 0.75.

Crystal	Length (mm)	PDE = 0.25	PDE = 0.75
		σ_{E_e} (MeV)	σ_{E_e} (MeV)
GSO(Ce)	120	4.8	4.4
LYSO	120	2.6	2.5
PWO	100	22.2	13.4

6.7 Detector rates

The detector single rates are important for high precision experiments, and should be suppressed as much as possible. One of the reasons is that high single counting rates of the detector would introduce false tracking and pileups and would mimic signal events. Table 6.10 summarizes detector rates for the electron tracker and the electron calorimeter. Those detector rates are much smaller than those proposed by a MECO-type detector. The reduction of the detector single rates mostly come from the curved solenoids adopted in the electron transport. This is one of the advantages of COMET.

Table 6.10: Detector singe rate : tracker and calorimeter.

	Timing	Tracker (kHz)	Calorimeter (kHz)	Energy (MeV)
DIO electrons	Delayed	10	10	50–60
Back-scattering electrons	Delayed	15	200	< 40
Beam flash muons	Prompt	< 150 [‡]	< 150 [‡]	15–35
Muon decay in calorimeter	Delayed	—	< 150 [‡]	< 55
DIO from outside of target	Delayed	< 300	< 300	< 50
Proton from muon capture	Delayed	—	—	—
Neutron from muon capture	Delayed	—	10	~ 1
Photons from DIO e^- scattering	Delayed	150	9000	$\langle E \rangle = 1$

[‡] Monte Carlo statistics limited numbers.

6.7.1 Decay-in-Orbit (DIO) electrons

The curved solenoid for the electron transport between the muon-stopping target and the detector provides huge suppression of the DIO electrons. The electron flux entering the detector solenoid is less than 300 kHz as shown in Table 6.10. Most of the background particles are time-delayed, so that the detector rates remain almost constant during the proton pulse cycle. This would be a substantial improvement over the previous MECO design, in which the detector experiences high rates during the beam flash. As the COMET

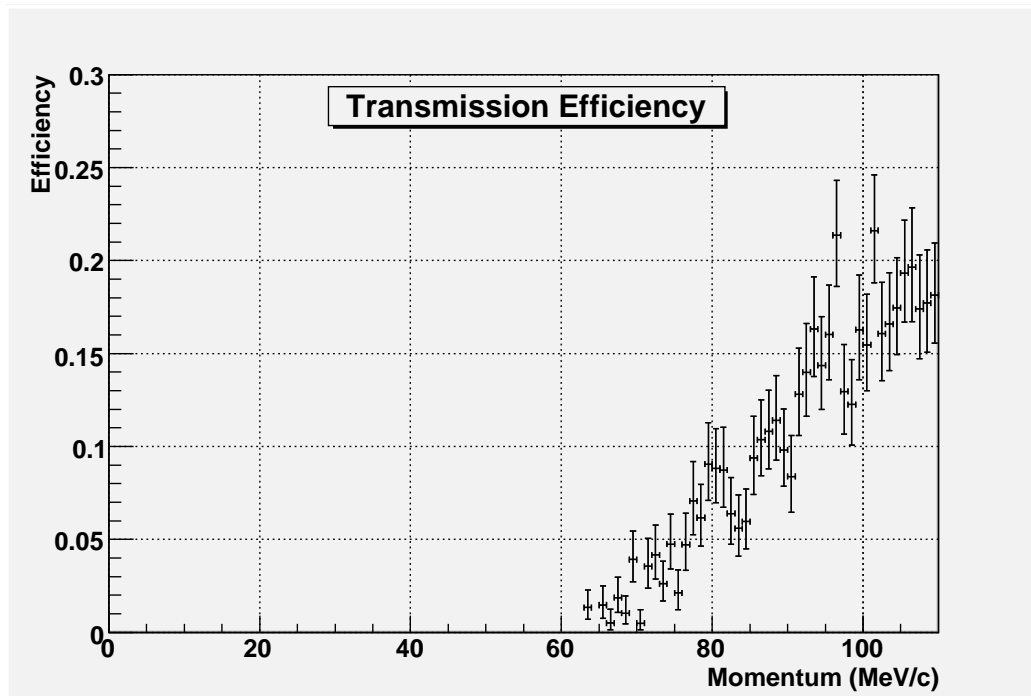


Figure 6.35: Transmission efficiency of the electron transport in the C-shape curved solenoid spectrometer.

detector remains operable during the beam flash, charged particles produced by prompt protons can be measured to study beam related backgrounds.

Figure 6.35 shows the transmission efficiency of the electron transport. It was estimated by Monte Carlo calculations with step-by-step transportation of charged particles in a non-uniform magnetic field of the curved solenoid with a compensation dipole field. When the vertical position of the DIO blocker is set at -20 cm , the number of expected DIO electrons hitting the detector is about 10 kHz , estimated by convoluting the transmission efficiency of the electron transport with the DIO momentum spectrum. Please note that the number is obtained by optimizing the DIO rates and the signal acceptance, which will be described in the detector section. Therefore, it could be reduced to be about 1 kHz at a further cost of the signal acceptance loss, or could be 100 kHz by increasing the signal acceptance if the detector can stand such a high rate. This adjustment can be made at the stage of detector commissioning with a real beam.

6.7.2 Back scattering electrons

Low energy electrons are back scattered from the DIO blocking slit and the inner wall of the transport solenoid. Most DIO electrons either stop or are forward scattered, hitting the walls again as the drift effect always pushes them in the same direction. Back scattered electrons, however, drift away from the walls and potentially mirror in the magnetic field. These electrons may eventually enter the detector solenoid and hit the detector. It is illustrated in Fig. 6.36. A Monte Carlo calculation estimates a detector rate of 150 kHz due to back scattered electrons which originally come from evenly distributed muon DIO in the

muon-stopping target.

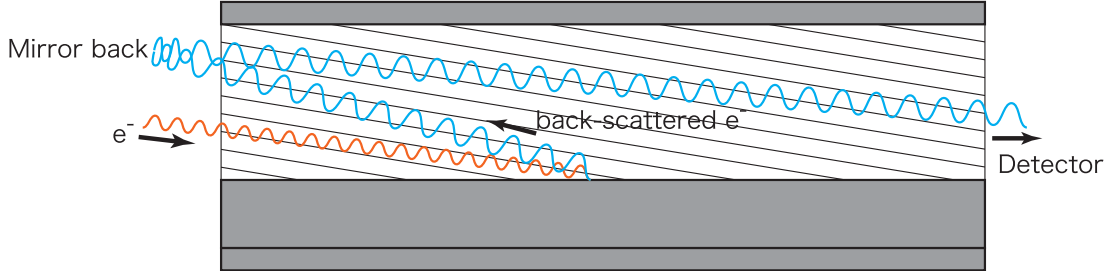


Figure 6.36: Illustration explaining the mechanism of how the back scattering electrons enter detector region.

6.7.3 Beam flash muons

A Monte Carlo calculation using MARS+G4beamline with a realistic beam distribution input, reveals that none of the beam flash muons hit the detector. However, the study was statistically limited, so that the present estimation provides only an upper limit of the rate less than 1 MHz for the entire detector. Such events associated with the muon beam flash can be removed in analysis by a timing cut.

Most of the beam muons that do not stop in the muon-stopping target but are blocked by the muon beam stop located downstream of the muon stopping target. However, if the momentum of a beam flash muon is higher than ~ 60 MeV/c, it may hit the tracking detector and is stopped in the calorimeter. These muons then can emit DIO electrons, increasing the calorimeter rate. Although a Monte Carlo estimation of this rate is statistically limited, an expected rate of less than 1 MHz is obtained.

On the other hand, if the momentum of the muons that are not blocked by the beam stop is less than ~ 60 MeV/c, they will be stopped in the DIO blocking slit. At this point, a DIO electron may be emitted. If the initial direction of the DIO electron is downstream, it will continue to hit the DIO blocker and rarely hit the detector. However, if the initial direction is backward, it acts as a back scattered electron and can hit the detector. The present estimation of such a background rate is statistically limited, but it is expected to be less than 150 kHz per plane.

6.7.3.1 Muon decays in the electron calorimeter

The beam flash muons passing through the electron transport might be stopped in the electron calorimeter, where μ -decay electrons are produced. They will increase the rate of the electron calorimeter in a delayed time window. The estimated rate is Monte Carlo statistically limited, but should be less than 1 MHz.

6.7.4 Particle and photon emission from nuclear muon capture

For aluminum, approximately 60% of stopped muons are captured by nuclei, and the muon nuclear captures produce protons, neutrons, and photons. Approximately 2 γ s, 2 neutrons, and 0.1 protons are emitted on average for each capture.

6.7.4.1 Protons from muon nuclear capture

The total instantaneous flux of protons exiting the stopping target is $\approx 1.6 \times 10^{10} \text{ s}^{-1}$ [109], and without their removal, rates in the individual tracking detector elements would be well above 1 MHz. In addition, these protons are emitted in a momentum range that is accepted by the magnetic transport system, and they have a mean ionization approximately 25 times that of a minimum ionizing electron. However, as discussed in earlier sections, the curved transport solenoid provides a huge suppression to low energy protons, since a positively charged proton drifts in the opposite direction to that of an electron. Thus essentially no protons are expected to enter the detector solenoid. In a straight solenoid system of a MECO type, a proton absorber to remove protons has to be installed, and it is known that it would degrade the momentum resolution of the electron detection in the electron tracker. It is absent in the COMET experiment.

6.7.4.2 Neutrons from muon nuclear capture

Neutrons are produced during the muon nuclear capture process. A neutron spectrum, typical for an Al target, can be estimated from experimental data [110]. Neutrons below 10 MeV are represented by a thermal distribution and have an exponential tail above 10 MeV. Detector rates can be calculated assuming two neutrons are emitted per capture. Neutron interactions in the detector can be neglected, but they could increase the calorimeter rates. In the COMET design, these neutrons cannot hit the calorimeter without passing through shielding which reduces the neutron flux at the calorimeter position by more than 3 orders of magnitude. In order to shield the calorimeter from neutrons produced by muon nuclear capture, 70 cm of iron and 20 cm of polyethylene are needed. The average neutron energy deposited in the calorimeter within 100 nsec is less than 0.01 MeV. As the intrinsic resolution of the calorimeter is $\leq 5\%$, pile up due to neutrons will not significantly effect the calorimeter resolution and the experimental trigger.

6.7.5 Target bremsstrahlung

Beam electrons emit bremsstrahlung radiation as they traverse the stopping target. These photons may Compton scatter and pair produce in the detectors. The pulsed beam and the muon beam line are designed to reduce the flux of low energy electrons that reach the stopping target during the active time window.

6.7.6 Cosmic muons

Cosmic muons may enter, or decay in (or near) the tracking detector and constitute a background that must be identified and removed. An active cosmic ray shield is placed to veto events that are coincident with a detector track.

6.8 Muon intensity monitor

The number of muons stopped in the muon-stopping target will be monitored by observing characteristic X-rays from muonic atoms. An X-ray detector will be used for this purpose. We are considering to employ a Ge(Li) detector to be located near the target. As in the case of SINDRUM II [22], it will be probably possible to locate the detector outside the target solenoid, and to observe X-rays through the magnet wall. Figure 6.37 shows an

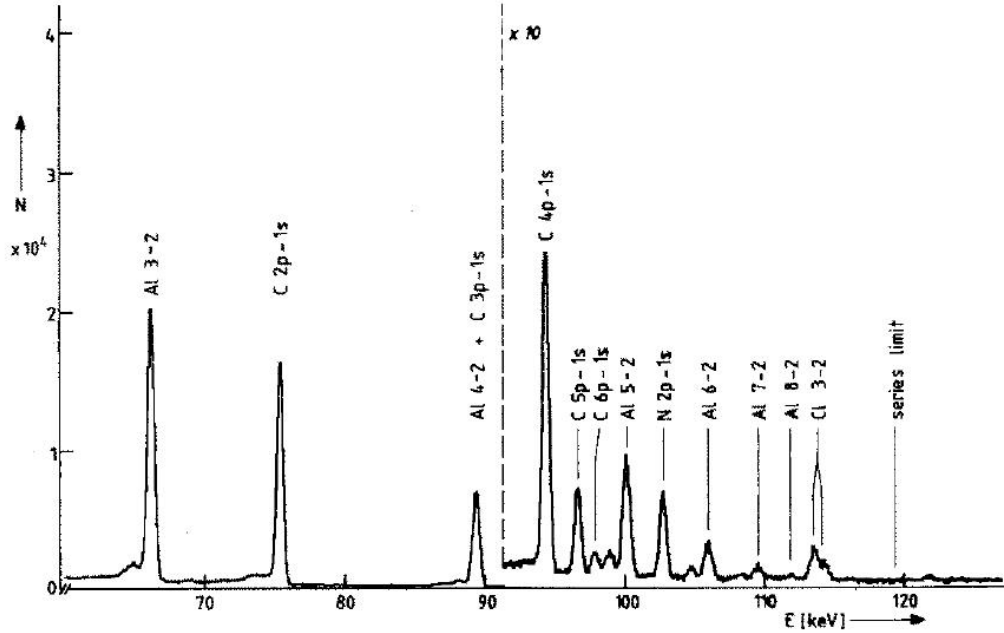


Figure 6.37: Spectrum of the muonic Balmer series in Al [111].

example spectrum of the muonic Balmer series in Al [111]. By using several lines (or even higher energy X-ray lines if their intensities are sufficient) to clearly separate background, the number of muons will be continuously monitored during data acquisition. Simulation will be necessary to evaluate this.

Chapter 7

Cosmic Ray Shield

The cosmic ray shield system consists of three main layers of components:

1. an outer shield,
2. a cosmic active veto counter system, and
3. an inner shield.

The outer shield is a block of heavy concrete that covers the whole detector area. The function of the outer shield is

- radiation safety shielding for humans outside of the experimental area,
- a shield for low energy cosmic nucleons, and
- a shield for skyshine neutrons.

The cosmic active veto counter system consists of four (or more) layers of plastic counters. Since the expected number of fake signals induced by cosmic muons is about 70, they should be properly tagged by the counter system so that any signal electrons associated with the cosmic veto counter activity could be rejected. Inefficiency of the cosmic veto system should be much less than 0.01. The inner shield protects the cosmic veto counter system from a large flux of neutrons coming from muon capture inside of the target solenoid. Without the inner shield, the signal rate of the cosmic veto counter system would be more than 500 MHz.

Please note that it is practically impossible to shield cosmic muons on the surface at sea level. Several meters of heavy concrete will provide only a limited reduction of the cosmic muon flux. The key to controlling the cosmic background is the cosmic veto counter system, and the outer and inner shields only support the function of the veto system.

7.1 Outer shield

The outer shield is a block of heavy concrete. The thickness of the outer shield is not yet fully optimized. The minimum thickness would be defined by looking at the rate of the veto counter system from skyshine neutrons. The calculation will be performed by using MCNPX code package in the near future.

7.2 Inner shield

The inner shield consists of , from outside to inside, an iron layer, a polyethylene layer and a lead layer. The iron layer will reduce fluxes of high energy neutrons, mostly $E_n > 2$ MeV, by 3–4 orders of magnitudes. The flux of low energy neutrons (which is called “fast neutrons”) would be increased since the high-energy neutrons slow down. As a result, the total neutron flux after iron shield is only one order of magnitude less than the original flux.

The polyethylene layer absorbs fast neutrons. The total neutron flux, including the low energy region, after polyethylene layer (20 cm) is almost three orders of magnitude reduced from the original flux. On the other hand, the gamma ray flux becomes high due to gamma-ray emission by fast neutron absorption. These gamma-rays are absorbed by the lead layer.

7.3 Cosmic active veto system

The cosmic veto system consists of four layers of plane plastic counters. We conservatively assume the inefficiency of the single layer is a few %. Four layers of counter would have an inefficiency of less than 10^{-4} . The requirement on inefficiency for each counter is less than 0.1. It should be mentioned that the backgrounds induced from cosmic rays can be estimated and measured at the time of beam off during proton acceleration cycle, since they are not related to a beam. The time of beam off is about 0.8 sec since the flat top time of the J-PARC MR is 0.7 sec, while one proton cycle is 1.5 sec.

Chapter 8

Data Acquisition System

8.1 Basic trigger concept

An event trigger is obtained by measuring the total energy of an electron that is absorbed in the calorimeter. The DIO electron energy spectrum falls as the 5th power of the difference between the energy of this electron and its kinematic endpoint where conversion electrons would be emitted. Setting a window about the endpoint energy (1–2 MeV around 105 MeV) provides a trigger that contains a sample of the falling DIO background and the endpoint region. By changing the lower edge of this window, the trigger rate can be adjusted to provide a compromise between the DAQ acquisition rate and a sampling of the DIO background spectrum.

The trigger is based on an analog summation of energy deposited in the calorimeter crystals within a time window. This information is processed by a trigger FPGA module which uses the total deposited energy, and the number of contiguous crystals that have a signal above a minimum energy threshold. It can be made as cascade structure, as shown in the schematic of the trigger system Fig. 8.1.

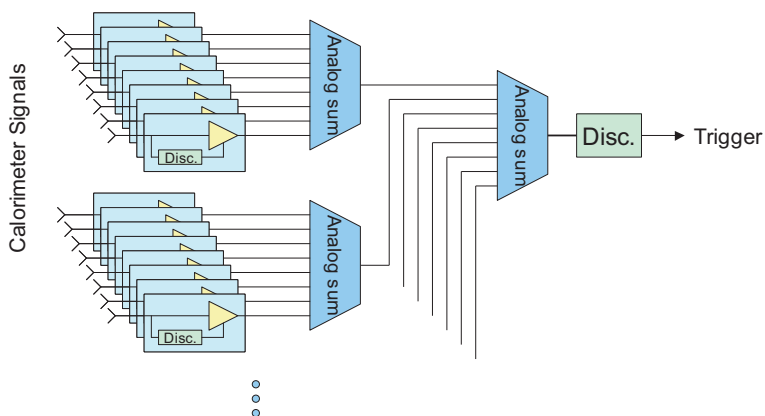


Figure 8.1: The trigger schematic by the analog summation.

Table 8.1: Estimation of numbers of readout channels and data size.

Detector	Number of channels	Number of Hits per event	Measurement factors	Data size
Calorimeter	1056	10 (shower) + 40 (4 BG events assumed)	Waveform (sampled at 250 Mhz)	200 (bytes/trigger)
Tracker	4160	40 (signal) + 4 (BG)	Timing and charge	352 (bytes/trigger)
Cosmic veto counter	1625	20 (10 MHz total rate assumed)	Timing and charge	80 (bytes/trigger)
Extinction Monitor	10		Waveform	12.5 kB

8.2 Data acquisition

8.2.1 Data flow rate estimation

COMET has several types of detectors, such as the electron tracker, the electron calorimeter, the cosmic-ray active shield, the late-arriving particle tagger, the proton extinction monitor, the muon intensity monitor, and others. It is anticipated that information from the calorimeter and extinction-monitor will be read out by a waveform digitizer such as the DRS3 ASIC [104] which is used in MEG experiment. The sampling rate of the calorimeter is planned to be 250 MHz with a width of about 400 ns. The extinction-monitor would be sampled at 500 MHz, that is triggered by the RF bunch-time from the J-PARC main ring with a width of approximately 2 μ s. The tracker is digitized and read as described in the tracking section, by an ASIC that provides both time and analog information. Numbers of the readout channels and the estimated data size are summarized in Table 8.1.

Data rates are based on simulation information summarized in Table 6.10. Electrons that hit the tracker are assumed to penetrate to the calorimeter, causing a hit in all the tracker arrays. A photon, on the other hand causes only a local hit in a specific tracker array. Assuming on average a hit multiplicity of 1.5, the singles rate on a tracker wire is $(460/208 + 150/832) \times 1.5 = 3.6$ kHz per wire. In the calorimeter only high energy photons and electrons shower. It is assumed that the simulated photon rate given in Table 6.10 is mainly from showered photons which would cover approximately 10 calorimeter crystals. Thus the singles rates in a crystal are approximately $(9670/1056) \times 10 = 92$ kHz per crystal. There is then an approximate 4% probability of at least 1 overlap of 2 showers within 400 ns.

The trigger rate can be assumed to be 10 kHz as estimated by simulations. As mentioned previously this may be tuned by changing the lower edge of the calorimeter trigger window. The data flow of the electron detector is 4 Mbytes/s and the data flow of the extinction-monitor is 125 Mbytes/s. The data of extinction monitor can be suppressed using the pedestal suppression and the simple data compression. We estimate the data flow of the extinction-monitor after the suppression to be approximately 25 Mbytes/s. The total data flow is estimated as about 30 Mbytes/s.

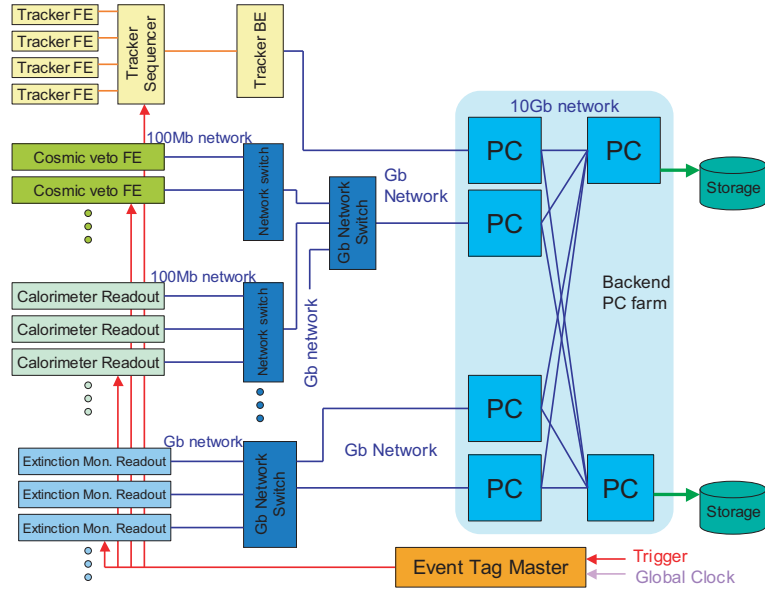


Figure 8.2: Network based DAQ system

8.3 Network based DAQ system

To handle the 30 Mbytes/s data flow, we plan to build a network based data acquisition (DAQ) system. A network based system has several advantages:

- High speed devices are commercially available at reasonable cost
- A network is flexible and easily modified
- A network offers direct control and monitoring of the DAQ FPGAs and DAQ operations

Each front-end will be locally controlled by an FPGA, programmed to read its detector and process an event structure, storing this information in a local memory from which it is read via a command from the system. Because each detector has a local buffer from which events are transferred to a system processor, an event builder must sort the data stream by event number, before event processing and storage. A PC farm, also controlled by a system computer, processes the data committing appropriate events to permanent storage, and transferring a sample for on-line monitoring.

A schematic view of a network configuration is shown in Figure 8.2. Such a network DAQ system can accept over 100MB/sec data flow.

Finally, there will be a second acquisition system for slow control and environmental monitoring. Environmental variables will be read every fixed number of beam spills and will be correlated with in time sequence with the data triggers.

Chapter 9

Simulation and Analysis

The desired sensitivity of the COMET experiment requires careful and thorough simulation of the signal and backgrounds and the identification of background sources. There are fundamental challenges posed by the nature of the experiment, in that its success could be affected by a single stray particle, arriving over timing windows of microseconds following the initial beam pulse containing of the order of 10^{13} protons.

The simulation, reconstruction and analysis software framework will be a key component in allowing the experiment to overcome these challenges.

9.1 Software requirements

In this section, we discuss the functionality that the software must supply, and the solutions we have available at the present time as we prepare for a fully-functional framework.

9.1.1 Proton beam and pion production

The simulation of the COMET experiment starts with the incoming proton beam and its collisions with the fixed target used to produce pions. The beam has a pulsed time-structure with pulses at approximately $1.2 \mu\text{s}$ intervals during a spill, which is obtained by only filling every other accelerator beam bucket in the Main Ring. The extinction of the proton beam between the pulses is one of the most critical aspects of the experiment, and this is achieved with a dedicated extinction system designed to remove particles arriving off-pulse, as described in Chapter 4. The aim is to have a beam extinction factor between pulses at the unprecedented level of about 10^{-9} , and simulations of the proton beam, together with the extinction system and associated beam monitors, will be very important in ensuring that we understand the beam fully and to investigate the effect on the measurement of the signal due to protons outside the pulse.

Here, the COMET software framework will need to interface closely with the proton beam simulation and monitoring code used in the proton beamline upstream of the experiment.

The protons, which have energies of about 8 GeV, slam into a fixed target, causing the production of a large number of hadrons. Currently, MARS [78] and the QGSP model in GEANT4 [79] have been used to simulate an 8 GeV proton bunch colliding with a fixed target. This gives the initial hadrons to be used for tracking through the beamline. There are discrepancies on the order of a factor of two or three between these simulations, and

detailed comparisons with data from dedicated hadron production experiments such as HARP [112] will be very important.

9.1.2 Particle transport

The initial particle distribution produced at the pion production target, and simulated by MARS, is then tracked through the muon transport part of the experiment using G4beamline [80], see Section 5.3. The simulation of the next part of the experiment, i.e. the stopping target through to the calorimeter, is simulated using a custom GEANT4-based application.

The successful operation of curved, high-field solenoids form the crux of the experiment, and it is important that the particle transport simulation includes accurate field models of these solenoid channels, in particular accurate simulation of the fringe fields of adjacent sections. This requires using a field map for the particle transport for the muon transport section and the spectrometer.

Separating the simulation of the muon transport beamline from the remainder of the experiment can however lead to certain background processes being excluded from the simulation, e.g. backward going secondary particles being reflected in the muon transport channel. It is therefore imperative that we combine the beamline and detector simulations in a single framework. There also needs to be the flexibility to study the effect of different particle interaction and decay models on the performance of the whole experiment and not just the detector.

9.1.3 Particle interactions

The simulation of particle interactions is done by GEANT4, which includes a number of models for different particle interaction processes as well as particle decay. The primary energy of particles in the COMET experiment is much lower than traditional high-energy physics experiments so understanding the applicability of each of the available models is essential. In particular, models for energy straggling, secondary particle production and nuclear interactions will need to be studied carefully. In many cases, the physics inputs for these effects may be measured as part of the COMET program itself. The current custom GEANT4-based application provides a good framework for applying these models to the latter half of the experiment; however this will also need to be made possible for the muon transport part.

9.1.4 Detector simulation

As well as including particle interaction effects in the tracker and calorimeter, the detector simulation also needs to include accurate simulation of the data acquisition and triggering electronics. The large signal-to-background ratio, as typified by the beam extinction requirements, requires the data acquisition and triggering systems to have a large dynamic range or be gated at the sub-microsecond level. Simulation of this will be needed to understand the experiment's measurement errors and thus its sensitivity.

The framework also needs to have the flexibility to allow simulation of the active cosmic ray shield, optimization of the passive cosmic ray and neutron shield geometry and to allow the study of different triggering configurations and their efficiencies. This will be very important for determining the rate of background events that are not flagged by the background rejection systems.

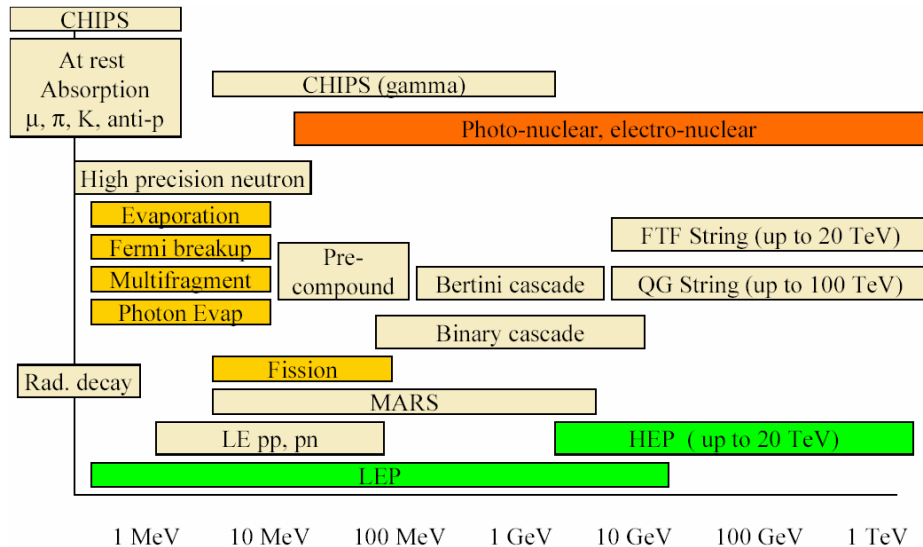


Figure 9.1: Hadronic interaction models in GEANT4, plotted against the relevant energies. The 100 MeV energy scale of the COMET experiment falls in an energy range where several models compete to describe the physics of hadronic interactions. (The GEANT4 Collaboration)

9.1.5 Simulation framework

The integral nature of the beamline and the detectors requires a new approach to the simulation of the experiment, since current simulation tools, such as GEANT4 and G4beamline, focus on beamline and detector aspects separately. Both have significant, but different, strengths as simulation tools for their respective systems, and COMET needs to take advantage of all of these in the same framework. Treating the experiment as a whole would reduce the possibility of certain background processes being excluded from the simulation. For an experiment like COMET, where individual events can impact its ability to succeed, it is crucial that all significant sources of backgrounds are included in the simulation.

A possible approach to combining the beamline and detector simulations would be to include the beamline components in a custom GEANT4-based application. One important task would be to implement time-varying electro-magnetic field maps. Although this is not a simple task it is likely to be easier than the converse solution of including data acquisition and triggering simulations in G4beamline.

9.2 Present status and future plans

The physics of hadron production at the energies of interest are not well understood, and the precise angular and momentum distributions of hadrons leaving the target cannot be accurately predicted at this time. Comparisons between data and simulations models, and their extrapolation to particle production at COMET, will be a very important task. Work of this nature is being done as part of the optimization of the design of the Neutrino Factory, and this will be leveraged to improve our understanding of the COMET beam.

The close relationship between the beamline and detector components of the COMET experiment requires the development of a framework that includes the functionality pro-

vided by G4beamline and GEANT4. The development of a new simulation framework that incorporates both the beamline and the detector is a large undertaking but would be beneficial for other similar experiments.

Discussions have already begun with the Mu2E experiment at Fermilab on developing a common software framework. In addition to saving duplication of effort, a single, powerful framework would also provide a common basis on which comparisons of the two experiments could easily be made. However, the framework would need to have the flexibility to implement specific models of detector and beamline components without unnecessary computational overhead. Forcing the use of a common framework across different collaborations and experimental setups could also introduce unnecessary inefficiencies. It may be that restricting compatibility requirements to the level of detector geometry and physics model interfaces is sufficient to allow such comparisons. The pros and cons of developing a common framework between COMET and Mu2E are currently being evaluated.

Since the establishment of a fully-working, integrated software framework will contribute greatly to the design optimization phase of the experiment, the decision to select the software solution that most suited to our needs must not be delayed. Therefore we plan to spend the coming months making this decision so that the most important aspects of the software can be brought to usable state as soon as possible.

Chapter 10

Calibration System

Calibration of the detector is always an important issue in any kind of particle physics experiment. In COMET, determination of the energy scale is most important to identify the $\mu^- - e^-$ conversion signal among DIO background electrons. Signal electron identification will be done by measuring its momentum with the tracker. Calorimeter information will support this. Alignment of the tracker supporting structures will be done with an optical survey when we install the tracker. Precise magnetic field measurement of the detector solenoid must be done on site. Such information will be stored in a database to be utilized in off-line analysis. Absolute momentum calibration will be done by using electrons generated by an on-site electron linac being installed in the experimental area. Figure 10.1 shows a schematic of the linac.

Because we do not need an intense beam for calibration, we may be able to utilize a radioactive source normally used in laboratories as a beam source. Electrons will be accelerated twice in the same but directionally opposite path, each of which can accelerate electrons up to 50 MeV, resulting in electron acceleration up to 100 MeV. The linac will be designed so that the electron beam energy can be variable within a range of $\pm 10\%$ and the precision of the beam energy less than 10^{-3} . Beam repetition rate can be as high as a few kHz for efficient acquisition of calibration data.

The electron beam will be injected to the muon stopping target or a dedicated calibration target made of a thin heavy-metal foil. Those electrons will scatter off target atoms via Mott scattering and enter the spectrometer. However due to the effect of energy loss in the target material the electron energy to be measured in the spectrometer will be slightly lower than the beam energy, depending on the target thickness. The muon -topping target might not be suitable for this purpose because the COMET electron spectrometer cannot identify the target disk where the electron is scattered and energy loss correction would be complicated.

The scattered electron will enter the curved solenoid and its momentum will be measured by the detector. It is necessary to design the magnet system so that we can inject electrons in this way. A possible procedure is to mount the target and the curved and detector solenoids on a movable stage and to slide the stage when we perform calibration. Coupling between the electron linac and target solenoid needs to be carefully designed with a vacuum junction. It is also important to separate the cooling system between the muon transport solenoid and target solenoid in this sense, which will be realized by using small GM-type refrigerators for target and downstream solenoids. The electron beam calibration will possibly be performed during shutdown periods. Stability of the electron tracker can be monitored continuously

Recirculating LINAC

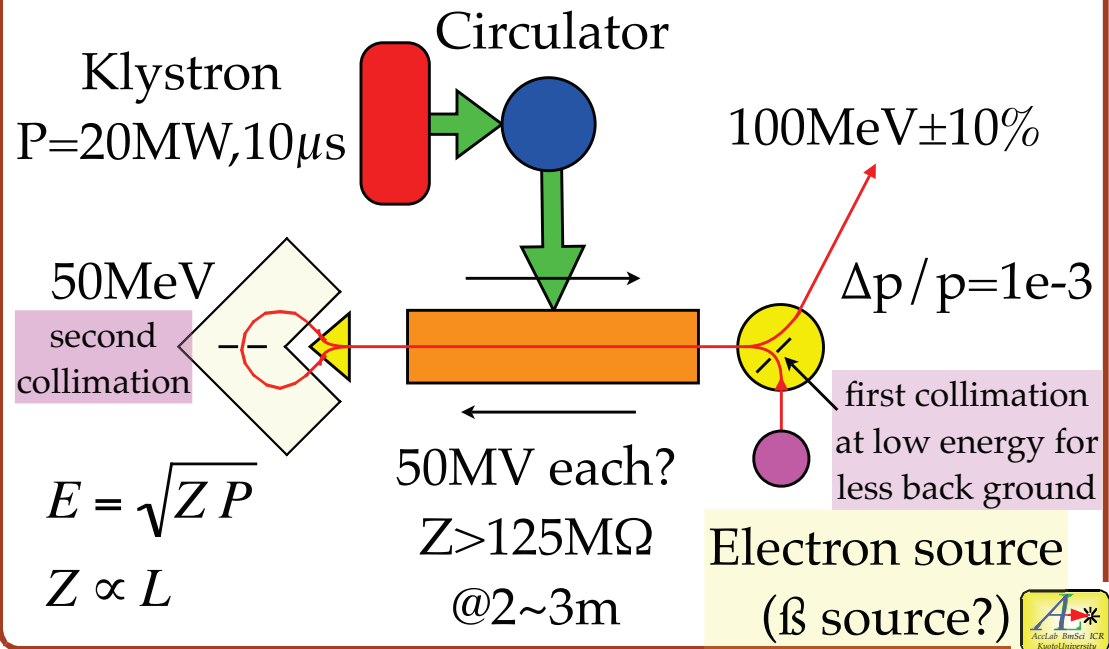


Figure 10.1: Schematic of the electron linac used for detector calibration.

during data acquisition by measuring the slope of the DOI electron spectrum.

Calibration of the calorimeter can be carried out in the electron beam calibration taking into account the effect of energy loss in the tracker material. During data acquisition period, crystal light yield will be monitored by using cosmic rays going through the crystal array vertically. Dedicated triggers can be prepared to take calorimeter cosmic-ray data during proton beam acceleration. Calorimeter photo-sensor calibration can be done independently by using a light source such as LEDs.

Chapter 11

Sensitivity and Backgrounds

This chapter describes estimations of the sensitivity for $\mu^- - e^-$ conversion signals and background events for the COMET experiment. With 2×10^7 sec running, the number of muons stopped in the muon-stopping target is estimated with the present design of the muon beam. A net signal acceptance, which is composed of the detector geometry and the event selection, is also evaluated for the present design of the detector. Based on these, a single event sensitivity of 2.6×10^{-17} for $\mu^- + \text{Al} \rightarrow e^- + \text{Al}$ can be achieved for 2×10^7 sec. The background events, which can be grouped into four categories, are estimated. They are intrinsic physics backgrounds, beam-related prompt backgrounds, beam-related delayed backgrounds and cosmic-ray and other backgrounds. The total expected number of background events at the above sensitivity is about 0.3 events. In the following sections, the expected signal sensitivity and backgrounds are described in detail.

11.1 Signal Sensitivity

11.1.1 Muon yields

Estimation of the yield of the muons stopped in the muon-stopping target is described. As shown in Chapter 4, the momentum and beam current of a proton beam from the J-PARC MR are planned to be 8 GeV and $7 \mu\text{A}$, respectively. It is also required that every other proton beam pulse is filled. As a result, the number of protons per the beam spill is about 6.4×10^{13} protons/spill, and an average number of protons per second is about 4.4×10^{13} protons/sec. With physics running of a total of 2×10^7 sec, the total number of protons available for the COMET experiment is about 8.5×10^{20} . As shown in Chapter 5, the number of muons transported to the muon-stopping target is about 0.0035 muons/proton with the muon beam collimators. With a muon stopping efficiency of 0.66, the total number of the muons stopped in the muon-stopping target is about 2.0×10^{18} for 2×10^7 sec running. The breakdown of the muon yields is summarized in Table 11.1. It should be noted that the pion production cross section for 8 GeV protons is different between different hadron production codes. The present estimation is based on the most conservative cross sections.

11.1.2 Total signal acceptance

The signal acceptance is obtained as a product of geometrical acceptance, the acceptance in event selection and the trigger acceptance. Table 11.2 summarizes the signal acceptance.

Table 11.1: Breakdown of the muon yield expected for COMET.

Total number of protons: N_p	8.5×10^{20}	
Proton kinetic energy	8	[GeV]
Harmonics of MR	8	
Bunch time spacing	657	[nsec]
Number of RF bunches filled with protons per spill	4	
Time between adjacent filled bunches	1314	[nsec]
Number of protons in each RF bunch	1.6×10^{13}	
Cycle time of MR (=spill period)	1.47	[sec]
Flat top for the slow extraction	0.7	[sec]
Number slow-extracted pulse in a spill	5.3×10^5	[pulses/spill]
Number of Protons in each slow-extracted pulse	1.2×10^8	
Average beam current	7.0	[μ A]
Average beam power	56	[kW]
Average proton intensity	4.4×10^{13}	[protons/sec]
Total running time	2.0×10^7	[sec]
Running time per year	1.0×10^7	[sec/year]
Number of stopped muons per proton: $N_{\mu/p}^{stop}$	0.0023	[muons/proton]
Rate of muons per proton transported to the target	0.0035	[muons/proton]
Muon stopped acceptance	0.66	
Number of stopped muons: $N_{\mu/year}^{stop}$	1.0×10^{18}	[muons/year]
Total number of stopped muons: N_{μ}^{stop}	2.0×10^{18}	

The geometrical acceptance and then the acceptance in event selection are described in detail in the subsequent subsections.

11.1.3 Geometrical acceptance

11.1.3.1 Solid angle with a magnetic mirroring effect

Since the muon-stopping target is placed in a graded magnetic field, a solid angle for detection of $\mu^- - e^-$ conversion electrons should be evaluated considering a magnetic mirroring effect, with which some muons going backward might be reflected forward, to the detector. The range of a polar angle of the detection for $\mu^- - e^-$ conversion electrons can be determined by distribution of a graded magnetic field. Now, a maximum field strength is about 3 T, and magnetic fields at the muon-stopping target range from 2.0 T to 2.6 T. From this, a maximum polar angle can be given by

$$\sin \theta > \sqrt{\frac{B_0}{B_{\max}}}, \quad (11.1)$$

where θ is the polar angle between the initial direction of $\mu^- - e^-$ conversion electron and the axis of the magnetic field, B_0 is the strength of the magnetic field at the initial position of the charged particle and B_{\max} is the maximum strength of the magnetic field. To obtain the solid angle, a Monte Carlo simulation was used; a value of 0.73 has been obtained. A naive estimation using Eq. 11.1 is in good agreement with the Monte Carlo evaluation.

Table 11.2: Breakdown of the signal acceptance.

Category	Item	Value
Geometrical	Solid angle with mirroring	0.73
	Muon beam stop	0.57
	Curved Solenoid Acceptance	0.47
Event selection	Track Reconstruction Efficiency	0.88
	Track Quality Cut Efficiency	0.89
	Transverse Momentum Cut Efficiency	0.83
	E/p Cut Efficiency	0.99
	Helix Pitch Cut Efficiency	0.99
	Momentum Selection Efficiency	0.72
	Timing Window Selection Efficiency	0.39
Trigger acceptance	Trigger acceptance and DAQ live efficiency	0.9
Total signal acceptance		0.031

11.1.3.2 The muon beam stop

The muon beam stop is a thick disk placed downstream of the last disk of the muon-stopping target. The diameter of the beam stop is 30 cm, while that of the target disk is 20 cm. The major purpose of the muon beam stop is to reduce the number of beam particles, which would hit the detector. An expected counting rate of the detector would be more than 1 GHz without the beam stop.

The muon beam stop also reduce the acceptance of μ^-e^- conversion electrons, especially for those whose transverse momentum is smaller than 40 MeV/ c . Monte Carlo simulations were used for the acceptance evaluation. As a result, the number of μ^-e^- conversion electrons that enter the detector reduces to 57% of those for the case of no muon beam stop. However, as shown later, the event selection of μ^-e^- conversion signals requires $p_T > 50$ MeV/ c , where p_T is a transverse momentum, in order to suppress the beam electron scattering background. It turns out that this event selection on p_T is correlated to the acceptance loss by the muon beam stop. Therefore, a net increase of the loss of the μ^-e^- conversion signal acceptance by the muon beam stop is estimated to be only 4% after all the event selections.

11.1.3.3 The electron transport

The curved solenoid in the electron transport removes most of the DIO electrons at the cost of the signal acceptance loss for the μ^-e^- conversion electrons. A maximum detector rate, dominated mostly by the DIO electrons, of 10 kHz can be tolerated. This requires that the height of the DIO blocker should be 20 cm below the median plane of the curved solenoid. In this case, as discussed before, the signal acceptance becomes 0.47.

11.1.4 Acceptance in the event selections

11.1.4.1 Track reconstruction

The tracking code that was used in this analysis includes multiple scattering effect by the “break point” method. The probability distribution function of the multiple-scattering effects was approximated by a Gaussian distribution, with the large angle tails are ignored. Because of this, the tracking code fails to find a proper track if the multiple-scattering angle is large. The track finding acceptance is therefore only 88%. In the future, the efficiency of tracking can be improved by using e.g. a Kalman filter.

11.1.4.2 Track quality

In this analysis, a good track is selected by requiring the probability of finding such a track being more than 5%, where the probability is calculated from the properly normalized χ^2 value of the track fitting. The acceptance is about 0.89.

11.1.4.3 Transverse momentum

In order to suppress the background from beam electron scattering, the transverse momentum is required to be $p_T > 50 \text{ MeV}/c$. After the acceptance of the muon beam stop is included, the acceptance of this event selection is 83%, since most of such tracks were already blocked by the muon beam stop.

11.1.4.4 E/p ratio

The event selection on the ratio of measured energy E versus measured momentum p is important to reject the background from cosmic muons, where primary cosmic muons directly hit the electron tracker. The expected cosmic muon background without this cut is 0.05 by assuming the inefficiency of the active cosmic veto is 10^{-4} . It is note worth that the assumption about the active cosmic veto inefficiency is quite challenging, therefore it is worth to prepare yet another means to reduce the cosmic background. The E/p cut requires $0.8 < E/p < 1.2$ for good events, and the number of cosmic muon background with this cut will be only 0.002. Therefore, even if the cosmic veto inefficiency fails to be 10^{-4} , for examples an order of magnitude worse, the number of background will be still small enough, 0.02. The acceptance loss with this cut is only 1%.

11.1.4.5 Helix pitch

For $\mu^- - e^-$ conversion electrons, the angle of the track with respect to the solenoid axis, θ_e , is mostly more than 0.6. The cosmic induced electrons produced in a 1 T field region could have $\theta_e < 0.6$. Therefore the cut is applied to suppress the cosmic ray induced electron backgrounds. The acceptance loss to $\mu^- - e^-$ conversion electrons is less than 1%.

11.1.4.6 Electron momentum

The momentum selection is the only way to discriminate the DIO backgrounds from $\mu^- - e^-$ conversion signals. Due to energy loss in the muon-stopping target, the momentum distribution of $\mu^- - e^-$ conversion signal has a large low energy tail. Because of this, when

the momentum region is selected to eliminate the DIO electron backgrounds, the signal acceptance is also reduced.

For the present event selection, the momentum window cut of $103.5 \text{ MeV}/c < p_e < 105.2 \text{ MeV}/c$ has been chosen. From Monte Carlo simulation, the signal acceptance is 72%, where the DIO background rate is about 0.15 events, which will be described in detail in Section 11.2.1.1. Further optimization of this momentum cut should be done in the analysis stage.

11.1.4.7 Time window of the measurement

The muons stopped in the muon-stopping target have the lifetime of a muonic atom. The time distribution of muon decays with the distribution of muon arrival timing is shown in Figure 11.1.

The $\mu^- - e^-$ conversion electrons are measured between the proton pulses to avoid beam-related background events. However, some beam-related backgrounds would come even after the prompt timing, as seen in Figure 11.2 for pions in a muon beam. Therefore, the measurement time window is selected to start after the prompt timing. Figure 11.3 shows the acceptance of $\mu^- - e^-$ conversion signals as a function of a starting time of the time window. Figure 11.4 also shows the expected number of the pions coming in the measurement window as a function of the starting time of the measurement time window. From this, a time window from 700 nsec to 1314 nsec is chosen, where the number of the pions in the measurement time window is expected to be about $10^{-17}/\text{proton}$.

The acceptance due to the time window cut, ε_{time} , can be given by,

$$\varepsilon_{time} = \frac{N_{time}}{N_{all}}, \quad (11.2)$$

$$N_{time} = \sum_{i=1}^n \int_{t_1+T_{sep}(i-1)}^{t_2+T_{sep}(i-1)} N(t) dt, \quad (11.3)$$

where N_{all} and N_{time} are the number of muons stopped in the target and the number of muons which can decay in the window, respectively, T_{sep} is the time separation between the proton pulses, t_1 and t_2 are the start time and the close time of the measurement time window, and n indicates the window for the n^{th} pulse. The time distribution of the muon decay timing $N(t)$ is obtained by Monte Carlo simulations. In our case, t_1 and t_2 are 700 nsec and 1314 nsec, respectively and T_{sep} is 1.47 μsec , and ε_{time} of 0.39 is obtained.

Similar distributions for a titanium target are shown in Figs. 11.5 and 11.6 for future consideration of a different target material.

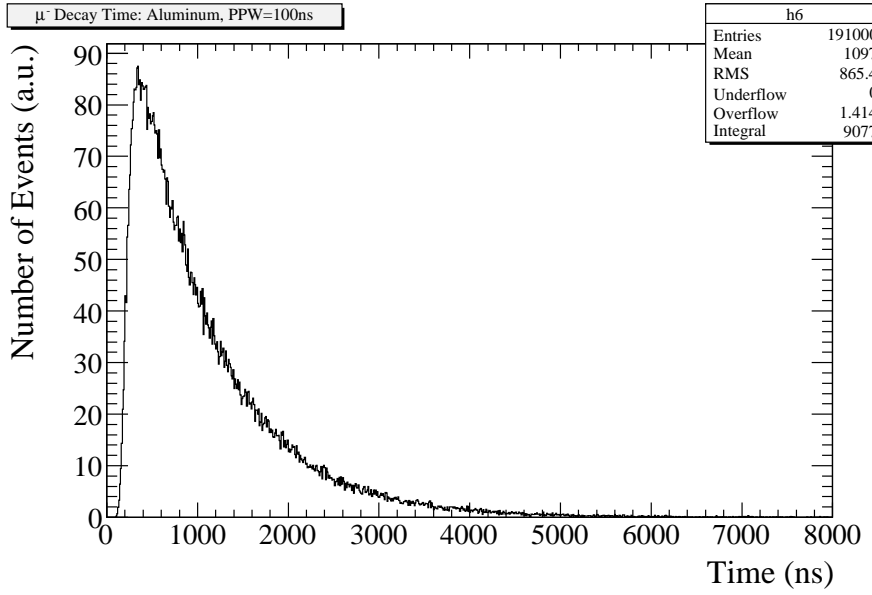


Figure 11.1: Time distribution of muon decays for an aluminum target. The lifetime of muons on Al is 864 nsec, and the width of the proton pulses is 100 nsec.

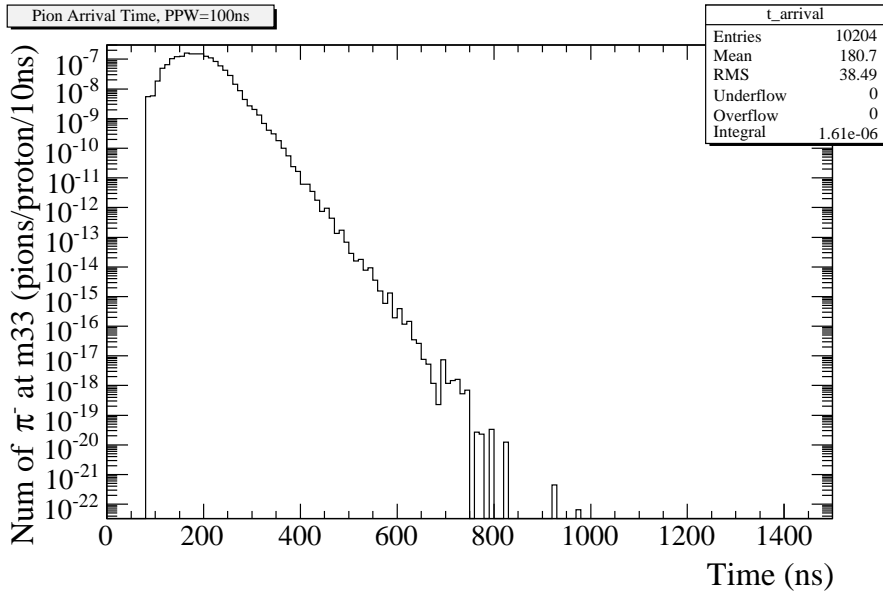


Figure 11.2: Time distribution of pion arrival at the muon stopping target. The histogram was made in such a way that pion decay was turned off and later survival probability was convoluted.

11.1.5 Single event sensitivity

The single event sensitivity is expressed as

$$B(\mu^- + \text{Al} \rightarrow e^- + \text{Al}) = \frac{1}{N_\mu^{stop} \cdot f_{cap} \cdot A_{\mu-e}}, \quad (11.4)$$

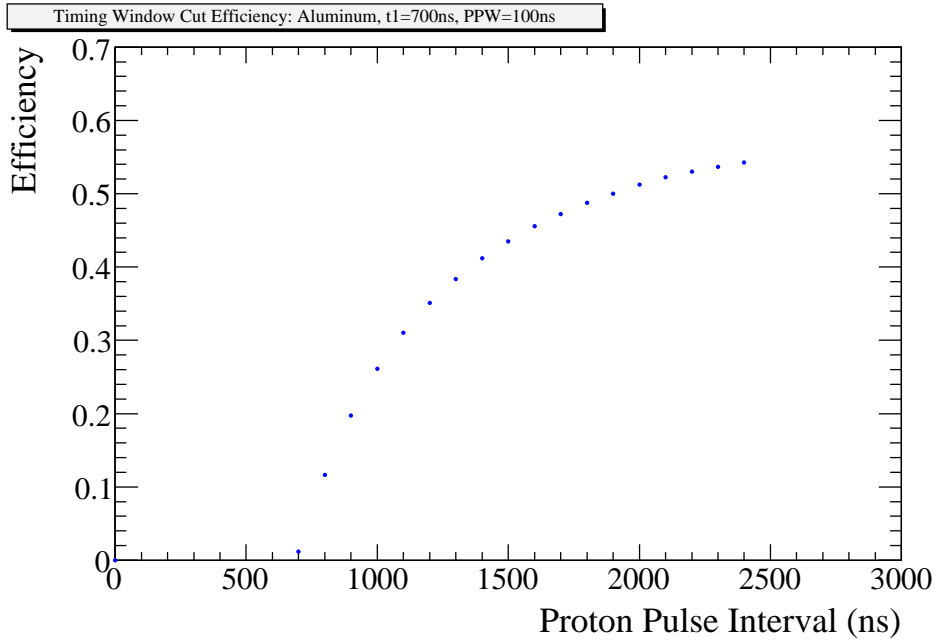


Figure 11.3: The acceptance of the time window cut ε_{time} as a function of the proton pulse interval T_{sep} for the aluminum target. The lifetime of muons on Al is 864 nsec and the width of the proton pulses is 100 nsec. $T_{sep}=1.314 \mu\text{s}$ gives ε_{time} of 0.39.

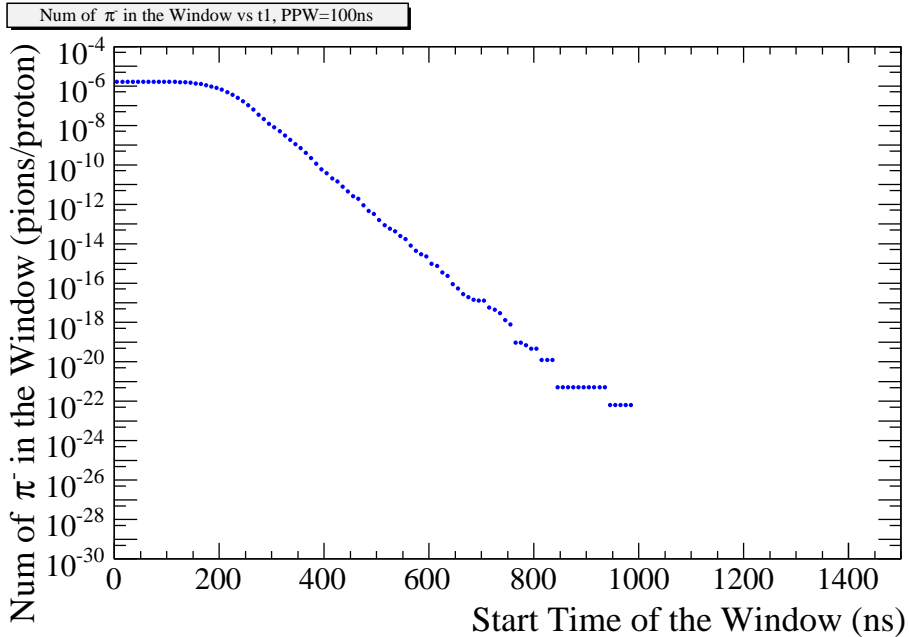


Figure 11.4: Expected numbers of pions in the time window of measurement, $N_{win}^{\pi^-}$, as a function of its starting time, t_1 . The number was given by integration of Fig. 11.2 from t_1 to the time that the next prompt particle arrive. Selecting $t_1=700$ nsec, $N_{time}^{\pi^-}$ is $1 \times 10^{-17} \pi^-/\text{proton}$.

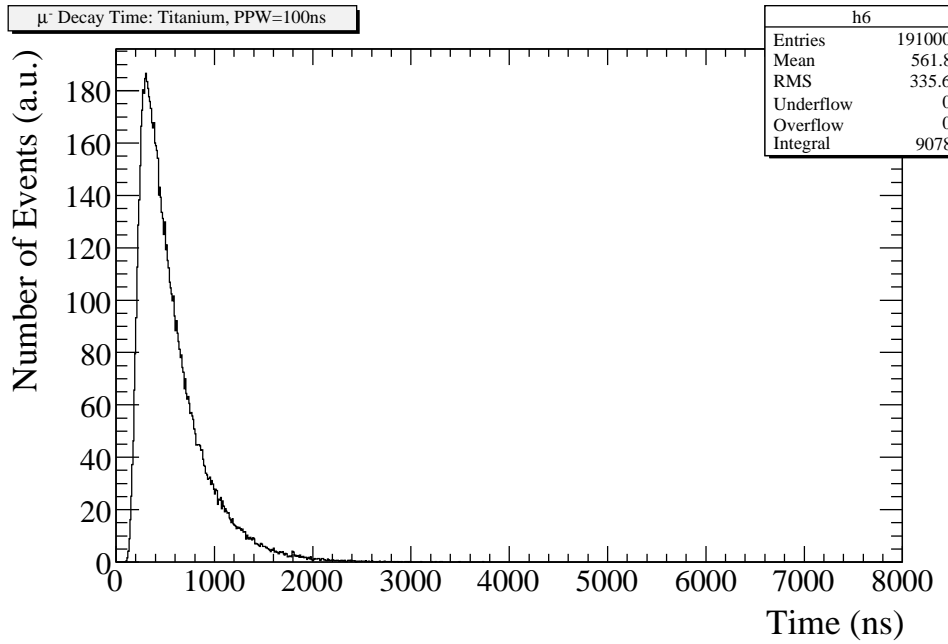


Figure 11.5: The time distribution of the muon decay time for the titanium target. The lifetime of muons on Ti is 330 nsec and the width of the proton pulses is 100 nsec.

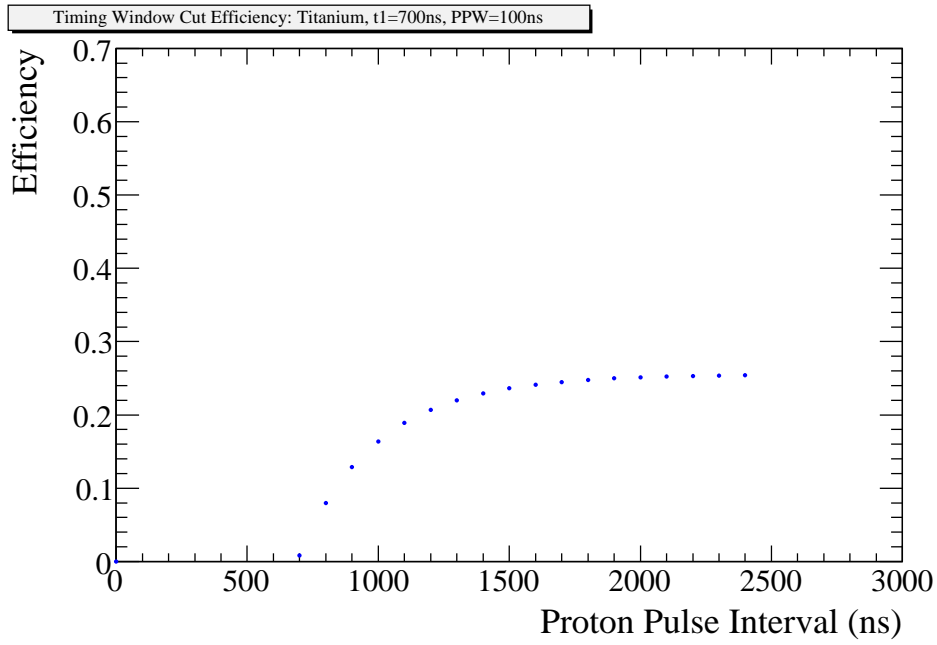


Figure 11.6: The acceptance of the time window cut ε_{time} as a function of the proton pulse interval T_{sep} for the titanium target. The lifetime of muons on Ti is 330 nsec, and the width of the proton pulses is 100 nsec.

where N_μ^{stop} is the number of muons stopping in the muon target, f_{cap} is the fraction of muon capture and $A_{\mu-e}$ is the detector acceptance. The fraction of muon capture for Aluminum is $f_{cap} = 0.61$.

Table 11.3 shows a summary of the signal sensitivity. The single event sensitivity of 2.6×10^{-17} can be achieved for 2×10^7 sec running.

Table 11.3: Summary of the expected sensitivity for 2.0×10^7 sec running.

Total number of protons: N_p	8.5×10^{20}	
Proton kinetic energy	8	[GeV]
Harmonics of MR	8	
Bunch time spacing	657	[nsec]
Number of RF bunches filled with protons per spill	4	
Time between adjacent filled bunches	1314	[nsec]
Number of protons in each RF bunch	1.6×10^{13}	
Cycle time of MR (=spill period)	1.47	[sec]
Flat top for the slow extraction	0.7	[sec]
Number slow-extracted pulse in a spill	5.3×10^5	[pulses/spill]
Number of Protons in each slow-extracted pulse	1.2×10^8	
Average beam current	7.0	[μ A]
Average beam power	56	[kW]
Average proton intensity	4.4×10^{13}	[protons/sec]
Total running time	2.0×10^7	[sec]
Running time per year	1.0×10^7	[sec/year]
Number of stopped muons per proton: $N_{\mu/p}^{stop}$	0.0023	[muons/proton]
Rate of muons per proton transported to the target	0.0035	[muons/proton]
Muon stopped acceptance	0.66	
Number of stopped muons: $N_{\mu/year}^{stop}$	1.0×10^{18}	[muons/year]
Total number of stopped muons: N_μ^{stop}	2.0×10^{18}	
Fraction of captured muon: f_{cap}	0.61	
Net acceptance: $A_{\mu-e}$	0.031	
Geometrical acceptance, fitting and selection criteria	0.09	
<i>Solid angle with mirroring acceptance</i>	(0.73)	
<i>Muon beam stop acceptance</i>	(0.57)	
<i>Curved solenoid acceptance</i>	(0.47)	
<i>Track reconstruction efficiency</i>	(0.88)	
<i>Track quality cut efficiency</i>	(0.89)	
<i>Transverse momentum cut efficiency</i>	(0.83)	
<i>E/p cut efficiency</i>	(0.99)	
<i>Helix pitch cut efficiency</i>	(0.99)	
<i>Momentum selection efficiency</i>	(0.72)	
Timing window selection efficiency	0.39	
Trigger acceptance and DAQ live efficiency	0.90	
Single event sensitivity = $(N_p \cdot N_{\mu/p}^{stop} \cdot f_{cap} \cdot A_{\mu-e})^{-1}$	2.6×10^{-17}	
90% confidence level upper limit	6.0×10^{-17}	
Events per 1×10^{-16} BR	3.8	

11.2 Background rejection

Potential background sources in the COMET experiment are grouped into four categories:

1. intrinsic physics backgrounds,
2. beam-related prompt backgrounds,
3. beam-related delayed backgrounds, and
4. cosmic background and other backgrounds.

Table 11.4 shows a list of some candidate backgrounds. They will be discussed below.

The intrinsic physics backgrounds come from muons that are stopped in the muon stopping target. They are called “physics backgrounds” because they appear from different muonic physics processes. Suppression of the physics backgrounds can only be achieved by improving the detection system.

The beam-related backgrounds are produced by any beam particles other than the muons stopped in the muon-stopping target. There are two groups for the beam-related backgrounds: one of which is those arising from protons leaking between the beam pulse (which is called “beam-related prompt background”), and the other is those which are produced by protons in the prompt pulses but arrive late between the beam pulses (which is called “beam-related delayed background”). For suppression of the former, the proton beam extinction is critical. The requirement of the on/off ratio of proton beam extinction of less than 10^9 is required at a signal sensitivity of less than 10^{-16} . For the latter, slowly-arriving particles of long (or relatively long) lifetime are important to consider. One of the

Table 11.4: Backgrounds.

Beam related prompt BG	
Radiative pion capture	$\pi^- + A \rightarrow \gamma + A'$ and $\gamma \rightarrow e^- + e^+$
Beam electrons	e^- scattering off a muon stopping target
Muon decay in flight	μ^- decays in flight to produce e^-
Pion decay in flight	π^- decays in flight to produce e^-
Neutron induced backgrounds	neutrons hit material to produce e^-
Beam Related Delayed BG	
Delayed-pion radiative capture	$\pi^- + A \rightarrow \gamma + A'$, $\gamma \rightarrow e^- + e^+$
Anti-proton induced backgrounds	\bar{p} hits material to produce e^-
Physics BG	
Muon decay in orbit	Decay of muons bound in a muonic atom
Radiative muon capture	$\mu^- + A \rightarrow \nu_\mu + A'$, $A' \rightarrow \gamma + A$, and $\gamma \rightarrow e^- + e^+$
μ^- capture with neutron emission	$\mu^- + A \rightarrow \nu_\mu + A'$, $A' \rightarrow n + A$, and neutrons produce e^-
μ^- capture with charged particle emission	$\mu^- + A \rightarrow \nu_\mu + A'$, $A' \rightarrow p(d, \alpha) + A$, and $p(d, \alpha)$ produce e^-
Cosmic BG	
Cosmic-ray induced backgrounds	

Table 11.5: Partial lifetimes of muon capture processes and their total lifetimes of μ^- s for various materials.

	Hydrogen	Aluminum	Titanium	Lead
Atomic number (Z)	1	13	22	82
Partial Lifetime (μs)		1.47	0.39	0.085
Lifetime of μ^- (μs)	2.2	0.88	0.33	0.082
DIO:MC	100:0	40:60	15:85	4:96

background candidates is anti-protons which are very slow. As another candidate, pions, which are copiously produced at the pion-production target, might have a finite probability coming late, depending on their pitch angle of helical trajectories.

The cosmic-ray backgrounds are one of the serious potential background sources. The number of the expected cosmic-ray background events is proportional to the total active running time of the measurement. There are several ways to suppress cosmic-ray backgrounds, such as (1) to veto them by active shielding, (2) to reduce the cosmic-ray fluxes of low energy by passive shielding, (3) event selection and (4) to minimize the total running time with a higher muon flux. The items (1) and (2) might cover not only the detector but also the muon beam line (to some extent). Item (4) requires improvement of detection which can run at a higher counting rate and it is not the option yet.

In the following sections, all of these backgrounds will be described in detail.

11.2.1 Intrinsic physics background

Negative muons stopped in a material are immediately trapped by the Coulomb potential of the nucleus of the material, and fall down to the 1S orbit. There are two major allowed processes in which a bound μ^- could proceed. They are

1. muon decay in orbit (DIO), and
2. nuclear muon capture (NMC).

These processes are allowed in the Standard Model at a high rate and become potential backgrounds in the search for $\mu^- - e^-$ conversion.

11.2.1.1 Muon decay in orbit

Muon decay in orbit (DIO) is a Michel decay $\mu^- \rightarrow e^- \nu_\mu \bar{\nu}_e$ of the muons that are bound in a muonic atom, under a Coulomb potential of the nucleus. Because of recoil of the nucleus, an electron from the Michel decay can be boosted, obtaining a high energy. The maximum energy of the e^- exceeds the end point energy of the ordinary Michel decay of 58.3 MeV and extends to the momentum region of the $\mu^- - e^-$ conversion signal.

The width of DIO process is obviously $1/2.2 \mu\text{s}$. The width of NMC depends on atomic Z of the material due to the difference in the overlap of the muon wave function and nucleus. It is smaller for small- Z material than large- Z material. Table 11.5 shows comparison between several different materials. We assumed that the material for the muon stopping target is Aluminum in the background study.

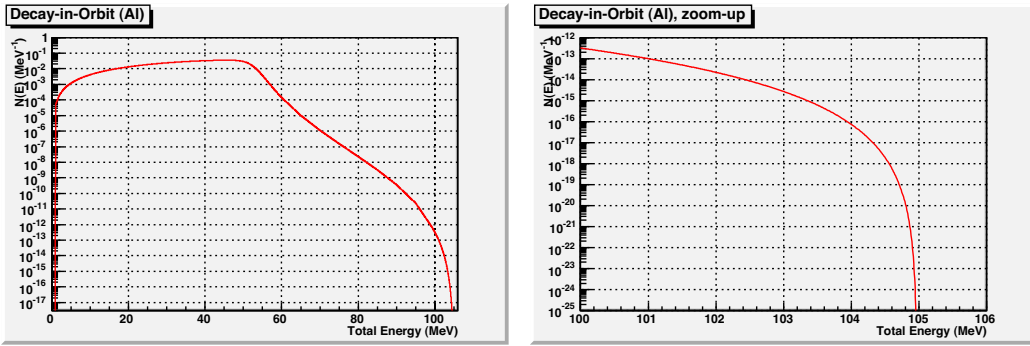


Figure 11.7: Total energy spectrum of electrons from muon decays in orbit for Aluminum.

The probability of a μ^- DIO having stopped in the Aluminum target is 40%. The energy spectrum of electrons from DIO is very similar to the Michel decay in free space. The difference lies in high momentum region in which the ordinary Michel decay should never produce electrons. Since DIO occurs in the Coulomb potential of nucleus, the nucleus recoils to share the final-state momenta and compensate momentum balance. As a result, the maximum energy of DIO electrons extends to the same energy of $\mu^- - e^-$ conversion electron. However, the intensity decreases rapidly with increasing electron energy. The spectrum shape is known to be approximated by $(E_{\mu-e} - E_e)^5$. Therefore, DIO electrons can be suppressed by raising the lower energy threshold of $\mu-e$ signal region at a cost of acceptance loss.

The DIO spectrum is expressed by the following formula [113]:

$$N_{\text{Shanker}}(E_e)dE_e = \left(\frac{E_e}{m_\mu}\right)^2 \left(\frac{\delta_1}{m_\mu}\right)^5 \left[D + E \cdot \left(\frac{\delta_1}{m_\mu}\right) + F \cdot \left(\frac{\delta}{m_\mu}\right) \right] dE_e, \quad (11.5)$$

where m_μ is the mass of the muon, $\delta \equiv E_{\max} - E_e$, $\delta_1 \equiv E_\mu - E_e - E_{\text{rec}}$. E_{\max} is the end-point energy (maximum electron energy), $E_\mu \equiv E_{\max} + E_{\max}^2/(2M_A)$, and E_{rec} is the nuclear-recoil energy given by $E_{\text{rec}} \equiv E_e^2/(2M_A)$. M_A is the mass of the recoiling nucleus. Coefficients D , E and F are functions of the Z number of nucleus, and given in a table in the article [113] for $Z = 12, 16, 18, 23, 25, 29, 34, 45, 55, 65$ and 82 . In this study, the coefficients for Aluminum ($Z = 13$) were calculated by linear interpolations; $D = 0.388 \times 10^{-21}$, $E = 1.03 \times 10^{-21}$, and $F = 2.27 \times 10^{-21}$.¹ The value E_μ is expressed as $E_\mu \equiv m_\mu - BE$, where BE is the muon binding energy. The muon binding energy for Aluminum is [114] 0.463 MeV, and thus the E_μ for Aluminum is $E_\mu = 105.195$ MeV, and the end-point energy is $E_{\max} = 104.97$ MeV.²

Since the Equation 11.5 is not valid for lower momentum region, $E_e < 90$ MeV, we took another spectrum given in [114], which is believed to be valid from 1 MeV up to 100 MeV. Both spectra were connected smoothly at around $E_e = 97$ MeV. Then, the total integration of the combined spectrum was normalized to a single decay of a bound muon. The electron total energy spectrum thus obtained is shown in Fig. 11.7. A GEANT4 Monte Carlo calculation was performed in order to estimate the number of DIO electrons in the signal region. The calculation was started from DIO electrons generated in the

¹ D , E , and F used in this study are slightly different from the values shown in the proposal, ($D = 0.36 \times 10^{-21}$, $E = 0.95 \times 10^{-21}$, and $F = 2.27 \times 10^{-21}$). This produces only a 5% of difference and it is negligibly small.

²The end-point energy of Aluminum given in [113] is 105.0 MeV.

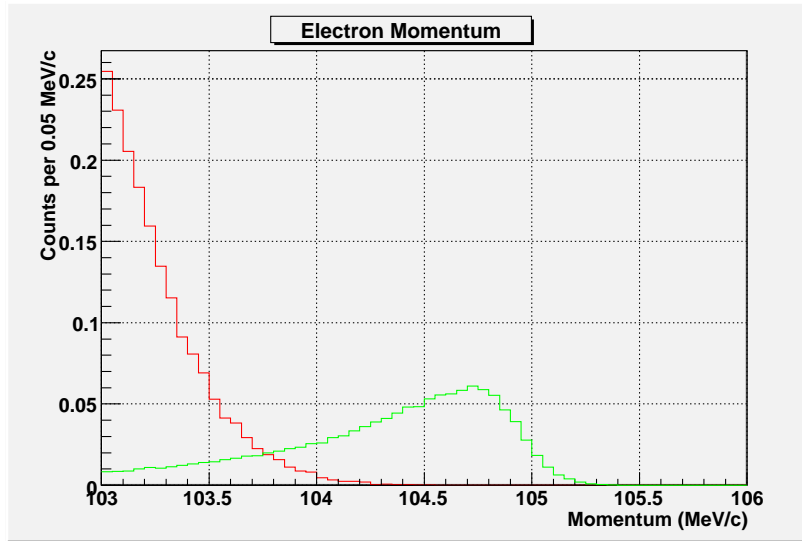


Figure 11.8: Electron momentum spectra of $\mu^- - e^-$ conversion signal and DIO background from a muonic atom of Aluminum. Both spectra correspond to 10^{20} stopped muons, which is 100 times more than the expected muon yield. The branching ratio if assumed to be 10^{-16} for $\mu^- - e^-$ conversion spectrum. The horizontal axis is the reconstructed momentum from the electron tracker system.

muon stopping target disks. The electron energy was generated according to the spectrum shown in Fig. 11.7. In order to complete the Monte Carlo calculation within a reasonable time, electrons with momentum larger than 103 MeV were generated. The fraction of such electrons is 8.8×10^{-16} . Figure 11.8 shows reconstructed electron momentum for both DIO and $\mu-e$ signal electrons. The generated number of electrons corresponds to 10^{20} stopped muons, which corresponds to 100 times the number for the proposed experiment. Standard analysis was applied for those spectra except for the momentum cut and the time window cut. After applying the time window cut and the momentum cut, the expected number of DIO electrons in the signal region ($103.5 < E_e < 105.2$ MeV) is 0.15. If we make the signal region narrower to $104.0 < E_e < 105.2$ MeV, the expected DIO background becomes 0.011 and the signal acceptance decreases by 22%. We use the standard cut ($103.5 < E_e < 105.2$ MeV) for this report.

11.2.1.2 Radiative muon capture

Muon nuclear capture is analogous to electron capture. It is given by

$$\mu^- + N(N, Z) \rightarrow \nu_\mu + N(N, Z - 1). \quad (11.6)$$

The daughter nucleus produced by nuclear muon capture is usually in an excited state and may emit γ s, neutrons and charged particles through de-excitation. They would become sources of fake signals.

Radiative muon capture (RMC),

$$\mu^- + N(A, Z) \rightarrow \nu_\mu + N(A, Z - 1) + \gamma, \quad (11.7)$$

followed by asymmetric e^+e^- conversion of the photon, is another source of intrinsic background events. In an Aluminum target, it is $\mu^- + \text{Al} \rightarrow \nu_\mu + \text{Mg} + \gamma$, where the endpoint of photon energy is 102.5 MeV. The probability per muon capture of producing a photon with energy exceeding 100.5 MeV is about 4×10^{-9} [115]. The conversion probability of a photon in the target is about 0.005, and the probability that the energy of the electron produced from the photon conversion exceeds 100 MeV is about 0.005. Thus, The probability of producing an electron above 100 MeV is about 10^{-13} . These electrons are all less than 102 MeV. It is only possible to observe such electrons in the signal region ($103.5 < E_e < 105.2$ MeV) if the tracking system mis-measures the electron momentum by more than 2.0 MeV larger than the real momentum. The probability of such a mis-measurement is evaluated to be less than 10^{-5} . This type of mis-measurement will occur due to errors in the pattern recognition of the tracker. In COMET, the average number of hits to the tracker plane in the detection time window is only 1 per proton pulse, and thus the pattern recognition error rarely occurs. The acceptance of the analysis without time window and total momentum cut is 0.13. The background rate from RMC is about < 0.001 at the signal sensitivity of 10^{-16} .

11.2.1.3 Muon capture with neutron emission

A typical energy spectrum of neutrons emitted from the muon capture process is shown in Fig. 11.9. The structure of the spectrum is decomposed to three parts as shown in the Fig. 11.9. The first part dominates the low energy region (< 7 MeV), which can be explained by the neutron evaporation of the excited daughter nucleus. The typical temperature of the excitation is about 1 MeV. The fraction of this component is almost 90%. However, there is no process to produce 100 MeV electrons from such a low energy neutron. Therefore, we focused on the other two components that could produce high energy neutrons and thus high energy electrons. In these processes, high energy neutrons are directly produced by the elemental process of the muon capture,

$$\mu^- + p \rightarrow \nu_\mu + n. \quad (11.8)$$

This neutron will escape the nucleus (direct process) or kick another neutron's escape (precompound process). Since the maximum energy of those neutrons will extend up to 100 MeV, it could produce background electrons if the neutron hit a nucleus and produced high energy photons which then convert to electron.

The inclusive energy spectrum for neutrons emitted after muon capture for Si and Ca is shown in Fig. 11.10, which is measured in Ref. [117]. They are consistent with an exponential dependence on the neutron energy given by the expression $P(E) = \exp(-\alpha E_n + \beta)$. The fit results for Si and Ca are summarized in Table 11.6. Since the probability is not much different for different materials, the values of Si are used for aluminum.

Background electrons coming from the neutrons from muon capture were estimated by GEANT3 simulation with GCALOR as a hadron package. The estimated background contamination into the signal region is less than 0.001.

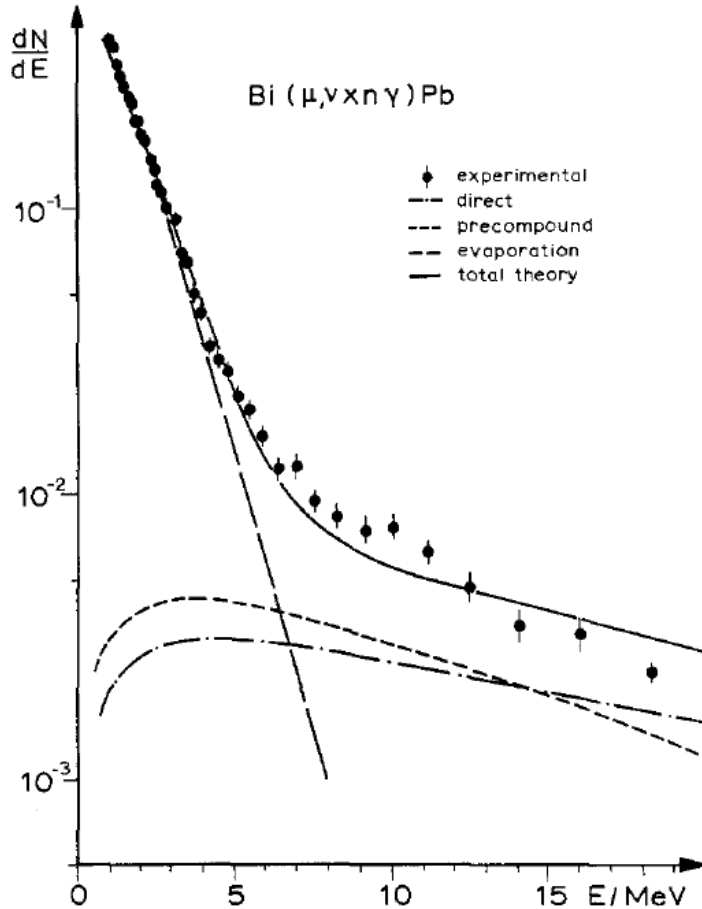
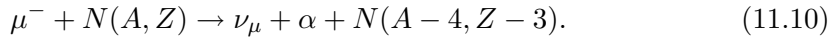
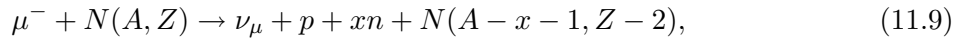


Figure 11.9: Experimental and theoretical neutron spectrum from the muon capture by Bi. The vertical scale is given in units per capture. This figure is reprint from [116]

11.2.1.4 Muon capture with charged particle emission

With a much lower probability than neutron emission, there are reaction channels involving the emission of protons and α -particles.



where (A, Z) is a nucleus with a mass number of A and an atomic number Z . From the cross section table in Ref. [118], the partial reaction probability of muon capture with charged particles is plotted against the Coulomb barrier. The classical Coulomb barrier V is calculated as

$$V = \frac{zZ'e^2}{r_0 A^{1/3} + \rho} \quad (11.11)$$

$$V[\text{MeV}] = \frac{zZ}{r_0[\text{fm}] A^{1/3} + \rho[\text{fm}]} \frac{197.3}{137.0} \quad (11.12)$$

where z and Z' are the charges of the outgoing particles and of the residual nucleus, respectively. r_0 is taken as 1.35 fm, and ρ as 0 fm for protons and 1.2 fm for α -particles. For

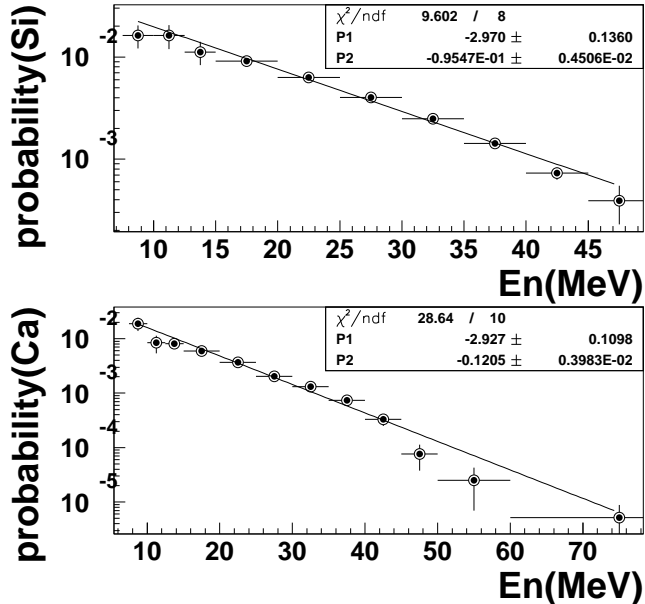


Figure 11.10: Probability of muon capture with a neutron as a function of neutron kinetic energy (E_n) for Si and Ca.

Table 11.6: The probability of muon capture with neutrons emission for Si and Ca by the expression of $P(E) = \exp(-\alpha E_n + \beta)$.

	α	β
Si	-0.096 ± 0.005	-2.970 ± 0.136
Ca	-0.121 ± 0.004	-2.927 ± 0.110

example, V for Aluminum is calculated as 5.4 MeV and 7.2 MeV for protons and α -particles, respectively. The probability of muon capture with outgoing charged particles is expressed an exponential function of the Coulomb barrier, and the results are summarized in Table 11.7. In Table 11.7, the probability for Aluminum and Titanium is also shown.

The kinetic energy spectrum of the outgoing charged particles is expressed as

$$P(E_c) = P_0 \exp(-E_c/E_0), \quad (11.13)$$

where P_0 is a normalization constant and E_c is the kinetic energy spectrum of the outgoing charged particles and E_0 is a parameter to determine the shape of the spectrum distribution [119]. The E_0 is expressed as a function of Z , which is shown in [119] as a table. Fitting a linear function, E_0 is determined as,

$$E_0 = 0.03614 \cdot Z + 7.103. \quad (11.14)$$

For aluminum ($Z=13$), E_0 is 7.6 MeV.

Table 11.7: The probability of muon capture with outgoing charged particles as a function of $\exp(\alpha V + \beta)$, where V is the Coulomb barrier. The probability for Al and Ti is also shown.

Reaction	α	β	Al	Ti
$P(p)$	-0.379 ± 0.017	-3.631 ± 0.187	5.2×10^{-3}	2.5×10^{-3}
$P(pn)$	-0.371 ± 0.022	-1.910 ± 0.186	3.0×10^{-2}	1.5×10^{-2}
$P(p2n)$	-0.383 ± 0.024	-2.104 ± 0.211	2.3×10^{-2}	1.1×10^{-2}
$P(p3n)$	-0.338 ± 0.121	-2.504 ± 1.141	1.9×10^{-2}	1.0×10^{-2}
$P(\alpha)$	-0.460 ± 0.030	-2.203 ± 0.267	7.0×10^{-3}	1.5×10^{-3}

Background electrons produced by charged particles from muon capture are estimated by GEANT3 simulation. In this simulation, GCALOR is used as the hadron package. The background is estimated to be less than 0.001.

11.2.2 Beam-related prompt background

As described, the beam-related prompt backgrounds are those arising from protons leaking between the beam pulse. These backgrounds are suppressed by the proton beam extinction.

11.2.2.1 Radiative pion capture

The radiative pion capture (RPC) background is caused by pions contaminated in the muon beam. Those pions are stopped in the muon stopping target, and are captured by an aluminum nucleus *immediately* to form an excited state of the daughter nucleus.

There are two processes, one of which produces directly a γ ray of high energy (direct process) and the other produces γ rays as an evaporate process of the excited daughter nucleus to their ground state. During these processes, a probability of γ ray emission is as high as 2%. Some of such emitted γ rays convert into e^- and e^+ in the target or in material outside the target. When the e^+e^- pair creation occurs in an asymmetric energy distribution and the e^- has a high energy, it would mimic $\mu^- - e^-$ conversion signals.

The probability of γ emission and the energy spectrum of γ s were extensively studied experimentally and theoretically more than 20 years ago. According to [120], the probability of γ emission has very small Z dependence. It is almost 2% for C, O, and Ca as shown in Table 11.8. The energy of γ from RPC ranges from 50 MeV to 140 MeV as shown

Table 11.8: Experimentally measured branching ratios of radiative pion capture. This table was taken from the Table 4 in [120].

^{12}C	$1.84 \pm 0.08, 1.92 \pm 0.91, 1.6 \pm 0.1$
^{16}O	$2.27 \pm 0.24, 2.24 \pm 0.48$
^{40}Ca	1.82 ± 0.05

in Fig. 11.11 The overall shapes of the spectra are very similar between C, O, and Ca. Therefore, we implemented the experimentally obtained spectrum for Ca to our Monte Carlo code for this study.

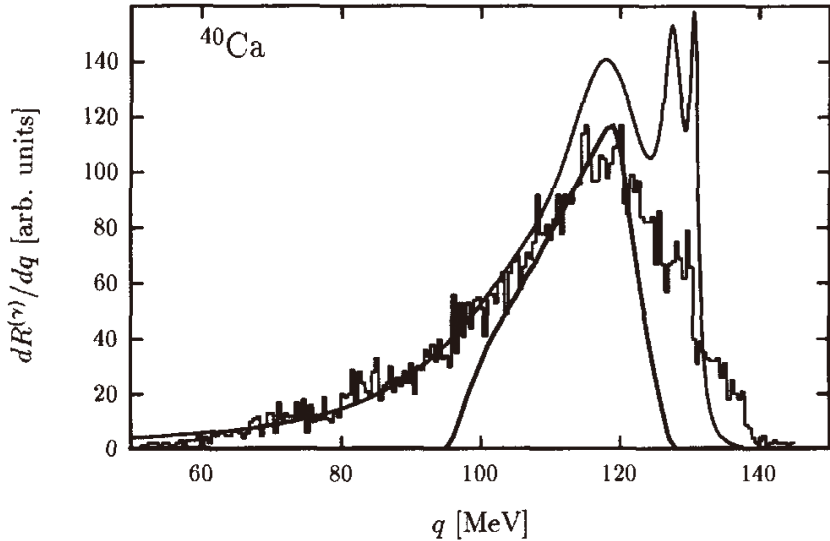


Figure 11.11: Momentum distribution of γ s from RPC. This figure was reprinted from [120]. The histogram is experimental data, and the lines are from some theoretical models.

The number of RPC backgrounds is expressed as

$$N_{\text{RPC}} = N_p \times R_{\text{extinction}} \times R_{\pi-\text{stop}/p} \times P_{\text{RPC}} \times P_{\gamma-e^-} \times A_{\text{geometry}} \times A_{\text{analysis}}, \quad (11.15)$$

where N_p is a total number of protons on the pion production target, $R_{\text{extinction}}$ is an extinction ratio of proton beam, $R_{\pi-\text{stop}/p}$ is a ratio between number of stopped π^- in a muon stopping target and number of initial protons, P_{RPC} is a branching ratio of gamma emission in the pion capture process, $P_{\gamma-e^-}$ is a probability of RPC-gamma converting to an electron probably in the muon stopping target, A_{geometry} is a detector acceptance of RPC-originated electrons in a μ -e signal region A_{analysis} is an analysis acceptance.

Parameters that have to be evaluated specifically for COMET are $R_{\pi-\text{stop}/p}$, $P_{\gamma-e^-}$, A_{geometry} , and A_{analysis} . In order to estimate those numbers, a Monte Carlo simulation was performed. Fifty million primary protons were generated to hit a production target made from Carbon by using MARS simulation code. Pions thus produced were transported through the muon beamline using G4beamline. A beam collimator placed at the exit of the muon beamline blocked most of pions. As a result, there is only 17.7 of π^- s out of 50M protons stopped in the muon stopping target: $R_{\pi-\text{stop}/p} = 3.5 \times 10^{-7}$. Please note that, since the number of π^- passing through the beam collimator is 24, $R_{\pi-\text{stop}/p} < 4.8 \times 10^{-7}$ even if the target thickness is increased to make all the pions stop in the muon stopping target.

In order to estimate other parameters, another Monte Carlo simulation was performed.

The simulation was started from RPC gamma rays generated directly inside the muon stopping target. The position of the gamma ray was uniformly distributed in the 17 target disks. The direction of the gamma was symmetric and the energy spectrum obeyed that of Fig. 11.11. The total number of gammas generated was 200 k, and 78 electrons arrived at the detector section. The number of electrons from 100 MeV/c to 105 MeV/c is only 8, thus the number of electrons entering to the signal region (103.5–105.2 MeV/c) would be only 3: $P_{\gamma-e^-} \times A_{\text{geometry}} = 1.4 \times 10^{-5}$.

The analysis efficiency for the RPC-gamma-produced electrons is broken down into the following components: They are track reconstruction efficiency of 88%, track quality cut efficiency of 89%, transverse momentum cut acceptance of 83%, and the other cuts (90%). Therefore, $A_{\text{analysis}} = 58\%$. These numbers are all the same as that for the signal electrons. The time window cut is not applied since the RPC background that is discussed here is a prompt background.

The rest of the parameters are quite trivial. N_p is 8.8×10^{20} for 2-years running. $R_{\text{extinction}}$ is 10^{-9} in this study, P_{RPC} is known to be 2%. As a result, we obtained $N_{\text{RPC}} = 0.05$.

11.2.2.2 Beam electrons

Beam electron background is caused by electrons contaminating in the muon beam. Electrons will scatter off the muon-stopping target and fake the signal electrons if the electron momentum is in the signal region (103.5–105.2 MeV/c). The number of beam electron background is express by

$$N_{e-\text{scat}} = N_p \times R_{\text{extinction}} \times R_{e-\text{col out}/p} \times R_{<95 \text{ MeV}/c} \times P_{e-\text{det}}, \quad (11.16)$$

According to the Monte Carlo simulation using MARS and G4beamline, There are 3067 electrons passing through the beam collimator for 50M primary protons. Therefore, the ratio between the number of electrons downstream of the beam collimator and the number of primary protons is $R_{e-\text{col out}/p} = 6 \times 10^{-5}$. The momentum distribution of electrons downstream of the beam collimator is peaked at 40 MeV/c, and quickly falls off as momentum increases. The number of electrons with momentum larger than 95 MeV/c in this simulation was zero.

Increasing the total number of protons in the simulation is not realistic due to the necessary CPU time. We modeled the momentum versus y -position distribution of electrons by using -1.24 MeV/cm of momentum dispersion. The momentum distribution at the same y -position is approximated by a Gaussian. Then, these electrons were passed through the beam collimator to produce the momentum distribution of electrons at the exit of the beam collimator. The ratio between the electrons with $p_e > 95$ MeV/c to the total number of electrons downstream of the beam collimator was obtained to be $R_{<95 \text{ MeV}/c} = 1.7 \times 10^{-5}$.

The probability of high-momentum (P_{total}) electrons scattered off the muon-stopping target and hit the detector is about 0.5%, which is not small enough to suppress the background. In order to achieve extra rejection to the beam electron background, the event selection using electron p_T is employed. Since the p_T of scattered electrons (with 90 MeV/c $< p < 110$ MeV/c) are mostly less than 50 MeV/c, the event selection with $p_T > 50$ MeV/c will provide background rejection of about two orders of magnitudes at a cost of 17% loss of signal acceptance (Transverse momentum cut acceptance). After all, the probability of scattered high-momentum electrons entering to the signal region is $P_{e-\text{det}} < 5.5 \times 10^{-5}$ (90% C.L.).

As a result, we obtained

$$N_{e\text{-scat}} < 0.1, \quad (11.17)$$

and this is limited by Monte Carlo statistics.

11.2.2.3 Muon decay in flight

Muons decaying in flight can produce energetic electrons that have sufficient total momentum (of about $p_{\text{total}} > 102 \text{ MeV}/c$) and transverse momentum (of about $p_T > 50 \text{ MeV}/c$). For the decay electrons to have $p_{\text{total}} > 102 \text{ MeV}/c$, the muon momentum must exceed $77 \text{ MeV}/c$ ($p_\mu > 77 \text{ MeV}/c$). A Monte Carlo simulation has been done to estimate the yield of muons of $p_\mu > 77 \text{ MeV}/c$ transported through the muon beam line and entering to the target region. The result is about 10^{-6} per incident proton. The probability for muons to decay in flight in the muon beam line is about 3×10^{-2} . The probability of having an electron energy of $103 \text{ MeV}/c < p_{\text{total}} < 105 \text{ MeV}/c$, and $p_T > 50 \text{ MeV}/c$ is less than 10^{-8} . With the beam extinction of 10^{-9} , the total background level from muon decay in flight is less than 0.0002. It improves the number obtained for MECO by two orders of magnitudes. The reason of the improvement may be the much higher momentum dispersion of the COMET muon beamline compared to that of MECO.

11.2.2.4 Pion decay in flight

Beam pions decaying to electrons ($\pi \rightarrow e + \nu$) are also a potential source of background. The π momentum must exceed $60 \text{ MeV}/c$ to make this background process. A Monte Carlo simulation was done to estimate the probability of pions with $p_\pi > 60 \text{ MeV}/c$ passing though the muon beam line and a beam collimator to enter the target region. The probability is only about 6×10^{-8} . The branching ratio of $\pi \rightarrow e + \nu$ is about 1.0×10^{-4} . The probability of the decay electron from $\pi \rightarrow e + \nu$ to have $E_e > 102 \text{ MeV}$ and $p_T > 50 \text{ MeV}/c$ is about 5×10^{-6} . With the beam extinction factor of 10^{-9} , the background level from pion decay in flight is less than 10^{-4} .

11.2.2.5 Neutron induced background

Background induced by neutrons in a beam with high kinetic energy coming through the muon beam line is estimated. Those neutrons could pass through the muon beam line by continuously reflecting from its inner sides. The neutrons which can produce electrons of 100 MeV must exceed its kinetic energy of 100 MeV. The rate and energy distribution of neutrons whose kinetic energy is more than $100 \text{ MeV}/c$ were examined by MARS simulations. It is about 3×10^{-7} neutrons/proton. And by using GEANT3 Monte Carlo simulation, an average transit time of those neutrons arriving at the muon stopping target is estimated and it is about 300 nsec, and much less than the waiting time of 700 nsec before detection window opens. Therefore, it is regarded as a prompt background. By using GEANT3 Monte Carlo simulation, the probability for those neutrons to produce electrons of about 100 MeV in energy was estimated and found to be about 10^{-7} . With the beam extinction of 10^{-9} , the background rate of neutron induced of this type is about 0.024.

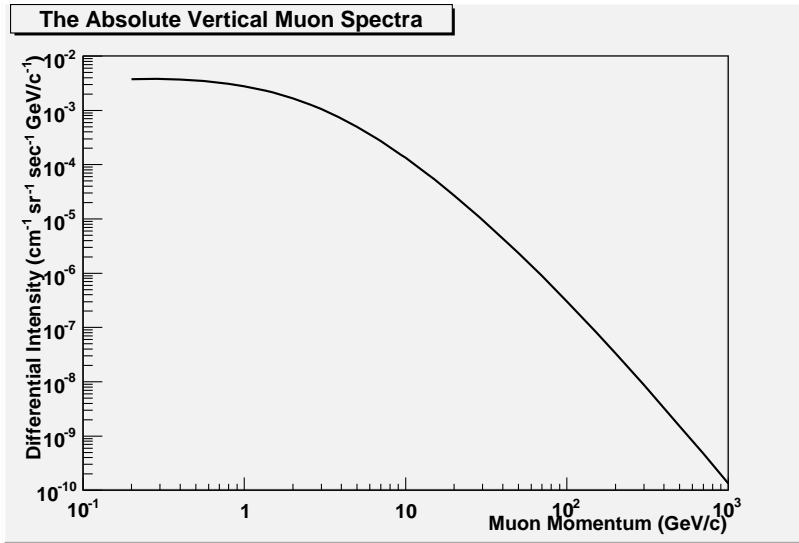


Figure 11.12: The absolute vertical muon spectrum.

11.2.3 Beam related delayed background

11.2.3.1 Radiative capture of delayed pions

This background is caused by RPC coming from late-arriving pions which take a very long time to traverse and arrive at the muon-stopping target very late. For those events, the proton extinction does not apply a rejection. However, since the detection window starts about 700 nsec after the proton pulse, those pions should live longer than 700 nsec. The probability for those late arriving pions surviving longer than 700 nsec is 1×10^{-17} (Figure 11.4) which should replace $R_{\text{ext}} \times R_{\pi-\text{stop}/p}$ in Eq.(11.15). As a result, the expected number of RPC background of this type is about 0.002 events. Please note that, this type of background is easily monitored by measuring the number of energetic electrons as a function of event time after the proton pulse. The detection time window can be appropriately adjusted during the analysis stage.

11.2.4 Cosmic ray background

Cosmic ray induced background can be divided into two categories:

1. Cosmic muons directly hitting the detector,
2. Electrons induced by cosmic muons hitting the detector.

A GEANT4 Monte Carlo calculation was performed to estimate the cosmic muon included backgrounds. In the calculation, the target solenoid, curved solenoid and detector solenoid were all covered by an iron shield with 70 cm thickness. The iron shield works as return yoke of the magnets, thus there should be a magnetic flux inside of the iron shield. However, for this particular calculation, the magnetic flux is assumed to be zero for the inside of the iron shields.

A vertical flux of cosmic muons at sea level is shown in Fig. 11.12 [121]. The angular distribution of cosmic muons is known to be $\propto \cos^2 \theta$ for typical muon energies ($\simeq 3$ GeV),

and it becomes steeper as the energy decreases and it flattens as the energy increases. In the Monte Carlo, the approximate formula given in [122] is employed to generate cosmic muon spectrum with a realistic angular distribution at sea level. This approximation formula was obtained by fitting 36 experimental data samples for the zenith angles ranging from 0° to 88.5° and energy ranges up to $100 \text{ GeV}/c$. It basically shows the proper energy dependence of the angular distribution. However, probably because of the polynomial expansion used in the approximation formula, the angular distribution in the GeV range is not exactly a $\cos^2 \theta$ shape, and it shows a dip around 0° . The difference between the angular shape of this formula and $\cos^2 \theta$ seems to be at the 10–20% level. This difference is negligible for our estimation.

The total number of cosmic muons generated in the Monte Carlo calculation is 5×10^7 events. They are uniformly distributed in $6 \text{ m} \times 6 \text{ m}$ square region that covers whole muon-target, curved and detector solenoids.

11.2.4.1 Electrons induced by cosmic muons

Figure 11.13 shows a 2D plot between electron momentum and cosine of electron track angle, where the angle is from the axis of the detector solenoid. It is apparent that the angle distribution for high energy electrons ($p > 80 \text{ MeV}/c$) does not exceed 0.5. On the other hand, the angle distribution for the μ - e signal electrons is known to be larger than 0.6. Therefore, an event selection condition requiring $\cos \theta > 0.6$, where θ is the angle of electron flight direction from the detector axis, is really powerful to suppress the cosmic induced electron backgrounds. After applying this cut, there is no event left in the momentum region $80\text{--}120 \text{ MeV}/c$, and the signal momentum region is only 3% of $80\text{--}120 \text{ MeV}/c$. The integrated cosmic muon flux at sea level is $0.015 \text{ cm}^{-1}\text{s}^{-1}$, and the total active time for $2 \times 10^7 \text{ s}$ of physics run is $2 \times 10^7 \times 0.7/1.5 \times 0.5/1.2$, where the second factor is the main ring duty cycle, and the third factor is the duty of COMET active time window. Thus, the number of cosmic muon induced electron background is 20.

In order to suppress this number to much less than 1, an active cosmic shield will be installed. The active cosmic shield is two layers of plastic scintillating counters covering the whole outer surface of the iron shield. A single layer will provide 99% of efficiency to tag a charged particle. The total tagging efficiency of the active cosmic shield would be, therefore, 99.99%. With this factor applied, the expected number of cosmic muon induced electron background becomes 0.002 for a $2 \times 10^7 \text{ s}$ physics run.

11.2.4.2 Direct hit of cosmic muons

Figure 11.14 shows a 2D plot between muon momentum and cosine of the muon track angle, where the angle is from the axis of the detector solenoid. The $\cos \theta$ dependence that was observed for the electrons is no longer visible. Without any additional cuts, the number of expected cosmic muon background would become 0.05, and heavily rely on the active shield performance. In order to avoid such a situation, another event selection is introduced, cutting on E/p , where E is measured by the calorimeter and p is measured by the tracker. The E/p of muons is generally less than 0.8. There is a small number whose E/p is higher than 0.8 for muons due to pile up of decay-in-orbit Michel electrons. This pile up is unavoidable since the lifetime of the μ^- is very short in heavy materials such as inorganic scintillator of the calorimeter. A suppression factor of 20 from the E/p cut is feasible according to a Monte Carlo simulation. The expected number of cosmic muon

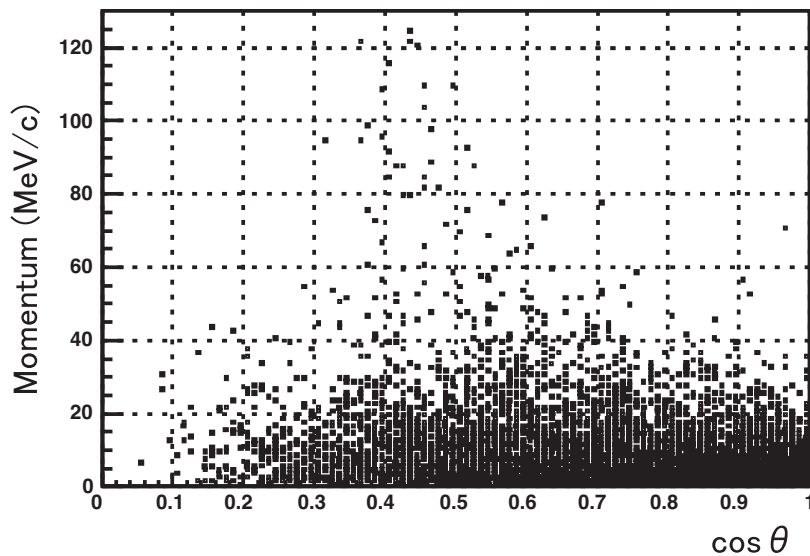


Figure 11.13: Two dimensional correlation between total momentum and angle from the detector axis for cosmic muon induced electrons.

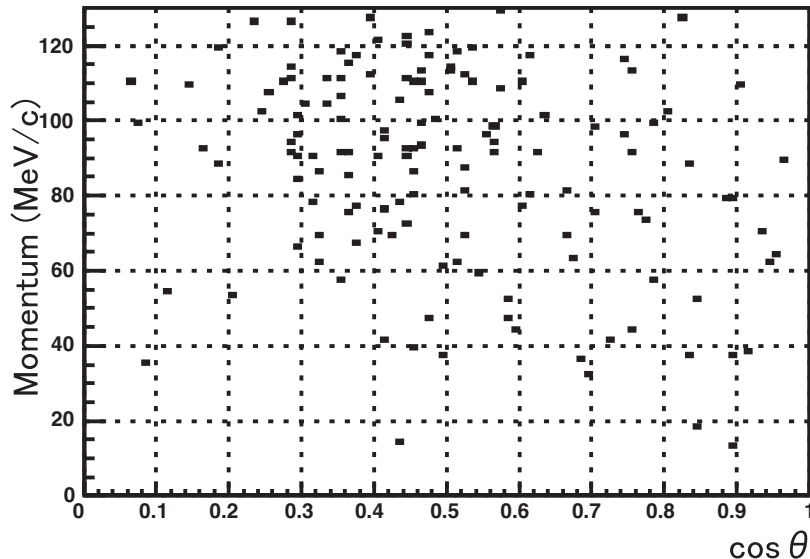


Figure 11.14: Two dimensional correlation between total momentum and angle from the detector axis for cosmic muon.

background becomes 0.002 for a 2×10^7 s physics run.

Table 11.9: Summary of Estimated Backgrounds.

Radiative Pion Capture	0.05
Beam Electrons	< 0.1 [‡]
Muon Decay in Flight	< 0.0002
Pion Decay in Flight	< 0.0001
Neutron Induced	0.024
Delayed-Pion Radiative Capture	0.002
Anti-proton Induced	0.007
Muon Decay in Orbit	0.15
Radiative Muon Capture	< 0.001
μ^- Capt. w/ n Emission	< 0.001
μ^- Capt. w/ Charged Part. Emission	< 0.001
Cosmic Ray Muons	0.002
Electrons from Cosmic Ray Muons	0.002
Total	0.34

[‡] Monte Carlo statistics limited.

11.2.5 Summary

Table 11.9 shows a summary of estimated backgrounds. The total number of background event is 0.3.

Chapter 12

Superconducting Solenoid

The superconducting solenoid magnets are one of the most critical components in order for the COMET experiment to achieve a high intensity muon beam and also a large solid-angle spectrometer for $\mu^- - e^-$ conversion signals. Superconducting solenoids are utilized for the whole beamline from pion capture through to the detector. There exist several technical challenges for the construction of the superconducting solenoid magnets used in the COMET experiment. The main challenges are

- A high magnetic field (of about 5 T) and radiation-hardness for the pion capture solenoid that surrounds the pion production target,
- Construction of curved solenoids with a compensating dipole field,
- Precise control of the magnetic field from pion capture to the detector, and
- Quench protection for a large-stored energy solenoid system in which all solenoids are magnetically coupled to each other.

Additionally, it would be beneficial to reduce the cost of superconducting solenoids as they are a major part of the cost of COMET.

12.1 Pion capture solenoids

12.1.1 Pion capture solenoid layout

Figure 12.1 shows a layout of the pion capture system, which consists of four different superconducting solenoid magnets.

12.1.2 Conductor choice and quench protection

The solenoid is designed to use aluminum stabilized conductor to reduce the heat load due to the secondary beam heat load. The parameters of aluminum stabilized conductor considered are summarized in Table 12.1. The cross sectional image of the conductor is shown in Figure 12.2. The conductor uses a Rutherford type cable with 14 copper stabilized strands. The cable is encased in the aluminum stabilizer by a conforming technology.

The capture solenoid consists of 4 coils. Coil 1 is the closest to the target and wound from the cable with edgewise solenoid winding with a 6-layer structure. Coils 2, 3, and 4 create the matching field to the transport solenoid. They are wound from the same cable

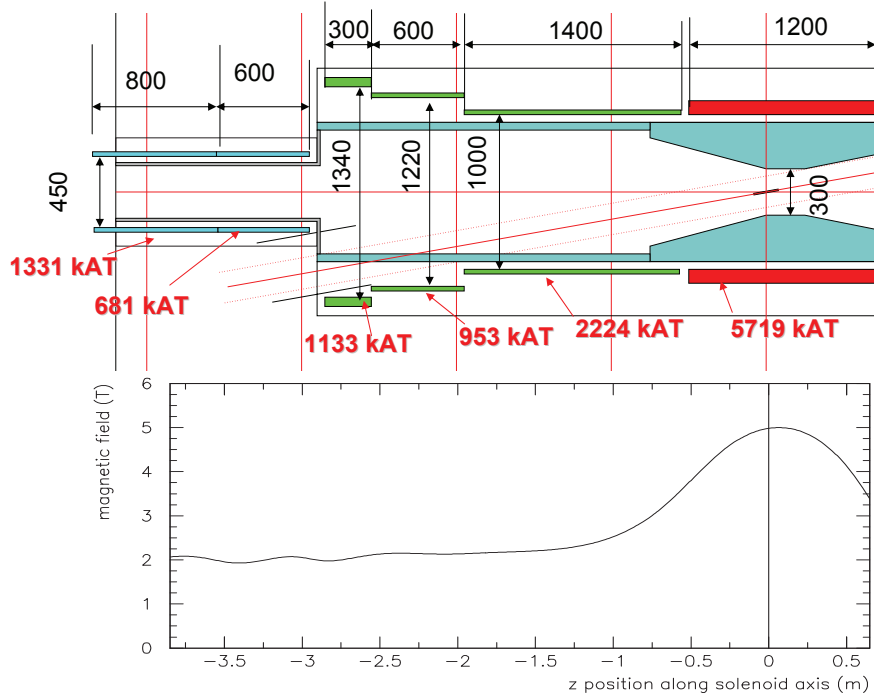


Figure 12.1: A layout of the pion capture solenoid system.

Table 12.1: Main parameters of aluminum stabilized conductor.

Item	Value
Cable Dimension (without insulation)	$15 \times 4.7 \text{ mm}^2$
Cable Dimension (with insulation)	$15.3 \times 5.0 \text{ mm}^2$
Strand Diameter	1.15 mm
Strand Number	14
Al/Cu/NbTi	7.3/0.9/1.0
Aluminum RRR	500
Copper RRR	50
NbTi Jc at 5 T 4.22 K	2700 A/mm^2
Al yield strength	55 MPa
Overall yield strength	150 MPa

with the same winding method, but have a 2-layer structure for coils 2 and 3 and a 4-layer structure for coil 4. The coils are structurally connected to each other making a single ridged cold mass. The cold mass is encased in the cryostat that provides the thermal insulation vacuum. The cryostat is then covered by an iron return yoke. There is about a 160 ton electromagnetic force between the yoke and the cold mass. The support structure will be designed such that the cold mass does not move with respect to the iron yoke. Figure 12.3 shows the computed flux lines in the capture solenoid system. A maximum magnetic field on the coils is about 5.5 T at coil 1 with an operation current of about 4 kA. The load line

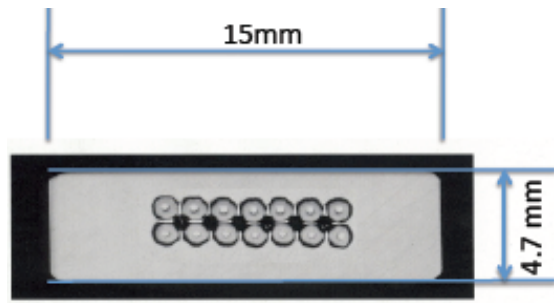


Figure 12.2: Cross section image of the aluminum stabilized superconductor.

curve of coil 1 is shown in Figure 12.4. The critical temperature at the operating point is about 6.5 K.

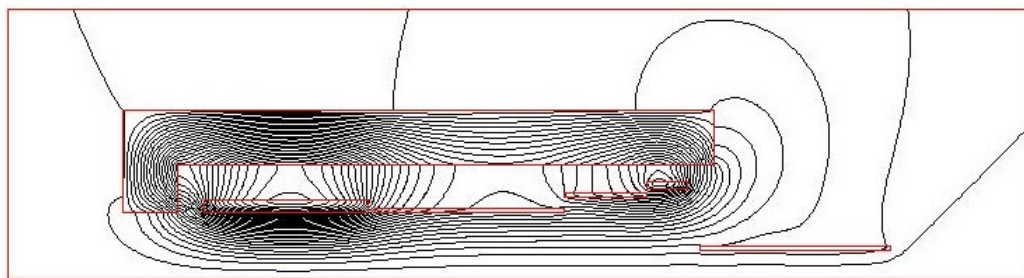


Figure 12.3: Computed flux lines in the capture solenoid system.

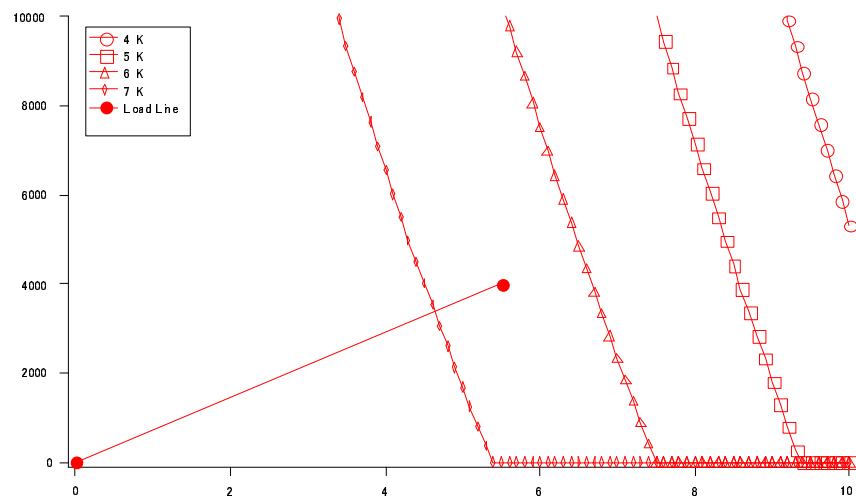


Figure 12.4: Critical current of aluminum stabilized superconductor as a function of temperature. The load line curve of Coil 1 is shown.

The quench protection of the solenoid is made mainly by an external dump resistor system. The dump resistor maybe set to 0.1 Ohm that gives maximum terminal voltage of 400 V during the dump. The inductance of the solenoid is about 2 H that results in a dumping time constant of 20 sec. The temperature rise of the conductor is estimated by the integral of current squared (MIITs)¹ that is shown in Figure 12.5 with the various residual resistances of aluminum stabilizer (RRR). The cable is designed with the aluminum RRR of about 500. The time constant defined by the protection dump circuit of 20 sec will give MIITs of 160. The resultant maximum temperature in the coil is about 100 K. There will be also a normal zone resistance in the coil that will enhance the current dumping. The maximum temperature is thus further reduced.

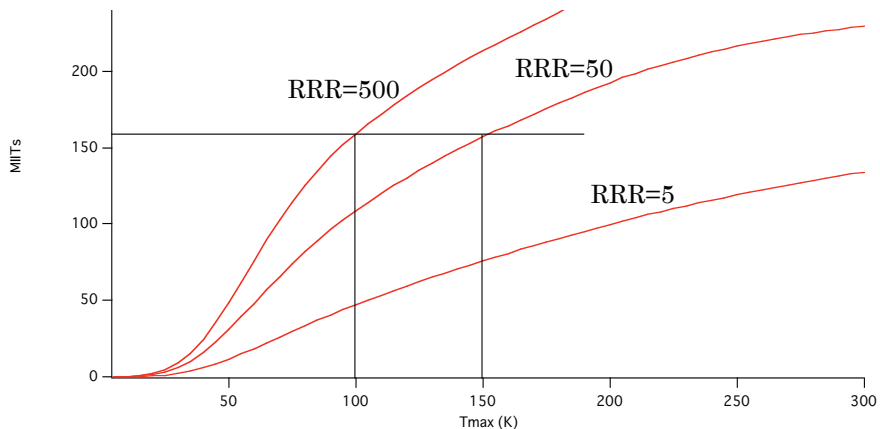


Figure 12.5: Temperature rise of aluminum stabilized superconductor. The curves are, from top to down, for aluminum RRR=500, RRR=50, and RRR=5.

12.1.3 Influence of radiation

Although the solenoid is protected by a tungsten shield, the coil is still subjected to a large amount of radiation. The heat load to the coil is estimated to be about 30 W overall and this must be removed. The heat removal is performed by aluminum strips installed in between coil layers that carry heat to cooling pipes attached to the coil ends and outer support cylinder. The maximum temperature in the coil is estimated to be less than 5.5 K. The critical temperature of the conductor at the operation current is estimated about 6.5 K. The temperature margin is thus estimated more than 1 K. Details of the cooling scheme must be examined carefully.

The radiation damage to the coil material is also a critical issue. A maximum lifetime neutron flux on the coil is estimated to be about 6.6×10^{21} neutron/m². A neutron flux can degrade the RRR of aluminum stabilizer. With 10^{21} neutron/m² observation of degradation starts and with 10^{22} neutron/m² degradation of about 1/100 is estimated. Figure 12.5 indicated that RRR degradation of about 1/10, RRR of 50, gives a maximum temperature of 150 K that is still acceptable. While, degradation of 1/100, RRR of 5, gives a maximum temperature of more than 300 K that is probably not acceptable. This rough estimation

¹MIIT is a time-integral of current squared and given by Mega I (current) \times I (current) \times T (time), namely MIIT.

indicates that the lifetime neutron flux of 6.6×10^{21} neutron/m² can be critical for the solenoid quench protection. The RRR degradation can be recovered by a thermal cycle to room temperature. The solenoid should be thermal cycled to the room temperature before significant degradation is observed. The degradation may be detected by warming up the solenoid to about 10 K and measuring the conductivity of the cable. If the degradation of the RRR is detected the solenoid should be warmed up to room temperature to recover RRR.

The radiation damage to the organic materials such as coil insulation must be investigated as well. The lifetime radiation dose on the coil is estimated about 4×10^5 Gy that is acceptable for most of the radiation hard organic materials such as polyimide. The large neutron flux, however, may also accelerate the damage and should be examined carefully.

12.2 Muon transport solenoids

The muon transport solenoid system consists of two bend solenoids that bend the muon beam 90 degree each. Some additional straight solenoids are also considered to connect the first bend solenoid and the second bend solenoid for the purpose of further extension of the total beam line length and an additional location for muon beam collimators. The solenoids have inner coil diameter of 450 mm that gives beam tube inner diameters of 350 mm. The bend sections are made from the 32 (16 each) short solenoids each 200 mm long and 32 mm coil thickness. The straight solenoids are in the range of 1000 to 800 mm long and the coil thickness is about 20 mm, except the last solenoid to connect the target solenoid that has length of 300 mm and coil thickness of 6.3 mm. The solenoids are connected in series and produce the solenoid field of about 2 T. In the bend solenoids, a small $\cos \theta$ dipole coil is also wound in each solenoid bobbin and produces a vertical field of about 0.02 T.

12.2.1 Conductor choice

The conductor used for the coil is NbTi based copper stabilized conductor. The conductor is used for magnetic resonance imaging, is commercially available and hence chosen to optimize cost. The typical conductor example has a strand diameter of 1.2 mm and copper to superconductor ratio of 4. The operation current of 100 A is selected to ensure the critical temperature of about 7.5 K. The conductor current density is estimated to be about 90 A/mm² and the coil overall density is about 80 A/mm².

12.2.2 Quench protection

The quench protection of the solenoid system is made by protection heaters attached to the solenoid coil. As shown in Figure 12.6, the heaters are connected in series with a protection dump circuit. The system will be designed to aim a dump time constant of 20 sec. The conductor MIITs computation gives the maximum coil temperature of about 200 K with a 100 A operation current with the 20 sec dump time constant.

12.2.3 Negative field gradient at the muon transport

A negative field gradient at the muon transport system is being considered at the old-MECO type and Mu2e. In the COMET design of the muon transport, a negative field gradient can be accommodated if it is necessary. The technical issue has been discussed

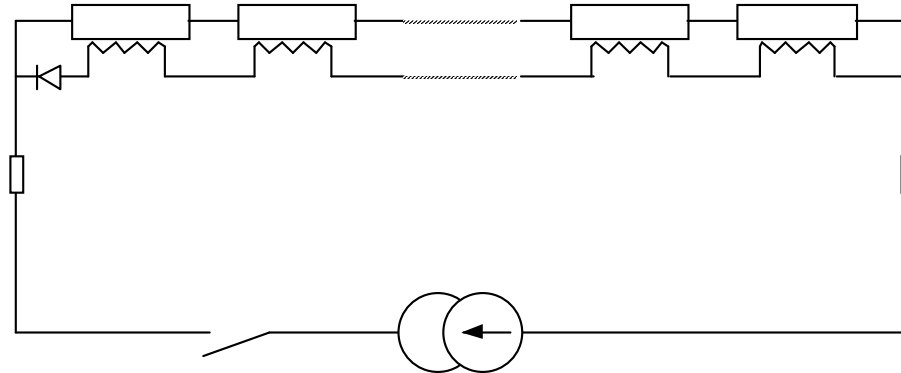


Figure 12.6: Quench protection scheme of transport solenoids.

with a magnet manufacture company, and it turns out that it is not difficult to make such solenoids. Detailed study will be carried out soon.

12.3 Muon-stopping target solenoid

The muon-stopping target solenoid is wound from the same conductor used for the transport solenoid. The operation current of 100 A is selected to keep the same aimed current dump time constant for the quench protection. Since the maximum field of the target solenoid is larger than the transport solenoid, the critical temperature is slightly lower, about 7.2 K. The value is still a comfortable safety margin. The quench protection combines an external dump circuit with a passive quench back of aluminum strip that also provide the cooling.

12.4 Cryogenics system for capture, transport and target solenoids

The solenoids for pion capture, muon transport and muon-stopping target are cooled by a helium refrigerator that provides two-phase liquid helium. The helium is supplied to the solenoid using a thermo-siphon system. The estimated heat loads are summarized in Table 12.2, with an overall heat load from those solenoids of about 150 W. The refrigeration power of at least 200 W at 4.4 K (which corresponds to the compressor power consumption about 100 kW at a room temperature) may be required for the refrigerator. The refrigerator system should be designed such that the thermal cycle to 10 K and the cycle to room temperature can be achieved in 6 hours and in one week respectively. The system also should be designed such that capture solenoid can be warmed up without warming up the other solenoids.

12.5 Electron transport solenoid and detector solenoid

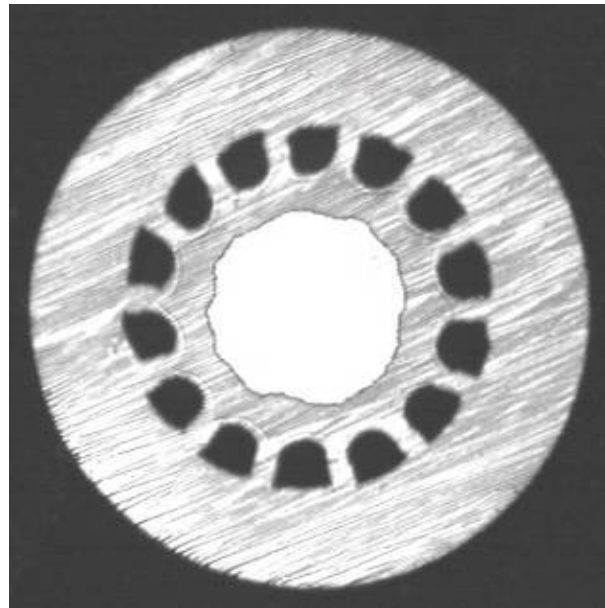
12.5.1 Conductor choice

For the electron transport solenoid and detector solenoid, a new type of superconductor based on MgB₂ is proposed. The main parameters of the conductor are summarized in

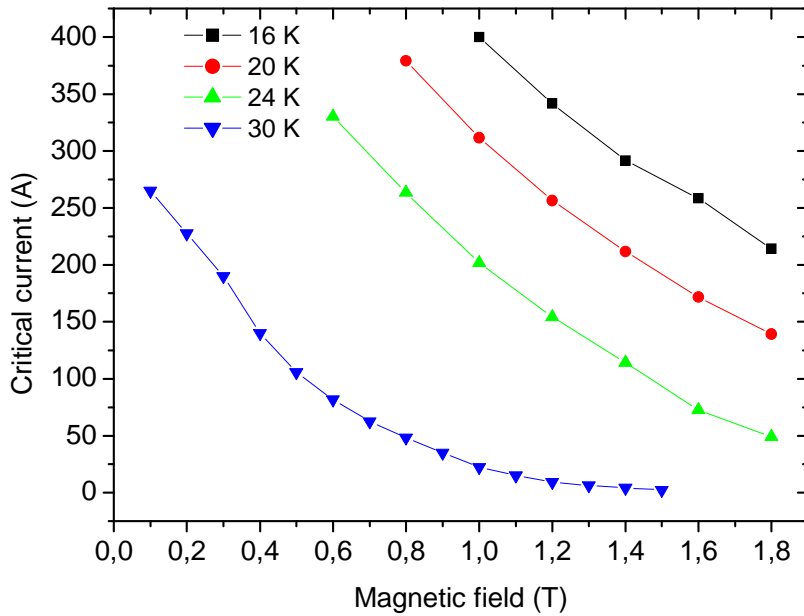
Table 12.2: Estimated heat loads.

Heat Load Item	Value
Beam to capture ($\times 2$)	60 W
Beam to transport ($\times 2$)	5 W
Static to Capture	15 W
Static to transport	10 W
Static to target	10 W
Static to control dewar TRT etc.	50 W

Table 12.3. The cross section of the superconductor is shown in Figure 12.7 and a critical current of the conductor is reported in Figure 12.8. The solenoid is designed such that the operation current is about 50 A, which results in the coil overall current density of about 40 A/mm². With the estimated coil maximum field of about 1.2 T, the critical temperature is estimated to be about 28 K. The coil can be cooled by two GM refrigerators for each solenoid. The coils can be cooled to below 10 K even with a single refrigerator giving a significant enthalpy margin because of large heat capacity compare to that of 4.5 K. The large enthalpy margin makes the solenoid practically quenchless. The quench protection may be made using the same scheme as the transport solenoid; that is use of dump resistors as quench protection heaters. The GM refrigerators provide structural independence from the other solenoids giving those solenoids relative freedom to move. Easier to move spectroscopy solenoids result in easier access to both the muon-stopping target and the detectors, allowing better maintenance.

Figure 12.7: Cross section of MgB₂ superconductor.

For the spectroscopy solenoids, the dipole magnets provide the vertical field of about 0.12 T. The curved dipole magnet wound from the MgB₂ superconducting wire is required.

Figure 12.8: Critical current of MgB₂ superconductor.

Details of the design are now under consideration.

12.6 Alternative magnet design

Another option for producing a curved solenoid channel with a vertical dipole field is to use the Double-Helix™ design from Advanced Magnetic Labs [123]. The Double-Helix™ magnet design uses two tilted solenoid windings that are tilted in opposite directions. The axial field components cancel giving a dipole field. The magnet is produced using a unique manufacturing process whereby the coil windings are formed by matching grooves in a composite substrate material into which the windings are placed. This allows

Table 12.3: Main parameters of MgB₂ superconductor.

Item	value
Strand Diameter (mm)	1.2
Composition	
MgB ₂ (Vol%)	14.6
Fe (Vol%)	10.8
Cu (Vol%)	13.8
Ni (Vol%)	15.8
Monel 400 (Vol%)	45.0

multiple layers of different pole configurations over the length of the cylinder which can also be curved. These qualities would be ideal for the curved transport channels as the design has the advantage of being able to produce a more uniform solenoid field over a region that is truly curved and not composed of a number of straight sections. Since the dipole winding would be on top of the solenoid winding, the current in it can be adjusted independently eliminating the need for any complex tuning mechanisms.

The down side to this design is the additional cost of the dipole winding coil material. However, initial discussions with AML have proven to be quite positive that this design can be very competitive compared to a more conventional superconducting magnet. The first step will be to perform tracking simulations using a calculated field map of the AML magnet to compare the performance with the curved tilted solenoid. This will allow a cost-performance comparison of the two transport channels.

Chapter 13

Experimental Layout

13.1 Layout at the NP hall

The following are the main considerations when designing the layout of the COMET experiment:

- the location of the pion production target
- the location of the beam dump
- the transportation of muons from the production target to the stopping target

These three issues must be considered together. in order for the experiment realized. Needless to say, the supplying of sufficient electricity and cooling water to experimental equipment is a general requirement that the layout of the experiment must allow for.

The pion production target needs to be located in a 50 to 100 kW primary beamline. The proton beam is expected to lose between 2 to 4 kW of its power as it passes the target and adequate radiation shielding between the target and beam dump must be provided. The target is located in a large pion capture solenoid. A chain of solenoid magnets then transport the pions from the target as they decay into muons. In addition, the experimental setup, including the muon stopping target, is contained in another chain of solenoid magnets. This implies that suppression of magnetic field leakage will be an issue in the design. These details will be addressed in the following.

Most of the experiments planned at the J-PARC NP hall will use secondary beamlines carrying particles produced in reactions between the primary protons and the material in a shared target. Some other experiments are planning to use the primary beam directly and are called primary beam experiments. The COMET experiment uses the proton beam extracted from the accelerator and directs it onto a custom target to produce pions and hence muons; it therefore has similar requirements to those of the primary beam experiments. Therefore, it will be beneficial to share the beamline with the other primary beam experiments to transport the proton beam from the accelerator to the experimental hall. The other primary beam experiments need proton beam energies of up to 30 GeV, with a beam power of less than 10 kW, while for the COMET experiment a proton beam energy of 8 GeV is preferable, to suppress backgrounds which may be caused by antiprotons at higher beam energies.

These conditions lead to a layout design where the COMET production target and the beam dump are located outside the current experimental hall. The straight section of the

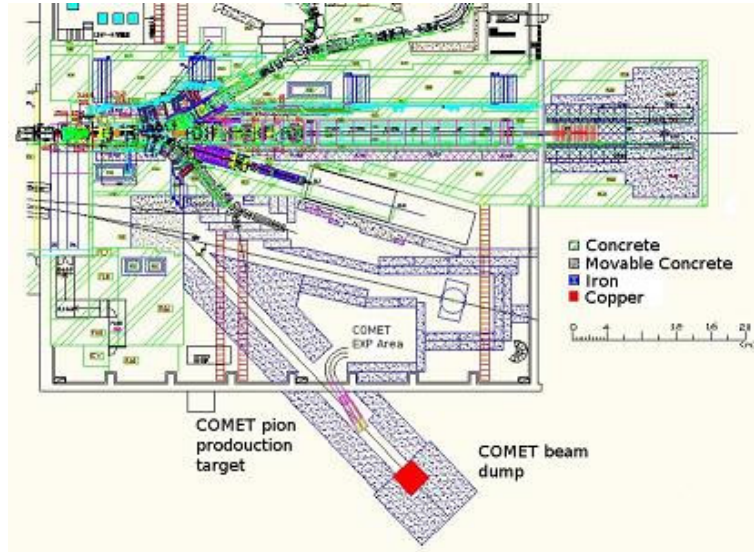


Figure 13.1: Possible layout of the target and beam dump.

primary beam transport can be shared with other primary beam experiments. Once in the experimental hall, an 8 GeV beam can be bent relatively easily compared to a 30 GeV beam, which will make it easier to direct to a location outside the experimental hall. Furthermore it is easier to construct the COMET target station and beam dump outside the hall from the view point of the civil engineering. The muon transport solenoid will carry pions/muons through the wall of the hall to the muon stopping target. The spectrometer solenoid, downstream of the stopping target, will be set back in the experimental hall where hall facilities such as a crane are available. Air conditioning might also be necessary to maintain the calorimeter crystal at the require temperature. Figure 13.1 shows a plan view of a possible layout of the experiment.

If the available space for COMET in the NP hall is limited, installing the whole experiment outside the hall may be a solution. In this case the hall crane will not be available and in addition we would need a building to include not only the target/dump but also the detector itself, which would increase costs. However this would allow for more flexibility in the layout, for example for an electron linac for detector calibration, which could be highly beneficial. A possible layout is shown in Figure 13.2.

In either case, radiation shielding for the whole beamline, transport solenoid and spectrometer solenoid is needed, together with magnetic shielding to suppress stray fields.

13.2 Proton beam dump

The proton beam dump is requested to have a capability to stop a proton beam of 56 kW¹ without distributing radiation around the experimental area above safety limits. The main part of the dump will be made of metal with relatively high thermal conductivity and high density so that the deposited heat can be taken away quickly with good radiation shielding. Concrete shielding will surround the main part to reduce the radiation level sufficiently at a reasonable cost. Currently we plan to use copper or iron for the main part of the beam

¹A 100 kW design is considered in parallel as a possible upgrade.

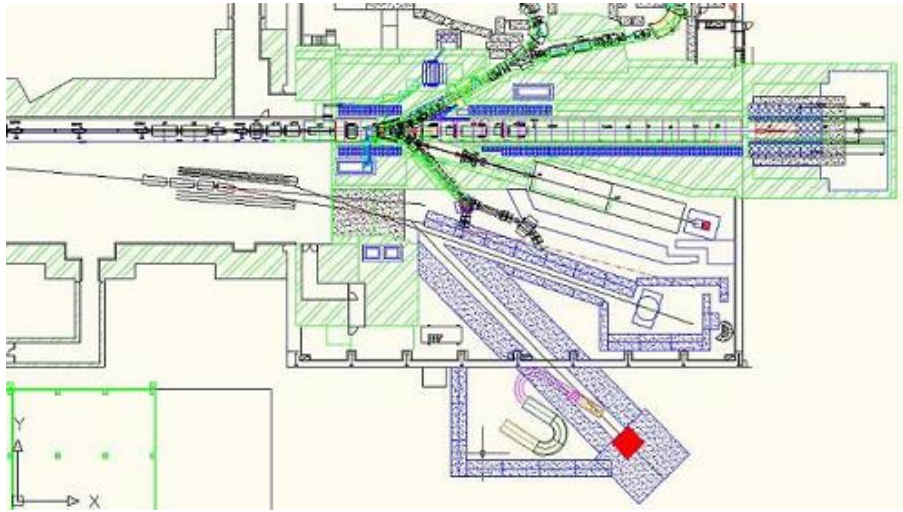


Figure 13.2: Possible layout of the detector outside the NP hall.

dump. Cooling with water will be probably necessary to keep the temperature of the metal below a certain level. For example in the case of copper, the maximum temperature must be kept below its softening temperature at around 200 °C. The shape of the metal needs to be optimized so that the proton beam impacts a wide area of the metal surface. This can be realized by making a hole with a special shape to fit the beam profile at the dump. Stress calculations must be done after completing the estimation of heat distribution. The metal will expand depending on its temperature during operation. Stress between the metal and concrete needs to be reduced below the maximum allowed stress of about a few MPa. Figure 13.3 shows a prompt dose distribution between the pion production target and beam dump estimated by a MARS calculation. The geometrical configuration is illustrated in Figure 13.4. According to the J-PARC regulation, the prompt dose must be reduced below 5 mSv/h at the environment boundary. Thus we need to cover the beam dump with at least a 5.5 m thick concrete wall or equivalent amount of material.

13.3 Radiation safety and radiation shielding

It is necessary to keep the radiation dose below a certain level and due to this sufficient amount of shielding material must be prepared. A careful (and conservative) estimation based on the simulation is absolutely critical. As already mentioned above, there will be a maximum dose along the proton beamline between the pion production target and the beam dump. The prompt dose level underground must be reduced to below 5 mSv/h on the surface of the shielding so as not to contaminate underground water. According to our simple calculation using MARS as already described, we need to locate 5.5 m thick concrete shield underneath the target. This is the reason why we have settled on a layout described above. The transport line of the primary beamline in the experimental hall needs to be shielded, too. The necessary thickness of the shielding wall is estimated to be 4 m from our experiences in KEK-PS and is confirmed to be sufficient by a calculation using the Sanford-Wang formula [124].

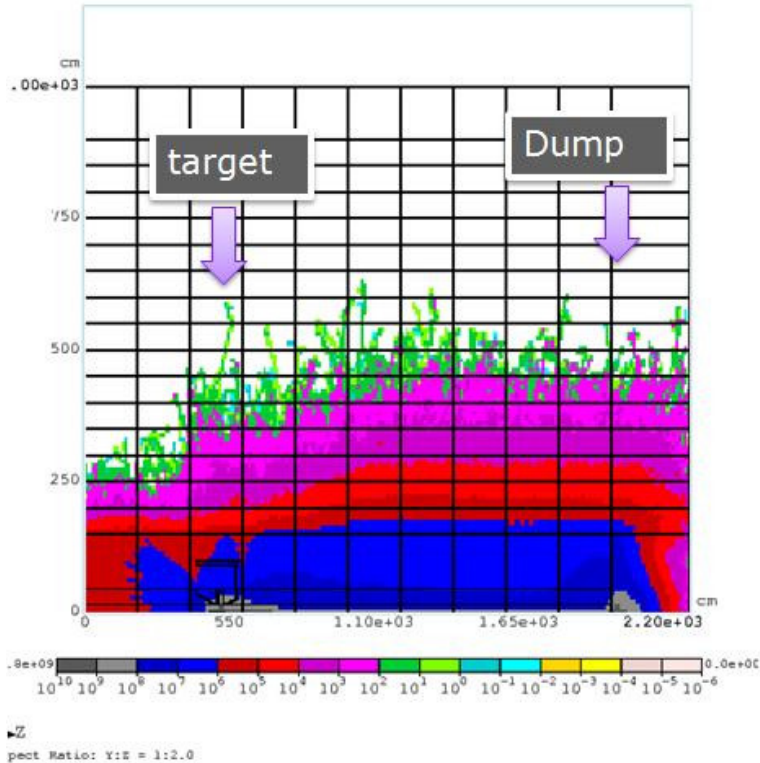


Figure 13.3: Prompt dose distribution between the pion production target and beam dump.

13.4 Magnetic field safety

The COMET experimental setup include many solenoid magnets to capture pions, to transport muons and to perform momentum analysis of electrons. Equipment used in the experiment might be affected by the magnetic field leakage although they can be protected by local shielding around them. We do not think that this will be a serious problem. However, one important issue we have to take into account is that the magnetic field strength around the COMET experimental setup must be reduced to as low as the earth's magnetic field in order not to disturb other experiments running in the hall. The detector will be surrounded by an iron cosmic-ray shield that can work as a return yoke of the spectrometer magnet. The transport solenoid and capture solenoid magnets need special care to reduce their stray fields by also using a return yoke. It might be difficult to realize this for the transport solenoid since it has a curved shape. In that case shielding the whole transport line by surrounding it with iron plates as in the case of the detector solenoid would be a solution. In any case it is important to continue design work with help of 3-dimensional magnetic field simulations.

13.5 Infrastructure

13.5.1 Power requirements

In this section, the electric power requirements are summarized. This includes electricity for the proton beam transport magnets, the pion capture solenoid and its refrigerator, the

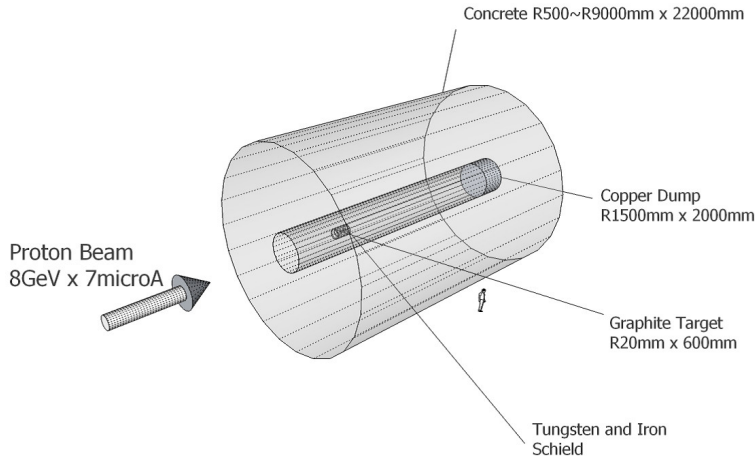


Figure 13.4: .

muon transport solenoid, the detector solenoid, and the detector components. Electricity for solenoid magnets will be supplied by a single power supply with 100 kVA output capability. These super-conducting magnets require cooling below critical temperature. The pion capture solenoid will be cooled with liquid helium thus we need to operate a refrigerator for helium liquefaction. We plan to install a 200W helium refrigerator. Power consumption of such a refrigerator is much reduced with current technology and is usually about 600 times the cooling power of helium. The other solenoid will be cooled by using small GM-type refrigerators directly mounted on solenoid magnets. Currently we estimate that 20 refrigerators will be required for this purpose. Electricity for the proton beam transport magnets is conservatively estimated based on real power consumption in 2008 J-PARC runs. In the COMET experiment, external extinction devices like AC-dipole magnets will be employed to improve the beam extinction level. An R&D program for the AC-dipole is currently in progress and it is not easy to estimate power consumption reliably. We therefore quote a number with a 100% uncertainty. Air conditioning and lighting in the experimental area are not considered yet but they are expected to be small. In addition, electricity for the cooling water facility is not considered here. Table 13.1 summarizes the estimated required electric power. A significant amount of electricity is necessary for power supplies for the beamline transport magnets and refrigerators. Proton beam transport magnets are shared with other experiments that use primary protons. They use A 30 GeV proton beam; here estimation of electric power is based on 8 GeV beam transport for the COMET experiment.

13.5.2 Cooling water requirement

The followings need cooling water for their operation:

- beam transport magnets and external extinction devices
- helium refrigerator compressor
- compressors for GM-type refrigerators

The necessary amount of cooling water for normal conductor magnets can be estimated by simply assuming a temperature increase of 20K in each device. In this case, 1 MW heat

Table 13.1: Power requirements in the COMET experiment.

Equipment	Power (MW)
Beam transport magnets	0.2
External extinction devices	0.2
Solenoid magnets	0.12
He refrigerator	0.12
GM-type refrigerators	0.2
Vacuum pumps	0.1
Detectors Electronics	< 0.02
DAQ system	< 0.02
Frontend computers	< 0.02
Total	1.0

Table 13.2: Cooling water requirement in the COMET experiment

Equipment	Cooling water (ℓ/min)
Magnets and extinction devices	400
Helium refrigerator compressor	120
GM-type refrigerator compressors	100

can be taken away by

$$\frac{1000 \text{ (kW)}}{4.1855 \text{ (kJ/(kg} \cdot ^\circ \text{C}) \times 20^\circ \text{C}} = 11.9 \ell/\text{sec} = 717 \ell/\text{min} \quad (13.1)$$

cooling water [125]. In this estimation we assume additional cooling water in order to compensate heat loss in the power supplies themselves and take a simple factor of $1000 \ell/\text{min}$ cooling water for 1 MW magnet cooling. Super-conducting magnets used in the COMET experiment do not need cooling water for direct cooling, however the compressor for the helium refrigerator and compressors for GM-type refrigerators require cooling water. The necessary cooling water for the compressor of the helium refrigerator is estimated in the same way as for the beam transport normal conductor magnets, thus we need $120 \ell/\text{min}$ cooling water. Cooling water for GM-type refrigerator compressors is estimated by using a commercial product² with 6 kW power which requires cooling water of $5 \ell/\text{min}$. Table 13.2 summarizes necessary amount of cooling water. Here we assume a cooling water temperature at $20\text{--}25^\circ \text{C}$.

13.5.3 Refrigeration Requirement

As already explained, the solenoid magnets to be used in the COMET experiment are all super-conducting magnets and hence need a refrigerator for cooling. The capture solenoid surrounding the pion production target will be exposed to heavy radiation. From the magnet operation point of view it is necessary to minimize the temperature increase caused

²Leybold vacuum COOLPAK 6000/6200.

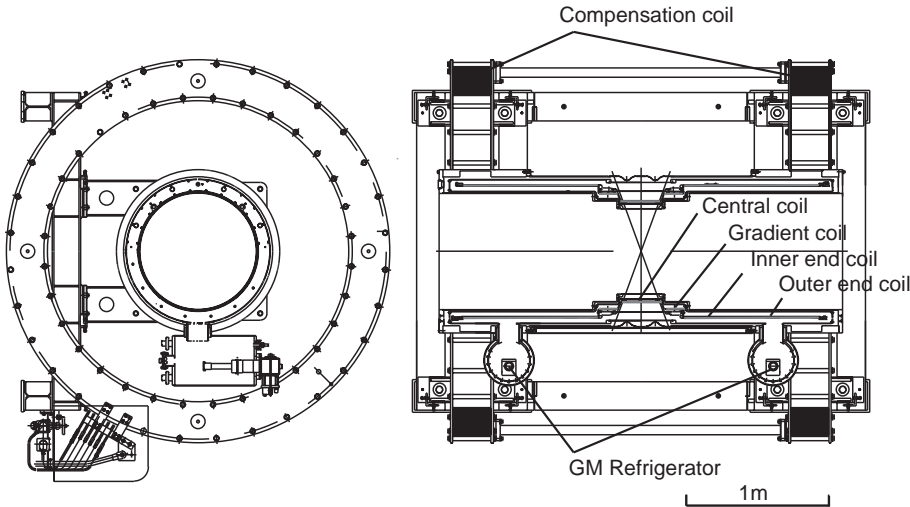


Figure 13.5: An example of super-conducting magnet using GM-type refrigerators directly mounted on it for cooling.

by radiation for safe operation of the magnet. In the current design this is realized by installing a tungsten shield block inside the capture solenoid to reduce particle penetration to the coil and utilizing aluminum stabilized super-conducting wire to reduce the mass of the wire. During normal data acquisition period of COMET, the heat load to the coil due to radiation is estimated to be $2 \cdot 10^{-5} \text{ W/g}$ for $8 \text{ GeV} \times 7 \mu\text{A}$ accelerator operation. Integrating this over the coil volume gives an estimated heat load of 10 W. There will be additional heat load caused by conduction. Although this highly depends on the design of the coil supporting structure in the cryostat, we estimate that this is small enough ($\ll 10 \text{ W}$). Currently we plan to install a 200W helium refrigerator so that we can manage coil cooling with a sufficient margin. It would be probably possible to use redundant cooling power for transport and detector solenoid magnets. However cooling of these magnets is better done by separate small refrigerators because those magnets needs to be separated off from the capture solenoid for maintenance work. We need 20 GM-type refrigerators for cooling the solenoid magnet chain of 20 m length. This assumption is based on the design of a similar magnet of 2.5 m length as shown in Figure 13.5 [126]. In this magnet the coil chain is cooled down to 4.2–4.4 K by using two GM-type refrigerators in 5 days. Each refrigerator³ has a two-stage cooling procedure of power 31 W and 1 W at 40 K and 4.2 K, respectively.

³SHI, SRDK-408D.

Chapter 14

Cost Estimate

The cost estimate for the whole COMET project is presented here. In the subsequent sections, some detailed descriptions for selected cost items are presented and the total cost estimate (with and without contingency) is given.

14.1 Superconducting solenoids

The most significant cost-driving items are the superconducting solenoids for the muon beam line and the detector. The muon beam line is composed of the pion capture solenoid and the muon transport solenoid, while the detector is composed of the muon-stopping target solenoid, the electron transport solenoid and the detector solenoid. The specifications of these solenoid magnets are shown in Table 5.7.¹

A preliminary quotation of the cost for all the solenoid magnets (without high-power refrigerators) has been obtained from a magnet-manufacture company, based on the specifications presented in Table 5.7. A total cost of about 35.7 Oku Japanese yen (JPY). Here “Oku” is 10^8 and one Oku JPY corresponds to a million US\$ when 1 US\$=100 JPY. The cost breakdown is summarized in Table 14.1.

The cost includes the power supplies, the magnet control system including quench-protection system, installation fee, the engineering design cost, and tax. The cost of a high-power refrigerator, which is used to cool the pion capture solenoid and the muon transport solenoid, is not included, but cryo-coolers, which are used to cool the muon-stopping target solenoid, the electron-transport solenoid and the detector solenoid are included.

¹In the original COMET proposal, a rough analytical cost estimation was made using two empirical formulas [127], which are given by

$$\text{cost (M US\$)} = 1.34 \times 0.844 \cdot U^{0.459} \quad (14.1)$$

$$\text{cost (M US\$)} = 1.34 \times 0.77 \cdot \Omega^{0.631}, \quad (14.2)$$

where U is a stored energy in units of MJ, and Ω is a product of a magnetic field and a volume in units of T·m³. For the superconducting magnets in the proposed experiment, equations (14.1) and (14.2) give 18.0 M US\$ and 20.9 M US\$, respectively. The conservative cost of 20.9 M US\$ corresponds to about 20.9 Oku Japanese yen (JPY)

Table 14.1: Preliminary cost quote for the superconducting solenoid magnets from a magnet-manufacture company. The specifications for the solenoid magnets are based on Table 5.7.

Item	Cost (Oku Yen)
Solenoid Magnets	
Capture and matching solenoids	9.8
Muon beam transport solenoids	6.8
Muon target, curved spectrometer, and detector solenoids	10.4
Power supplies	2
Magnet control system	1
Design and installation fee	5
Tax	0.7
Total (with tax)	35.7

14.2 Proton beam line

A new proton beam line with magnets and a proton beam dump in the NP experimental hall, where the COMET beam line and detector are accommodated, are needed. The breakdown is presented in Table 14.2.

Table 14.2: Preliminary cost for the proton beam line

Item	Cost (Oku Yen)
Proton “B” line construction*	7
Proton beam line for COMET including AC dipole magnets	10
Proton beam dump	2
Radiation shielding	3
Total	22

* This item can be removed if the proton B line is considered as a shared item.

The cost of the “B” proton beam line would cover the proton beam line from the branching point from the proton “A” proton beam line to the NP experimental hall. This section of the proton beam line can be shared by other experimental users, and therefore this can be removed from the COMET cost estimate if it is regarded as a common item.

The proton beam line for COMET in Table 14.2 starts from the branching point of the B line in the NP experimental hall shown in Figure 14.1. The cost of external proton-extinction devices such as AC dipoles is also included in this item. The sub-total cost is about 10 Oku JPY.

The cost of a proton beam dump (for about 50 kW proton beam power) of about 2 Oku JPY is listed. The cost of radiation shielding (made of mostly concrete), installed in the NP experimental hall, of about 3 Oku JPY is also included.

14.3 Civil construction and infrastructure

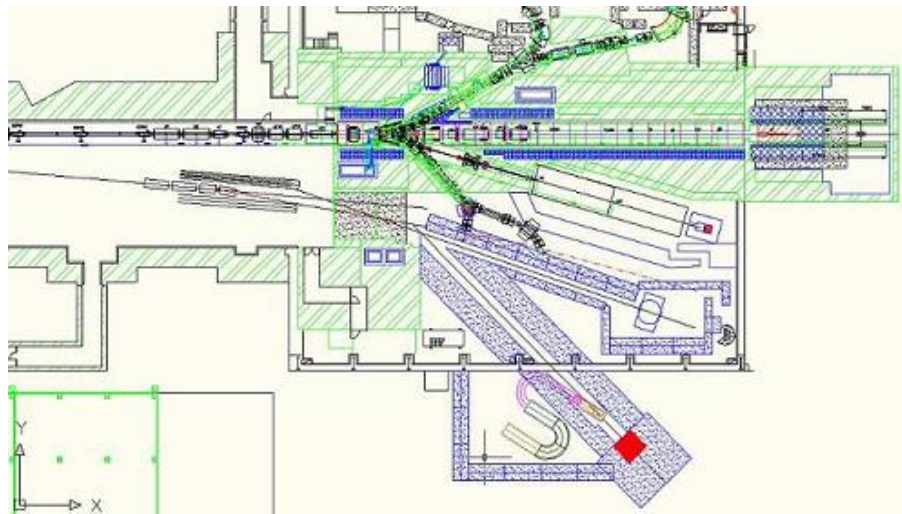


Figure 14.1: Possible layout of the detector outside the NP hall.

An experimental hall extension is needed when the COMET beam line and the detector are installed. It requires an extra excavation of a cavern south of the NP experimental hall, as shown in Figure 14.1. The cost of the extension of the experimental hall and of the construction of a building associated with it is about 3 Oku JPY. This cost also includes an electricity supply and a cooling water system.

The cost of refrigeration of about 4.7 Oku JPY includes compressors, a gas buffer tank and a cooling tower.

Table 14.3: Preliminary cost for the civil construction and infrastructure.

Item	Cost (Oku Yen)
Extension of the NP experimental hall	3
Refrigeration	4.7
Total	7.7

14.4 Detectors

The detectors include an electron tracker based on gas straw chambers and an electron calorimeter based on scintillating crystals.

14.5 Summary of cost estimate

Table 14.4 summarizes the total cost estimate for COMET. An estimation with 20 % contingency is also given.

Table 14.4: Cost estimate of the COMET experiment (2009).

Item	Cost (Oku JPY)
Proton beam line	
Proton beam line magnets	17
Proton beam dump	2
Radiation shielding for a proton beam line	3
Superconducting Solenoid	35.7
Detector	
Electron tracker	2.1
Electron calorimeter	2.3
Cosmic ray shield	3
DAQ system	0.5
Infrastructure	
Refrigeration	4.7
Pion production system and tungsten shielding	2.3
Civil construction	
Extension of the NP experimental hall	3
Total	75
Total (with 20% contingency)	90

Chapter 15

Schedule

Figure 15.1 shows the schedule of the COMET experiment. In our current plan, we will start engineering runs in 2016 and start physics data acquisition one year later in 2017. Construction takes four years which is dominated by superconducting magnet construction. Detector construction is estimated to be finalized in 5 years including an R&D period of 3 years. Details of the schedule concerning each part are described in the following.

15.1 Technical design report

We plan to finalize our Technical Design Report (TDR) one year after submitting this CDR. Technical details necessary for constructing each component will be described in the report. Design work for construction will be done in parallel. Submission of the TDR will be a critical milestone for starting construction.

15.2 Main ring

A series of extinction studies including abort line measurement will be repeated from time to time before starting construction. An attempt to perform bunched slow extraction will be an important issue. In this schedule chart we allow 3 years study of the proton beam, however this is to be repeated until necessary performance of the proton beam is proven. In case we need modification of the RF system to change the harmonics number in RCS (and also MR), this must be evaluated before the start of engineering runs. This means that the schedule of the main ring study may change depending on the situation of the beam performance achieved in studies.

15.3 Proton transport line

Development of an external extinction device, that is AC dipole, is a key part of the proton transport line design and construction. We estimate two years R&D and four years construction time including developing other conventional magnet system. Concerning magnets other than AC dipoles, they are conventional and existing magnets and power supplies are expected to be used for this purpose. In case we need to upgrade the power station and cooling water facility in the NP hall, additional cost will be necessary. However this is not a technically challenging issue and everything can be managed in time by the KEK facility group.

15.4 Magnets and pion production target

R&D work on the pion production target will continue for two years focusing on cooling techniques. Construction of the pion capture solenoid will be a technical challenge to achieve such a complicated and high magnetic field in a hard radiation environment. Operation and the maintenance scheme of the pion capture solenoid needs to be carefully considered before construction. Such details will be summarized in the coming TDR. Production of the capture magnet is estimated to take four years. This include production time of superconducting wires necessary for the magnet construction. Construction of the muon transport solenoid and detector solenoid is thought to be technically easier than construction of the pion capture solenoid. Because of this, construction will be performed in parallel and is estimated to be completed in two years.

15.5 Experimental area

As described in Chapter 13, the COMET pion production target and beam dump will be located outside the NP hall. This certainly requires civil engineering work in the hall and the area nearby. The work should be arranged in such a way that other experiments being executed in the hall can continue their data acquisition. In our current schedule, area construction work is scheduled to be started in 2013 and continues for two years including detector installation in 2015.

15.6 Detector

We evaluate necessary detector R&D period of three years and construction time of two years. The COMET detectors, tracker, calorimeter, and cosmic-ray shield do not require any technical challenges such as the proton beam, external extinction devices, and the pion production target and capture solenoid. Therefore, we consider that construction of the detectors can be constructed in a timely manner to fit in with the whole construction schedule.

15.7 Data acquisition

The data acquisition system will be constructed using conventional techniques as described in Chapter 8. We estimate three year preparation time for setting up the DAQ system. We believe that this is sufficient to prepare the DAQ system to start engineering runs and following physics DAQ.

15.8 Simulation

Simulation will play an important role in such a rare-decay search experiment like COMET. In the schedule described here, six years are allocated for simulation development. However as in the case of other rare-decay search experiments, continuous improvements of the simulation will be required. We certainly intend to do this. Detector optimization needs reliable simulation output before construction, and later offline analysis requires full simulation for a thorough understanding of the background.

15.9 Offline analysis

The offline analysis program should be prepared together with the simulation. It is also important to provide feedback information for hardware optimization during the engineering run period. We evaluate that this development should be started sometime around 2013 in parallel to other developments and construction. Before this we need to carefully choose between employing an existing framework or developing our own.

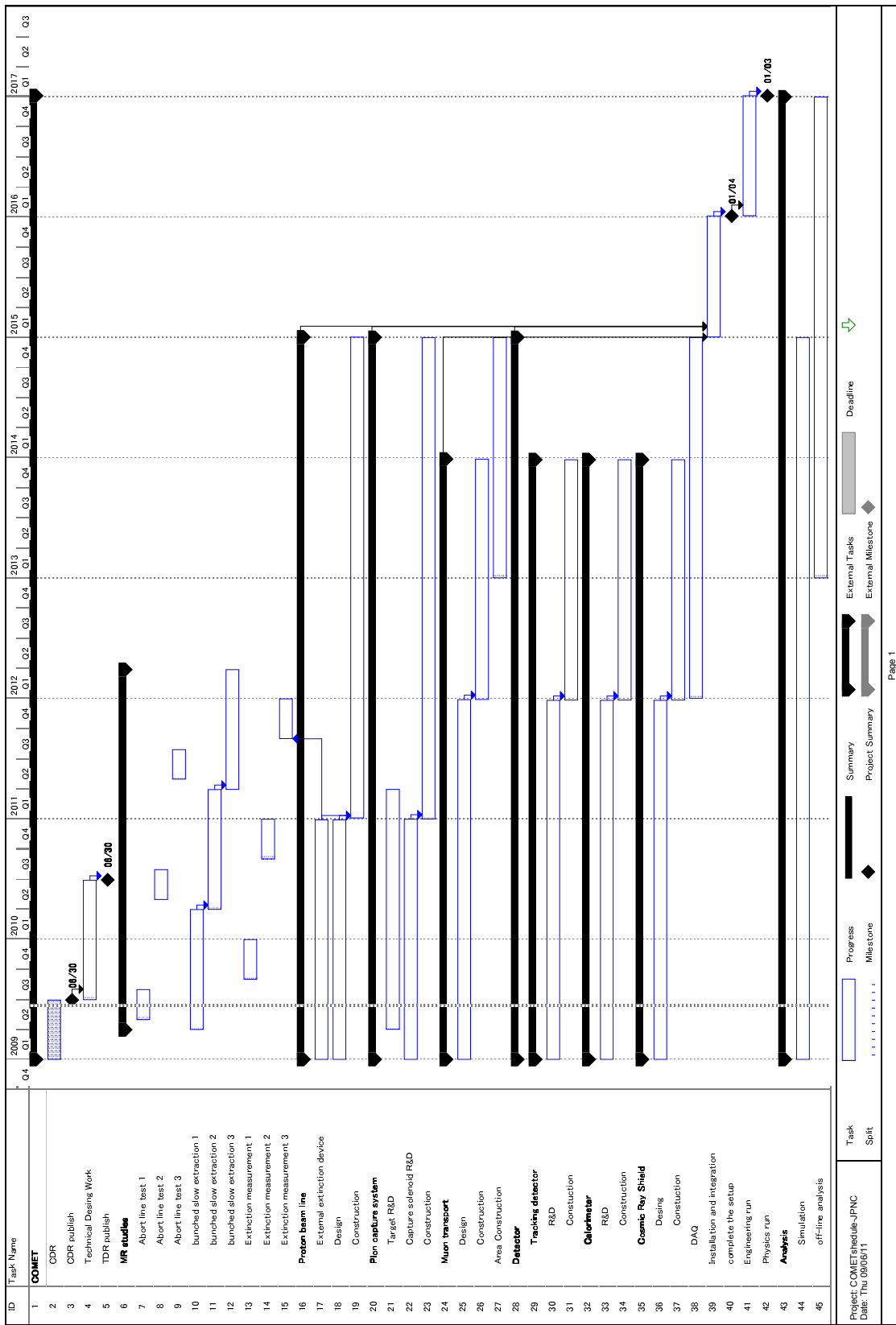


Figure 15.1: Schedule of the COMET experiment

Chapter 16

R&D Plan

In this chapter our R&D plan toward the start of experiment construction is described.

16.1 Measurement of intrinsic proton beam extinction

As repeated many times, proton beam extinction is a key issue in the COMET experiment. An achieved extinction value will determine the sensitivity of the experiment. Better extinction will provide better control of the background until we reach the sensitivity of the order of 10^{-16} .

The COMET collaboration has been working with the Muon Task Force (MTF) of KEK, which has been established to investigate facility issues to realize the COMET experiment. Extinction measurement is one of MTF's major projects. There are two methods proposed to measure the proton beam extinction [128]. One is to directly see the proton beam in the main ring (MR). Two sets of hodoscopes installed in the abort line of the MR play this role. The hodoscopes are viewed by multi-anode photomultipliers (PMTs) in the beam duct vacuum. The PMT has a very fast response while the signal dynamic range is limited. It is possible to inspect an empty bucket sitting in front of a filled bucket. We need to excite the abort line kicker so that an empty bucket is kicked to the abort before the following filled bucket arrives. Actually this can be realized by controlling the filling order of the MR buckets with protons from the RCS. Measurements will be performed during accelerator studies. The current detector is a prototype composed of plastic scintillator, which will eventually be damaged by radiation. Thus, we plan to upgrade the detector after several trials using the real proton beam and to install an extinction monitor that can permanently stay in the abort line. This monitor is suitable for accelerator studies since we can provide we can provide "quick" feed back to the accelerator. Development of this monitor is foreseen in three years in collaboration with the J-PARC accelerator group. We may also need an improvement of the chopper in the Linac.

Another method proposed by the MTF is to use the secondary beam. We measure time structure of prompt secondary beam around 1.0 GeV/c relative to the MR RF timing. The relative time distribution will be accumulated for more than 10^9 secondary particles. We need to control the momentum slit of the secondary beam line so that the mean of the number of secondary particles arriving at the counter should be around one per one proton bunch¹ in order to suppress pile-up and to reduce the ambiguity of normalization. The proton beam will be extracted from the MR with bunched-slow extraction and injected on

¹Here we suppose the bunch-to-bunch width of the proton beam of $\sim 1 \mu\text{sec}$

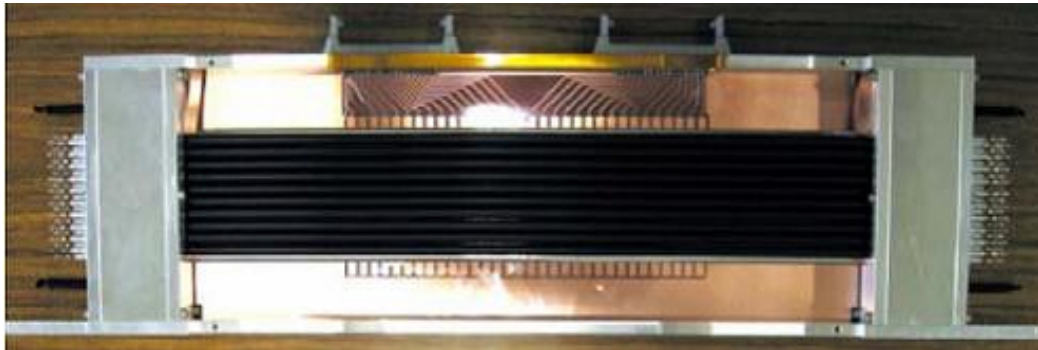


Figure 16.1: Photograph of the prototype electron tracker with seamless straw-tubes.

the T1 target in the NP hall. Spill control for bunched-slow extraction can be attempted in this study. We plan to repeat this measurement for three years. The first two years will be spent to establish the measurement technique and third year will be devoted to a special study with the external extinction device system using AC dipoles.

In our current design the proton bunch structure formation relies only on the chopper in the Linac. This might not guarantee the beam quality at a sufficient level. We have to clarify whether we need new hardware installation to improve the chopping quality during the R&D work of the proton beam extinction measurement.

16.2 Electron tracker

As already described in detail in Section 6.5, design work of the electron tracker has been almost completed including readout electronics. Prototype study has been also carried out and necessary performance has already been proven [129]. In this prototype study we successfully produced a seamless straw-tube instead of ordinary wound-type straw tubes. Seamless straw-tubes have various advantages over ordinary wound-type straw tubes, in particular, in terms of mechanical strength and narrower wall thickness. These advantages are extremely beneficial for the COMET experiment where precise electron momentum measurement around 100 MeV/c is a critical issue. Figure 16.1 shows a photograph of the prototype composed of seamless straw-tubes of 350 mm length. An anode position resolution of 112 μm has been obtained in a beam test with this prototype. We need further detailed technical design work before construction but we do not need to invest much resource for R&D work on the electron tracker.

16.3 Electron calorimeter

It is necessary to select the calorimetry material to be used. Fast response and short decay time of the signal is required so that the calorimeter signal can be used for event triggering in the data acquisition system. That helps also to associate a hit in the calorimeter with a track in a simple manner. Moderate energy resolution is probably sufficient since the tracker system provides superior information of electron momentum although this does not exclude achieving good energy and time resolutions within reasonable production cost. We are considering to use cerium doped GSO crystals or LYSO crystals as described in Section 6.6.



Figure 16.2: Photograph of stacked crystals for a prototype electron calorimeter composed of 160 GSO(Ce) crystals of $4 \times 6 \times 30$ mm 3 .

We have already started R&D work on the calorimeter using cerium doped GSO crystals. We constructed a prototype module by stacking commercially available GSO(Ce) crystals for PET application as shown in Figure 16.2. Crystal performance was investigated with PMT readout in a beam test using 150 MeV electrons. Studies with LYSO crystals have just started. Readout with MPPC was also tried taking into account operation of photo sensors in magnetic field and production cost. Results obtained in the test has been imported to Monte Carlo simulation to estimate the energy resolution of the calorimeter. Optimization including the crystal and photon detector selection is necessary.

Our R&D will proceed like the following. We will spend 1.5 years for crystal selection. Production of sample crystals has been already started in Russia and other places. Selection and performance test of the photon detector, including their readout electronics, will be performed in parallel. Candidates detectors are APD and MPPC. Although the MPPC is an attractive device, we need to investigate basic characteristics such as stability, radiation hardness, and linearity. Then we invest a half year to construct a prototype before evaluating the final prototype performance in one year. Engineering design needs to be done in parallel to this R&D work as is done in the electron tracker system.

16.4 Cosmic veto system

The cosmic veto system will be a simple detector although it is required to cover large area with sufficient uniformity. We can simply employ a conventional detector technology such as plastic scintillator with photo sensor readout or resistive plate chamber (RPC). Mechanical structure of the detector and readout system with reasonable cost will be studied for three years. Installation procedure and maintenance scenario needs to be considered carefully

since this will be a largest counter necessary to cover the whole COMET detector.

16.5 Superconducting magnet

The pion capture solenoid will be constructed by using an aluminum stabilized conductor as described in Chapter 12. Specification of the conductor is summarized in Table 12.1. The coil itself must be thin to reduce radiation load. This is the reason why we selected this conductor. Strength of the electromagnetic force between the cold mass and return yoke will be as large as 160 t. This means that careful design is necessary although we can build a rigid support structure differently from usual spectrometer magnets necessary to be transparent including whole structure. Quench protection design has been already considered based on our experience. The cooling scheme must be examined to realize operation at 5 K under COMET radiation load condition with allowed temperature increase of 1.3 K. There are certainly many technical issues involved in the construction. However almost all of them are thought to be cleared without critical difficulties based on our experience accumulated in KEK Cryogenic Center.

Construction of muon transport and stopping target solenoids is expected to be easier since field strength is less than that of the capture solenoid and radiation load will be also less. The conductor used for them will be NbTi copper stabilized conductor, which is widely used in MRI magnets and commercially available. Quench protection design is already in our scope as in the case of the capture solenoid. We are conducting R&D work to study the structure of the curved solenoid. The solenoid will be constructed by arranging coil “pancakes” electrically and thermally connected in series along the curve. We are studying basic parameters like cooling performance and electromagnetic forces between pancakes by constructing a prototype comprising of three pancakes (Fig. 16.3). After completing this R&D work for about one year, we will start the engineering design of the magnet.

We plan to utilize a new type of super-conductor, MgB₂, for electron-transport and detector solenoids. We do not have much experience with this conductor for magnet construction. In this sense we probably need certain R&D work to finalize the design. However the estimated critical temperature will be as high as 28 K for these solenoids, providing us a sufficient temperature margin for operation. Thus effort in R&D work will be to study how much we can tolerate critical design parameters compared to other solenoids using NbTi conductors. For these reasons, the cryogenic center of KEK and Osaka University has decided to construct one prototype coil for the muon transport using MgB₂ superconductor. The MgB₂ superconductor were purchased from an Italian manufacture company and the coil construction was completed. Tests of the coil are underway.

16.6 Pion production target

Significant R&D work is thought to be necessary for the pion production target, but a tungsten target with water cooling can probably be adopted as described in Chapter 5. It is preferred to use a heavier metal target since a larger pion production rate is expected. When constructing the target, target cooling under radiation dose needs to be carefully considered otherwise the target would melt down. Supporting structure design including realization of cooling will be done with complete 3-dimensional modeling and finite element analysis. The system will stay in a heavy radiation environment. Due to this, a maintenance scenario needs to be carefully considered for the case of unexpected failure of the target

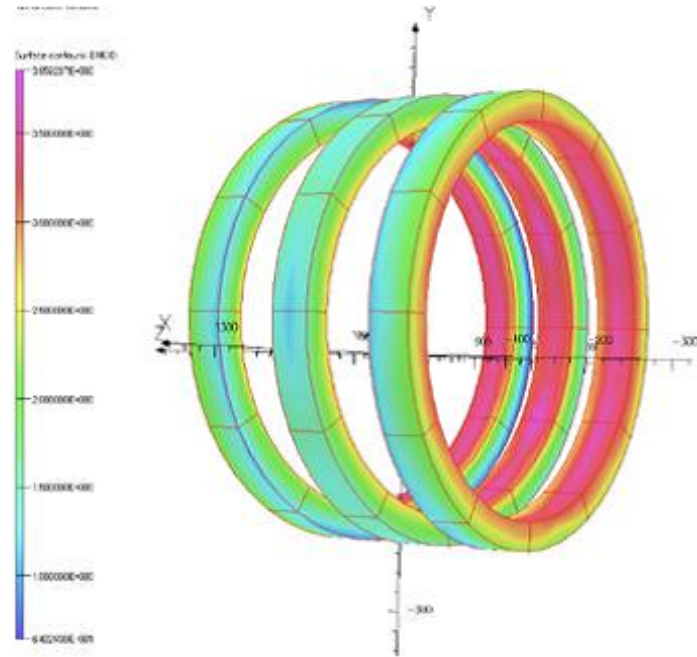


Figure 16.3: Arrangement of three “pancake” coils for R&D work.

system. A graphite target with gas helium cooling is considered as a backup solution. This type of target has been developed and employed in the T2K experiment and is known to work stably although we need to take into account periodic maintenance work since graphite would deteriorate after certain amount of radiation on it.

Chapter 17

Summary

This report presents the conceptual design of a new experiment, COMET (COherent Muon to Electron Transition), to search for coherent neutrino-less conversion of muons to electrons ($\mu^- - e^-$ conversion), in the presence of a nucleus, $\mu^- + N(A, Z) \rightarrow e^- + N(A, Z)$, with a single event sensitivity $B(\mu^- N \rightarrow e^- N) < 10^{-16}$.

Flavor transitions between the charged leptons (Charged Lepton Flavor Violation, cLFV) have great potential to reveal new physics phenomena beyond the Standard Model. Many models of such physics, such as those based on supersymmetric grand unification (SUSY-GUT), supersymmetric seesaws (SUSY-Seesaw) and extra dimensions, require the existence of cLFV that is accessible to realizable future experiments.

Muons provide the best laboratory to study cLFV as they can be produced in substantial numbers and have a sufficiently long lifetime for precise measurements of their decays. Present accelerators can produce about 10^{15} muons/year, and it is anticipated that it will be possible to produce 10^{18} – 10^{19} muons/year with a new high intensity source that is proposed in conjunction with the main J-PARC proton synchrotron ring (MR).

The main processes which are accessible for cLFV are the decays $\mu \rightarrow e\gamma$, $\mu \rightarrow eee$ and $\mu^- - e^-$ conversion. Of these, $\mu^- - e^-$ conversion has the best sensitivity to new physics, as the potentially measurable branching ratio of about 10^{-16} is significantly better than the limits expected with current technology for the $\mu \rightarrow e\gamma$, $\mu \rightarrow eee$ processes. Within the Standard Model, modified to take account of neutrino oscillation, the expected rate is less than 10^{-50} and so any observation of a $\mu^- - e^-$ conversion would be a clear signal of physics beyond the Standard Model. A measurement $\leq 10^{-16}$ for $\mu^- - e^-$ conversion, which is the COMET goal, is a factor of 10,000 better than that of current experiments.

This report present a new experiment (COMET) of searching for coherent neutrino-less $\mu^- - e^-$ conversion in a muonic atom of aluminum, $\mu^- + Al \rightarrow e^- + Al$, at a sensitivity of $B(\mu^- Al \rightarrow e^- Al) < 10^{-16}$ at J-PARC.

COMET will use a bunched proton beam, slow-extracted from the J-PARC MR. Beam bunching will be necessary to reject beam-related backgrounds. The experimental setup consists of high magnetic-field solenoids for pion capture, C-shaped curved solenoids with momentum selection, and a C-shaped curved solenoid spectrometer. The experiment will require about 2×10^{18} stopping muons, which, with the expected transmission of muons in our muon beamline, will require about 8.5×10^{20} protons of 8 GeV on target.

This new initiative has been taken to achieve an early and timely start of a series of searches for $\mu^- - e^-$ conversion. We consider that the proposed experiment would have large opportunity for great discovery and J-PARC is the best proton facility to carry out this

important experiment.

Bibliography

- [1] Neddermeyer S.H., and Anderson C. D., 1937, *Phys. Rev.* **51** 884
- [2] Yukawa H, 1935, *Proc. Math. Soc. Jpn.* **17** 48
- [3] Heitler W, 1938, *Proc. R. Soc. London A* **166** 529
- [4] Nordheim L W, 1939, *Phys. Rev.* **55** 506
- [5] Sakata S, and Inoue, T, 1946, *Prog. Theor. Phys.* **1** 143
- [6] Tanikawa Y, 1947, *Prog. Theor. Phys.* **2** 220
- [7] Conversi M. , Pancini E. , and Piccioni O. 1947 *Phys. Rev.* **71** 209
- [8] Pontecorvo B, 1947 *Phys. Rev.* **72** 246
- [9] Hincks E P and Pontecorvo B, 1947 *Phys. Rev.* **73** 246
- [10] Steinberger J, 1948 *Phys. Rev.* **74** 500
- [11] Lagarrigue A, and Peyrou C, 1952, *Acad. Sci. Paris, C. R.* **234** 873
- [12] Lokonathan S , and Steinberger J, 1955, *Phys. Rev.* **98** 240
- [13] Steinberger J, and Wolfe H. B. 1955 *Phys. Rev.* **100** 1490
- [14] Nishijima K, 1957 *Phys. Rev.* **108** 907
- [15] Schwinger J, 1957 *Ann. Phys.* **2** 407
- [16] Danby G, *et al.* *Phys. Rev. Lett.* **9** 36
- [17] Maki Z, Nakagawa M, and Sakata S, *Prog. Theor. Phys.* **28** 870
- [18] Kobayashi M, and Maskawa T, *Prog. Theor. Phys.* **49** 652
- [19] Brooks M L *et al.* (MEGA Collaboration) 1999 *Phys. Rev. Lett.* **83** 1521
- [20] Bellgardt U *et al.* 1988 *Nucl. Phys. B* **229** 1
- [21] Wintz P 1998 in *Proceedings of the First International Symposium on Lepton and Baryon Number Violation*, edited by H.V. Klapdor-Kleingrothaus and I.V. Krivosheina (Institute of Physics Publishing, Bristol and Philadelphia), p.534. Unpublished.
- [22] Burtl W *et al.* (The SINDRUM II Collaboration) 2006 *Eur. Phys. J. C* **47** 337

- [23] Willmann L *et al.* 1999 *Phys. Rev. Lett.* **82** 49
- [24] Hayasaka K *et al.* (Belle Collaboration) 2005 *Phys. Lett. B* **613** 20
- [25] Abe K *et al.* (Belle Collaboration) 2004 *Phys. Rev. Lett.* **92** 171802
- [26] Aubert B *et al.* (BaBar Collaboration) 2004 *Phys. Rev. Lett.* **92** 121801
- [27] Krolak P *et al.* 1994 *Phys. Lett. B* **320** 407
- [28] Ambrose D *et al.* (BNL E871 Collaboration) 1998 *Phys. Rev. Lett.* **81** 5734
- [29] Lee A M *et al.* 1990 *Phys. Rev. Lett.* **64** 165
- [30] Arisaka K *et al.* 1998 *Phys. Lett. B* **432** 230
- [31] Akers R *et al.* (OPAL Collaboration) 1995 *Z. Phys. C* **67** 555
- [32] Abreu P *et al.* (DELPHI Collaboration) 1997 *Z. Phys. C* **73** 243
- [33] Fukuda Y, *et al.* (Super-Kamiokande Collaboration) 1988 *Phys.Rev.Lett.* **81** 1562-1567
- [34] Fukuda S, *et al.* (Super-Kamiokande Collaboration) 2001 *Phys.Rev.Lett.* **86** 5656
- [35] Cheng T. P., and Li L. -F. , 1977 *Phys. Rev. D* **16** 1425
- [36] . Lee B. Robert Shrock R, , 1977 *Phys. Rev. D* **16** 1444
- [37] Petcov S. T, 1977 *Sov. J. Nucl. Phys* **25** 340
- [38] Marciano W, and Sanda A. -I 1977 *Phys.Lett. B* **67** 303
- [39] Glashow S. L, Iliopoulos J, and Maiani L, 1970 *Phys. Rev. D* **2** 1285
- [40] Datta A, Kong K, and Matchev K. T. 2005 *Phys. Rev D* **72** 096006
- [41] Kuno Y and Okada Y, 2001 *Rev. of Mod. Phys.* **73** 151
- [42] Yanagida T, in *Proceedings of the Workshop on Unified Theory and Baryon Number of the Universe*, edited by Sawada and Sugamoto, Report KEK-79-18 (1979); Gell-Mann M, Ramond P, and Slansky R, in *Supergravity*, edited by D.Z. Freedman and P. van Nieuwenhuizen (North-Holland, Amsterdam, 1979)
- [43] F. Borzumati and A. Masiero, 1986 *Phys. Rev. Lett* **57** 961.
- [44] Hisano J, Moroi T, Tobe T, Yamaguchi M, and Yanagida T 1995 *Phys. Lett. B* **357** 576
- [45] Hisano J and Nomura D 1999 *Phys. Rev. D* **59** 116005
- [46] Sato J amd Tobe T, 2001 *Phys. Rev. D* **64** 113016
- [47] Cirigliano V, Kitano R, Okada Y, and Tuzon P, arXiv:0904.0957v1 [hep-ph]
- [48] Arkani-Hamed N , Cohen A. G., and Georgi H , 2001 *Phys.Rev.Lett.* **86** 4757
- [49] Arkani-Hamed N, Cohen A.G. , Katz E, and Nelson A E. 2002 *JHEP* **0207** 034

- [50] Cheng H.-C, Low I, 2003 *JHEP* **0309** 051
- [51] Hubisz J, Lee S, and Paz G, 2006 *JHEP* **0606** 041
- [52] Choudhury S. R., Cornell A. S., Deandrea A, Gaur N, and Goyal A, 2007 *Phys. Rev. D* **75** 055011
- [53] Blanke M, Buras A. J., Duling B, Poschenrieder A, Tarantino C 2007 *JHEP* **0705** 013
- [54] Aguila F, Illana J.I. , Jenkins M. D., 2009 *JHEP* **0901** 080
- [55] Randall L, and Sundrum R, 1999 *Phys. Rev. Lett.* **83** 3370
- [56] Appelquist T , Cheng H. -C , and Dobrescu B, 2001 *Phys. Rev. D* **64** 035002
- [57] Grossman Y, and Neubert M, 2000 *Phys. Lett. B* **474** 361
- [58] Gherghetta T, and Pomarol A, 2000 *Nucl. Phys. B* **586** 141
- [59] Agashe K, Blechman A, and Petriello F, 2006 *Phys. Rev. D* **74** 053011
- [60] Matsumoto S , Sato J , Senami M , and Yamanaka M, 2007 *Phys. Lett. B* **647** 466
- [61] Masiero A, Profumo S, Vempati S K, and Yaguna C E 2004 *JHEP* 0403:046
- [62] Shanker O 1982 *Phys. Rev. D* **25** 1847
- [63] Watanabe R, Fukui M, Ohtsubo H and Morita M, 1987 *Prog. Theor. Phys.* **78** 114; Watanabe R, Muto K, Oda T, Niwa T, Ohtsubo H, Morita R and Morita M, 1993 *At. Data Nucl. Data Tables* **54** 165
- [64] Bryman D A, Blecher M, Gotow K and Powers R J 1972 *Phys. Rev. Lett.* **28** 1469
- [65] Badertscher A *et al.* 1982 *Nucl. Phys. A* **377** 406
- [66] Bryman D A *et al.* 1985 *Phys. Rev. Lett.* **55** 465
- [67] Ahmad S *et al.* 1988 *Phys. Rev. D* **38** 2102
- [68] Dohmen C *et al.* (SINDRUM II Collaboration) 1993 *Phys. Lett. B* **317** 631
- [69] Honecker W *et al.* (SINDRUM II Collaboration) 1996 *Phys. Rev. Lett.* **76** 200
- [70] Bachman M *et al.* 1997, a research proposal to Brookhaven National Laboratory AGS “A Search for $\mu^- N \rightarrow e^- N$ with Sensitivity Below 10^{-16} , Muon – Electron COnversion”
- [71] “Proposal to Search for $\mu^- + N \rightarrow e^- N$ with a Single Event Sensitivity Below 10^{-16} (Mu2e Experiment)” by the Mu2e collaboration, Fermilab, October 10, 2008.
- [72] Barkov L M *et al.* 1999, a research proposal to PSI “Search for $\mu^+ \rightarrow e^+ \gamma$ down to 10^{-14} branching ratio”
- [73] Futo Y *et al.* 2008 *Proc. of the 30th ICRC* **2** 203-206
- [74] Ikegami M 2007 *High Energy Physics News, JAHEP* **25-4** 177

- [75] Tomizawa M *et al.* 2002 *EPAC2002*, 1058-1060
- [76] Kiyomichi A *et al.* 2007 *Proc. of the 4th Annual Meeting of Particle Accelerator Society of Japan*, 410-412
- [77] Carey D. C., Brown K. L., and Rothacker F. 1998 *A Computer Program for Designing Charged Particle Beam Transport Systems*, Fermi National Laboratory
- [78] N.V. Mokhov, "The Mars Code System User's Guide", Fermilab-FN-628 (1995); O.E. Krivosheev, N.V. Mokhov, "MARS Code Status", Proc. Monte Carlo 2000 Conf., p. 943, Lisbon, October 23-26, 2000; Fermilab-Conf-00/181 (2000); N.V. Mokhov, "Status of MARS Code", Fermilab-Conf-03/053 (2003); N.V. Mokhov, K.K. Gudima, C.C. James *et al.*, "Recent Enhancements to the MARS15 Code", Fermilab-Conf-04/053 (2004); <http://www-ap.fnal.gov/MARS/>.
- [79] *Nucl. Inst. and Meth. A* **506** (2003) 250-303; *IEEE Transactions on Nuclear Science* **53** No. 1 (2006) 270-278.
- [80] Thomas J. Roberts *et al.*, "G4beamline Particle Tracking in Matter-Dominated Beam Lines", EPAC'08, Genoa (2008), p. 2776.
- [81] Computer Simulation Technology Electro-magnetic Studio,
<http://www.cst.com/Content/Products/EMS/Overview.aspx>
- [82] The MECO experiment, see <http://mu2e.fnal.gov/public/GeneralInformation.shtml>
- [83] W. Bloom and L. Rolandi, **Particle Detection with Drift Chambers**, Springer-Verlag, 1993
- [84] <http://www.cern.ch/garfield>
- [85] P. V. Vavilov, *Sov. Phys. JEPT* **5**(1957)749; L. D. Landau, *J. Phys USSR* **8**(1944)201
- [86] **Review of particle Properties**, *Phys. Rev. D***66**(2002)010001-195; U. Fano, *Ann. Rev. Nucl. Sci.* **13**(1963)1
- [87] I. Lehraus, *et al.*, *Nucl. Inst. and Meth.* **153**(1982)3 61
- [88] <http://cyclo.mit.edu/drift/www/>
- [89] T.J. Liu MECO Technical Report 38, Unpublished
- [90] Clearcast LU, US Epoxy, Inc., 268 Route 112, Patchogue, NY 11772
- [91] G. Xu and E. V. Hungerford, *IEEE Trans. on Nucl. Sci.* **53**(2006)549
- [92] J. M. Butler, *et al.*, *Nucl. Inst and Meth.* bf A290(1990)122;
- [93] V. Bondarenko, *et al.*, Technical report, CERN (unpublished);
- [94] C. Kendziora, *et al.*, FERMILAB-PUB-02-241-E, Oct 2002.
- [95] J. Popp, MECO Vacuum Memo 32 Unpublished, 2005
- [96] G. De Cataldo, *et al*, *Nucl. Inst. and Meth.* **A409**(1998)73; E. Barbarito, *et al.*, *Nucl. Inst. and Meth.* **A381**(1996)39.

- [97] F. M. Newcomer, *et al.*, *IEEE Trans. Nucl. Sci.* **43**(1996)1725; T. Akesson, *et al.*, *Nucl. Inst and Meth.* **449**(2000)446; R. L. Chase, *et al.*, *Nucl. Inst and Meth.* **A409**(1998)328
- [98] O. Sasaki and M. Yshida, *IEEE Trans. on Nucl. Sci.* **46**(1999)1871
- [99] R. Szczygiel, *Meas. Sci. Tech.* **18**(2007)2413
- [100] H. Hamrita, *et al.*, *Nucl. Inst. and Meth. A* **531**(2004)607
- [101] B. Lewandowski, *Nucl. Inst. and Meth. A* **494**(2002)21
- [102] S. F. Dow, *et al.*, *IEEE Trans. Nucl. Sci.* **46**(1999)785; A. J. Lanford, *Nucl. Inst. and Meth.* **409**, (1998) 654.
- [103] L. I. Ruckman and G.S. Varner, arXiv:0805.2225 15 May 2008
- [104] S. Ritt, *IEEE Nucl. Sci. Conference Record*, **4** (2007)2485
- [105] Hamamatsu Co., "MPPC technical information", (2009)
- [106] M. Yokoyama *et al.*, "Mass production test of Hamamatsu MPPC for T2K neutrino oscillation experiment," arXiv:0807.3147 [physics.ins-det].
- [107] K. Deiters *et al.*, *Nucl.Instrum. and Meth. A* 461 (2001) 574-576
- [108] A. Vacheret, M. Noy, M. Raymond and A. Weber, "First results of the Trip-t based T2K front end electronics performance with GM-APD," PoS **PD07**, 027 (2006).
- [109] Y. G. Budyashov, *Soviet Physics JETP* 33, 11 (1971); P. Singer, *Springer Tracts in Modern Physics* 71, 39 (1974); S. Sobottka and E. L. Wolls, *Phys. Rev. Lett.* 20, 596 (1967); L. Vilgelmova *et al.*, *Sov. J. Nucl. Phys.* 13, 310 (1971); A. Wytttenbach *et al.*, *Helv. Phys. Acta* 49, 776 (1976)
- [110] N. Mukhopadhyay, *Rep. Prog. Phys.* 30, 1 (1977); T. Kozlowski, *Nucl. Phys.* A436, 717 (1985)
- [111] F. J. Hartmann *et al.*, *Z. Phys. A***305** (1982)189
- [112] M. Bonesini, "Particle production vs. energy: how do simulation results match experimental measurements?", Proceedings of Science(Nufact08)092, (2008)
- [113] O. Shanker, *Phys. Rev. D* 25 (1982) 1847.
- [114] R. Watanabe *et al.*, *Atomic Data and Nucl. Data Tables* 54 (1993) 165.
- [115] MECO Technical Proposal, August 1, 2001, unpublished.
- [116] W.U.. Schröder *et al.*, *Z. Phys.* 268 (1973) 57–64.
- [117] Kozlowski T *et al.*, 1985 *Nucl. Phys. A* **436** 717
- [118] Wytttenbach A *et al.*, 1978 *Nucl. Phys. A* **294** 278
- [119] Krane K S *et al.*, 1979 *Phys. Rev. C* **20** 1873
- [120] J.E. Amaro *et al.*, *Nucl. Phys. A* 623 (1997) 529–547.

- [121] O.C. Allkofer, K. Carstensen and W.D. Dau, *Phys. Lett. 36B* (1971) 425–427.
- [122] J. Kempa and I.M. Brancus, *Nucl. Phys. B* 122 (2003) 279–281.
- [123] Description of the Double-HelixTMtechnique,
<http://www.magnetlab.com/technology/double-helix/>
- [124] J. R. Sanford and C. L. Wang, Brookhaven National Laboratory, AGS internal report, 1967 (unpublished); C. L. Wang, *Phys. Rev. Letters* 25, 1068 (1970); ibid. 25, 1536(E) (1970).
- [125] K.H. Tanaka *et al.*, KEK Internal Report 2002-8.
- [126] W. Ootani *et al.*, Proceedings of 18th International Conference on Magnet Technology.
- [127] Palmer R B and Berg J S, 2004 in *Proceedings of EPAC 2004*, Lucerne, Switzerland p.1807.
- [128] Muon Task Force Report, J-PARC PAC meeting, Unpublished
- [129] Y. Takubo *et al.*, *Nucl. Inst. and Meth. A* **551** (2005) 271